PHYSIK - DEPARTMENT

CHAIR FOR EXPERIMENTAL PHYSICS AND ASTROPARTICLE
PHYSICS, E15

Lepton track reconstruction in LENA and attenuation length measurements in liquid scintillators

Diploma Thesis

DOMINIKUS HELLGARTNER
8. APRIL 2011

TECHNISCHE UNIVERSITÄT MÜNCHEN

Abstract

Liquid scintillator detectors, like the proposed 50 kt LENA (**L**ow **E**nergy **N**eutrino **A**stronomy) detector, are generally known for their low energy threshold and their high energy resolution. Just recently, it was realized that a reconstruction of lepton tracks with energies above a few 100 MeV is possible in liquid scintillator detectors, despite the isotropic light emission, by exploiting the arrival times of the photons.

In the scope of this thesis a reconstruction algorithm for sub-GeV neutrino events in LENA was developed. The performance of this algorithm was determined by tests on events simulated with a Geant4-based Monte Carlo code.

First, methods were devised to discriminate between electron and muon tracks. As the performance of the pulse-shape analysis was found to be unsatisfactory regarding the electron contamination of the muon-track identification below 1 GeV, the algorithm developed in this thesis uses the distinct signal of the muon decay to select muon tracks.

As a preliminary stage, a reconstruction for pure electron and muon tracks was developed. It utilizes a likelihood fit to the integrated charge and the arrival time of the first detected photon at each PMT. With this method, a vertex resolution between 2 and 7 cm, an angular resolution from 1.5 to 5 degrees and an energy resolution of about 0.5% were achieved. The performance of the muon-track fit was found to be superior to the electron-track fit. Subsequently, the reconstruction was modified to include the interaction vertex in the track fit. To constrain the energy range, a β-beam from CERN to Frejus was assumed, with the focus on the $\overset{(-)}{\nu_\mu}$ appearance channel. At the low energies of the β-beam, the predominant interaction channel is quasi-elastic scattering off a nucleon. Hence, the event topology assumed for the fit consists of a quasi-pointlike vertex and an additional lepton track. It was found that final-state muon tracks with kinetic energies above 200 MeV can be reliably reconstructed. The results of the track fit were subsequently used to reconstruct the neutrino energy, assuming the target nucleon to be at rest. Due to nuclear effects, the obtained energy resolution was not optimal. It was found that better results can be obtained by determining the incident neutrino energy exploiting the overall number of photons detected in the event. A discovery potential for a $\gamma = 100$ β-beam from CERN to Frejus with LENA as far detector was determined. The 3-σ discovery potential for $\sin^2(2\vartheta_{13})$ was found to be at about 10^{-2}. Furthermore, results show that the discovery potential is currently limited by $\pi^\pm$ background. Therefore, to further improve the discovery potential, a better algorithm to discriminate against $\pi^\pm$ is necessary.

Due to the large size of the LENA detector, the energy threshold, the energy resolution, and the tracking and position reconstruction capabilities of will primarily be determined by the attenuation length of the scintillator. Furthermore, the attenuation length is an important input parameter for Monte Carlo simulations. In the scope of this thesis, an experiment to measure the attenuation length of liquid scintillators was designed and constructed. Compared to former experiments, it featured a significantly longer measuring length (3 m) in order to precisely measure also scintillators with relatively large attenuation lengths of $\gtrsim 10$ m. Although, there are currently no conclusive results, we show that the experiment can be improved by better optics and by removing contaminations from the scintillator.

Contents

Chapter 1

Introduction: Neutrinos

To be able to explain the experimentally observed features of the beta decay without violating energy and (angular) momentum conservation, Pauli proposed the neutrino in 1930 [1]. After this proposal it took nearly 30 years until Reines and Cowan finally detected neutrinos [2].

Today, more than 50 years after its discovery, some neutrino properties like the mixing angle ϑ_{13}, the CP-violating phase δ, the mass hierarchy and, in particular, if neutrinos are Majorana or Dirac particles, remain totally unknown. Nevertheless, neutrinos have already been used to probe astrophysical objects like the sun and supernovae. Hence, the proposed 50 kt LENA detector has been designed as a next-generation detector for low-energy neutrino astrophysics, motivated by the outstanding success of its predecessors Borexino [3] and KamLAND [4]. Until recently, liquid scintillator detectors were confined to neutrino energies at the MeV scale, as their ability to reconstruct higher energy events was doubted. The basic problem is the isotropic photon emission in a scintillator which does not allow to reconstruct a track via the observed charge distribution, as it is common practice in water Cerenkov detectors. Track reconstruction is nevertheless possible in liquid scintillators by exploiting the arrival time pattern of the detected photons [5, 6]. This allows reconstructing neutrino events at the GeV scale. Possible sources of neutrinos in this energy range are atmospheric neutrinos or long-baseline neutrino beams extending the LENA physics program to the search for the missing neutrino mixing parameters.

As previous work on the reconstruction of high-energy neutrino interactions in a liquid scintillator was predominantly done in the regime of above-GeV neutrino energies, a reconstruction algorithm for sub-GeV neutrino events was developed in this thesis. The performance of the algorithm was evaluated using a Geant4-based Monte Carlo simulation of the LENA detector. Finally, the resulting performance of LENA as a far detector of a beta beam in terms of the ϑ_{13} discovery potential was evaluated.

In the current chapter a brief overview of the present knowledge of neutrino physics including the most common detection techniques for neutrinos will be given. Chapter 2 will outline the experimental setup as well as the physics program of the LENA detector. A fundamental requirement of any neutrino event reconstruction is the ability to discriminate quasi-elastic charged-current events induced by different neutrino flavors. As this is possible by determining the flavor of the created lepton, Chapter 3 will present the results of different approaches to discriminate between electron and muon tracks. As an initial step towards a complete event reconstruction, an algorithm to reconstruct single muon and electron tracks will be detailed in Chapters 4 and 5 together with its obtained

performance. After introducing the basic concepts and properties of a β-beam, Chapter 6 will describe an advanced algorithm to reconstruct complete neutrino events along with the performance for β-beam events. It will conclude with a determination of the ϑ_{13} discovery potential of a $\gamma = 100$ β-beam from CERN to Frejus with LENA as a far detector. Supplementing the work on the track reconstruction, Chapter 7 will focus on the set-up and the construction of a laboratory-scale experiment to determine the attenuation length of different liquid scintillators. It is an important input quantity for Monte Carlo simulations as well as for the decision which scintillator to use in LENA.

1.1   Neutrinos in the standard model

The standard model of particle physics (SM) contains three families of different lepton flavors. Each flavor consists of a charged lepton and the corresponding neutrino as well as the respective antiparticles. While the charged leptons can be right-handed as well as left-handed, the neutrinos are left handed by definition. Hence, the lepton states of the SM are arranged in left handed isospin doublets and right handed isospin singlets

$$\begin{pmatrix} \nu_e \\ e^- \end{pmatrix}_L , \begin{pmatrix} \nu_\mu \\ \mu^- \end{pmatrix}_L , \begin{pmatrix} \nu_\tau \\ \tau^- \end{pmatrix}_L , e_R^- , \ \mu_R^- , \ \tau_R^- , \tag{1.1}$$

where the indexes L and R denote left handed and right handed fields [7]. The absence of right handed neutrinos in the SM implies that the neutrino mass is exactly zero. A non vanishing neutrino mass would lead to a nonconservation of neutrino chirality and therefore to the appearance of right handed neutrinos.

As neutrinos do neither carry electric nor strong charge they couple only to the weak gauge bosons $W^\pm$ and Z^0. The energy scales dealt with in this thesis are below 1 GeV and therefore far below the scale of electroweak unification, leading to a strong suppression of neutrino interaction probabilities due to the mass of the gauge bosons. Typical neutrino cross sections within this energy region are in the order of $\sigma_\nu \sim 10^{-42}\,\text{cm}^2$ [8].

Several experimental results can only be explained by neutrino flavor oscillations which in turn require a non vanishing neutrino mass contrary to the SM. This is detailed in the following sections.

1.2   Vacuum neutrino oscillations

Extending the SM to massive neutrinos can be done in two ways. The most straight forward solution is to include right handed neutrinos. This immediately allows introducing the neutrino mass by a Yukawa coupling to the Higgs field. In this case neutrinos can be described by Dirac's equation, therefore, they are called Dirac neutrinos [7].

Ettore Majorana [9] proposed a different approach. He introduced neutrino masses assuming that the neutrino is its own antiparticle. Therefore the right handed neutrino normally needed for a mass term is replaced by the charge conjugated left handed neutrino. The created mass terms violate lepton number L: $\Delta L = 2$. These neutrinos are called Majorana neutrinos [8].

Regardless which mechanism nature has chosen, introducing neutrino masses allows a separation between neutrino mass eigenstates $|\nu_i\rangle$, $i \in \{1, 2, 3\}$ and the eigenstates of

weak interaction $|\nu_\alpha\rangle$, $\alpha \in \{e, \mu, \tau\}$. These two orthogonal bases are connected by the unitarian Pontecorvo-Maki-Nakagawa-Sakata matrix U which is the equivalent to the CKM-matrix in quark mixing [7]

$$|\nu_\alpha\rangle = \sum_i U_{\alpha i}|\nu_i\rangle \ \longleftrightarrow \ |\nu_i\rangle = \sum_\alpha U^*_{\alpha i}|\nu_\alpha\rangle. \tag{1.2}$$

For antineutrinos $U_{\alpha i}$ has to be replaced by $U^*_{\alpha i}$.
In the three flavor case U is commonly parametrized as [10]

$$U = \begin{pmatrix} c_{12}c_{13} & s_{12}c_{13} & s_{13}e^{-i\delta} \\ -s_{12}c_{23} - c_{12}s_{23}s_{13}e^{-i\delta} & c_{12}c_{23} - s_{12}s_{23}s_{13}e^{-i\delta} & s_{23}c_{13} \\ s_{12}s_{23} - c_{12}c_{23}s_{13}e^{-i\delta} & -s_{12}c_{23} - s_{12}c_{23}s_{13}e^{-i\delta} & c_{23}c_{13} \end{pmatrix} \cdot \begin{pmatrix} e^{i\alpha_1/2} & & \\ & e^{i\alpha_2/2} & \\ & & 1 \end{pmatrix}, \tag{1.3}$$

where c_{ij} and s_{ij} is short for $\cos(\vartheta_{ij})$ and $\sin(\vartheta_{ij})$, respectively, with the mixing angles ϑ_{ij}. δ and $\alpha_{1,2}$ are CP-violating phases. As $\alpha_{1,2}$ only influence physics for neutrinoless double beta decay experiments, i.e. are only relevant if the neutrino is a Majorana particle, but do not affect neutrino oscillation, they are omitted from this point on.

Neutrinos are produced and detected via weak interaction. Thus, the flavor basis is used to calculate transition matrix elements. Contrary, neutrino propagation has to be calculated using the mass eigenstates to make the kinetic energy a good quantum number. Assuming a continuous source, propagation can be described by plane waves[1]

$$|\nu_i(t)\rangle = \exp(-iE_i t) \ |\nu_i(0)\rangle. \tag{1.4}$$

The total energy E_i of a neutrino can be expressed as a function of the neutrino mass m_i and the neutrino momentum p_i

$$E_i = \sqrt{\boldsymbol{p}_i^2 + m_i^2} \approx |\boldsymbol{p}| + \frac{m_i^2}{2|\boldsymbol{p}|} \approx E + \frac{m_i^2}{2E}, \tag{1.5}$$

where $m_i \ll |\boldsymbol{p}_i|$ is assumed which is true for every measurable neutrino source. Furthermore, the assumption is used that all mass eigenstates have the same momentum $\boldsymbol{p}_i = \boldsymbol{p}$. The probability $P(\alpha \to \beta)$, that a neutrino produced in flavor eigenstate $|\nu_\alpha\rangle$ is detected in flavor eigenstate $|\nu_\beta\rangle$, is the squared modulus of the transition amplitude:

$$P(\alpha \to \beta) = |\langle\nu_\beta|\nu(t)\rangle|^2, \qquad |\nu(t=0)\rangle = |\nu_\alpha\rangle. \tag{1.6}$$

Using Equations (1.2),(1.4) and (1.5) and the approximation $v_\nu/c \approx 1$, Equation (1.6) can be transformed to [7, 10]

$$P(\alpha \to \beta) = \sum_{i,j} U_{\alpha i}U^*_{\beta i}U^*_{\alpha j}U_{\beta j} \exp(-i2\Delta_{ij}) = \tag{1.7}$$

$$= \delta_{\alpha,\beta} - 4\sum_{i>j}\Re(U^*_{\alpha i}U_{\beta i}U_{\alpha j}U^*_{\beta j})\sin^2(\Delta_{ij}) + 2\sum_{i>j}\Im(U^*_{\alpha i}U_{\beta i}U_{\alpha j}U^*_{\beta j})\sin(2\Delta_{ij}) \tag{1.8}$$

$$\Delta_{ij} = 1.27 \, \frac{m_i^2 - m_j^2}{\text{eV}^2}\frac{L}{\text{km}}\frac{\text{GeV}}{E} =: \pi\frac{L}{L_0}, \tag{1.9}$$

---

[1]Here the convention $\hbar = c = 1$ is used.

where L is the distance between source and detection and L_0 the oscillation length.

The probability to detect a neutrino emitted in the flavor eigenstate $|\nu_\alpha\rangle$ in a different flavor eigenstate $|\nu_{\beta \neq \alpha}\rangle$ is therefore non-vanishing and oscillating in space, a behavior commonly called neutrino oscillation. Note that this phenomenon only occurs if not all $\Delta m_{ij}^2 = m_i^2 - m_j^2 \equiv 0$. Therefore, the observation of neutrino oscillations immediately implies that there is at least one mass eigenstate with an non vanishing rest mass.

Equation (1.9) shows that the oscillation frequency is proportional to $\Delta m_{ij}^2/E$, whereas the amplitude is given by the mixing matrix elements (cf. Equation (1.8)), i.e. by the mixing angles and the CP violating phase.

The last part of Equation (1.8) only contributes if $(U_{\alpha i}^* U_{\beta i} U_{\alpha j} U_{\beta j}^*) \notin \mathbb{R}$, i.e. if $\delta \neq 0$ and $\alpha \neq \beta$. Hence, only appearance experiments can be used to look for CP violating effects. In disappearance experiments, only the non-CP violating part of (1.8) contributes to the oscillation probability where Δm_{ij}^2 only appears to even powers of two. From such an analysis it is therefore neither possible to determine the sign of Δm_{ij}^2, nor an absolute neutrino mass.

It is instructive to take a look at the case of only two neutrino flavors, where the transition matrix U is a real two dimensional rotation matrix determined by only one mixing angle ϑ and there is only one mass difference Δm^2. This leads to the transition probability of

$$P(\alpha \to \beta) = \sin^2(2\vartheta) \cdot \sin^2(\Delta). \tag{1.10}$$

In this simple case the transition probability is a plain harmonic oscillation with amplitude $\sin^2(2\vartheta)$ and a frequency proportional to Δm^2.

Event though Equation (1.8) is obtained for plane waves, the same result is recovered in a more careful analysis using wave packets [8] as long as

$$\sigma_p \gg \frac{\Delta m_{ij}^2}{\bar{p}} \quad \text{and} \quad \sigma_x \gg |v_i - v_j| L \tag{1.11}$$

are fulfilled, where σ_p is the spread in momentum and σ_x is the spread in space of the wave packet. The uncertainty in momentum thus has to be large enough to allow the transition into a different mass eigenstate, while the uncertainty in space has to be large enough to allow for a significant spatial overlap of the wave packet with the lighter and the heavier mass eigenstate, despite their different velocities.

1.3 Neutrino oscillations in matter

The following discussion is done in the simplified two flavor case. Assuming again plane waves the propagation of neutrinos can be described in the vacuum case as [7]:

$$i\frac{d}{dt}|\nu_i\rangle = \frac{m_i^2}{2p}|\nu_i\rangle \quad \Leftrightarrow \quad i\frac{d}{dt}|\nu_\alpha\rangle = \sum_\beta \frac{m_{\alpha\beta}^2}{2p}|\nu_\beta\rangle, \quad m_{\alpha\beta} = \sum_i U_{\alpha i} m_i^2 U_{\beta i}^*. \tag{1.12}$$

Note that the term proportional to the energy of the neutrino was omitted as it does not contribute to oscillations.

While transversing through matter, neutrinos interact with the surrounding material via weak interaction. For low energy neutrinos, the predominant effect is the coherent forward scattering on electrons [11]. The effect of the neutral current (NC) interactions is independent of the flavor and therefore can be absorbed in a global phase which does not show up in the oscillation. In contrast, the CC interaction singles out the electron neutrino, giving rise to an additional potential for the electron neutrinos which can be interpreted as an additional term in m_{ee}^2 [7]

$$m_{ee}^2 \rightarrow m_{ee,m}^2 = m_{ee}^2 + 2\sqrt{2}G_F N_e E =: m_{ee}^2 + A, \tag{1.13}$$

where G_F is Fermi's constant and N_e is the electron number density of the transversed matter. In the case of electron antineutrinos A has to be replaced by $-A$. To get the mass eigenstates in matter, $m_{\alpha\beta,m}^2$ has to be diagonalized. This results in a new effective mixing angle ϑ_m and a new effective mass splitting Δm_m^2 of the energy eigenstates in matter [8]:

$$\sin(2\vartheta_m) = \frac{\sin(2\vartheta)}{\sqrt{(\frac{A}{\Delta m^2} - \cos(2\vartheta))^2 + \sin^2(2\vartheta)}} \tag{1.14}$$

$$\Delta m_m^2 = \Delta m^2 \sqrt{\left(\frac{A}{\Delta m^2} - \cos(2\vartheta)\right)^2 + \sin^2(2\vartheta)}. \tag{1.15}$$

Both quantities show a resonant behavior with respect to A with the resonance condition $\frac{A}{\Delta m^2} = \cos(2\vartheta)$. Note that A depends on the electron number density as well as on the neutrino energy. Hence, the value of A is determined by both, the neutrino properties and the properties of the matter it passes through.

For neutrino beams, matter effects have to be considered, as the beam passes through the earth. The most important oscillation channel in this context is the so called "golden channel", i.e. the $\overset{(-)}{\nu_e} \rightarrow \overset{(-)}{\nu_\mu}$ oscillation channel [12], which provides maximum sensitivity yo the unknown mixing parameters. The full analytic oscillation formula for constant matter density, taking all three flavors into account (see e.g. [13]) is physically not intuitive. Assuming that the beam is tuned to the first oscillation maximum in Δm_{13}^2, $\Delta_{12} \ll 1$ as $\frac{\Delta_{12}}{\Delta_{13}} = \frac{\Delta m_{12}^2}{\Delta m_{13}^2} \sim 10^{-2}$. Therefore, the analytic formula can be expanded in Δ_{12} and $\sin(\vartheta_{13})$ to get a physically more intuitive result [12]:

$$P(\overset{(-)}{\nu_e} \rightarrow \overset{(-)}{\nu_\mu}) = s_{23}^2 \sin^2(2\vartheta_{13})\left(\frac{\Delta_{13}}{B_\mp}\right)\sin^2(B_\mp) + c_{23}^2 \sin^2(2\vartheta_{12})\left(\frac{2\Delta_{12}}{AL}\right)^2 \sin^2\left(\frac{AL}{2}\right)$$

$$+ J\frac{2\Delta_{12}}{AL}\frac{\Delta_{13}}{B_\mp}\sin\left(\frac{AL}{2}\right)\sin(B_\mp)\cos(\pm\delta - \Delta_{13}) \tag{1.16}$$

$$J = c_{13}\sin(2\vartheta_{12})\sin(2\vartheta_{23})\sin(2\vartheta_{13})$$

$$B_\mp = \left|\frac{AL}{2} \mp \Delta_{13}\right|,$$

where the upper sign is for neutrinos and the lower for antineutrinos. The first two terms correspond to effective oscillations driven by Δm_{13}^2 and Δm_{12}^2, while the last term is the interference term between the two oscillations. The interference term is the leading term

in $\sin(2\vartheta_{13})$. As matter effects influence the mass differences as well as the mixing angles, they influence both, amplitude and phase of the oscillation formula. The oscillation formula is dependent on all currently unknown mixing parameters ϑ_{13}, δ and the sign of Δm_{13}^2. Therefor a measurement of $P(\overset{(-)}{\nu_e} \to \overset{(-)}{\nu_\mu})$ is principally sensitive to all these quantities. The problem is tough, that the sensitivity to all three parameters gives rise to the problem of degeneracies, i.e. sets of the unknown parameters which produce very similar transition probabilities. For a thorough discussion of the degeneracies see [14].

To solve the degeneracies it is required to combine different baselines and/or energies. As matter effects strongly enhance the dependence of $P(\overset{(-)}{\nu_e} \to \overset{(-)}{\nu_\mu})$ on the mass hierarchy, it is e.g. possible to use one very short baseline where matter effects are neglectable to measure δ and ϑ_{13} and a longer baseline to determine the mass hierarchy. Alternatively, the so called magic baseline, defined by $AL = 2\pi$. Using this baseline, only the first term in Equation (1.16) remains allowing for a clean measurement of ϑ_{13} and the mass hierarchy. The remaining mixing angle ϑ_{13} has to be determined by an additional short baseline experiment [14].

1.4   Real time neutrino detection

As neutrinos do not carry an electric charge, they cannot be detected directly. Neutrino detection therefore always means detecting a final state charged particle produced in a neutrino interaction.

The interaction rate in a detector is $R \propto \sigma_\nu \Phi_\nu m_{\text{target}}$ where Φ_ν is the neutrino flux and m_{target} is the active target mass. As the neutrino cross-section is very low and available neutrino sources are limited in intensity, huge detectors at the ton scale are required in order to get sufficient interaction rates. Furthermore, a good background reduction is required in order to be able to extract a significant signal.

Contrary to radiochemical detectors (cf. [15, 16]), real time neutrino detectors measure the energy and interaction time of every detected neutrino event. One approach is to exploit the Cherenkov effect in water as presented in Section 1.4.1. Another possibility, based on liquid scintillator is described in Section 1.4.2. A more recent idea is to use a giant liquid Argon time projection chamber, which is detailed in Section 1.4.3.

1.4.1   Water Cerenkov

Charged particles passing through a medium emit Cerenkov light if they travel faster than the speed of light in the medium. The passing particle polarizes polar molecules which emit spherical light waves. Their interference leads to a light cone similar to the shock wave cone produced by a supersonic airplane. The opening angle of the light cone φ relates to the speed of the particle $v = \beta c$ via

$$\cos(\varphi) = \frac{1}{\beta n(\lambda)}, \tag{1.17}$$

with $n(\lambda)$ being the wavelength dependent index of refraction of the passed material. Hence, the maximum opening angle $(\beta \to 1)$ is $\cos(\varphi) = 1/n$. Equation (1.17) implies that $\beta > \beta_{thr} = \frac{1}{n}$ has to be fulfilled for Cerenkov emission, which imposes a physical

energy threshold for particle detection:

$$E_{thr} = \left(1 - \frac{1}{n^2}\right)^{-\frac{1}{2}} E_0, \qquad (1.18)$$

with E_0 being the rest energy of the particle. Neglecting the wavelength dependence of the index of refraction, the amount of produced photons rises with decreasing wavelength. However, there are no X-rays produced as the index of refraction in this wavelength range is basically one. Therefore, most photons are produced in the UV regime [17].

The Cerenkov photons can be used to detect secondary particles produced by neutrino interactions. If the particle is above threshold and the track is contained in the active volume of the detector, a ring-like light pattern is produced on the wall of the detector, which is equipped with photosensors. This ring like structure allows to reconstruct the kinetic energy and the direction of the secondary particle as has been demonstrated for instance by the Super Kamiokande experiment for solar neutrinos [18]. While the direction of the neutrino and the direction of the secondary particle are only loosely correlated for MeV neutrinos, this correlation improves at higher energies. A discrimination between electron and muon tracks is possible as electron rings tend to be more diffuse than muon rings due to the higher deflection of electrons by multiple scattering. Given a charged-current quasi-elastic interaction (for details see Section 6.2), this allows to determine the flavor of the detected neutrino in case its energy is sufficient to produce muons.
Today, the largest water Cerenkov experiment is the Super Kamiokande experiment which uses 32kt of water[2] contained in a cylindrical tank as Cerenkov medium [19]. Water is very suitable for such a detector as it is cheap, easy to purify, features long optical attenuation length and is non hazardous. Currently, there are plans for water Cerenkov Detectors with even higher mass: The Hyper Kamiokande detector is a planned successor for Super Kamiokande in Japan with a total mass of order 1 Mt. The corresponding European proposal is the MEMPHYS detector with an aimed total mass of about 500 kt [20].

1.4.2   Liquid scintillator

A charged particle produced by a neutrino interaction in a liquid scintillator excites the delocalized π-electrons inherent to an organic scintillator. They are typically provided by one or more benzene rings. Some of the excited states decay radiatively [22]. The emitted light serves as signature for the neutrino interaction. It is generally detected by PMTs at the walls of the detector.
Compared to water Cerenkov detectors, liquid scintillator detectors feature an about 50 times higher number of photoelectrons per MeV deposited energy which leads to an increased energy resolution as well as a lower threshold. An organic scintillator features multiple excited electronic states as depicted in Figure 1.1. Ionizing particles traveling through the scintillator typically populate the S_{ni} states which quickly ($\sim$ps) decay via internal conversion into the S_{10} state. These decays are non radiative. Most S_{10} states decay radiative into the ground state or one of its associated vibrational levels, giving rise to the fastest component of the scintillation light. This component typically is very fast with decay times of a few ns.

---

[2]This mass corresponds to the water contained in the inner detector.
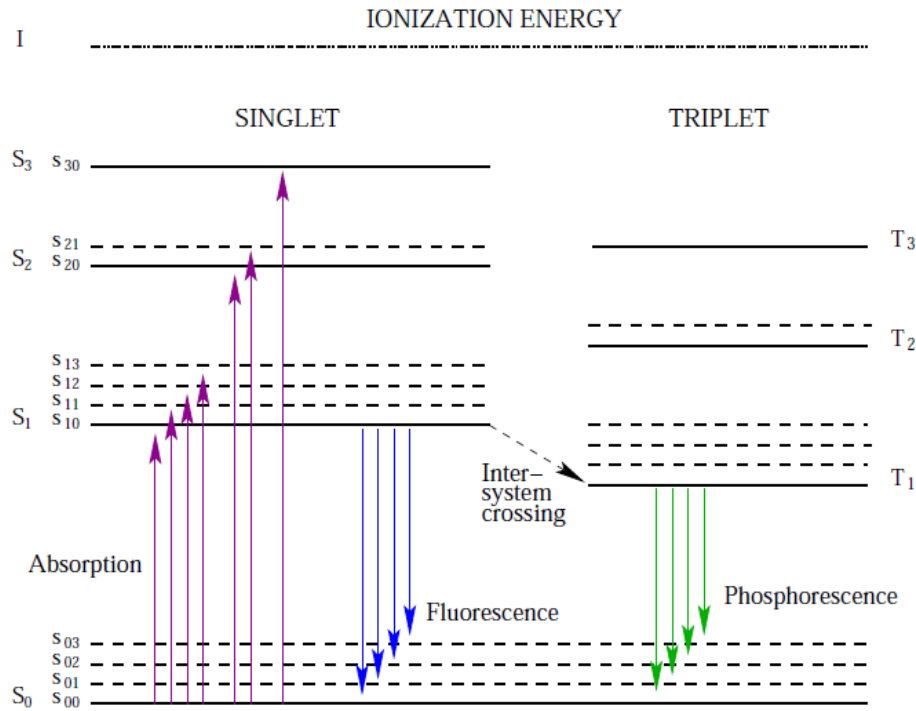
Fig. 1.1: Energy level scheme of delocalised π-electrons [21]. The black lines show the different energy levels, the violet arrows show the transitions induced due to absorptions and the blue and green arrows show the transitions responsible for the fast and the slow component of the scintillation light, respectively. Each electronic state S_n and T_n is accompanied by multiple vibrational states. The ground state is a singlet state, while the excited states can be singlet as well as triplet states. As radiative decays from triplet into singlet states are suppressed, the decay time of triplet states exceeds the singlet state decay time by at least one order of magnitude.

A fraction of the excited S_{10} states can be transferred to the lowest triplet state T_1. As the transition between the triplet state and the singlet ground state is forbidden, the decay time of the triplet state is typically one order of magnitude slower than for the singlet state[23]. Most slow decays are in fact delayed fast decays, where the energy from a T_1 stat is transfered to an excited S state, e.g. via intermolecular collisions, which subsequently decays radiatively [21].

Scintillators are typically compound systems, consisting of a major component, the solvent, and a minor component at typical concentrations of a few grams per liter, which is called the solute or the primary flour. Energy deposited in the scintillator is typically absorbed by the solvent. It is non-radiatively transferred to the solute via Förster transitions on the time scale of picoseconds. The subsequent decays of the excited states of the solute cause the scintillation light. The solute is chosen to produce light in a region where the solvent has maximum transparency and to have only small self absorption of the produced light, which is further suppressed due to its low concentration.

Many scintillators contain an additional third component featuring a large stokes shift, which is called secondary flour or wavelength shifter. It absorbs the photons emitted by the primary flour and re-emits them at higher wavelengths in order to shift the scintillation spectrum in a wavelength region were the scintillator is more transparent.

The number of produced photons per unit path length, $\frac{dL}{dx}$, is dependent on the energy

deposited per unit path length, $\frac{dE}{dx}$. In general the correlation is non-linear. It can be approximated by the empirical Birks' formula [23]

$$\frac{dL}{dx} = \frac{A \cdot \frac{dE}{dx}}{1 + k_B \cdot \frac{dE}{dx}}, \tag{1.19}$$

where A is a normalization constant and k_B the so called Birk's constant. For $k_B \cdot \frac{dE}{dx} \ll 1$, the produced light is proportional to the deposited energy. This is typically true for light singly charged particles like electrons and muons above a certain energy threshold where the particles are practically minimum ionizing [22]. In contrast, at the energies dealt with in this thesis, heavier particles like protons or alphas are not minimum ionizing, i.e. their energy loss is $\left\langle \frac{dE}{dx} \right\rangle \propto \frac{z^2}{\beta^2}$ [23], where z is the charge of the particle and $\beta = \frac{v}{c}$ its speed. Hence, the heavier the particles's rest mass is compared to its kinetic energy, the higher its stopping power and the larger the influence of quenching.

A typical example for a liquid scintillator experiment is the Borexino experiment at the LNGS in Italy. It is a spherical detector with an onion-shell like design featuring a fiducial volume of 100 t. Using this configuration, the energy threshold for electron recoils from neutrino electron scattering in of order 200 keV determined by the ^{14}C background while the intrinsic energy threshold is as low as a few 10 keV. [3]. Borexino's proposed successor is the $\sim$50kt LENA detector, which is presented in detail in Chapter 2.

1.4.3   Liquid argon

Another option to detect neutrinos is a detector based on liquid argon (LAr). An ionizing particle passing through LAr leads to a three fold signal. First, charged particles above threshold emit Cerenkov light. As LAr has similar optical properties than water, a readout of the Cerenkov light is in principle possible but usually not performed. Second, LAr ions created by the transversing particle can form excimers from two ions. Their decay produces scintillation light predominantly at $\lambda \sim 128$ nm [24], with a fast decay constant of about 6 ns [25]. LAr is basically transparent at this wavelength. Therefore, the scintillation light is detectable even in larger detectors. Finally, the transversing particle produces free electrons along its track. Given a sufficient purity of the LAr, electrons can be drifted by an external electric field over macroscopic distances. LAr detectors can be run in two phase mode with a gas phase above the liquid. Electrons drifted to the liquid gas interface are transfered from the liquid into the gas phase by a high electric field. In the gas phase, the electron signal is amplified using proportional amplification in gases and subsequently detected by a standard gas detector readout scheme [26].

The setup proposed for GLACIER [27] features a cylindrical LAr tank with a vertical cylinder axis with the gas phase being on top of the liquid. The produced electrons are drifted towards the gas phase via a vertical drift field of 1 kV/cm and, once in the gas phase, amplified and detected by a two dimensional readout grid covering the whole lid of the detector. Therefore, the spatial distribution of the detected electrons already provides a two-dimensional projection of the event. Three-dimensional event information can be calculated from the drift time of the electrons, with the start time of the electron drift given by the scintillation light produced by the interaction. It is detected by an array of wavelength-shifter covered PMTs at the bottom of the detector. Detectors relying on this technique are commonly referred to as LAr time projection chambers, after the more

parameter	best fit ($\pm 1 - \sigma$)	$2 - \sigma$	$3 - \sigma$
$\Delta m_{21}^2 \approx \Delta m_{23}^2 [10^{-5}$ eV$^2]$	$7.59^{+0.23}_{-0.18}$	$7.22 \; - \; 8.03$	$7.03 \; - \; 8.27$
$\|\Delta m_{31}^2\| [10^{-3}$ eV$^2]$	$2.40^{+0.12}_{-0.11}$	$2.18 \; - \; 2.64$	$2.07 \; - \; 2.75$
$\sin^2(\vartheta_{12})$	$0.318^{+0.019}_{-0.016}$	$0.29 \; - \; 0.36$	$0.27 \; - \; 0.38$
$\sin^2(\vartheta_{23})$	$0.50^{+0.07}_{-0.06}$	$0.39 \; - \; 0.63$	$0.36 \; - \; 0.67$
$\sin^2(\vartheta_{13})$	$0.013^{+0.013}_{-0.009}$	≤ 0.039	≤ 0.053

Tab. 1.1: Results of global fit to experimental results from [30]. The results columns show the best fit value with the one sigma error as well as the 2 and 3σ confidence intervals.

conventional time projection chambers (TPC) filled with pure gas. The LAr TPC is superior to all other detector options when it comes to the reconstruction of complicated interactions vertices featuring multiple tracks, making it especially suitable for high energy events. The largest currently running LAr detector ICARUS at the LNGS features a volume of 600t, but is based on a different readout scheme featuring multiple small modules [28]. Significant engineering challenges have to be solved to scale such a detector to the required size for a multi kt detector especially concerning the required purity to achieve the drift lengths necessary for such a huge detector. Currently there is R&D going on with the aim of building a 100 kT LAr detector[26]. Furthermore, the LBNE collaboration considers a 34 kt LAr detector as an option for a far detector of the Fermilab to Homestake neutrino oscillation project [29].

1.5   Current knowledge of neutrino properties

Despite all difficulties in detecting neutrinos, former and current neutrino experiments have managed to determine many neutrino parameters.
One important milestone was the observation of neutrino oscillations at high significance, using neutrinos from various sources. The first experiment to see a compelling evidence for ν_μ disappearance was the Super Kamiokande experiment that analyzed at the angular distribution of atmospheric neutrinos [31]. Later its results also established the oscillatory behavior [32]. Additionally a very precise measurement of the Δm_{12}^2-driven reactor neutrino oscillations ($\bar{\nu}_e \leftrightarrow \bar{\nu}_\mu$) was performed by the KamLAND experiment [33]. Neutrino flavor transitions have also been observed by solar neutrino experiments. This case is special as, due to the high electron densities in the sun, matter effects are important for neutrino energies above 1 MeV. This reduces the measure electron neutrino survival probability for the high energy part of the solar neutrino spectrum
The neutrino mixing parameters can be extracted from a global analysis of all available data . Table 1.1 shows the results including the global fit uncertainties [30].
Despite all effort, there are still a few open questions concerning oscillation parameters. Most prominently, there is still no evidence for the mixing angle ϑ_{13} to be non-zero. The current upper bound is set by the CHOOZ experiment [34]. Along with its successor, the Double Chooz experiment, which just recently finished filling the far detector, a multitude of other experiments both beam and reactor based will search for ϑ_{13}.
While for ϑ_{13} at least an upper limit can be obtained, nothing is known about the value

of CP-violating phase δ. This is due to the fact that all angles of the mixing matrix (1.3) have to be known to determine δ. Therefore, the observation of ϑ_{13} and δ is closely linked: Any observations on δ is connected to a determination of ϑ_{13} and might even be impossible in case ϑ_{13} is zero.

Additionally, there are open questions concerning neutrino masses. First of all, the sign of the squared mass difference Δm_{31}^2 has not yet been determined, while the sign of the other squared mass difference is fixed due to the MSW effect in the sun. This gives rise to two possible hierarchies, the normal hierarchy $m_1 \ll m_2 < m_3$ and the inverted hierarchy $m_3 \ll m_1 < m_2$. Furthermore, the absolute mass scale of the neutrinos has not been determined yet. The best direct experimental bound is from the Tritium decay experiment Mainz [35]: $m_\nu^2 = \sum_i |U_{ei}^2| m_i^2 < 2.2$ eV (90 % CL), while cosmology is able to set a lower, though model dependent, bound for the neutrino mass $\sum m_\nu < 1$ eV (95 % CL) [36]. The KATRIN-Experiment currently under construction aims to lower the direct bound by one order of magnitude to 0.35 eV (90% CL) [37].

Chapter 2

The LENA project

Especially for low neutrino energies at the MeV scale, liquid-scintillator detectors like Borexino [3] and KamLAND [4] show a superior performance compared to water Cerenkov detectors, due to their high light yield and low energy threshold (cf. 1.4). However, these detectors are too small to detect rare processes, like diffuse supernova neutrinos or proton decay, with significant statistics. This gave rise to the proposal [38] of a new $\sim$50 kt liquid scintillator neutrino detector in Europe, the LENA detector (**L**ow **E**nergy **N**eutrino **A**stronomy).

The basic setup and the arising technical issues are described in Section 2.1, while Section 2.2 presents possible locations for LENA. Finally, the chapter concludes with a short overview of the broad physics program accessible by LENA in Section 2.3.

2.1 Detector design

The overall geometry of LENA is sketched in Figure 2.1. In contrast to the Borexino experiment, which is spherical, a cylindrical shape is preferred to maximize the expected photoelectron yield, which is effectively limited by the attenuation of the scintillation light in the organic liquid ($\lambda_{att} \sim 10$ m). An onion shell like design is used to protect the active volume against external radioactivity.

The scintillator is contained in a cylindrical nylon vessel of 96 m height and 13 m radius. The scintillator mixture used for the target is not fixed yet. While maximizing the light yield, it should minimize fluorescence decay times, scattering and absorption lengths. The most promising candidates for solvents are PXE (1,2-dimethyl-4-(1-phenyletyl)-benzene) [40] and LAB (linear alkylbenzene) [41]. The most prominent candidates for the primary flour are PPO (2,5-diphenyl-oxazole) and PMP (1-phenyl-3-mesityle-2-pyrazolin), while bis-MSB (1,4-bis-(o-methyl-styryl)-benzene) [21] is preferred as secondary flour. Due to the varying densities of the scintillator solvents, the fiducial mass varies between 45 and 53 kt [39]. It is more than 100 times larger than Borexino.

The fiducial volume is surrounded by two meters of non-scintillating buffer, whose density is adapted to the liquid scintillator to reduce buoyancy forces. Its purpose is to shield the target volume against external radioactivity, mainly from the photomultipliers (PMTs) and the detector tank.

The scintillation light is detected by PMTs which are arranged on a scaffolding on the inner side of the tank wall. In order to achieve the desired energy resolution for deposited energies below 1 MeV, an optical coverage of about 30% is required. Which PMT type
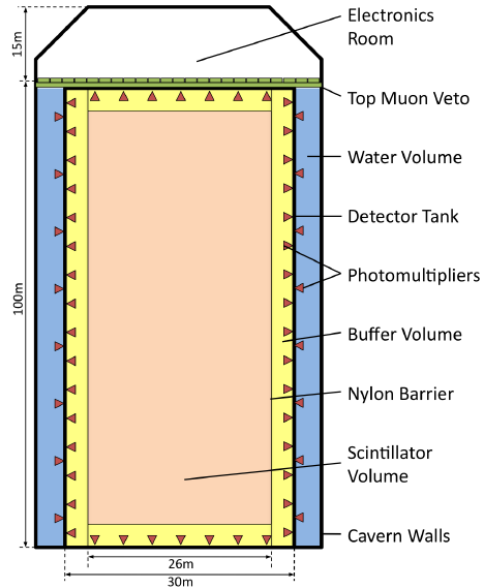
Fig. 2.1: Sketch of the LENA detector [39]. The center of the detector (red) is filled with liquid scintillator and provides the active volume of the detector. It is surrounded by a 2 m thick buffer of non scintillating liquid (yellow) which protects the target volume from external radioactivity. Both liquids are contained in a detector tank. The PMTs which detect the scintillation light are mounted on a scaffolding on the inside of the tank. The tank is surrounded by water (blue) providing protection from fast neutrons from the surrounding rock and acting as a Cerenkov based muon veto. It is read out via additional PMTs on the outside of the tank. On the top of the detector there are additional detectors (green) supplementing the muon veto. Note that the ratio of PMTs in the inner vessel and PMTs for the muon veto is not shown correctly and that the cavern walls need not be exactly vertical but might have another shape which is more favorable in terms of rock-engineering.

will be used in the final experiment is not yet decided. The current design aims at PMTs with eight or ten inch diameter and light concentrators ("winston cones"), leading to ∼47 000-63 000 PMTs for the inner detector. The effect of the light concentrators, which were already applied in Borexino and the CTF[1] [42], on the detector performance is currently investigated.

A cylindric tank, made either of steel of concrete, surrounds the inner detector. While the concrete tank is cheaper and favorable for construction, it features a higher radioactivity than the steel tank. At the same tank diameter this leads to a reduced fiducial volume for low energy physics [43].

The whole detector will be surrounded by at least two meters of water, serving as an active muon veto as well as a shielding against fast neutrons that are produced by cosmic muons in the rock [44]. As most of the muons traversing the detector in a deep underground laboratory are vertical [45], the top of the detector will be instrumented with one or several planes of segmented muon veto detectors to enhance spatial and directional resolution for throughgoing muons. Possible detectors are either resistive plate chambers or plastic scintillator panels.

Currently there are multiple choices for the PMT readout system. The most appealing, but also the most expensive, solution would be to equip each PMT with its own Flash

---

[1]**C**ounting **T**est **F**acility, a prototype for the Borexino detector

ADC[2] continuously sampling the PMT output. This would allow to tag the arrival times of individual photons.

Another approach is pursued by the PMm[2] project: Here 16 PMTs are grouped together and controlled by one custom designed front-end board, the so called ASIC [46]. The ASIC can save the pulse start time as well as the integrated charge of each PMT pulse and send it to a central DAQ center in case a trigger occurred. Furthermore, it provides the high voltage (HV) for the PMTs using power over Ethernet. Therefore, for 16 PMTs, only one module and one cable is necessary, which leads to a significant reduction in costs as well as in ambient radioactivity emanated by the cabling running inside the cylinder.

2.2 Possible locations

The search for a possible detector site for LENA is preformed in the framework of the LAGUNA design study [47], which is proposed to be continued in the LAGUNA-LBNO study addressing detector cost and safety issues [48]. The original site study considered seven different sites [49]. From the point of view of rock engineering, no significant show stoppers have been found. For the LENA physics program however, a significant shielding against cosmic rays of at least 4000 mwe[3] is required. Applying this criteria only two sites of sufficient depth remain:

- **Center for underground physics in Pyhäsalmi (CUPP):** A metal mine in central Finland. Feasibility studies showed that a cavern suitable for LENA could be excavated at a depth of 1440 meters, corresponding to about 4000 mwe [50]. Furthermore, the reactor antineutrino flux at this location is very low due to the large distance from central European nuclear power plants. However, this background will rise moderately in the future, as one more nuclear power plant is currently under construction in Finland and two more plants have been approved to be built [51].

- **The Laboratoire Souterraine de Modane (LSM)**: An underground laboratory adjacent to a highway tunnel connecting Italy and France under the Frejus mountain. The overall rock shielding amounts to 4800 mwe. The muon flux is nevertheless comparable to CUPP, which features a better shielding for inclined muons. The reactor antineutrino flux is very high as the laboratory is located close to many French nuclear power plants.

2.3 Low energy physics

2.3.1 Solar neutrinos

The sun releases energy via the fusion of protons to ^{4}He corresponding to the sum reaction

$$4p + 2e^- \longrightarrow \quad ^4_2\text{He} + 2\nu_e + 26.73\,\text{MeV}. \tag{2.1}$$

---

[2]Flash ADCs are very fast analogue digital converters which allow a continuous sampling of the signal with sampling rates of up to a few GS/s.

[3]**m**eters of **w**ater **e**quivalent
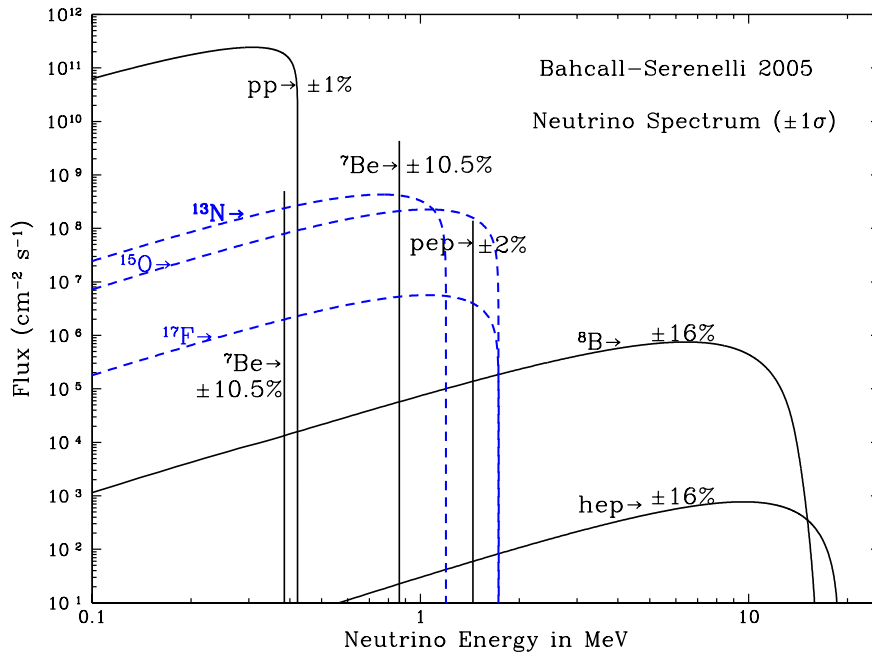
Fig. 2.2: The solar neutrino spectrum as expected from the standard solar model [52]. The solid black lines show neutrinos originating from the pp chain while the dashed blue lines show neutrino spectra originating from the CNO-cycle.
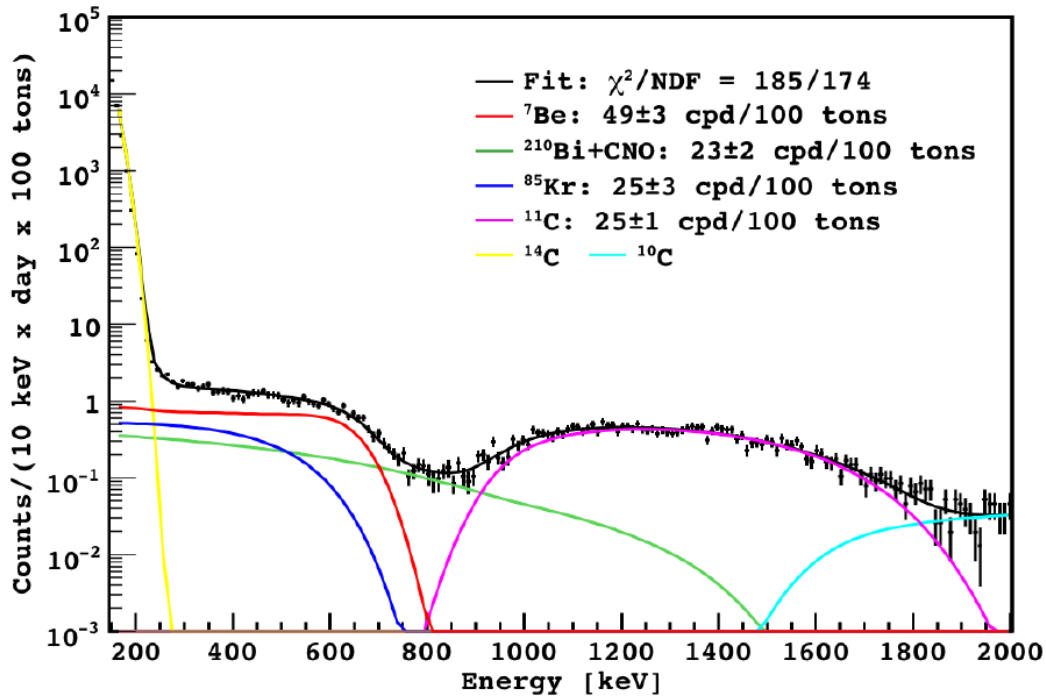
Fig. 2.3: Electron recoil spectrum as seen by the Borexino detector. The black points show the data, whereas the lines show the result of a global fit to the electron recoil spectrum from ^{7}Be neutrinos as well as to the radioactive backgrounds. The black line shows the total fit function while the colored show the different contributions to the total fit function.

The fusion process takes place in several steps, either via the so called pp-chain or via the CNO-cycle [7]. Most energy is produced via the pp-chain, while the CNO-cycle, contributes only to a small fraction, which is however not precisely known up to now. The resulting neutrino spectrum can be calculated in the well established framework of the standard solar model [52] and is shown in Figure 2.2.

Electron recoils from neutrino electron scattering are used to detect solar neutrinos. Water Cerenkov detectors can only access the ^{8}Be- and the hep neutrino fluxes due to their rather high energy threshold of order 5 MeV. on the other hand, the energy threshold for liquid scintillators is determined by the endpoint of the β-decay spectrum of ^{14}C intrinsic to the scintillator, i.e. around 250 keV. Therefore, lower energy neutrinos like ^{7}Be, pep, CNO and maybe even pp neutrinos are principally accessible. Unfortunately, the light produced by electron recoils is not a unique signal for neutrino interactions, but can also be due to radioactivity in or around the detector. While most of the radioactive background can be reduced by the active muon veto, spacial cuts and pulse shape analysis, the remaining recoil spectrum of the innermost 100 t still containes some backgrounds due to β-emitting isotopes dissolved in the target liquid. From the resulting spectrum shown in Figure 2.3 the signal rate of ^{7}Be-neutrinos is extracted by spectral fits [53]. The spectroscopic resolution of LENA will be inferior to Borexino, as the photoelectron yield will be lower. This is due to the increased distances the light has to travel through the scintillator, leading to an attenuation of the light. On the other hand, statistics in LENA might surpass Borexino by more than two orders of magnitude.

Assuming the radiopurity levels of Borexino are also achieved in LENA, a rate of $\sim 8\,000$ electron recoil events per day is expected. For the ^{7}Be neutrinos, this leads to a sub percent discovery potential for flux modulation over a wide frequency range. This allows the search for density oscillations in the neutrinosphere of the sun, so called g-modes, as well as probing the solar cycle with neutrinos and the search for day/night variations [54]. From the solar neutrino spectrum in Figure 2.2, it is evident that the maximum energies of the CNO neutrinos and the energy of the pep neutrinos are in the range between 1 and 2 MeV, leading to an expected recoil spectrum that extends up to slightly above 1 MeV. The observed spectrum in Borexino shows, that this energy region is dominated by the ^{11}C background. ^{11}C is a radionuclide produced by ^{12}C spallation caused by cosmic muons passing through the detector. Due to the higher rock overburden, the expected background rate in LENA is about five times lower than the presently observed rate in Borexino. This background can be further reduced applying the three fold coincidence method [55] and pulse shape discrimination of positrons [56]. This will allow a high statistics measurement of ~ 500 CNO neutrinos per day providing information on the solar metallicity. Furthermore, a measurement of the pep neutrino rate would give valuable information on the ν_e survival probability in the transition region from vacuum to matter-dominated oscillations [39].

Even though the expected rate of pp neutrino events above a threshold of 250 keV is still 25 d^{-1} discriminating these events from the ^{14}C background will be challenging [57].

2.3.2 Supernova neutrinos

Core-collapse supernovae (SNe) mark the end of stars with a total mass of more than about eight solar masses. The total of the released gravitational energy is in the order of 10^{53} erg $= 10^{46}$ J. About 99% of this energy is radiated away in neutrinos, making SNe
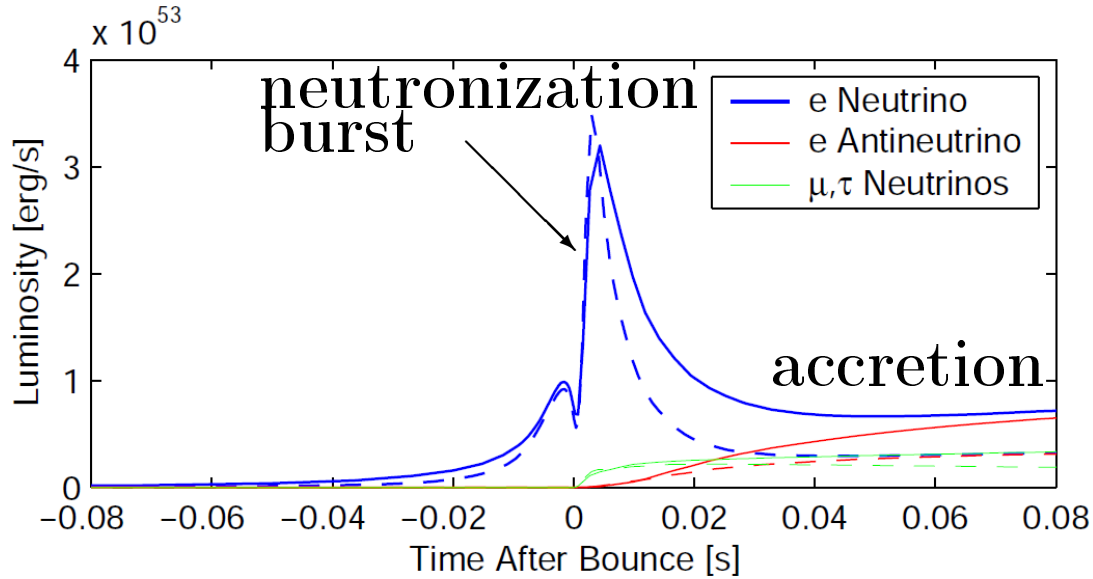
Fig. 2.4: Time evolution of the SN neutrino luminosity [58]. The dashed and the solid lines show the result for a progenitor star with $13 \, M_\odot$ and $40 \, M_\odot$, respectively. The fluxes are sampled at a radius of $150 \, km$. An appropriate time of flight correction has been applied.

one of the most intense neutrino sources known. In our galaxy, the expected SN rate is of the order of 1-2 SN per century [59].

The starting point of a SN is a heavy star near the end of its lifetime. It has an onion like structure with a core composed mainly of Fe and Ni. Fe cannot be fused to heavier nuclei as the binding energy per nucleon is maximal Hence, the burning in the core has stopped. Without radiation pressure, the Fe core is mainly supported by the Fermi pressure of the electron gas. Its mass increases due to the additional Fe produced by the Si burning in the next shell. When the core approaches the critical mass of $\sim 1.4 \, M_\odot$, the Fermi pressure cannot balance the gravitational pressure any longer - the core starts to collapse. The collapse is triggered when the electron energy becomes high enough to drive the reaction

$$^{56}\text{Fe} + e^- \longrightarrow {}^{56}\text{Mn} + \nu_e \qquad (2.2)$$

which further reduces electron densities and therefore the Fermi pressure. Further energy is lost by photo dissociation of iron [60]. Note that via reaction (2.2) electron neutrinos are produced. Most of these neutrinos are unable to escape the core of the star due to the high densities. This phenomenon is called neutrino trapping. The collapse is finally stopped when the core reaches nuclear densities. The core bounces and a shock wave is created running outwards through the star. On its way out it dissociates the Fe nuclei to alphas and neutrons. Directly behind the shock wave additional neutrinos are produced via electron capture. Note that these neutrinos are initially trapped, too. When the shock advances far enough, the vast number of trapped neutrinos can start to leave the dying star. This leads to a huge number of neutrinos neutrino being emitted in a very short time, the so called neutronization burst [61].

In most simulations, the shock does not initially destroy the star and has to be revived. The underlying process is still not totally understood. According to current models, the shock initially stalls for up to a few $100 \, ms$. During this so called accretion phase, neutrino emission is mainly driven by material falling on the stalled shock front. During this phase

the fluxes of electron(anti)neutrinos are higher than the fluxes of the remaining flavors. Most important for the observation of an SN neutrino signal, is the subsequent cooling of the newly created proto-neutron start: Due to its huge density, the gravitational energy released in the collapse is irradiated away mainly by neutrinos. In this way, about 99% of the binding energy is carried away by $\nu\bar{\nu}$ pair production of all flavors. [60].

The time-dependent neutrino flux is shown in Figure 2.4. The huge ν_e peak at small positive times is the neutronization burst. Note that during the cooling phase, ν and $\bar{\nu}$ of all flavors are produced at equal luminosities, but - dependent on the SN model - at different mean energies.

LENA will allow a high statistics measurement of the neutrino signal for a SN inside our galaxy. A standard SN (8 solar masses, distance 10 kpc) will lead to 10 000 to 15 000 detected neutrino events in LENA, dependent on the SN model. While the main detection channel is be the inverse beta decay

$$\bar{\nu}_e + p \longrightarrow n + e^+ \qquad n + p \longrightarrow {}^2\mathrm{H} + \gamma\,(2.2\,\mathrm{MeV}), \qquad (2.3)$$

which is only sensitive to $\bar{\nu}_e$, there are also flavor insensitive channels and channels for ν_e only [21]. Inverse β-decay events can be discriminated from the other channels by their distinct delayed coincidence signals, given by a prompt signal from the positron and a delayed signal due to neutron capture on hydrogen. LENA will be able to measure the total neutrino flux and spectrum from a SN as well some flavor specific spectra. The time development of the signal will yield valuable insight in the SN explosion mechanism, while the analysis of flavor specific fluxes and spectra might reveal information about ϑ_{13}, the mass hierarchy and neutrino neutrino interactions [62].

Finally, note that the observation of a near by SN puts significant requirements for the maximum event rate that has to be handled by the DAQ system.

2.3.3 Diffuse supernova background neutrinos

The cosmic neutrino background produced by core-collapse SN throughout the universe is known as the diffuse supernova neutrino background (DSNB). A detection of these neutrinos will allow to derive constraints on the average SN neutrino spectrum as as well as on the core-collapse SN rate. Currently, the best upper limit for the DSNB $\bar{\nu}_e$-flux $\Phi_{\bar{\nu}_e}^{\mathrm{DSNB}}$ is given by the Super Kamiokande experiment [64]: $\Phi_{\bar{\nu}_e}^{\mathrm{DSNB}} < 1.2\,\bar{\nu}_e\mathrm{cm}^{-2}\mathrm{s}^{-1}$ for $E_\nu > 19.3\,\mathrm{MeV}$ at 90% CL

Similar to the detection of SN neutrinos, the highest count rate for the DSNB neutrinos is expected via the inverse beta decay channel (2.3) [21]. This channel is sensitive to the neutrino energy as most of the energy is transfered to the positron due to the kinematics of reaction (2.3). Current models predict an event rate of $\sim$10 per year in LENA. Despite of this low rate, the delayed coincidence signature of the inverse beta decay allows to eliminate most of the background. Nevertheless, there is still remaining background to be considered.

First of all, there are other $\bar{\nu}_e$ sources which lead to a background which cannot be distinguished from the signal. One relevant $\bar{\nu}_e$ source are nuclear power plants. Neutron-rich nuclei produced in fission reactions inside a reactor undergo beta decay, producing $\bar{\nu}_e$. As already pointed out in Section 2.2, this background is strongly dependent on the detector position. Figure 2.5 shows the reactor $\bar{\nu}_e$ spectra for Frejus and Pyhäsalmi in comparison to the expected DSNB signal. Further $\bar{\nu}_e$ are produced in the upper atmosphere by the
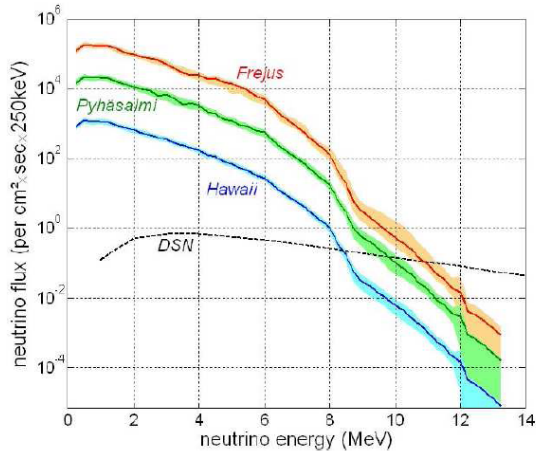
Fig. 2.5: The reactor $\bar{\nu}_e$ spectrum for Frejus (red line), Phyäsamli (green line) and Hawaii (blue line). The dashed line shows the expected flux of DSNB $\bar{\nu}_e$ for comparison [63].
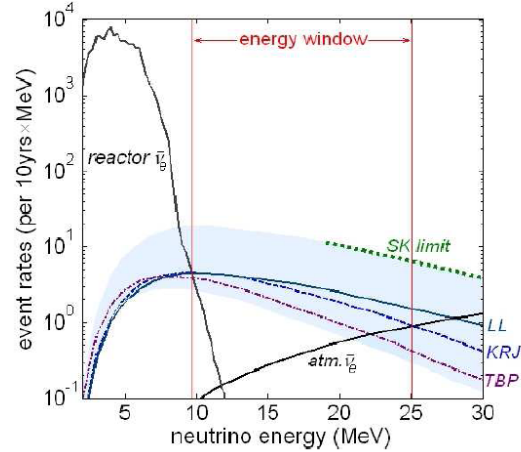
Fig. 2.6: Expected event rates for reactor $\bar{\nu}_e$, atmospheric $\bar{\nu}_e$ and $\bar{\nu}_e$ in LENA. The shown rates are computed for the Pyhäsalmi location and assume a measurement time of ten years. The shaded area accounts for the theoretical uncertainty of the DSNB $\bar{\nu}_e$ flux. The green dotted line shows the present Super Kamiokande limit. The lines labeled with LL, KRJ and TBP show the expected event rates predicted by different SN models. [57]

reactions of cosmic rays with the nuclei in the atmosphere. The flux of this background is dependent on the detector location, though not as strong as the reactor $\bar{\nu}_e$ background. Both $\bar{\nu}_e$ sources have a different energy spectrum than the DSNB and can therefore be handled spectroscopically. The corresponding detection window for the DSNB from 10-30 MeV is shown in Figure 2.6. Note that the detection window for conventional water Cerenkov detectors is considerably smaller as they are not able to exploit the delayed coincidence of the inverse β-decay[4] and therefore cannot discriminate against low energy muons, ^{8}B and hep neutrinos as well as radionuclides produced by cosmic ray muons [63]. In addition to the $\bar{\nu}_e$ backgrounds, there are a few backgrounds mimicking the delayed coincidence signal of the inverse β-decay. One possibility are cosmogenicly produced β-n-emitters. Fortunately, the only candidate with a high enough Q-value to add to the signal is ^{9}Li. Its life time is short enough to be associated with its mother muon ($T_{1/2} = 178$ ms). Vetoing a cylinder of two meters radius around a muon track for two seconds is therefore sufficient to reduce this background by 98% [43].

Furthermore, fast neutrons produced by muons in the rock can mimic a delayed coincidence by inducing a proton recoil (prompt signal) and subsequent neutron capture (delayed signal). This background is strongly reduced as the muon veto already provides a good shielding from fast neutrons which can be additionally improved by a fiducial volume cut. The remaining background can be tackled using the difference in pulse shapes for pulses induced by protons and positrons. The residual background rate in this channel is expected to be about one event in ten years for a twelve meter fiducial radius [44].

---

[4]At least if they are not loaded with Gadolinium [65].
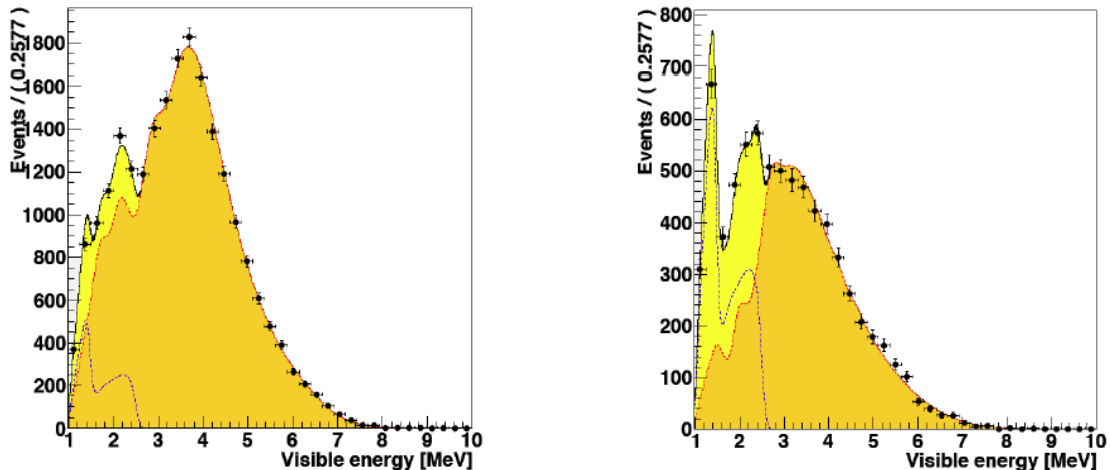
Fig. 2.7: The expected oscillated geoneutrino energy spectrum, neglecting DSNB neutrinos, after one year of data-taking [43]. The left histograms shows the situation for the Frejus location (left) and the Pyhäsalmi location (right) with the future Finish reactors taken into account. The red curve with the orange filling shows the expected reactor $\bar{\nu}_e$ flux and the blue dashed curve the expected geoneutrino signal. The yellow shaded area indicates the contribution of the genoeutrinos to the total signal. Due to the lower reactorneutrino background, the Pyhäsalmi location is advantageous for geoneutrino detection.

A more dangerous background is given by NC reactions of atmospheric neutrinos on carbon, where a neutron is knocked out of the nucleus mimicking the delayed signal

$$\overset{(-)}{\nu_x} + {}^{12}\,\mathrm{C} \longrightarrow \overset{(-)}{\nu_x} + {}^{11}\,\mathrm{C}^{(*)} + n, \quad x = e, \mu, \tau. \tag{2.4}$$

The expected event rate in the detection window surpasses the DSNB signal by approximately one order of magnitude. If ^{11}C is produced in the ground state, this background can be discriminated by looking for the ^{11}C decay. However, if the ${}^{11}C$ is produced in an excited state (probability $\approx 2/3$), it will deexcitate mainly via p, n, d and α emission. As the daughter nuclei are either stable of have a half life of 50 days or more, it is not possible to use their decays to veto this background. Again, the idea is to discriminate against those events using pulse shape analysis. The efficiency of this method is currently investigated by a Monte Carlo study.

2.3.4   Geoneutrinos

Geoneutrinos are generated by the decays of radionuclei in the earth which typically belong to the natural uranium and thorium chains or are due to ^{40}K. While these decays contribute a significant amount to the earth's total heat production they also produce neutrinos. Detection of these so called goneutrinos opens a new window to determine the distribution of radioisotopes in the earth testing current earth models. As neutrinos easily penetrate matter, the observation of geoneutrinos in principle allows investigating the the composition of the Earth crust, mantle and core. In comparison, geologic studies based on drill cores only scratch the outer crust.

Geoneutrinos have been detected by KamLAND [66] and recently by the Borexino experiment [67]. Statistics of current detectors are pretty low though prohibiting stringent constraints on earth models. Note that this field of neutrino physics is not accessible for

water Cerenkov detectors as the spectral endpoint of the geoneutrino spectrum is below the detection threshold.

About 1000 geoneutrino events per year are expected in LENA depending on the location. Due to the low event rates, geoneutrinos can only be detected with the inverse beta decay channel, as the delayed coincidence signature allows an effective suppression of internal and external radioactive backgrounds. Assuming the Borexino radiopurity conditions are met, the remaining radioactive background will be of order ten events per year. Hence, the predominant background for geoneutrinos are once again reactor antineutrinos [68]. Figure 2.7 shows the expected positron spectrum due to ν_e from reactors and geoneutrinos for both locations. Due to the lower reactor antineutrino background Pyhäsalmi provides the superior performance in geoneutrino detection . Nevertheless, both locations will allow a measurement of the geoneutrino flux at the percent level after a few years as well as the determination of the uranium/thorium rate [43].

It was also proposed to measure the direction of the arriving geoneutrios via the displacement of the neutron capture with respect to the positron signal. However, simulations show, that the average displacement exhibited is weak and only in the case of a very strong (20 TW) geoneutrino contribution from the core, a significant result is expected [68]. Information on the U/Th abundances differentiating the crust and mantle will therefore require a joint analysis of LENA and at least one more liquid scintillator detector at the 10 kt scale on the oceanic crust.

2.4   Physics in the GeV range

2.4.1   Proton decay

Extending the standard model to Grand unified theories (GUTs) typically leads to baryon number violation and therefore to an unstable proton. The proton decay branches favored by GUTs based on SU(5) or SU(10) typically are

$$p \longrightarrow l^+ + \pi^0 \qquad \text{with } l \in \{\text{e}, \mu\}. \tag{2.5}$$

The most stringent limits for these decay modes are set by the Super Kamiokande experiment with $\tau(\text{e}\pi^0) > 8.2 \cdot 10^{33}\,\text{a}$ and $\tau(\mu\pi^0) > 6.6 \cdot 10^{33}\,\text{a}$ at 90% CL. These results have already ruled out minimal SU(5) models [69].

In SUSY theories another decay channel dominates:

$$p \longrightarrow \bar{\nu} + K^+. \tag{2.6}$$

These events are very difficult to tag for water Cerenkov detectors, as the K^+ is produced at an energy below the Cerenkov threshold. Therefore, only indirect searches remain which suffer from poor detection efficiency. Nevertheless, the best current limits are again set by Super Kamiokande with $2.3 \cdot 10^{33}$ at 90% CL [70].

In a liquid scintillator detector like LENA, the stopping K^+ induces a well-visible signal, which is monoenergetic for free protons. The kaon decay provides a further signal delayed by the kaon lifetime of 15 ns plus further signals from subsequent decays. This very distinct signature can be used for a highly efficient background discrimination. A non-observation of the proton decay in LENA after ten years of measurement would allow to push the limit on the kaon branch (2.6) to $4 \cdot 10^{34}$ at (90% CL) [71].
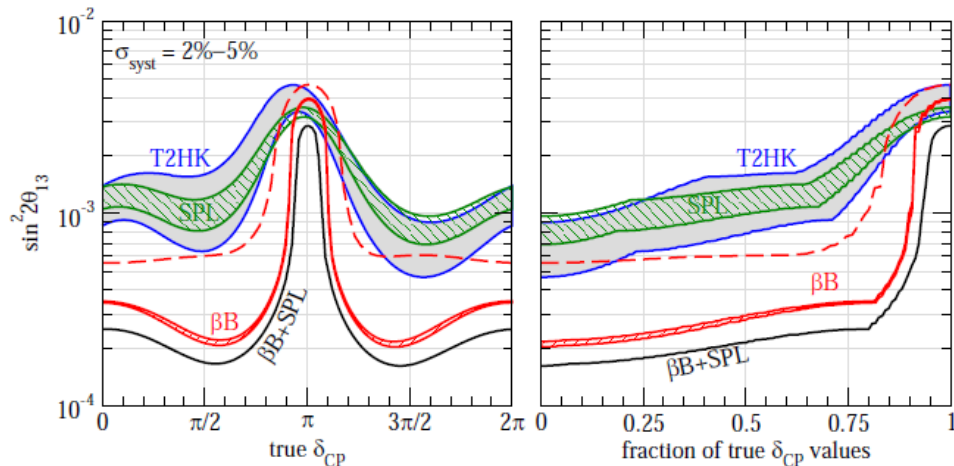
Fig. 2.8: The 3-σ-discovery reach of various neutrino beams for $\sin^2(2\vartheta_{13})$ of a 500 kt water Cerenkov detector at Frejus (MEMPHYS) [72]. On the left the 3-σ-$\sin^2(2\vartheta_{13})$-discovery reach as a function of the CP-violating phase δ is shown while the right displays the fraction of all δ for which ϑ_{13} can be discriminated from zero dependent on the true value of $\sin^2(2\vartheta_{13})$. The green and red band show the discovery reach for a superbeam and a β-beam, respectively, while the black line shows the combined discovery reach. If the assumed values for the intensity of the β-beam are off by a factor of two, its discovery potential would be reduced to the dashed line. For comparison, the gray shaded band with blue border shows the discovery reach of T2HK, a similar project in Japan.

2.4.2 Long baseline neutrino beams

As already indicated in Section 1.5, there are still a number of undetermined parameters in neutrino mixing. Beyond the scope of reactor neutrino disappearance experiments, a further way to investigate ϑ_{13}, δ and the mass hierarchy, is to scrutinize oscillations based on long baseline neutrino beams (LBNB). The primary advantage of neutrino beams in comparison to reactor neutrino experiments is the larger neutrino energy. This allows appearance experiments and therefore opens the window to search for CP-violating effects (cf. Section 1.2).

The dominant interaction channel is, depending on the energy of the beam, quasi-elastic scattering of a neutrino on a nucleon, resonant pion production or deep inelastic scattering. In charged current reactions the flavor of the scattered neutrino can be determined by tagging the flavor of the final state lepton. See Section 6.2 for details on the interaction of neutrinos on the GeV scale.

As neutrinos carry no electric charge they cannot be directly accelerated. Therefore, a neutrino beam is always a beam of secondary particles and employs only kinematic focusing. Currently there are multiple ideas how to produce a neutrino beam:

- **Superbeam:** In nowadays neutrino beams, the neutrinos are produced by shooting high energy protons on a light target. The pions produced in this reactions are then focused by a magnetic horn into a decay tunnel where they decay mainly via $\pi^\pm \rightarrow \mu_\pm + \overset{(-)}{\nu_\mu}$. Therefore, this beam type contains $\overset{(-)}{\nu_\mu}$ and a small but unavoidable admixture of $\overset{(-)}{\nu_e}$ due to the suppressed decay mode of the pion $\pi^\pm \rightarrow e^\pm + \overset{(-)}{\nu_e}$ as well

as $\overset{(-)}{\nu_e}$ and $\overset{(-)}{\nu_\mu}$ from muon decays. Switching between a ν_μ and a $\bar{\nu}_\mu$ beam is possible by selecting the charge of the pions which are focused in the decay tunnel.

Compared to current neutrino beams, a superbeam is fed by a proton beam of more than 1 MW in power. It also requires a target able to cope with such an intensive beam.

The signature in a superbeam experiment is primarily the $\overset{(-)}{\nu_\mu} \longrightarrow \overset{(-)}{\nu_e}$ appearance [73]. Therefore, the $\overset{(-)}{\nu_e}$ contamination of the beam limits its physics reach. A detector has to provide a good electron/muon discrimination focusing on the rejection of muon events. This should be possible, at least at high energies, due to the different track lengths of electrons and muons at the same energy [73]. An important background are ν_μ NC interactions producing in π^0s. The π^0s decay into two gammas which create electromagnetic cascades. Hence, these events can be misidentified as ν_e interactions. Electron muon discrimination at lower energies will be discussed in detail in Chapter 3.

- **Neutrino-factory:** In a neutrino factory a primary beam is used to produce $\mu^\pm$ which are bunched, accelerated and fed into a decay ring with two straight sections. In these straight sections the muons decay and produce neutrinos via $\mu^- \longrightarrow \nu_\mu + \bar{\nu}_e + e^-$ and $\mu^+ \longrightarrow \bar{\nu}_\mu + \nu_e + e^+$. The "golden channel" at a neutrino factory is the $\overset{(-)}{\nu_e} \to \overset{(-)}{\nu_\mu}$ appearance channel [12]. As ν_μ $(\bar{\nu}_\mu)$ are always produced along with a $\bar{\nu}_e(\nu_e)$ a target detector for such a beam has to be able to discriminate between ν_μ and $\bar{\nu}_\mu$ interactions. Hence, the charge of the leptons produced in CC interactions have to be tagged. As this will require a magnetization of the detector, LENA, equipped with conventional PMTs, cannot be used for this particular beam type [43].

- **β-beam:** In a β-beam, a primary beam is used to produce radioactive isotopes which are subsequently accelerated and fed into a decay ring. The β-decays of these isotopes produce a pure $\overset{(-)}{\nu_e}$ beam. The isotopes proposed for such beams are ^{18}Ne for ν_e and ^{6}He for $\bar{\nu}_e$ production, respectively [74]. In realistic setups that employ currently existent accelerators an acceleration of these ions up to $\gamma \sim 100$ seems to be possible. The resulting beam is rather low in energy, with a peak flux around 300 MeV. As the first oscillation maximum associated to ϑ_{13} is at $\frac{L}{E} \approx \frac{1}{2}\frac{\text{MeV}}{\text{km}}$, only short baselines as e.g. CERN[5]-Frejus (L = 130 km) are possible.

  For a β-beam , the analysis depends on the $\overset{(-)}{\nu_e} \longrightarrow \overset{(-)}{\nu_\mu}$ appearance channel. Therefore, a far detector for such a beam should be able to discriminate $\overset{(-)}{\nu_\mu}$ from $\overset{(-)}{\nu_e}$ events with only very little $\overset{(-)}{\nu_e}$ contamination. In LENA, this is possible for CC events via the detection of the decay of the produced $\mu^\pm$. Details are discussed in Chapter 3. Furthermore, the spectral information, which is hampered by nuclear effects at the energies of realistic β-beams, is important. Hence, the ability to reconstruct the β-beam-events is crucial. A dedicated track reconstruction is detailed in Section 4 and 5 for muons and electrons with the energy range of interest being set by the β-beam. The application of the results on a β-beam to LENA is finally presented in Section 6.

---

[5]European Organization for Nuclear Research

A comparison of the ϑ_{13} discovery potentials of a 500 kt water Cerenkov detector using a superbeam and/or a β-beam are presented in 2.8. The β-beam clearly outperforms the superbeam for most values of δ. However, for values of ϑ_{13} close to the current limit, the much more cost effective spuerbeam would be sufficient. Part of this work is to study the performance of LENA as far detector in a β-beam experiment. First results are presented in Section 6.4.

2.4.3 Atmospheric neutrinos

Atmospheric neutrinos are produced by interactions of high energy cosmic rays with the nuclei of the atmosphere. These interactions give rise to hadronic showers, consisting mainly of pions and kaons. Charged pions and kaons predominantly decay to muons, thereby producing neutrinos. If the produced muons decay before they reach the ground, their decay releases two more neutrinos, $\overset{(-)}{\nu_e}$ and $\overset{(-)}{\nu_\mu}$ [76].

While constituting a background for the diffuse SN-background search (see Section 2.3.3), atmospheric neutrinos can also be used to probe neutrino oscillations. As neutrinos can penetrate the earth and the usable atmospheric neutrino spectrum is continuous ranging from 100 MeV to tens of GeV, there is a huge spectrum of L/E values which can be investigated. To determine the baseline, the zenith angle of the incoming neutrino has to be known. This is possible for higher neutrino energies where the momentum of the particles generated in neutrino interactions is basically parallel to the neutrino momentum, due to kinematic focusing. For lower energies, this effect can no longer be used on an event by event basis, but still at a statistical level.

The range of features possibly observable with atmospheric neutrinos is wide, as the high neutrino energies allow for ν_τ appearance experiments which are principally sensitive to CP-violation. Furthermore, at certain energies, matter effects in the earth influence the oscillation probabilities. An exact measurement of the oscillation probabilities is therefore sensitive to the mass hierarchy. Figure 2.9 shows the oscillation probabilities for ν_e. The three columns present the situation for different $\sin^2(2\vartheta_{13})$.

To obtain the physical parameters, the measured zenith-angle versus energy distributions have to be compared with the expectations obtained by Monte Carlo simulations. The ratio of $(\nu_\mu + \bar\nu_\mu)$ to $(\nu_e + \bar\nu_e)$ is predicted with highest accuracy [76]: at low energies it is close to two as all muons decay before reaching the ground. It rises for higher energies.

LENA will allow a high statistics measurement of atmospheric neutrinos. Due to its large volume, especially the large height, many events induced by atmospheric neutrinos will be fully contained in the active volume, thus leading to an excellent energy resolution up to energies of a few tens of GeV. The analysis will require to reconstruct both, the energy and the momentum direction of the incident neutrino. A technique for the reconstruction at sub-GeV energies is developed in Chapters 4 and 5, while the reconstruction of more complex events at higher energies is discussed in [5]. The final performance of the LENA detector will strongly depend on its capability to discriminate between ν_e and ν_μ. In quasi-elastic CC interactions, this differentiation is possible by discriminating between electron and muon tracks which is discussed in Chapter 3. Other neutrino interaction types can mimic this signatures as e.g. the NC production of π^0 that decays into two γ-rays can be mistaken as an electron like event. The capabilities of LENA to discriminate against these backgrounds still have to be assessed and are currently studied by Monte Carlo simulations.
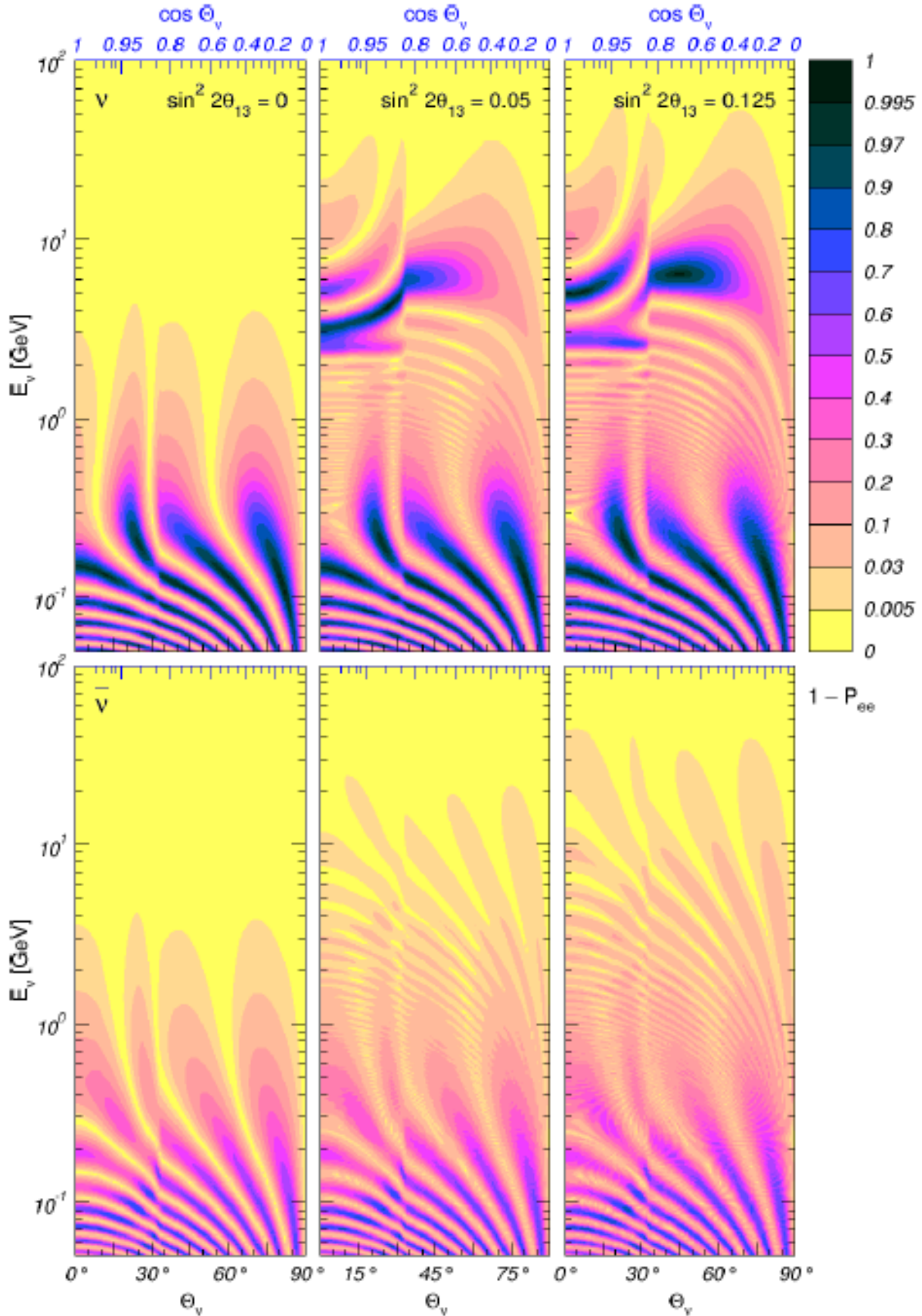
Fig. 2.9: The canvases show the oscillation probability of ν_e (upper row) and $\bar{\nu}_e$ neutrinos (lower row) to any other flavor dependent on the zenith angle of the neutrino Θ_ν and the neutrino energy E_ν. The three columns depict the results for different values of $\sin^2(2\vartheta_{13})$ [75].

Chapter 3

Lepton flavor discrimination in the GeV range

In a neutrino beam experiment, the sensitivity to neutrino oscillation parameters depends on the capability to identify the neutrino flavor. For a β-beam the primary task is to distinguish between electron and muon tracks. To test the discrimination algorithms, both electron and muon tracks are simulated with a Geant4 [77, 78] Monte Carlo simulation.The input parameters used in this simulation are presented in Section 3.1. Section 3.2 introduces an algorithm for a first approximate position determination of the event. This is a prerequisite for discriminating electrons and muons due to their differences in the overall pulse shape (see Section 3.3), as well as for the search for the muon decay, which is investigated in Section 3.4.

3.1 Simulation setup

The detector implemented in the simulation reproduces the cylindrical setup of LENA described in Section 2.1. It is sketched in Figure 3.1. For details see [44]. The center of the detector is chosen as origin for the coordinate system. The rotational symmetry axis of the cylinder defines the z-axis. PXE is used as scintillator in the simulation. Its implemented properties are summarized in Table 3.1. An initial light yield of 10^4 photons per MeV is assumed. Light is emitted with a time structure given by the deexcitation of the scintillator molecules. In the Monte Carlo the multiple decays of the fluorescence of the real scintillator are described in a simplified picture with only two effective components, a fast and a slow one. The light propagation over macroscopic distances in the scintillator results in an attenuation of the signal. The various effects are described by an absorption length, a Rayleigh scattering length as well as an absorption-reemission length. For details see Chapter 7. The macroscopic transport is treated wavelength independent, using effective values corresponding to a wavelength of 430 nm, the peak emission of the used wavelength shifter.

To speed up the simulation, an effective light yield (LY) of $2 \cdot 10^3$ photons MeV^{-1} is used while the quantum efficiency of the PMTs is set to 100%. This is equivalent to the more realistic case of a LY of 10^4 photons MeV^{-1} and a quantum efficiency of 20%.

The design value for the optical coverage in LENA is 30%. In the simulation, this is realized in a simple PMT setup, consisting of only N_{PMT}=13 742 PMTs of 20 inch diameter
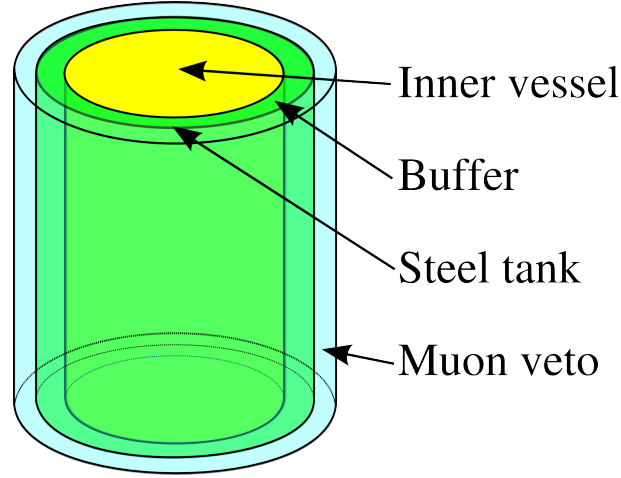
Fig. 3.1: Simplified LENA set up used in the simulation. The central cylinder (yellow) is the PXE filled active volume, It is surrounded by another cylinder with buffer fluid (green). Its surface is implemented as a 4 cm thick steel tank. The outermost cylinder (blue) is the water filled muon veto. All cylinders are of 100 m height and have a radius of 13 m, 15 m and 17.04 m, respectively. The PMTs arranged on the inner wall of the steel cylinder are not shown here.

Name	Symbol	Value
Light yield	ϵ_L	$2000\,\mathrm{MeV}^{-1}$
quantum efficiency of PMTs	ϵ_{PMT}	100%
Fast fluorescence decay constant	τ_f	$2.9\,\mathrm{ns}$
Slow fluorescence decay constant	τ_s	$29\,\mathrm{ns}$
Weight of fast component	Γ_f	0.8
Refractive index	n	1.565
Absorption length	λ_{abs}	$20\,\mathrm{m}$
Rayleigh scattering length	λ_r	$51\,\mathrm{m}$
Absorption/Reemission scattering length	λ_{iso}	$40\,\mathrm{m}$
Reemission decay time constant	τ_{iso}	$1.2\,\mathrm{ns}$
Birk's constant	k_B	$0.15\,\mathrm{mm\,MeV}^{-1}$

Tab. 3.1: Properties of PXE based scintillator used in the Geant4 simulation.

which saves computation time. They are positioned on rings of constant height z as well as on the top and on the bottom of the detector. The PMT photocathode is placed at 50 cm distance from the wall, represented by a flat disc with a photosensitive front side. The time jitter is assumed to be of Gaussian shape with $\sigma_t = 1\,\text{ns}$. PMT specific artefacts as prepulses, late pulses and afterpulses as well as dark noise are neglected.

Generally speaking, the effects of read out electronics are not implemented in the simulation. The time of every photon hit is recorded for each PMT, corresponding to an ideal Flash ADC-based readout scheme. In the subsequent analysis, two additional read-out configurations are implemented: In the minimal read out configuration only the hit time of the first detected photon as well as the total number of detected photons are recorded for each PMT. As this configuration does not allow to look for the signals created by secondary decay products, an additional intermediate read out configuration, inspired by the Borexino electronics [3], was introduced. In this approach, each photon detected by an idle PMT causes a trigger as well as an inhibit preventing a new trigger for the next 90 ns. The trigger time as well as the integrated charge during the inhibit are subsequently stored.

3.2   Center of charge

A general prerequisite for any analysis in a detector with the dimensions of LENA is the spatial reconstruction of the signal and the background events. Neglecting for the moment any spatial extension of the event, a point like energy deposition can be assumed from which the light is emitted isotropically. The number of photons registered by individual PMTs depends on the distance to the light source. Therefore, the most straight forward idea to obtain the event position is to use a charge weighted barycenter $\boldsymbol{x}_B$ of the PMT positions

$$\boldsymbol{x}_B = \sum_{i=1}^{N_{\text{PMT}}} \boldsymbol{x}_i \cdot q_i, \tag{3.1}$$

where $\boldsymbol{x}_i$ and q_i are the position and the charge of the ith PMT, respectively. While this approach works well for events close to the center of the detector substantial deviations from the true position appear for events with larger radii. As scattering and absorption are neglected in Equation (3.1), more light is lost by photons crossing the whole detector than for the ones registered by nearby PMTs.

Therefore, the true center of charge has to be determined by an appropriate fit. Beyond the collected charge, the hit time of the first photon of each PMT can be used. Time of flight based algorithms yield good results for pointlike low energy events. However, they are sensitive to the tracks being a non point-like objects. In general a time based point fit applied to an extended object like a high-energy lepton does not converge. Hence, this approach is not applicable here.

As the integrated charge of the individual PMTs has a much weaker dependence on the extension of the track it is suited best for determining the event position. For a point like event at the position $\boldsymbol{x}_p$, the mean charge expected on the ith PMT μ_i is

$$\mu_i \propto \frac{1}{|\boldsymbol{x}_p - \boldsymbol{x}_i|^2} \cdot \left(\frac{\boldsymbol{x}_p - \boldsymbol{x}_i}{|\boldsymbol{x}_p - \boldsymbol{x}_i|} \cdot \hat{\boldsymbol{n}}_i \right) \cdot \exp\left(-\frac{|\boldsymbol{x}_p - \boldsymbol{x}_i|}{\lambda_{abs}} \right), \tag{3.2}$$

where $\hat{\boldsymbol{n}}_i$ is the normal vector of the i$^{\text{th}}$ PMT pointing outwards. The first two terms of Equation (3.2) correspond to the solid angle covered by the PMT with respect to the event position, while the last part takes light absorption in the scintillator into account. The influence of scattering is neglected here to keep the algorithm fast and simple.

The missing constant in the calculation of μ_i is determined by the "normalization" requirement

$$\sum_{i=0}^{N_{\text{PMT}}} \mu_i = q_{tot},$$ (3.3)

where q_{tot} is the total charge collected in the event.

Given the mean expected charge on the i$^{\text{th}}$ PMT, the probability of the PMT being hit by q_i photons is given by the Poisson distribution [23]

$$P(q_i|\mu_i) = \frac{\mu_i^{q_i}}{q_i!} \exp(-\mu_i).$$ (3.4)

Therefore, the probability of a point like event featuring a specific hit distribution $\boldsymbol{q}$ is:

$$P(\boldsymbol{q}|\boldsymbol{x}_p) = \prod_{i=1}^{N_{PMT}} P\left(q_i|\mu_i(\boldsymbol{x_p})\right).$$ (3.5)

Given $P(\boldsymbol{q}|\boldsymbol{x}_p)$, $\boldsymbol{x}_p$ can be found using the likelihood function $L(\boldsymbol{x}_p|\boldsymbol{q})$ which is defined as

$$L(\boldsymbol{x}_p|\boldsymbol{q}) := P(\boldsymbol{q}|\boldsymbol{x}_p).$$ (3.6)

Note that L is not a probability density function (PDF) as it is not normalized with respect to $\boldsymbol{x}_p$. It can be shown [23] that the value of $\boldsymbol{x}_p$ for which L is maximal constitutes an unbiased estimator for the true value of $\boldsymbol{x}_p$. Hence, the charge barycenter of the track corresponds to the maximum of L with respect to $\boldsymbol{x}_p$. It is equivalent to the minimum of

$$\mathcal{L} = -\ln\left[L(\boldsymbol{x}_p|\boldsymbol{q})\right] = \sum_{i=1}^{N_{PMT}} \left[q_i \ln(\mu_i) - \mu_i - \ln q_i!\right].$$ (3.7)

This quantity is called the "negtive logarithmic likelihood" (NLL). The practical advantage of minimizing $\mathcal{L}$ compared to maximizing L is the increased numerical stability: The probable values for L span multiple orders of magnitude due to the many factors contained in $P(\boldsymbol{n}|\boldsymbol{x}_p)$. Numerically, minimizing $-\ln(L)$ is much less demanding. The function minimization is performed based on the `MINUIT` [79] package from the ROOT [80] framework, using the `MIGRAD` minimization algorithm.

In Figure 3.2 the fit results are shown for a sample of 500 muons muons with an energy of 300 MeV, traveling from the coordinate origin along the negative x-axis. Their average track length is 130 cm. The reconstructed values for $\boldsymbol{x}_p$ are not centered on the middle of the track but to a point 40 cm from the track end. This is caused by the rise of the deposited energy per unit path length towards the end of the track (Bragg Peak). Due to the different energy loss mechanism, this is not valid for electrons. Their reconstructed barycenters tend to be closer to the start of the track.

For further evaluation, the distance ρ of the reconstructed barycenters to the track is
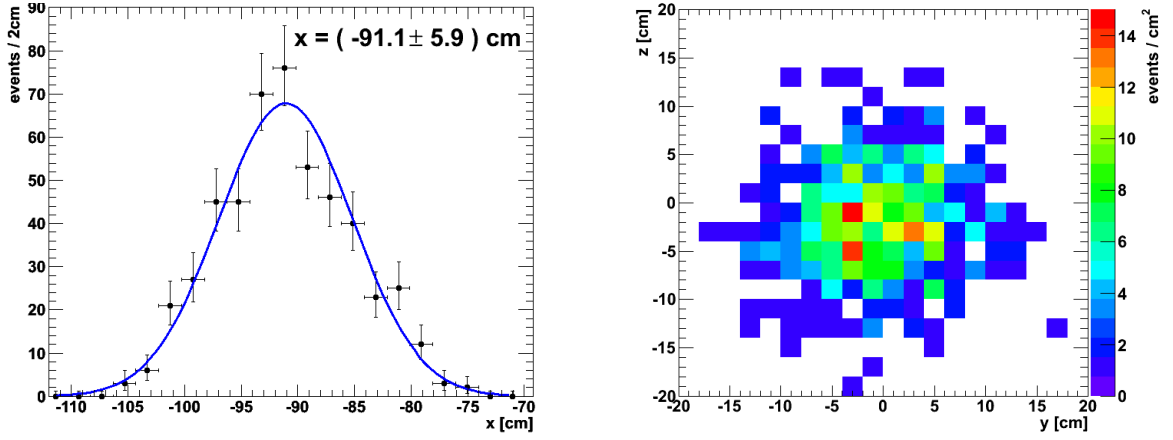
Fig. 3.2: Results of the barycenter fit for 300 MeV muons traveling from the center of the detector in negative x-direction (500 events). The reconstructed x-coordinates of the barycenters are shown on the left. The Gaussian fit result is (-91.1 ± 5.9) cm. Note that there are two outliers at -120 cm and -190 cm which are not shown in this plot. The barycenter of the track is in the rear part of the ≈ 130 cm long track, due to the Bragg-peak of the energy loss. The right plot shows the distribution of the coordinates perpendicular to the track. The obtained barycenter positions are centered around the expected value $y = z = 0$.
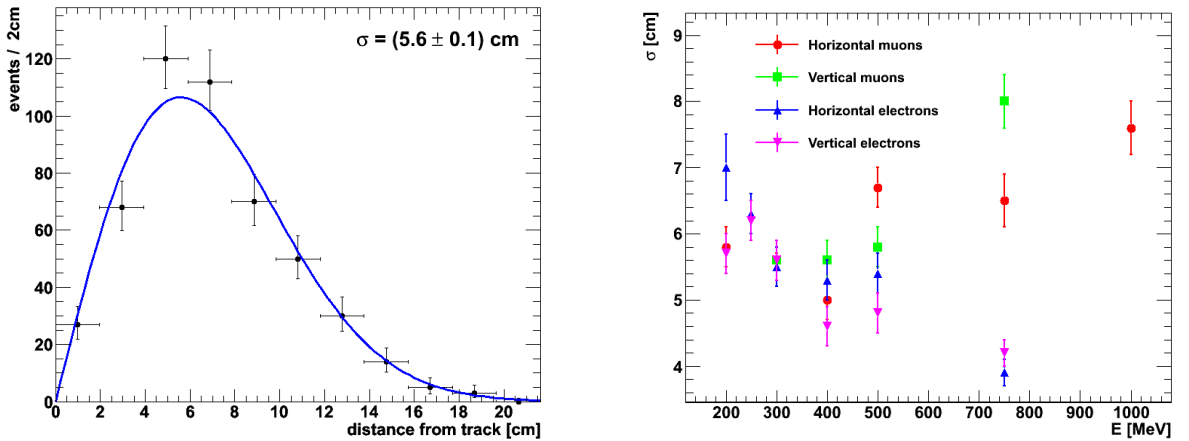
Fig. 3.3: The left plot shows the distribution of the distance ρ of the reconstructed barycenters to the track for 500 simulated 300 MeV muons traveling from the center of the detector in negative x-direction. From a fit with $P(\rho) \propto \rho \cdot \exp(-\frac{\rho^2}{2\sigma^2})$ the resolution (5.6 ± 0.1) cm is obtained. The plot on the right hand side displays the fit results with errors as a function of energy, lepton flavor and orientation.
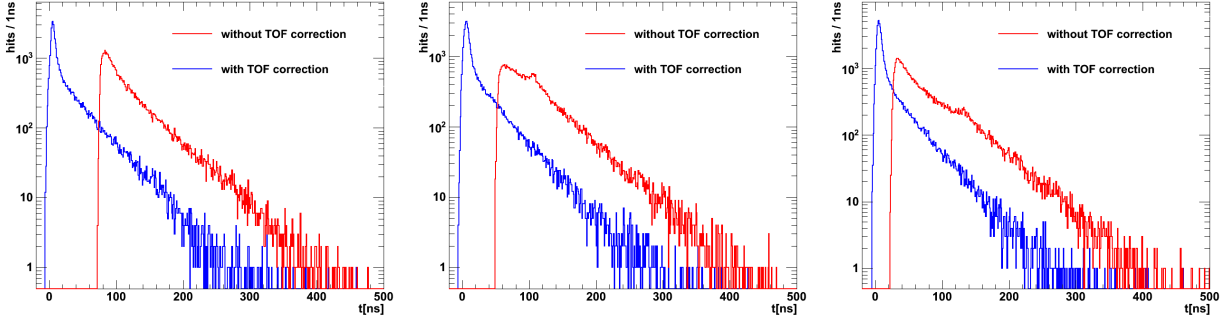
Fig. 3.4: Average raw and TOF-corrected pulses pulses for 300 MeV muons started at the center of the detector (left), at x = 5 m (middle) and x = 10 m (right). All detected photons are displayed. The middle and right plots show that raw pulses tend to have secondary peaks or shoulders which are created when the photons arrive at the far side of the wall. In contrast, the shape of the TOF-corrected pulse is sharper and much less position-dependent. As the TOF correction is done with respect to the track barycenter and not to the actual point of origin of the individual photon, there are some photons which have a negative TOF-corrected hit time.

histogramed. Assuming that the obtained resolution is the same for both coordinates $x_{1,2}$ perpendicular to the track and that the obtained distribution is Gaussian, the PDF for $x_{1,2}$ is given by

$$P(x_1, x_2)dx_1dx_2 = \frac{1}{2\pi\sigma^2} \exp\left(-\frac{x_1^2 + x_2^2}{2\sigma^2}\right) dx_1dx_2. \tag{3.8}$$

The coordinates $x_{1,2}$ are chosen to be zero if the reconstructed barycenter is directly on the track. Therefore, the distance spectra distribution is described by

$$P(\rho)d\rho = \int_0^{2\pi} P(\rho, \varphi)\rho \cdot d\rho \; d\varphi = \frac{\rho}{\sigma^2} \exp\left(-\frac{\rho^2}{2\sigma^2}\right) d\rho, \tag{3.9}$$

with $\rho = \sqrt{x_1^2 + x_2^2}$ and the azimuth angle φ. The additional factor of ρ results from the volume element introduced by the transition to cylindrical coordinates. The resolution σ can be determined by a fit of $P(\rho)$ to the barycenter distribution. Figure 3.3 shows distribution and fit for 300 MeV muons traveling from the origin along the negative x-axis. The right side displays the obtained sigma values as a function of the lepton energy. Both, the cases of electrons and muons as well as vertical and horizontal tracks are shown. For muons, there is an optimal energy where this fit works best. The fit performance decreases towards low energies due to lower statistics while for high energies the straight track is deflected by multiple scattering. For electrons on the other hand the resolution monotonously improves with rising energy because multiple scattering is suppressed at higher energies. Furthermore, the barycenter of electron tracks is rather close to the start point of the track, while the barycenter is in the rear half for muon tracks. Therefore, the barycenter is much less influenced by multiple scattering for electron than for muon tracks.
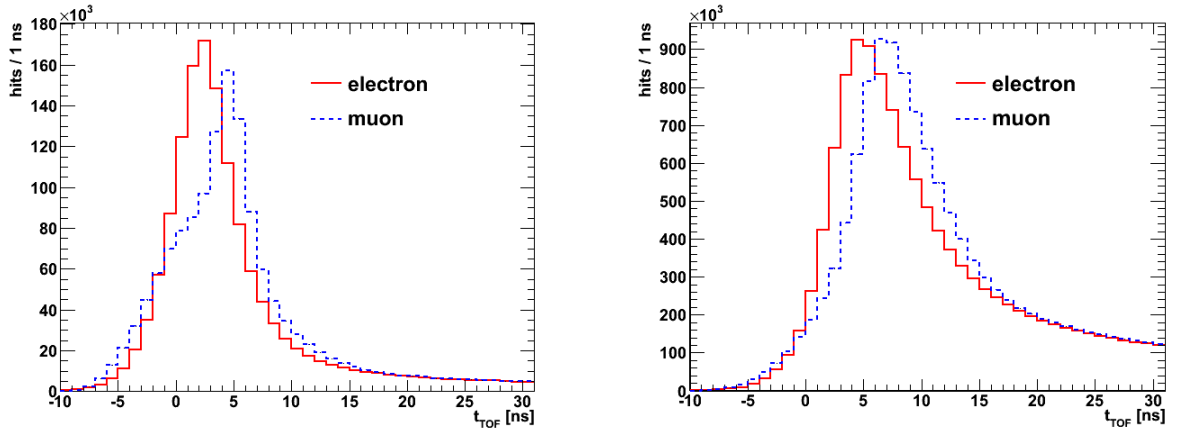
Fig. 3.5: Average electron and muon pulses for a kinetic energy of 500 MeV. The simulated muons and electrons where always started at the center of the detector. The average pulse shapes were created from 100 events where the lepton traveled in negative x-direction and 100 events where the lepton propagated in negative z-direction. The left hand side shows the results obtained using only the first hit of each PMT while the results on the right side feature the full hit information.

3.3 Pulse shape discrimination

Due to their different rest masses, the energy loss per unit path length differs for electrons and muons. Therefore, electron and muon tracks can be distinguished via their different pulse shapes. This was investigated in [21]. In the following, a time of flight (TOF) correction is is included in the pulse shape analysis, further improving discrimination efficiency.

The position of the event has a larger influence on the pulse shape than the flavor of the particle. It can be removed by a TOF correction of the photons with respect to the reconstructed barycenter $\boldsymbol{x}_p$. Therefore, the TOF-corrected hit time of an individual photon is defined as

$$t_{\mathrm{TOF}} := t - \frac{|\boldsymbol{x}_p - \boldsymbol{x}_{\mathrm{PMT}}|}{c/n}, \tag{3.10}$$

where $\boldsymbol{x}_{\mathrm{PMT}}$ is the center of the PMT which detected the photon. The effect of the correction is depicted in Figure 3.4 which compares TOF-corrected pulses with raw pulses for different event position. Clearly, TOF correction significantly reduces the position dependence of the pulse shape. Hence, for the rest of this chapter, TOF-corrected hit times instead of the absolute hit times are used.

This allows searching for differences in the pulse shapes of electrons and muons. Muons tend to have a relatively constant energy loss distribution for most of the track and a peak at its end. In contrast, electrons lose most of their energy in the first part of the track and typically feature a smaller range than muons. Therefore, electron pulse shapes are expected to have a smaller FWHM than muon pulse shapes and to have a steeper rise. To confirm this assumptions, it is useful to average over multiple pulses to suppress event-by-event fluctuations.

 Averaged pulses for muons (dashed blue) and electrons (solid red) at a kinetic energy of 500 MeV are displayed in Figure 3.5: On the left the pulse shapes based on the first hit in each PMT are shown, while on the right all detected photons are included. The results

confirm the expectation of electrons having a shorter pulse with a smaller risetime. Note that the difference between the electron and the muon pulse is more striking if only the first PMT hits re used.

The steeper rise and smaller FWHM of electron pulses motivates the use of two parameters for the flavor discrimination: First, the risetime of the pulse, defined as the time needed to go from 10% to 90% of the maximum pulse height. Second, the width of the pulse at 1/6 of its maximum value. The chosen height of 1/6 of the maximum pulse height corresponds to an optimum discrimination capability for muons versus electrons using only first hits.

Figure 3.6 shows the obtained distributions for electrons and muons with energies of 500 MeV (upper row) and 1 GeV (lower row) as a function of risetime and width. Each plot features the results from in total 200 tracks of each lepton flavor, half are propagated along the negative x-axis the other half along the negative z-axis. All tracks are started at the center of the detector. The plots on the left feature the results obtained using only first hit information, while the plots on the right include all detected photons. The resulting distribution for electrons shows a higher spread caused by the larger event-by-event fluctuations of electron tracks. At both energies a positive selection of a pure electron sample is possible with an efficiency of more than 73% at 500 MeV and more than 96% at 1 GeV featuring only very little muon contamination. The same is true for muon selection at 1 GeV. However, a 500 MeV muon sample will contain a significant electron background of order 30%. The comparison of first-hit and full pulse shape distributions shows no significant difference in pulse shape capability.

For 1 GeV, the distributions for the muon tracks cluster in two different regions due to the different pulse shapes created by muons parallel and perpendicular to the symmetry axis of the detector. This reveals, that even such a simple plot already contains informations about the track direction.

3.4   Tagging the muon decay

Section 3.3 shows that pulse shape analysis on its own is not sufficient obtain a pure muon sample for energies below ~ 1 GeV. Therefore, at these energies, additional muon tagging is required. An efficient approach is to exploit the delayed signal of the muon decay,

$$\mu^- \longrightarrow e^- + \bar{\nu}_e + \nu_\mu, \tag{3.11}$$

with a characteristic lifetime of $\tau_\mu = 2.2\,\mu$s [10]. Muons can be identified by the time coincidence of a prompt signal from the track and a delayed signal from the decay electron, while electrons produce only the prompt track signal.

The search for the muon decay electron cannot be done based alone on the first photons of each PMT. Therefore, for the reminder of this Section the medium readout configuration introduced in Section 3.1 is used; i.e. each PMT is inhibited 90 ns after each triggering photon. Photoelectrons collected during this time are added to the first photon signal.

Figure 3.7 displays the TOF-corrected overall pulse shape for a 300 MeV muon. It features three peaks: Two of them are due to light from the primary track. The first peak is created by the first photons emitted from the track that arrive at the PMTs directly. The second peak corresponds to photons from the afterglow of the track, causing re-triggers after the inhibits of the first triggers have ended. The third peak is the signal from the
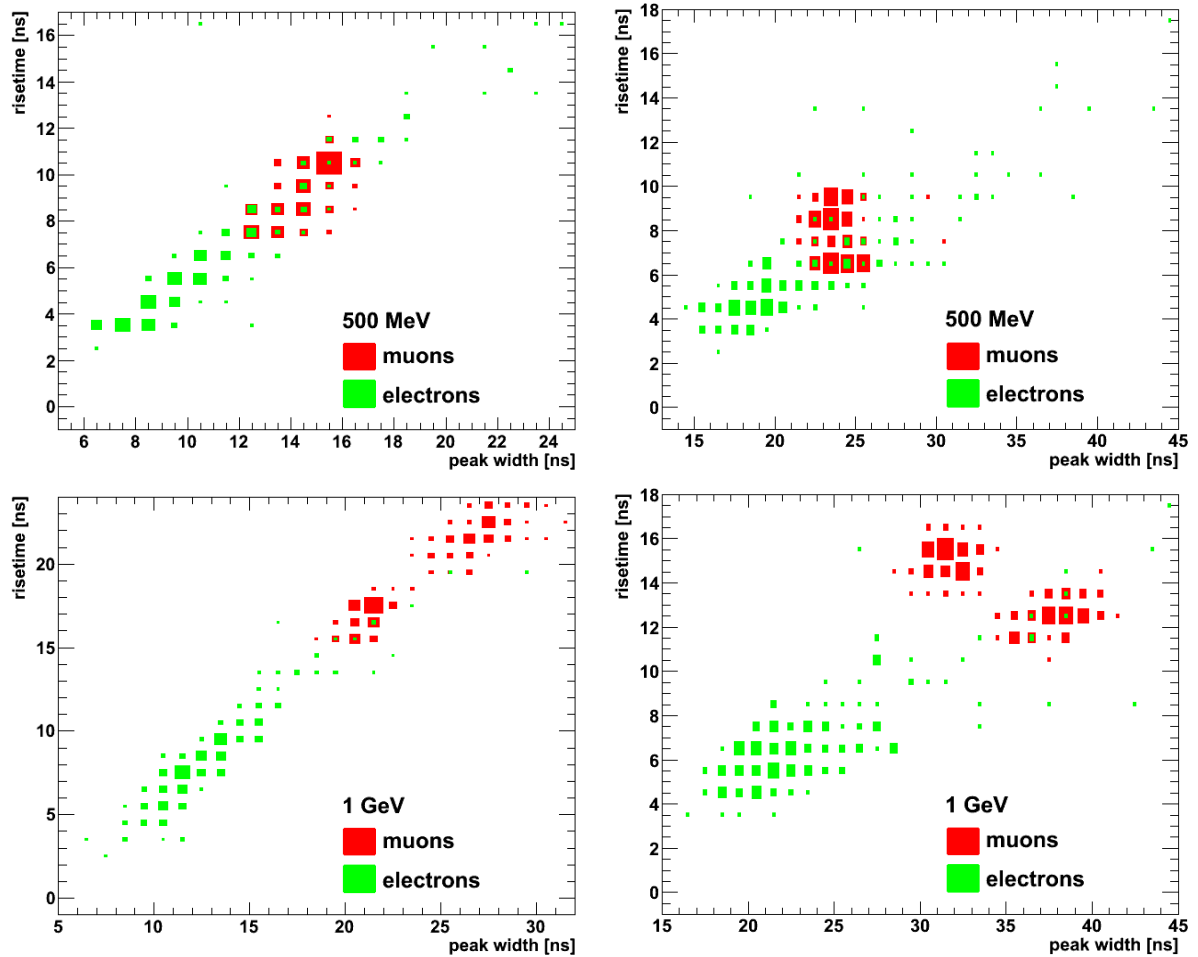
Fig. 3.6: Resulting distributions in the peak width-risetime plane for electrons (green) and muons (red). All leptons were started at the origin. For each flavor 100 tracks parallel to the z-axis and 100 tracks parallel to the x-axis were incorporated in each plot. The size of the drawn boxes indicates the number of leptons in the corresponding bin. The left hand plots were created using only first hit information while the results on the right hand side include the full photon information.
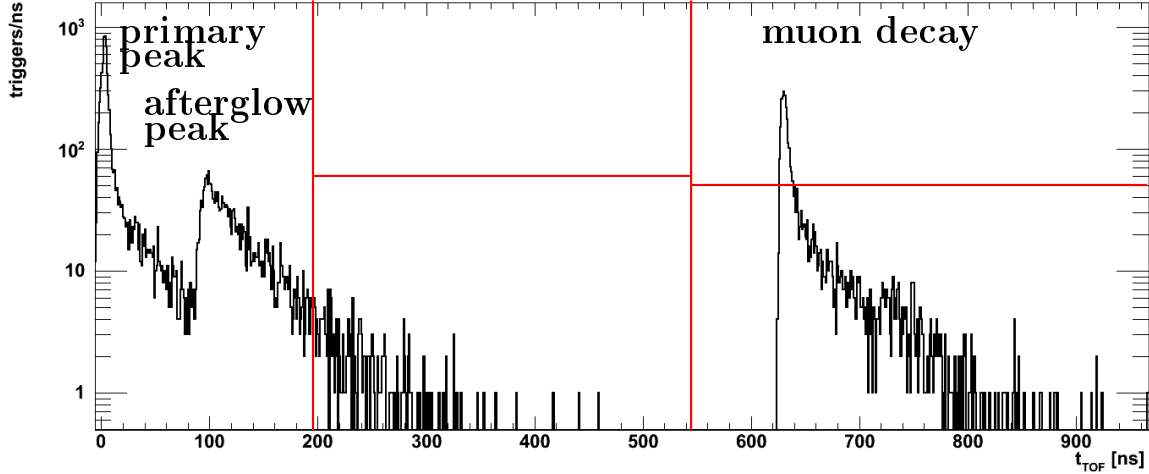
Fig. 3.7: TOF-corrected trigger time distribution for a 300 MeV muon. Three overall structures are visible: The primary peak is produced by the first light each PMT sees from the muon track. The afterglow peak is an artifact obtained as the inhibit time of the PMT is short enough that after the end of the inhibit there is still enough delayed light from the primary track to cause a new trigger on many PMTs. This second peak is roughly the inhibit time of 90 ns behind the first peak. The third peak is due to the electron produced in the muon decay.
The red lines indicate the time (vertical) and height thresholds used for tagging the muon decay.

muon decay electron. The muon tagging algorithm has to identify this peak instead of the re-triggers of the primary event.
 The algorithm is based on a histogram of the TOF-corrected hit times of all PMT triggers similar to Figure 3.7. Subsequently, the time of the first maximum t_{max} is determined. To suppress the re-triggers all entries with $t < t_{max} + 190$ ns are discarded. For later times a decay peak is identified if it exceeds the threshold of 60 triggers/ns in at least two consecutive bins which corresponds to about 6 MeV of deposited energy. This threshold is introduced to avoid identifying the decaying flank of the primary pulses as the muon decay and to get rid of rare late pulses caused by knock out neutrons from ^{12}C. To increase the efficiency, the threshold is lowered to 50 triggers/ns ($\sim$5.3 MeV) for $t > t_{max} + 540$ ns as soon as the primary pulse has died away. The time and pulse height thresholds used are indicated in Figure 3.7 by red lines.
The parameters are tuned to provide maximum rejection against misidentification of electrons as muons. Consequently, none of the 7250 simulated pure electron tracks was wrongly identified as a muon. Therefore, the probability of wrongly assigning an electron as a muon is $p_{mis} < 4.2 \cdot 10^{-4}$ at 95% CL . The efficiency for identifying muon tracks is $\epsilon = (85.1 \pm 1.4)\%$.
There are two physical causes for the deviation of the efficiency from unity: First the exclusion of the 190 ns after the first peak also disposes some decays. Approximating the peak of the distribution with the time of creation and neglecting the muon time dilation, the loss in unidentified decays is

$$\Delta\epsilon_t = \int\limits_0^{190\,\text{ns}} P_{dec}(t)dt = \int\limits_0^{190\,\text{ns}} \frac{1}{\tau_\mu}\exp\left(-\frac{t}{\tau_\mu}\right)dt = 8.3\%, \qquad (3.12)$$
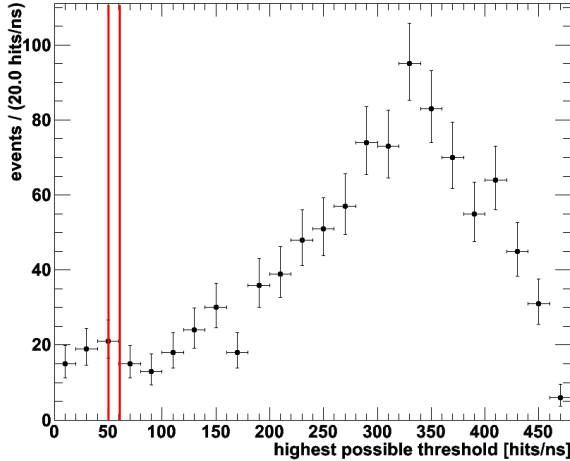
Fig. 3.8: Maximum possible pulse height threshold that allows the decay to pass the trigger. The two red lines mark the two trigger thresholds used in the analysis. The loss in efficiency due to the trigger thresholds are $\Delta\epsilon_{th}^h = (5.5 \pm 0.07)\%$ and $\Delta\epsilon_{th}^l = (4.4 \pm 0.06)\%$ for the higher and lower threshold, respectively.
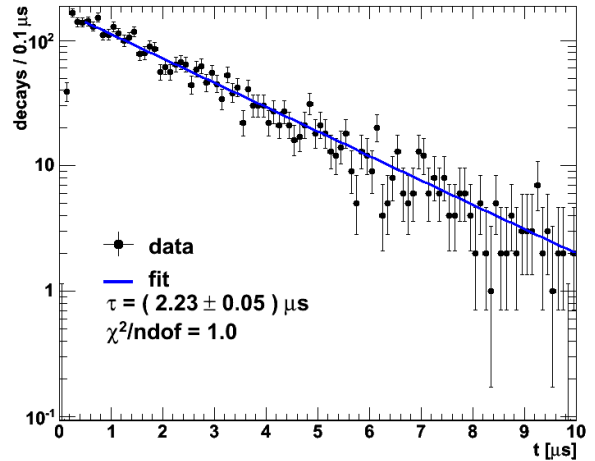
Fig. 3.9: Histogram of the reconstructed muon decay times. The blue line shows the result of fitting an exponential to the data. The muon decay time is recovered within errors and the goodness of fit is excellent. The fit is not extended over the whole range to get rid of threshold effects close to the time threshold of the muon search.

with $P_{dec}(t)dt$ being the PDF for the muon at rest to decay at a time t after its creation. Second, as already mentioned, the cut on the pulse height leads to a loss in efficiency. To assess this loss 1000 muons at rest were simulated. For each of these muons the maximum possible threshold to pass the cut is determined. The results are histogramed in Figure 3.8. For a threshold of 60 and 50 triggers/ns, $\Delta\epsilon_{th}^h = (5.5 \pm 0.07)\%$ and $\Delta\epsilon_{th}^l = (4.4 \pm 0.06)\%$ of all decays are below the threshold and thus not identified as a decay. Taking both components of the efficiency loss together one obtains $\Delta\epsilon \approx 13\%$ which is a bit below the actually observed value of about 15%. There are two main reasons for this discrepancy: First the approximation that the peak of the track pulse can be identified with the time of creation as used in equation (3.12) is generally not valid. Typically the peak is some ns after the creation of the particle which means that the actual threshold time is a bit bigger than 160 ns therefore increasing $\Delta\epsilon_t$. Looking at decays of muons at rest used to estimate $\Delta\epsilon_{th}^{l,h}$, the TOF correction is done with respect to the center of the muon decay, not with respect to the track. Therefore, the obtained peaks are a bit sharper and therefore higher than in reality leading to a shift to higher thresholds. This means that $\Delta\epsilon_{th}$ is also estimated a bit to small.

To test whether the pulses identified as muon decays are all due to muon decays, the TOF-corrected start times of the identified delayed pulses $t_{\text{TOF}}^{\text{dec}}$ are histogramed. The result is displayed in fig 3.9. Fitting an exponential to the distribution, returns the lifetime of the muon within errors and features a excellent goodness of fit (χ^2/ndof = 1.0) indicating that the reconstructed pulses are really due to muons.

Chapter 4

Muon-track reconstruction

Apart from lepton flavor identification, the reconstruction of lepton tracks is a task central to the analysis of high energy events. Reconstruction means the determination of the kinetic properties of the lepton at its vertex.

This chapter deals with the reconstruction of pure muon tracks, i.e. neglecting any other particles produced in a neutrino interaction. Furthermore, only contained tracks, i.e. tracks totally enclosed in the active volume of the detector, are dealt with. Additionally, all simulated tracks are close to the vertical center of the detector so that boundary effects appearing at the top and the bottom of the detector can be neglected. The basic principles used for the reconstruction are explained in Section 4.1 along with the quantities used to characterize a track. Section 4.2 introduces an analysis which determines input parameters that are used for the final global fits to the total event which provide track and energy information and are detailed in Section 4.3.

4.1 Fundamentals

4.1.1 Basic idea

Using the directionality of the photons emitted due to the Cerenkov effect is a well established technique to reconstruct the track of a particle in water Cerenkov detectors. In contrast, photon emission in liquid scintillators is isotropic. Therefore, it was only recently realized that track reconstruction is possible in unsegmented liquid scintillator based detectors, exploiting not only the spatial distribution of the hit PMTs but also the photon arrival times on the PMTs (e.g. [5, 6]).

The basic principle can be understood by considering a particle traveling straightly for a certain time through the scintillator at the speed of light and then stopping abruptly. At each point of the track photons are emitted isotropically. Approximating the isotropic photon emission as a spherical wave, i.e. taking the limit $N_{\mathrm{photons}} \to \infty$ and assuming prompt photon emission, Huygens principle can be used to construct the first photon surface as depicted in Figure 4.1. As the speed of the particle exceeds the speed of light in the scintillator, a structure resembling a Cerenkov cone develops. Obviously, the first photon surface is a clear indicator of the track's direction and can therefore be used to reconstruct the track. Note that in contrast to the Cerenkov effect there is no interference between the emitted waves in a liquid scintillator as each photon is emitted independently from all others.
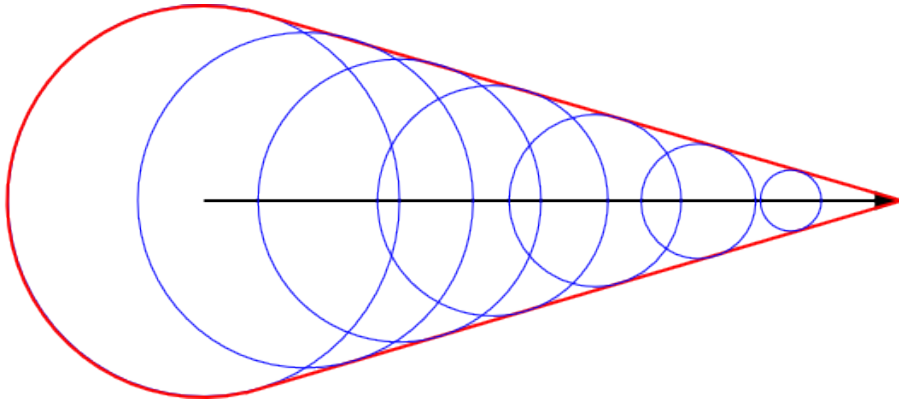
Fig. 4.1: Construction of the first photon surface (red) by superposition of spherical waves (blue) created by a particle transversing the scintillator (black). The image is not to scale.
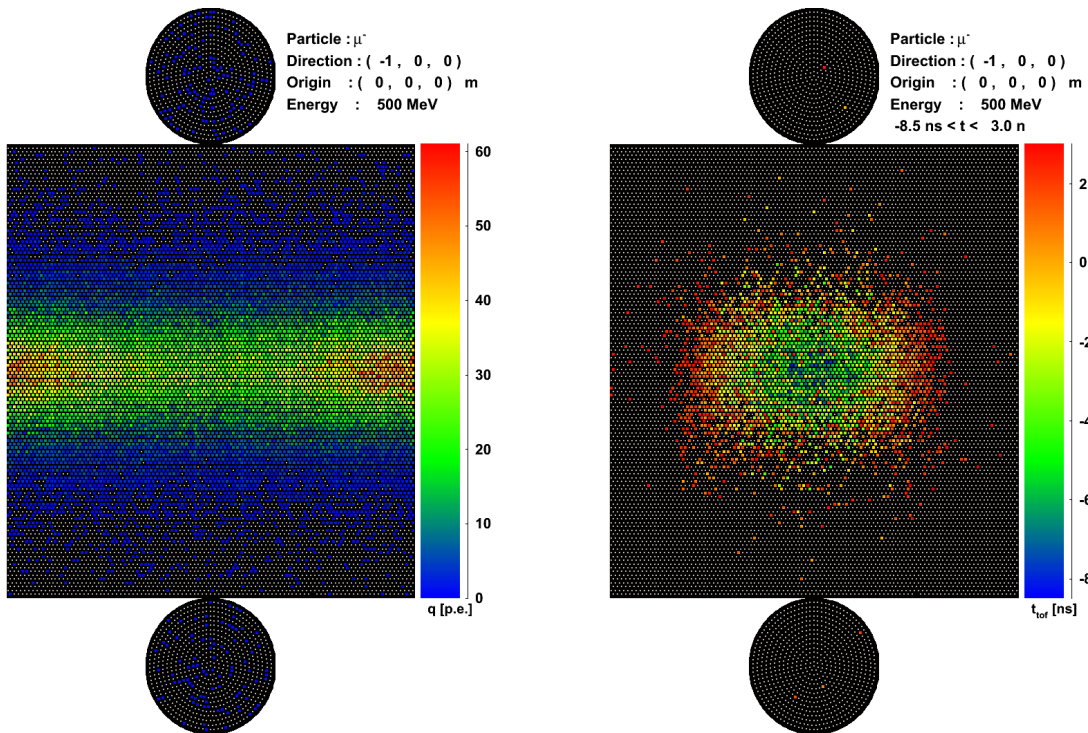
Fig. 4.2: Signal of a 500 MeV muon in LENA. The color coded information denotes the charge seen by each PMT on the left and the hit time of the first photon on each PMT after a time of flight correction with respect to the charge barycenter of the track on the right. The circles represent the lid and the bottom of the detector while the rectangle is the wall of the cylinder with the z-axis facing upwards. The center of the rectangle corresponds to the point where the positive x-axis intersects with the wall.

Figure 4.2 shows an example of the signal obtained for a simulated track: A 500 MeV muon traveling from the center of the detector towards the tank wall. Depicted on the left side of Figure 4.2 is the charge distribution which features only a slight asymmetry due to the displacement of the track's center of charge with respect to the symmetry axis of the detector. The TOF-corrected first hit time distribution is displayed on the right side of Figure 4.2, showing only PMTs featuring a TOF-corrected hit time of less than 3 ns. The observed distribution is clearly anisotropic and can therefore be used to reconstruct the photon direction.

Note that the barycenter of the charge distribution is on the opposite side from the barycenter of the shown TOF-corrected hit time distribution. The position of the barycenter is in the rear part of the track (see Section 3.2), i.e. on the negative x-axis. In contrast, the minimum of the TOF-corrected first hit time distribution is defined by the intersection of the extension of the track in start point direction with the wall i.e. where the positive x-axis meets the wall (see Section 4.2.3).

4.1.2   Fit parameters

In dedicated tracking detectors, like e.g. the ATLAS inner detector [81], track reconstruction is a two-step process: First a set of points the track passes through is reconstructed from the measured data which is subsequently fitted with a physical model for the track. This is not possible in a scintillation detector like LENA as there is no way to tell from where exactly a detected photon originated. Therefore, the two steps have to be merged and the fit of the physical model has to be done directly to the signal.

This already means that it is basically impossible to include any event-by-event fluctuations in the fit. Therefore, the physical model used here is the continuous slowing down approximation (CSDA) for a straight track [82]. In this approximation, the muon is propagated along the track, replacing the actual values for the stopping power with the mean value: $-\frac{dE}{dx} \approx \left\langle -\frac{dE}{dx} \right\rangle$. Furthermore, the possibility of a muon decaying in flight is neglected. This implies that all properties of the track including its length are determined by the parameters of the muon at the vertex, i.e. its four-momentum p and its space-time coordinates x_s. As the four momentum has to fulfill $p^\mu p_\mu = m_\mu^2 c^2$, the total number of parameters is reduced from eight to seven.

The space-time coordinate of the start point is most conveniently parametrized in normal Minkovsky space $x = (t_s, \boldsymbol{x}_s)$. However, a different parametrization is advantageous for the momentum: The direction of the muon is expressed in spherical coordinates ϑ and φ. Furthermore the total energy of the muon E is replaced by its kinetic energy T as the latter is equivalent to the total energy a contained muon deposits in the scintillator. Hence, the complete set of parameters is

$$\boldsymbol{X} = (\boldsymbol{x}_s, t_s, \vartheta, \varphi, T). \tag{4.1}$$

4.2   Determination of start parameters

Determining an estimation for the track parameters is not done for all parameters at once. Instead, a multiple step approach is used. In a first step presented in Section 4.2.1, an estimate for the energy of the track is obtained. Using this information, the tracks can be divided in two subgroups according to their orientation with respect to the symmetry
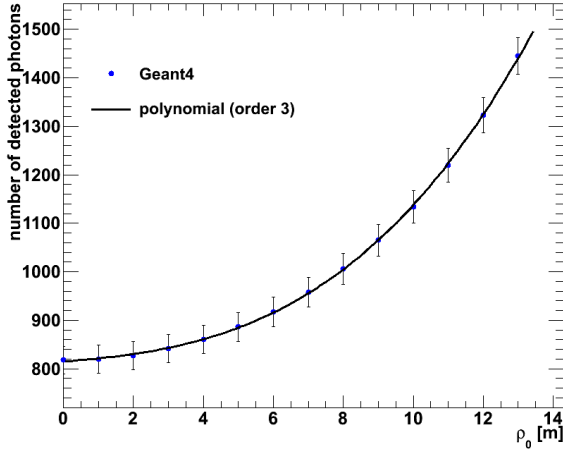
Fig. 4.3: Number of detected photons for a 1MeV electron event at different radii. For each point the mean value of 3000 electron events has been plotted. The errors represent the event-by-event spread of the number of detected photons. Note that for this plot the whole detector wall was used as photosensitive volume. Therefore, the obtained numbers have to be multiplied with the photocoverage to obtain the actual results. The blue line is a polynomial of order three that has been fitted to the data.
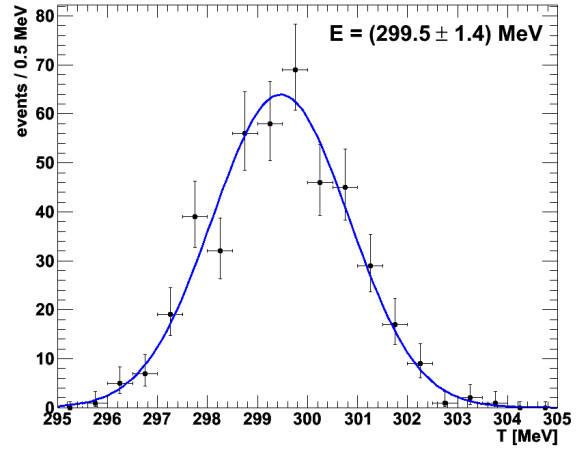
Fig. 4.4: Results of the energy estimation for 500 muons with 300 MeV kinetic energy. Only muons with an identified decay electron are used for this plot. Additionally the decay time of the muon is required to be greater than 250 ns to avoid the influences of muon decays. The obtained distribution was fitted with a Gaussian. The quoted value represents the mean of the Gaussian, the quoted error the 1-σ width.

axis of the detector, as detailed in 4.2.2. For each of this subgroups, an estimate for the start point of the track and its direction can be obtained, which is described in Sections 4.2.3 and 4.2.4, respectively. Finally, Section 4.2.5 deals with the estimation of the event start time.

4.2.1   Energy estimate

To get a first energy estimate, the same approximation as in Section 3.2 is used, i.e. the event is approximated as a point-like energy deposition at the barycenter $\boldsymbol{x}_p$. Furthermore, if a decay electron has been found, only photons with a TOF-corrected hit time of $t_{\text{TOF}} < t_{\text{TOF}}^{dec}$, where t_{TOF}^{dec} is the TOF-corrected time of the muon decay, are used for the analysis to get rid of the effects of the muon decay.

Muons are minimum ionizing during most of their lifetime leading to a steady low energy deposit. Therefore, $k_B \frac{dE}{dx} \sim 0.15 \, \frac{\text{mm}}{\text{MeV}} \cdot 2 \, \frac{\text{MeV}}{\text{cm}} = 0.03 \ll 1$, i.e. quenching can be neglected according to Birk's formula (1.19). Using this approximation, the total number of produced photons N_γ is proportional to the total deposited energy in the scintillator, i.e. to the kinetic energy of the muon.

Figure 4.3 shows the number of detected photons N_γ^{det} versus the radius coordinate of light emission ρ_0 for constant N_γ. The number of detected photons rises with the radius due to the decreasing absorption in the scintillator. Therefore, a spatial correction has to be done. Fitting the radius dependency obtained in Figure 4.3 with a polynomial of order
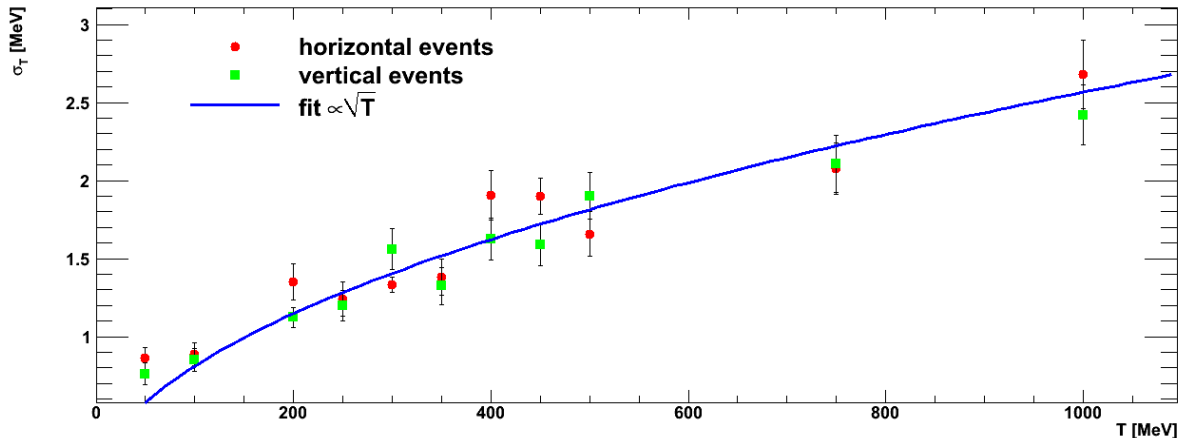
Fig. 4.5: 1-σ errors for horizontal and vertical muons as a function of the kinetic energy. Muons of both orientations are started in the center of the detector, but show no significant difference. The fit $\propto \sqrt{T}$ is done to both orientations at once. The resulting energy resolution is $\frac{\Delta T}{T} = \frac{(8.1\pm0.1)\%}{\sqrt{T/\text{MeV}}}$.

three yields an acceptable result. Assuming that $N_\gamma^{det}(\rho_0 = 0) \propto T$, the energy estimate is calculated to

$$T = a \cdot N_\gamma^{det}(\rho_0 = 0) = a \cdot \left(\frac{N_\gamma^{det}(\rho_0 = 0)}{N_\gamma^{det}} \right)(\rho_0) \cdot N_\gamma^{det} \qquad (4.2)$$

with $a = 6 \cdot 10^{-3}$ MeV being the proportionality constant determined at $T = 500$ MeV and $\left(\frac{N_\gamma^{det}(\rho_0 = 0)}{N_\gamma^{det}} \right)(\rho_0)$ being calculated via the polynomial obtained from Figure 4.3. Note that the number of photo electrons for a given number of produced photons is also a function of the z-coordinate of light emission. This effect is neglected here as all simulated tracks do not deviate more than ~ 10 m from the center of the detector, which is much smaller than the height of the detector. Significant effects are expected for events closer than ~ 25 m to the top or the bottom of the detector.

The energy results obtained from this analysis are plotted in Figure 4.4 for 300 MeV muons. To get rid of the influences of muon decays on the energy estimate, an event is required to feature a decay time of at least 250 ns[1]. Fitting the energy distribution with a Gaussian leads to the 1-σ-error of a single event of about 0.5%. To further characterize the potential of the energy estimation, Figure 4.5 shows the obtained 1-σ errors as a function of the kinetic energy of the muon. Assuming that the main error is due to the photon statistics and that the influence of the finite extension of the track can be neglected, the error should follow $\Delta T \propto \Delta N_\gamma^{det} = \sqrt{N_\gamma^{det}} \propto \sqrt{T}$. A corresponding fit yields for the overall energy resolution

$$\frac{\Delta T}{T} = (8.12 \pm 0.12)\% \cdot \sqrt{\frac{\text{MeV}}{T}}. \qquad (4.3)$$

The standard error of the mean is not shown, as these deviations are generally small and compatible zero as expected. Therefore, the fit accuracy is more than sufficient to serve as input for the reconstruction of the tracks.

---

[1] A discussion of the effects of the muon decay on the energy resolution can be found in Section 4.3.4.
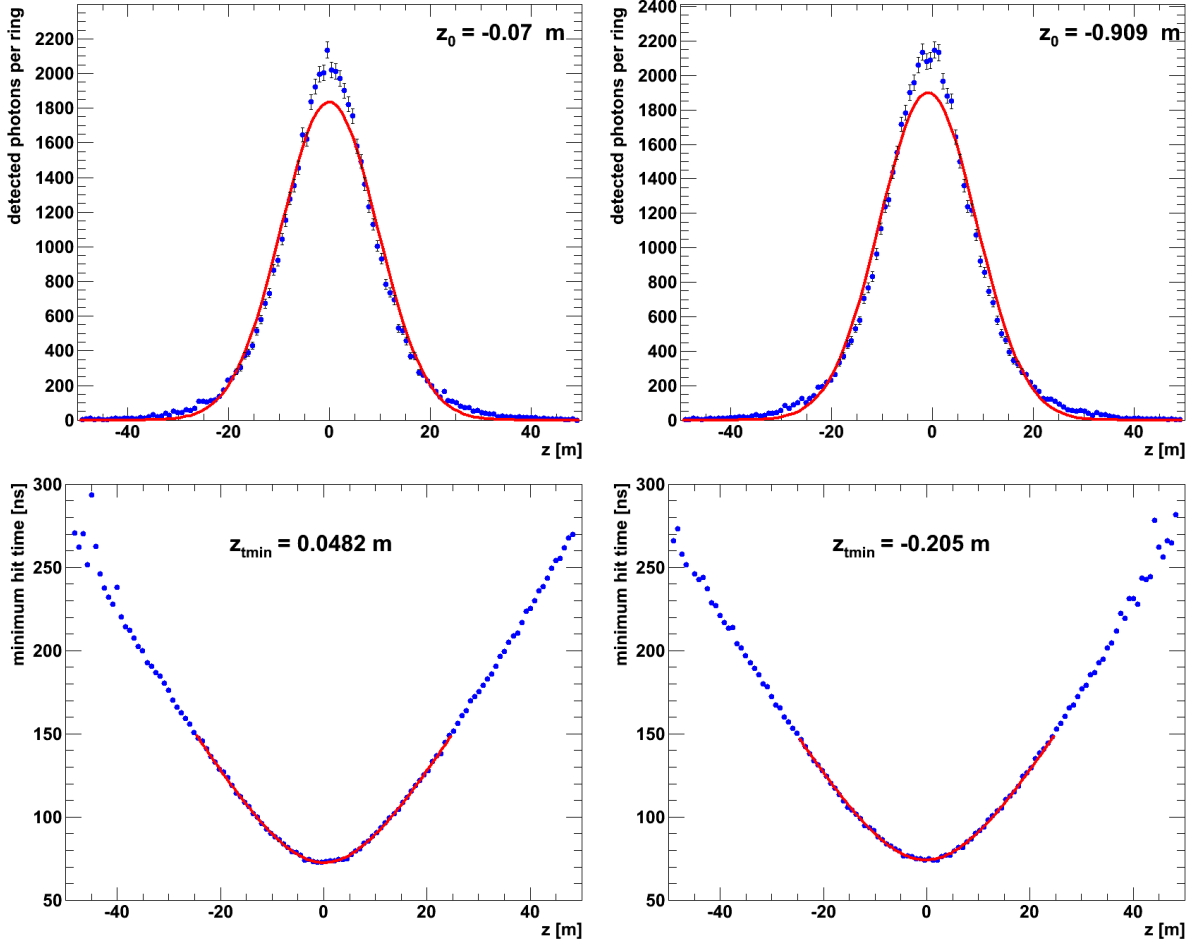
Fig. 4.6: Photons per PMT ring (top) and hit times of the first photon in each ring (bottom) for 300 MeV muons traveling from the center of the detector along the negative x-axis (left) and along the negative z-axis (right). The fits to the top-panel distribution return z_0 as the mean of the Gaussian. The bottom panels display fits assuming a point-like light source. The value z_{tmin} corresponds to the z-coordinate of the assumed source. Note that for horizontal events $z_0 \approx z_{tmin}$ while the two values are distinct for vertical tracks.

4.2.2 Horizontal-vertical discrimination

As the LENA detector is not spherically symmetric but has a distinguished symmetry axis events have to be divided into tracks more parallel (vertical) ore more perpendicular (horizontal) to the z-axis. The basic reason is the light attenuation in the scintillator: For a horizontal muon traveling from the center of the detector along the negative x-axis, the spherical wavefronts created by the start point and the end point of the track (cf. Figure 4.1) are well visible. In contrast, the straight lightfronts from the sides of the track are only partially visible, as the light traveling towards the ends of the cylinder is typically absorbed or at least scattered before it reaches a light detector. For vertical tracks along the z-axis its the other way round: Now, the side wavefronts are clearly visible, while the spherical lightfronts from start- and endpoint are basically invisible. Therefore, the obtained first photon hit distributions are quite different. Note that this problem only concerns the first estimates presented in this section. For the global fits presented in Section 4.3, the working principle is independent of the track direction.

The basic idea to discriminate between horizontal and vertical tracks is the fact that, for muon tracks, charge barycenters and start points are well separated (see Section 3.2 for results on the barycenter position). Therefore, the z-component of the vector connecting start point and charge barycenter should be larger for vertical tracks.

For a fast determination of the z values of both quantities, each single ring of PMTs is used as an entity. Figure 4.6 shows the charge per ring and the first photon hit time in each ring for a horizontal (left) and a vertical (right) track. The maximum of the charge-per-ring distribution is a good estimator for the z-coordinate of the barycenter. As shown in the upper panels of Figure 4.6, it is determined by a Gaussian fit over the ring versus z-coordinates and associating the mean of the Gaussian z_0 to the center of charge. In the lower panels of Figure 4.6, the time of the first photon hit in each ring is plotted versus the z-coordinate of the PMT ring. Assuming instant emission of an infinite number of scintillation photons as well as a point-like event and neglecting light scattering, the obtained first hit time distribution is determined only by the distance between the point of photon emission and the nearest PMT in each ring. Therefore, it is fitted with

$$t_{\min}(z) = t_s + \frac{n}{c}\sqrt{(z - z_{\mathrm{tmin}})^2 + (\rho_{\mathrm{PMT}} - \rho_0)^2}, \qquad (4.4)$$

where z_{tmin} and ρ_0 are the cylindrical z and radial coordinates of the assumed pointlike event and $\rho_{\mathrm{PMT}} = 14.5\,\mathrm{m}$ is the radius at which the PMTs are installed. As can be seen from Figure 4.6, the fit works quite well despite the strong simplifications made in its derivation. The coordinate z_{tmin} is associated with the z-coordinate of the start point. Note that the fit principally also determines t_s and ρ_0. As results suffer from large errors for both values, only z_{tmin} is used for further analysis.

Comparing left and right panels of Figure 4.6, the difference $z_0 - z_{\mathrm{tmin}}$ is small as expected for horizontal muons while being significantly larger for vertical muons. To cancel out the energy dependence of the difference, it is divided by the tracklength calculated from the CSDA, $L^{\mathrm{CSDA}}(T)$, using the kinetic energy from the energy estimate. Therefore, the estimator to distinguish between horizontal and vertical events is

$$\zeta = \frac{|z_0 - z_{\mathrm{tmin}}|}{L^{\mathrm{CSDA}}(T)}. \qquad (4.5)$$

Currently, all muon events with $\zeta > 0.24$ are assumed to be vertical which provides the optimum performance at $500\,\mathrm{MeV}$ kinetic energy. Figure 4.7 shows the efficiency of this discrimination as a function of the kinetic energy, regarding only strictly horizontal and strictly vertical events. They can be distinguished with nearly absolute efficienciy for $T > 250\,\mathrm{MeV}$. To further investigate the behavior of the algorithm, the ratio of muon tracks identified as horizontal and vertical is shown in Figure 4.8 as a function of the zenith angle ϑ with respect to the z-axis, using $T = 300\,\mathrm{MeV}$. The obtained results show a smooth transition from small ϑ, where most of the tracks are correctly identified as vertical, to $\vartheta \approx 90$ degrees where the majority of the tracks is recognized as horizontal. Note that the transition does not occur at 45 degrees but between 30 and 40 degrees. This does not matter for the subsequent analysis though, as the reconstruction code for horizontal tracks works well even for muons at relatively small ϑ.
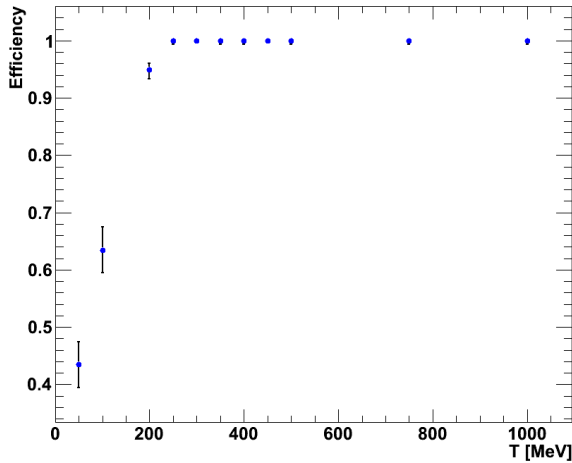
Fig. 4.7: The efficiency for horizontal vertical discrimination versus the kinetic energy of the particle. For this plot, only strictly horizontal and strictly vertical tracks were used. For energies above $250\,\mathrm{MeV}$, the discrimination is nearly absolute. The indicated errors are at the 1-σ level.
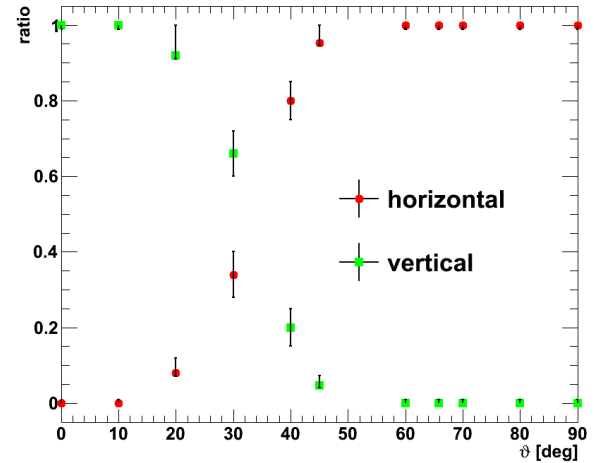
Fig. 4.8: The percentage of muon tracks ($T = 300\,\mathrm{MeV}$) identified as horizontal or vertical as a function of the track angle relative to the z-axis. A smooth transition from large vertical to large horizontal percentages with increasing angle is found.
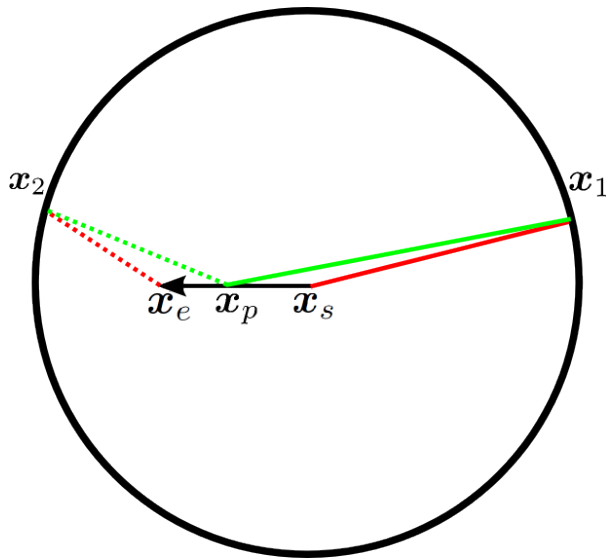
Fig. 4.9: Sketch to illustrate the dependence of the TOF-corrected hit time on the PMT position relative to the track direction. The TOF-corrected hit time at point $\boldsymbol{x}_1$ is the TOF the photon needs to travel from $\boldsymbol{x}_s$ to $\boldsymbol{x}_1$ (solid red line) minus the TOF between $\boldsymbol{x}_p$ and $\boldsymbol{x}_1$ (solid green line). The same is true for the TOF-corrected hit time of $\boldsymbol{x}_2$ (dashed lines), but additionally the TOF of the muon has to be added. Therefore, the TOF-corrected hit time of $\boldsymbol{x}_1$ is smaller than the TOF-corrected hit time at $\boldsymbol{x}_2$.
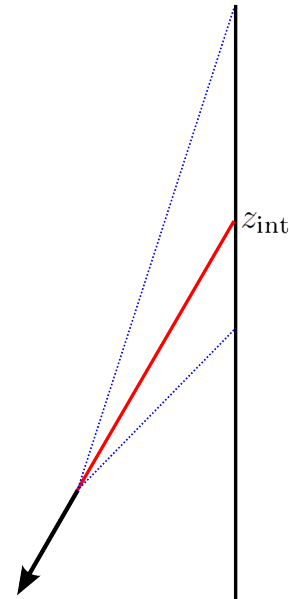
Fig. 4.10: Sketch illustrating the problem in the determination of z_{int}. The photons above z_{int} travel longer ways in the scintillator and are therefore more likely to be absorbed (compare the upper blue dashed line with the lower blue dashed line).

4.2.3   Horizontal tracks: Using first TOF-corrected hits for track estimation

The reconstruction of the muon direction for events running towards the cylinder wells is based on the characteristic shape of the distribution of TOF-corrected first hit times (cf. Figure 4.2).

To determine how this pattern is connected to the track direction, it is instructive to compare the expected TOF-corrected hit times at different points on the cylinder, using the simplification that all photons are emitted instantaneously. An example situation is sketched in Figure 4.9 for a purely horizontal track traveling from the center of the detector in negative x-direction. Adopting the model light front displayed in Figure 4.1, the TOF-corrected hit time $t_{\mathrm{TOF}}^{\boldsymbol{x}_1}$ for a photon detected at the point $\boldsymbol{x}_1$ is given by

$$t_{\mathrm{TOF}}^{\boldsymbol{x}_1} = \frac{n}{c} \left(|\boldsymbol{x}_s - \boldsymbol{x}_1| - |\boldsymbol{x}_p - \boldsymbol{x}_1| \right). \tag{4.6}$$

In Figure 4.9, the distance $|\boldsymbol{x}_s - \boldsymbol{x}_1|$ is shown as a solid red line, while $|\boldsymbol{x}_p - \boldsymbol{x}_1|$ is visualized in solid green. Figure 4.9 illustrates that $|\boldsymbol{x}_s - \boldsymbol{x}_1| < |\boldsymbol{x}_p - \boldsymbol{x}_1|$ must hold. Therefore, $t_{\mathrm{TOF}}^{\boldsymbol{x}_1} < 0$. The difference between $|\boldsymbol{x}_s - \boldsymbol{x}_1|$ and $|\boldsymbol{x}_p - \boldsymbol{x}_1|$ is maximal and $t_{\mathrm{TOF}}^{\boldsymbol{x}_1}$ minimal, when $\boldsymbol{x}_1$ corresponds to the intersection of the extension of the track in start point direction with the detector wall $\boldsymbol{x}_{\mathrm{int}}$. To calculate the TOF-corrected hit time $t_{\mathrm{TOF}}^{\boldsymbol{x}_2}$ for $\boldsymbol{x}_2$, the time the muon needs to travel from the start to the end of the track $t_\mu(\boldsymbol{x}_e)$ has to be added:

$$t_{\mathrm{TOF}}^{\boldsymbol{x}_2} = \frac{n}{c} \left(|\boldsymbol{x}_e - \boldsymbol{x}_2| - |\boldsymbol{x}_p - \boldsymbol{x}_2| \right) + t_\mu(\boldsymbol{x}_e). \tag{4.7}$$

As $t_\mu(\boldsymbol{x}_e) > 0$, $t_{\mathrm{TOF}}^{\boldsymbol{x}_2}$ is always larger than $t_{\mathrm{TOF}}^{\boldsymbol{x}_1}$. Moreover, the difference between $|\boldsymbol{x}_p - \boldsymbol{x}_2|$ and $|\boldsymbol{x}_e - \boldsymbol{x}_2|$ is smaller as the barycenter is in the rear part of the track.

Hence, the PMT featuring the minimal TOF-corrected hit time is located at the intersection of the extension of the track against the direction of the muon with the detector wall. This conclusion is verified by Figure 4.2. The muon causing the displayed light pattern travels from the center of the detector in negative x-direction and consequently produces the first TOF-corrected hits where the positive x-axis intersects with the wall, i.e. in the center of the wall-plane shown in Figure 4.2.

Starting from this result, the idea for reconstructing a track is to first reconstruct the point at the wall with the minimum TOF-corrected hit time, $\boldsymbol{x}_{\mathrm{int}}$. The vector connecting this point with the barycenter $\boldsymbol{x}_p$ corresponds to the track direction. In a final step the start point of the track is reconstructed, by calculating the distance $|\boldsymbol{x}_p - \boldsymbol{x}_s|$ from the CSDA model for the energy loss.

Reconstructing the mantle coordinate of minimum t_{TOF}:

First, the PMTs with the 500 smallest TOF-corrected first hit times are selected. Their positions are subsequently histogramed as a function of φ_{PMT} and z_{PMT}. The free parameter, a, in the range of the φ_{PMT}-distribution $\varphi_{\mathrm{PMT}} \in [a - \pi, a + \pi]$, $a \in \mathrm{R}$ is chosen to suppress boundary effects, i.e. to minimize the height of the distribution at the boundary. Assuming that the center of the φ_{PMT}-distribution corresponds to the φ coordinate of $\boldsymbol{x}_{\mathrm{int}}$, the mean of a Gaussian distribution fitted to the φ_{PMT}-distribution serves as an estimator for φ_{int}.

Determining the z-coordinate of $\boldsymbol{x}_{\mathrm{int}}$ in the same way works fine for events with tracks

parallel to the x-y plane but fails for inclined tracks. The problem is illustrated in Figure 4.10 for an inclined muon track: Photons arriving above z_{int} have to travel a longer distance through the scintillator and are therefore more likely to be scattered and/or absorbed than their counterparts with $z < z_{\mathrm{int}}$. The obtained distribution is therefore no longer centered around z_{int}. Using the mean as an estimator therefore leads to a substantial systematic shift towards the barycenter of the track. This problem is solved at least partially by weighting the events in the z_{PMT}-histogram. The weights obviously have to increase with rising distance of the PMT from $\boldsymbol{x}_s$. This leads to a loss in resolution for strictly horizontal tracks as the hits deviating from this plane are enhanced. The empirically derived weighting factor ensuring a sufficient resolution for both inclined and is horizontal muons is

$$w = \frac{\exp(-\frac{|\boldsymbol{x}_{\mathrm{PMT}} - \boldsymbol{x}_p|}{\lambda_{\mathrm{scat}}})}{1 - \exp(-\mu_i)}, \tag{4.8}$$

where λ_{scat} is the scattering length defined as $\frac{1}{\lambda_{\mathrm{scat}}} = \frac{1}{\lambda_{\mathrm{iso}}} + \frac{1}{\lambda_r}$. The expected charge collected by the PMT μ_i as defined in equation (3.2) neglecting the proportionality constant. It takes into account two effects: The smaller the probability that a PMT has at least one hit, the smaller the probability that it detects the first TOF-corrected hit time photons. Consequently, PMTs with a small probability to have at least one hit have to be weighted with a high weight. Hence, the weighting factor has to be proportional to the inverse probability that the PMT has at least one photo electron. $w \propto [1 - \exp(-\mu_i)]^{-1}$. Contrary, the farther the PMT is away from the point of light emission, the higher the probability for a loss of information due to scattering, i.e. the weight of the PMT has to be decreased. Thus, the weighting factor is proportional to the probability that a photon is not scattered on its way to the PMT $w \propto \exp(-\frac{|\boldsymbol{x}_{\mathrm{PMT}} - \boldsymbol{x}_p|}{\lambda_{\mathrm{scat}}})$. The distribution obtained after weighting is is fitted with a Gaussian whose mean is used as estimator for z_{int}.

Reconstructing the direction of the track:
After reconstructing $\boldsymbol{x}_{\mathrm{int}}$, an estimate for the direction $\hat{\boldsymbol{d}}$ can be reconstructed simply as $\hat{\boldsymbol{d}} = \frac{\boldsymbol{x}_p - \boldsymbol{x}_{\mathrm{int}}}{|\boldsymbol{x}_p - \boldsymbol{x}_{\mathrm{int}}|}$. The angular deviations of the reconstructed from the true Monte Carlo directions, $\Delta\varphi'$, are histogramed in Figure 4.11, based on 300 MeV muons traveling from the center of the detector in negative x-direction. Most of the reconstructed directions are pretty close to the expected direction while there are some outliers with higher angular differences. Assuming that the events with $\Delta\varphi' < 20\,\mathrm{deg}$ feature a Gaussian distribution in solid angle around the true value, the distribution can be fitted with

$$P(\Delta\varphi') \propto \sin(\Delta\varphi') \cdot \exp\left[-\frac{(\Delta\varphi')^2}{2(\Delta\varphi)^2}\right]. \tag{4.9}$$

Here, the term $\sin(\Delta\varphi')$ is the solid angle element, which is required due to the use of spherical coordinates. The fit parameter $\Delta\varphi$ serves as an estimate for the obtained angular resolution. Figure 4.12 shows the dependence of $\Delta\varphi$ on the kinetic energy for muons traveling from the center of the detector along the negative x-axis. As expected, the obtained angular resolution improves with rising kinetic energy, as the flight time of the muon as well as the distance between the start point and the barycenter of the track increases. This leads to higher differences in the TOF-corrected hit times and therefore to a more precise location of the minimum.
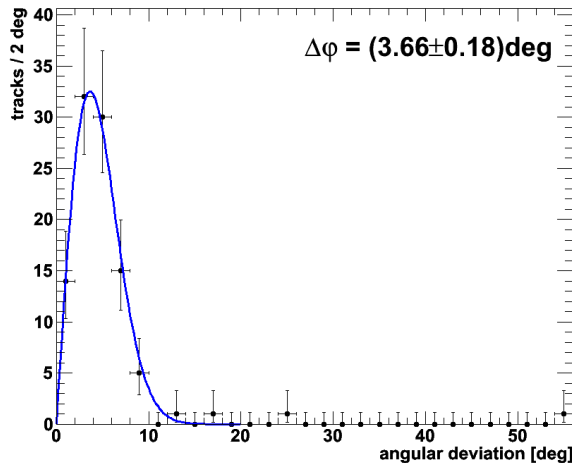
Fig. 4.11: Angular deviation $\Delta\varphi'$ of the reconstructed track directions from the true track directions for 300 MeV muons traveling from the center of the detector along the negative x-axis. The events with an angular deviation of less than 20 degrees have been fitted $\propto \sin(\Delta\varphi') \cdot \exp(-(\Delta\varphi')^2/2(\Delta\varphi)^2)$.
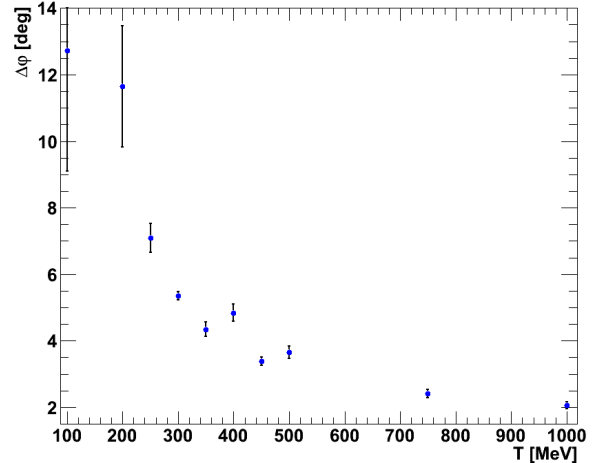
Fig. 4.12: Dependence of the angular resolution on the kinetic energy of the muon for purely horizontal muons. The direction of higher energetic muons can be determined better, as the flight time of the muon as well as the distance $|\boldsymbol{x}_p - \boldsymbol{x}_{\text{int}}|$ rises, increasing the difference between the expected first hit times on the PMTs. Hence, $\boldsymbol{x}_{\text{int}}$ is determined with a higher accuracy.

Reconstructing the start point of the track:
With the direction and the barycenter of the track known, the start point $\boldsymbol{x}_s$ of the track is determined by its distance to the barycenter. This distance is best calculated in a coordinate system with one axis parallel to the track and the origin at the start point of the track. The coordinate along the track, s, is therefore defined via

$$\boldsymbol{x} = s \cdot \hat{\boldsymbol{d}} + \boldsymbol{x}_s. \tag{4.10}$$

The barycenter coordinate s_p is given by the energy-loss weighted mean of the track

$$s_p = \int\limits_0^l ds \; s \cdot \left\langle \frac{dE}{dx} \right\rangle (\beta(s)), \tag{4.11}$$

with l being the length of the track. Evaluating this equation is mathematically demanding as $\left\langle \frac{dE}{dx} \right\rangle (\beta(s))$ depends on $\beta = \frac{v}{c}$. Calculating $\beta(s)$ is not trivial as this quantity again depends on the energy loss. For the same reason, calculating $l(T)$ given by the equation $\beta(l) = 0$ is not straightforward. This problem has already been handled in [83] and machine readable results for $\left\langle \frac{dE}{dx} \right\rangle (\beta(s))$ are provided at [84]. As this source did not provide data for PXE, the data for benzene was used instead. This is legitimate because the stopping power divided by the density of the fluid depends only on on the chemical composition which is similar for benzene and PXE [40].
The start points estimated with this method are histogramed in Figure 4.13 for 300 MeV muons traveling from the center of the detector along the negative x-axis. The results are given using the coordinate s as defined in Equation (4.10). The reconstructed start

points show a significant systematic shift in track direction, which is most probably due to the use of an approximate $\langle \frac{dE}{dx} \rangle$-table. The results are nevertheless sufficient to serve as input parameters for the final fits. Moreover, there are some outliers. They are caused mainly by two reasons. First, they can be due to a badly reconstructed $\boldsymbol{x}_p$ and second, they can be caused by errors in the determination of the angle. Usually, both problems appear at the same time, as a badly reconstructed $\boldsymbol{x}_p$ causes a deviation from the expected TOF-corrected first hit time spectrum and therefore a malfunction of the algorithm for determining the track direction.
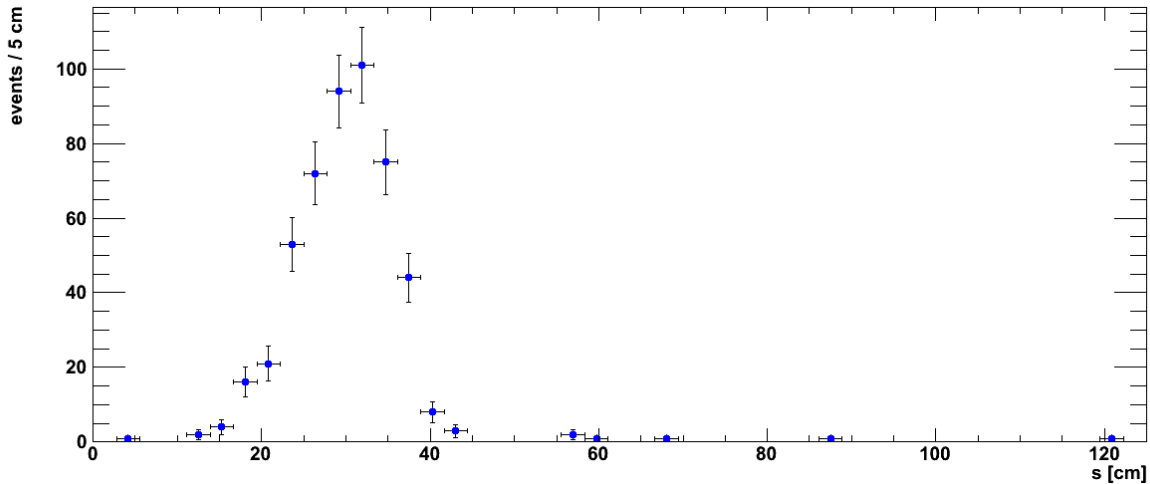
Fig. 4.13: Obtained start points projected on the track. s is the coordinate along the track defined by Equation (4.10).

4.2.4   Vertical tracks: Using PMT rings for track estimation

For vertical events, $\boldsymbol{x}_{\mathrm{int}}$ cannot be determined, as it is typically located on the lid or the bottom of LENA. There, only very few photons arrive due to the small solid angle of the PMTs seen from an interaction in the middle of the detector, as well as due to light attenuation in the scintillator. Therefore, a different algorithm is used in this case.

The idea of the algorithm is based on the assumptions already made in Section 4.1.1 which lead to the cone-like first light surface displayed in Figure 4.1. Figure 4.14 shows the resulting situation for a purely vertical track: As the track is parallel to the cylinder wall, the point where the light front first hits the detector corresponds to the z-coordinate of the start point $\boldsymbol{x}_s$. Furthermore, looking only at the plane perpendicular to the track direction containing $\boldsymbol{x}_s$, the first light front corresponds to a point-like event. Using this observations, the start point $\boldsymbol{x}_s$ can be reconstructed which defines the track together with its barycenter $\boldsymbol{x}_p$.

As estimator for the z-coordinate of $\boldsymbol{x}_s$ the result z_{tmin} of the fit to the minimum hit time in each PMT ring versus z is used (cf. Section 4.2.2). From Equation (4.4) it is obvious that it represents the minimum of the fitted distribution.

To obtain the x and y coordinates the first photon hit times of the PMTs in the ring containing the first overall hit are analyzed. The first hit time of the PMTs in this ring are plotted in Figure 4.15 dependent on the azimuth angle of the PMT φ_{PMT} for a 300 MeV muon traveling from $(10, 0, 0)$ m along the positive z-axis. Assuming an isotropic
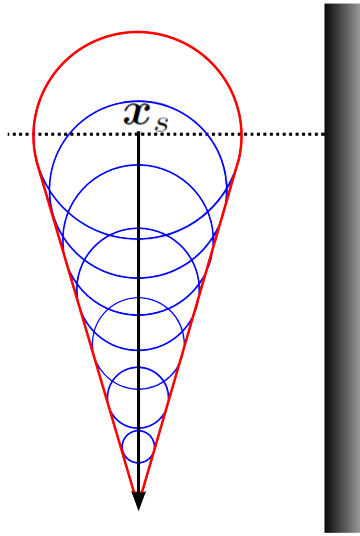
Fig. 4.14: Sketch of the light front created by an exactly vertical track. The position where the light front first hits the wall marks the height of the start point z_s. Furthermore, looking only at the x-y plane containing the start point (dashed line), the light front is identical to the light front created by a point source.
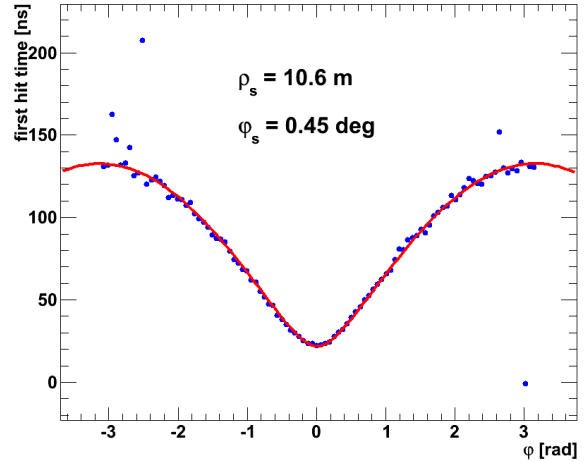
Fig. 4.15: The first hit times of each PMT plotted versus the azimuth angle of the respective PMT for a 300 MeV muon traveling from $(10,0,0)$ m along the z-axis. The obtained results are fitted assuming a point like light source. The quoted values are the results for the position of the source in the associated plane given in polar coordinates.
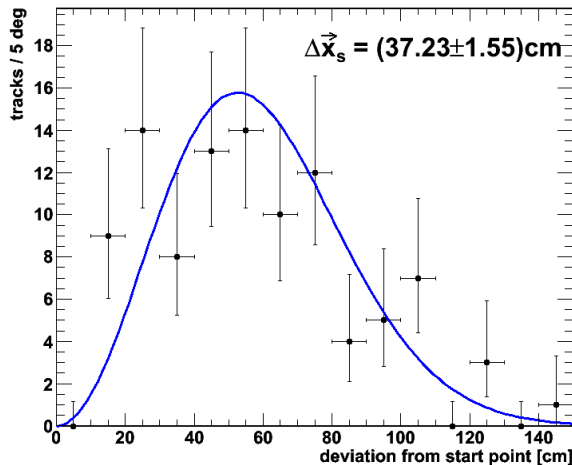
Fig. 4.16: Spectrum of the distances of the estimated from the true start point for 300 MeV muons traveling downwards from the center of the detector. The distribution was fitted assuming a the distribution to be a three dimensional Gaussian wit $\sigma_{x_s} = \sigma_{y_s} = \sigma_{z_s} = \Delta \boldsymbol{x}_s$. The result is displayed in the upper right corner of the plot.
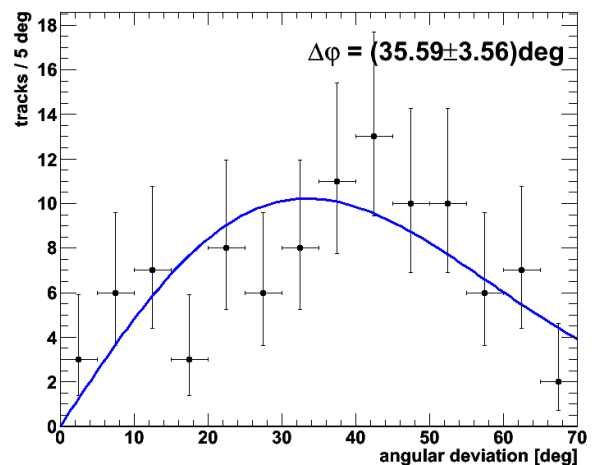
Fig. 4.17: Angular deviation of the estimated track to the Monte Carlo Truth for 300 MeV muons traveling downwards from the center of the detector. The obtained distribution was fitted the same way as in Figure 4.11 with the result being displayed in the upper right corner of the plot.

photon emission at the start point of the track (ρ_s, φ_s), the arrival time of the first photon at the PMT $(\rho_{\mathrm{PMT}}, \varphi_{\mathrm{PMT}})$ is given by

$$t_{\mathrm{first}}(\varphi_{\mathrm{PMT}}) = t_s + \frac{n}{c}\sqrt{\rho_{\mathrm{PMT}}^2 + \rho_s^2 - 2\rho_{\mathrm{PMT}} \cdot \rho_s \cdot \cos(\varphi_{\mathrm{PMT}} - \varphi_s)}, \qquad (4.12)$$

where the square root expresses the distance between the PMT and the light emission which is calculated with the law of cosine. Fitting $t_{\mathrm{first}}(\varphi_{\mathrm{PMT}})$ to the obtained values leads to a good result which is shown in Figure 4.15 as a red line. There are a few deviations though for PMTs with $|\varphi_{\mathrm{PMT}}| \approx \pi$ which are due to the fact that these PMTs are on the side of the wall most distant to the track and therefore have a low or even vanishing integrated charge. For these PMTs, the assumption of the first light front breaks down. The resulting start point resolution obtained for 300 MeV muons traveling downwards from the center of the detector is displayed in Figure 4.16. The obtained distribution has a much higher spread than the one obtained for the horizontal muons displayed in Figure 4.13 which is mainly due to the fact that the PMT ring with the first overall hit is used as the ring being closest to the track start point. This is very prone to statistical fluctuations.

Combining the reconstructed start point of the track with its barycenter returns the direction of the track. The angular deviations of the estimated tracks obtained from the same muons that are used in Figure 4.16 are histogramed in Figure 4.17. As already expected due to the limited resolution obtained for the start point of the track, the angular resolution is inferior to the angular resolution obtained for horizontal tracks. The dependence of the angular resolution on the kinetic energy of the track is displayed in Figure 4.18. As the start point estimation depends only on the first light front from the start point, which is independent of the muon energy, the accuracy of the start point estimation does not depend on the energy. The angular resolution nevertheless improves with rising energy as the distance between the start of the track and the barycenter is rising nearly linearly with energy. As the barycenter is reconstructed at a much higher accuracy than the start point, the error of the barycenter can be neglected to first order. Using this assumptions, the angular deviation of the reconstructed track from the true track is

$$\Delta\varphi = \arctan\left(\frac{\Delta\rho_s}{|\boldsymbol{x}_s - \boldsymbol{x}_p|}\right) \approx \frac{\Delta\rho_s}{|\boldsymbol{x}_x - \boldsymbol{x}_p|} \propto \frac{1}{T}, \qquad (4.13)$$

with $\Delta\rho_s$ being the projection of the deviation of the reconstructed and the true start point in a plane perpendicular to the true track. Hence, the results presented in Figure 4.18 are fitted with a hyperbola. The resulting curve shown in blue fits the data well, thereby confirming the considerations above.

4.2.5   Start time estimate

The last remaining unknown parameter is the start time of the event. The algorithm takes the first hit time of each PMT and applies a TOF correction with respect to the start point of the track. The resulting values are subsequently histogramed and the center of the maximum bin is used as an estimator for t_s. This approach features two significant shortcomings: To get a stable maximum bin, a relatively large bin width in the order of 1 ns has to be chosen, which introduces a relatively large quantization error. Moreover, the maximum of a hit distribution is more connected to the end point of a track than to
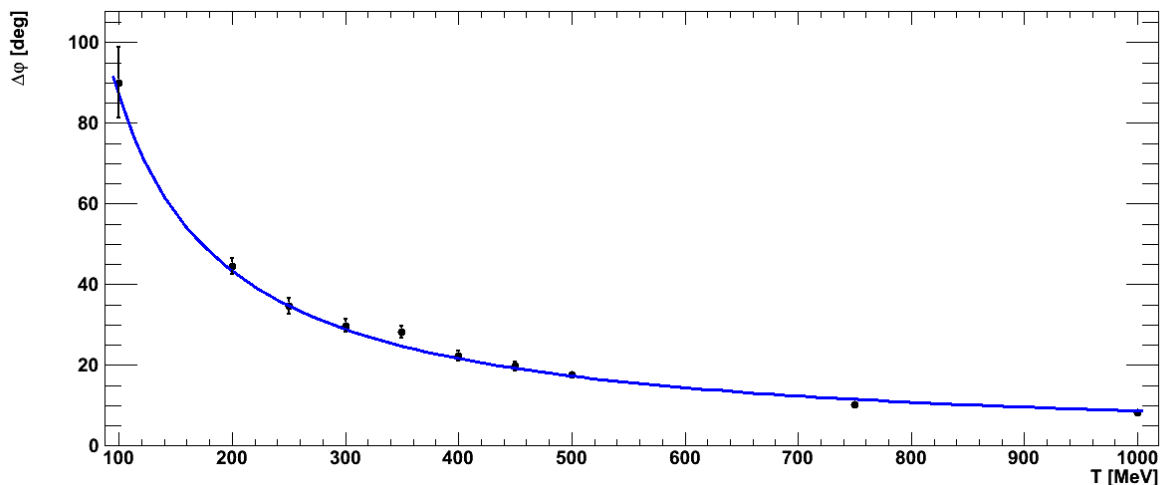
Fig. 4.18: Dependence of the angular resolution of purely vertical muons on the kinetic energy of the track. The fit of the obtained values with a hyperbola yields an acceptable goodness of fit (χ^2/ndof ≈ 1.7), indicating that the increase in resolution with T is mainly due to the enhanced distance between start point and barycenter.
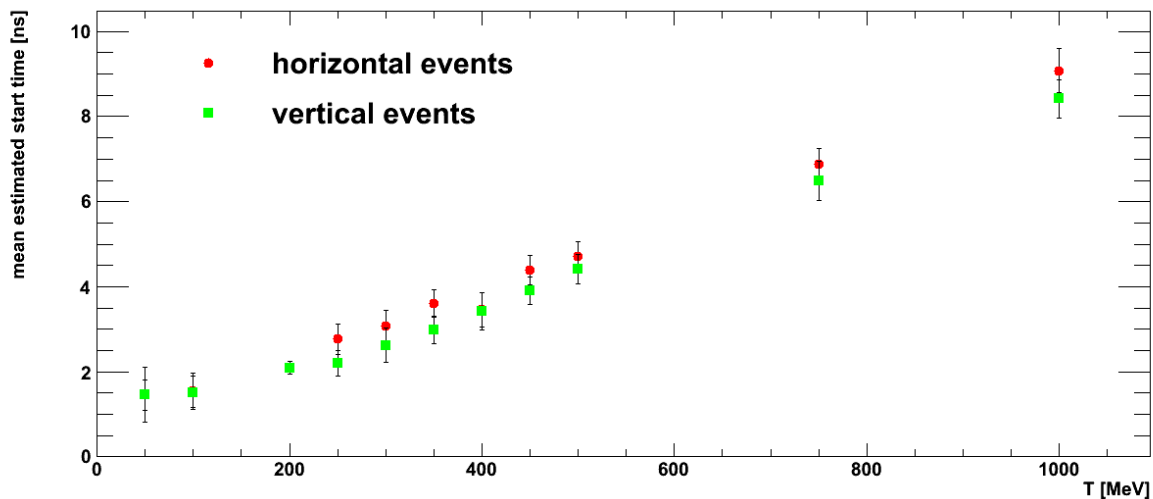
Fig. 4.19: Estimated mean start time plotted versus the kinetic energy of the track for purely horizontal tracks and purely vertical events. The error bars indicate the sample spread of the obtained event start time distributions. Obviously the obtained values feature a significant systematical shift.

the start point, due to the Bragg peak in energy loss. The latter problem is much more serious than the first one, as it does not only introduce a spread, but also a systematical error on the estimates of the event start time which exceeds the spread of the obtained values. The systematic shift is clearly visible in the results depicted in Figure 4.19, which shows the obtained mean values together with the sample spreads for horizontal tracks and vertical tracks, respectively. The observed systematical shift rises with energy as the time corresponding to the end point increases.

Despite all these problems, the results obtained with the current algorithm are sufficient to seed the global fits presented in Section 4.3. Nevertheless, an improvement of the start time algorithm is planned. As a first step, the results obtained in Figure 4.19 can be used to compensate for the systematic shift.

4.3   Final fits

To obtain more precise muon-track reconstruction a global fit is performed, which takes the signal of all PMTs into account. The signal used for the fit is the integrated charge collected by each PMT, $\boldsymbol{q} = (q_i)$, and the arrival time of the first photon, $\boldsymbol{t} = (t_i)$, on each PMT. This choice is very conservative as this amount of information requires only the minimal electronic setup (cf. Section 3.1).

Similar to the estimation of the charge barycenter in Section 3.2 the best fit values for the track parameters $\boldsymbol{X} = (\boldsymbol{x}_s, t_s, \vartheta, \varphi, T)$ are determined by minimizing the negative logarithmic likelihood

$$\mathcal{L}(\boldsymbol{X}|\boldsymbol{q}, \boldsymbol{t}) = -\ln\left[L(\boldsymbol{X}|\boldsymbol{q}, \boldsymbol{t})\right] = -\ln\left[P(\boldsymbol{q}, \boldsymbol{t}|\boldsymbol{X})\right], \tag{4.14}$$

with $P(\boldsymbol{q}, \boldsymbol{t}|\boldsymbol{X})$ being the PDF that a muon described by the parameters $\boldsymbol{X}$ produces the signal $(\boldsymbol{q}, \boldsymbol{t})$. The basic structure of this PDF is presented in Section 4.3.1, while Sections 4.3.2 and 4.3.3 go into details about the main parts of the PDF. The results obtained with this fit are finally presented in Section 4.3.4.

4.3.1   Basic structure of the probability density function

The PDF $P(\boldsymbol{q}, \boldsymbol{t}|\boldsymbol{X})$ is of very high dimension due to the large number of PMTs N_{PMT}. Assuming that all PMTs are independent of each other, this high dimensional structure can be broken down to

$$P(\boldsymbol{q}, \boldsymbol{t}|\boldsymbol{X}) = \prod_{i=1}^{N_{\mathrm{PMT}}} P_i(q_i, t_i|\boldsymbol{X}), \tag{4.15}$$

where $P_i(q_i, t_i|\boldsymbol{X})$ is the PDF that the PMT of number i detects q_i photons and has a first hit time of t_i given a muon track with the parameters $\boldsymbol{X}$. This assumption should generally hold very well. The only effect correlating different PMTs is electronic crosstalk which is not present in the simulation and should be no problem in a well set up experiment. Additionally, assuming that all PMTs are equal, each PMT is characterized solely by its position $\boldsymbol{r}_i$ and its orientation which is described by its normal vector $\hat{\boldsymbol{n}}_i$ pointing outwards. Therefore, $P_i(q_i, t_i|\boldsymbol{X})$ can be replaced by the PDF $P(q_i, t_i|\boldsymbol{X}, \boldsymbol{r}_i, \hat{\boldsymbol{n}}_i)$ that a PMT defined by $(\boldsymbol{r}_i, \hat{\boldsymbol{n}}_i)$ measures the signal (q_i, t_i) given a track with parameters $\boldsymbol{X}$

leading to

$$P(\boldsymbol{q}, \boldsymbol{t} | \boldsymbol{X}) = \prod_{i=1}^{N_{\mathrm{PMT}}} P(q_i, t_i | \boldsymbol{X}, \boldsymbol{r}_i, \hat{\boldsymbol{n}}_i). \tag{4.16}$$

The number of PDFs to be calculated is therefore reduced from an individual PDF for each PMT to one single PDF at the cost of introducing two more parameters. While this approach is totally sufficient for reconstructing simulated events, a real experiment will require the introduction of further parameters to account for the intrinsic differences in the performance of individual PMTs.

Even though all PMTs are treated as equal in the simulation, they can be subdivided into two groups for any given event: active PMTs which detected at least one photon, and inactive PMTs which detected no photon at all. For the latter group, the PDF cannot depend on the arrival time of the first photon. Therefore, equation (4.16) can be rewritten to

$$P(\boldsymbol{q}, \boldsymbol{t} | \boldsymbol{X}) = \prod_i^{\mathrm{inactive}} P(q_i = 0 | \boldsymbol{X}, \boldsymbol{r}_i, \hat{\boldsymbol{n}}_i) + \prod_i^{\mathrm{active}} P(q_i, t_i | \boldsymbol{X}, \boldsymbol{r}_i, \hat{\boldsymbol{n}}_i), \tag{4.17}$$

with the first product running over all inactive PMTs and the second product running over all the active PMTs.

$P(q_i, t_i | \boldsymbol{X}, \boldsymbol{r}_i, \hat{\boldsymbol{n}}_i)$ can be further factorized using the definition of conditional probability [85]

$$P(q_i, t_i | \boldsymbol{X}, \boldsymbol{r}_i, \hat{\boldsymbol{n}}_i) = P(q_i | \boldsymbol{X}, \boldsymbol{r}_i, \hat{\boldsymbol{n}}_i) \cdot P(t_i | \boldsymbol{X}, \boldsymbol{r}_i, \hat{\boldsymbol{n}}_i, q_i). \tag{4.18}$$

This allows rewriting the total PDF once more to obtain the final form

$$P(\boldsymbol{q}, \boldsymbol{t} | \boldsymbol{X}) = \prod_i^{\mathrm{inactive}} P(q_i = 0 | \boldsymbol{X}, \boldsymbol{r}_i, \hat{\boldsymbol{n}}_i) + \prod_i^{\mathrm{active}} P(q_i | \boldsymbol{X}, \boldsymbol{r}_i, \hat{\boldsymbol{n}}_i) \cdot P(t_i | \boldsymbol{X}, \boldsymbol{r}_i, \hat{\boldsymbol{n}}_i, q_i). \tag{4.19}$$

The charge PDF $P(q_i | \boldsymbol{X}, \boldsymbol{r}_i, \hat{\boldsymbol{n}}_i)$ will be detailed in Section 4.3.2 while the timing PDF $P(t_i | \boldsymbol{X}, \boldsymbol{r}_i, \hat{\boldsymbol{n}}_i, q_i)$ will be explained in Section 4.3.3.

4.3.2   Probability density function for the integrated charge

As already pointed out in Section 3.2 the charge PDF is given by the Poisson distribution (3.4)

$$P(q_i | \boldsymbol{X}, \boldsymbol{r}_i, \hat{\boldsymbol{n}}_i) = \frac{\mu^{q_i}}{q_i!} \exp(-\mu_i), \quad \mu_i = \mu_i(\boldsymbol{X}, \boldsymbol{r}_i, \hat{\boldsymbol{n}}_i). \tag{4.20}$$

where μ_i is the expected charge on the PMT i. It can be calculated via

$$\mu_i(\boldsymbol{X}, \boldsymbol{r}_i, \hat{\boldsymbol{n}}_i) = \int\limits_{\boldsymbol{x}_s(\boldsymbol{X})}^{\boldsymbol{x}_e(\boldsymbol{X})} ds \quad \left\langle \frac{dL}{dx} \right\rangle (s) \cdot \frac{\Omega(\boldsymbol{s}, \boldsymbol{r}_i, \hat{\boldsymbol{n}}_i)}{4\pi} \cdot \exp\left(-\frac{|\boldsymbol{s} - \boldsymbol{r}_i|}{\lambda_{\mathrm{att}}} \right) \frac{1}{R(\boldsymbol{s}, \boldsymbol{r}_i)}, \tag{4.21}$$

with the attenuation length $\lambda_{\mathrm{att}} = (\lambda_{\mathrm{abs}}^{-1} + \lambda_{\mathrm{r}}^{-1} + \lambda_{\mathrm{iso}}^{-1})^{-1}$ and the direct ratio $R(\boldsymbol{s}, \boldsymbol{r}_i)$ which is the ratio of the photons arriving at the PMT unscattered to the total integrated charge.. The first term in the integrand describes the mean number of photons produced per unit track length at a given point of the track, the second accounts for the solid angle of the PMT, and the last two terms account for scattering and absorption.

The **solid angle coverage** of the PMT in far field approximation is given by

$$\Omega(\boldsymbol{s}, \boldsymbol{r}_i, \hat{\boldsymbol{n}}_i) = \frac{A_{\mathrm{PMT}}}{|\boldsymbol{s} - \boldsymbol{r}_i|^2} \left(\frac{\boldsymbol{r}_i - \boldsymbol{s}}{|\boldsymbol{r}_i - \boldsymbol{s}|} \cdot \hat{\boldsymbol{n}}_i \right), \tag{4.22}$$

with A_{PMT} being the surface area of the PMT. The first term considers the dependence of the solid angle on the squared distance. The second term projects the surface of the PMT in a plane perpendicular to the connection between the PMT and the point of light emission, i.e. takes into account that most PMTs do not directly face the event.

The **mean number of photons** emitted per unit path length is a function of the mean deposited energy per unit path length. The dependency is given by Birk's formula (1.19) Therefore, $\langle \frac{dE}{dx} \rangle (s)$ has to be calculated. Here, the same problem already encountered in Section 4.2.3 appears. The calculation of the energy loss at one point depends on the energy of the particle at that specific point of the track. Due to the stricter requirements for accuracy in track fitting compared to Section 4.2.3, a different solution is chosen here: $\langle \frac{dL}{dx} \rangle (s)$ is obtained from Geant4. For this purpose, sets of muon tracks were simulated at different energies and the light produced per unit path length was recorded. Subsequently, the mean track length is calculated for each set of muons with constant energy and all tracks are scaled to this length. The $\langle \frac{dL}{dx} \rangle (s)$-table is then obtained by averaging over all tracks in one set. To get the $\langle \frac{dL}{dx} \rangle (s)$ for intermediate energies the table for the next higher energy is used starting at the point where the kinetic energy of the muon has already dropped to the required energy.

An example for an obtained $\langle \frac{dL}{dx} \rangle (s)$-table is visualized in Figure 4.20. The expected behavior of an 1 GeV muon is reproduced: The particle is minimum ionizing during most of the track and features a significant increase in energy loss and in the number of photons emitted as soon as the speed of the particle significantly deviates from the speed of light.

If every scattered photon was lost to detection, the influence of **scattering and absorption** would be given by the simple exponential decay $\exp\left(-\frac{|\boldsymbol{s} - \boldsymbol{r}_i|}{\lambda_{\mathrm{att}}} \right)$. However, as a substantial proportion of scattered photons will be detected, this approach significantly underestimates the number of expected photons. Following the approach of [86], a correction factor $1/R(\boldsymbol{s}, \boldsymbol{r}_i)$ is included in equation (4.21), which takes the difference into account. The direct ratio $R(\boldsymbol{s}, \boldsymbol{r}_i)$ is hence defined as

$$R(\boldsymbol{s}, \boldsymbol{r}_i) = \frac{P(\text{hit,not scattered} | \boldsymbol{s}, \boldsymbol{r}_i)}{P(\text{hit} | \boldsymbol{s}, \boldsymbol{r}_i)} = P(\text{not scattered} | \text{hit}, \boldsymbol{s}, \boldsymbol{r}_i)), \tag{4.23}$$

where $P(\text{hit} | \boldsymbol{s}, \boldsymbol{r}_i)$ and $P(\text{hit,not scattered} | \boldsymbol{s}, \boldsymbol{r}_i)$ are the probabilities that a photon emitted at $\boldsymbol{s}$ hits the PMT at $\boldsymbol{r}_i$ and in addition without being scattered, respectively. $P(\text{not scattered} | \text{hit}, \boldsymbol{s}, \boldsymbol{r}_i))$ is the probability that a photon from $\boldsymbol{s}$ which hits the PMT at $\boldsymbol{r}_i$ is not scattered. This quantity is very difficult to calculate as this would involve an infinite sum over products of multidimensional integrals. Therefore, it is obtained from the Monte Carlo simulation, by simulating 1 MeV electrons at several positions in the detector. The problem is that $R(\boldsymbol{s}, \boldsymbol{r_i})$ is six-dimensional. Hence, it can only be obtained from a simulation featuring very high statistics. Furthermore, evaluating the obtained table at points between the supporting points would require a six dimensional interpolation, which requires too much computation time. Hence, the dimensionality has to be
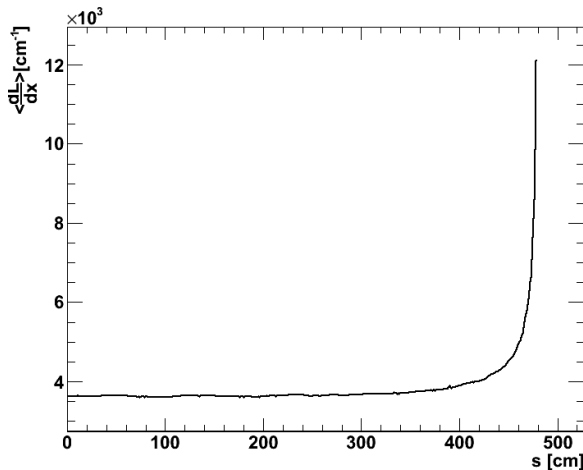
Fig. 4.20: Mean energy loss per unit path length for a $1\,\mathrm{GeV}$ muon dependent on the distance to the start point. During most of its life time the muon is minimum ionizing therefore the energy loss and the light yield are nearly constant. Only during the last half meter the deviation form the speed of light gets significant leading to a rapidly rising energy loss and therefore a higher number of produced photons.
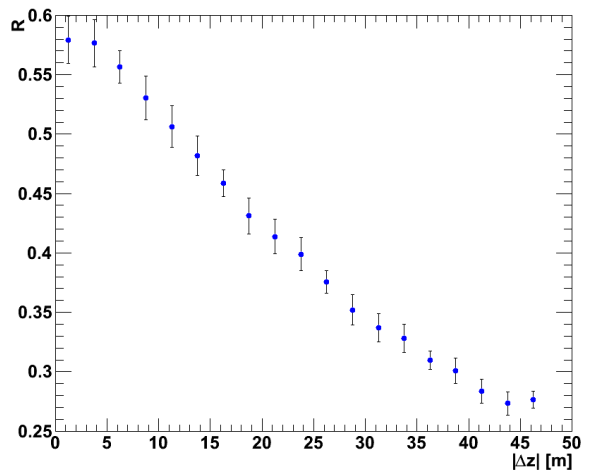
Fig. 4.21: Direct indirect ratio versus z as obtained from Geant4. The dependencies on the other variables have been averaged out. The error bars indicate the spread of the obtained R values for a fixed value of $|\Delta z|$.

reduced.

Using cylindrical coordinates, R can be expressed as $R = R(\boldsymbol{s}(\rho_s, z_s, \varphi_s), \boldsymbol{r_i}(\rho_r, z_r, \varphi_r))$. Exploiting the cylindrical symmetry of the detector, R merely depends on the absolute difference in azimuth $|\Delta\varphi| = |\varphi_s - \varphi_r|$ between the point of photon emission and detection. Neglecting the lid and the bottom of the detector and extending the wall to $\pm\infty$ in z-direction leads to a translation invariance in z, allowing to replace (z_s, z_r) with $|\Delta z| = |z_s - z_r|$. This assumption furthermore fixes the radial coordinate of the PMTs, i.e. $\rho_r = \text{const}$. The dimensionality of R can therefore be reduced to three,

$$R(\boldsymbol{s}(\rho_s, z_s, \varphi_s), \boldsymbol{r_i}(\rho_r, z_r, \varphi_r)) \approx R(\rho_s, |\Delta\varphi|, |\Delta z|), \qquad (4.24)$$

allowing for a proper tabulation of the required values.

Figure 4.21 shows the dependency of R on $|\Delta z|$ where the other variables are averaged out. The error bars indicate the spread of the obtained R values for a given $|\Delta z|$. With increasing $|\Delta z|$, the obtained ratio drops as the distance between production and detection of the light and therefore the probability of scattering rises. Note however that even for $|\Delta z| \approx 0$ the obtained ratio is in the order of two thirds i.e. even for the closest PMTs one third of the detected light is scattered. Consequently, scattering cannot be neglected in LENA due to the large dimensions of the detector.

4.3.3   Probability density function for the first hit time

The calculation of the PDF for the first hit time $P(t_i | \boldsymbol{X}, \boldsymbol{r}_i, \hat{\boldsymbol{n}}_i, q_i)$ is done in two steps. First the overall PDF for the hit time of any photon $P_o(t | \boldsymbol{X}, \boldsymbol{r}_i, \hat{\boldsymbol{n}}_i)$ is computed. Note that this distribution does not depend on the integrated charge collected at the PMT of

interest as each photon is taken to be independent of the others. The first hit time PDF is then calculated in a final step from P_o.

As the **overall PDF** does not depend on the integrated charge, it can be constructed by a weighted superposition of the hit time distributions one would expect from each track element. The weighting factor is given by the number of photons expected from the respective track element $\left(\frac{d\mu_i}{ds}\right)(s, \boldsymbol{X}, \boldsymbol{r}_i, \hat{\boldsymbol{n}}_i)$, i.e. the integrand of Equation (4.21). To calculate the hit time distribution, multiple effects have to be taken into account:

- The expected hit time of the photon t_{sh} at the PMT for instantaneous photon emission, no scattering and no PMT time jitter

- The decay time distribution of the scintillator

- The finite time resolution of the PMT

- The finite size of the PMTs

- Scattering in the scintillator.

As the implementation of the first three effects is quite straight forward, while the latter two require more effort, it is instructive to start with a prototype overall PDF $\tilde{P}_o$ including only the first three effects and afterwards implementing the remaining effects step by step. As already pointed out in Section 3.1 the decay time distribution of the scintillator is a superposition of two exponential decay modes and the time jitter of the PMT is taken to be Gaussian. The overall hit time distribution is then given by the convolution of the two distributions. Therefore,

$$\tilde{P}_o(t|\boldsymbol{X}, \boldsymbol{r}_i, \hat{\boldsymbol{n}}_i) = \quad \frac{1}{\mu_i} \int_{\boldsymbol{x}_s(\boldsymbol{X})}^{\boldsymbol{x}_e(\boldsymbol{X})} ds \ \left(\frac{d\mu_i}{ds}\right)(s, \boldsymbol{X}, \boldsymbol{r}_i, \hat{\boldsymbol{n}}_i) \cdot S_1(t - t_{sh}(\boldsymbol{X}, \boldsymbol{s}, \boldsymbol{r}_i)) \qquad (4.25)$$

$$S_1(t) = \quad \mathcal{N}\left[\left(\sum_{i\in\{s,f\}} \frac{\Gamma_i}{\tau_i} \exp\left(-\frac{t'}{\tau_i}\right)\right) \otimes \left(\frac{1}{\sqrt{2\pi}\sigma_t} \exp\left(-\frac{t'^2}{2\sigma_t^2}\right)\right)\right](t) \qquad (4.26)$$

$$t_{sh}(\boldsymbol{X}, \boldsymbol{s}, \boldsymbol{r_i}) = \qquad\qquad t_s + \Delta t_\mu(\boldsymbol{x}_s, \boldsymbol{s}) + \frac{|\boldsymbol{s}-\boldsymbol{r}_i|}{c/n}, \qquad\qquad (4.27)$$

with $\mathcal{N}$ being a normalization constant defined by $\int\limits_{-\infty}^{\infty} dt \ S_1(t) = 1$ and $\Delta t_\mu(\boldsymbol{x}_s, \boldsymbol{s})$ being the time the muon needs to travel from the start point of the track to $\boldsymbol{s}$ which is obtained from Geant4 along with the $\left\langle\frac{dL}{dx}\right\rangle$-table as described in Section 4.3.2. S_1 is the hit time distribution which one track element would cause on the PMT shifted by $-t_{sh}$. It is plotted in Figure 4.22 along with its components from the slow and fast decay component of the scintillator. At this stage, S_1 is neither dependent on the position of light emission nor on the position of the PMT, as the major position dependence from the expected arrival time of the photon is absorbed in $t_{sh}(\boldsymbol{X}, \boldsymbol{s}, \boldsymbol{r}_i)$.

The first additional consideration to be included is the **finite size of the PMTs**. As the PMTs in LENA will not feature any position resolution over the photocathode there is no way to determine where on a PMT a specific photon has hit. The flight times of the photons from the point of creation to the PMT depend on where exactly the photon has
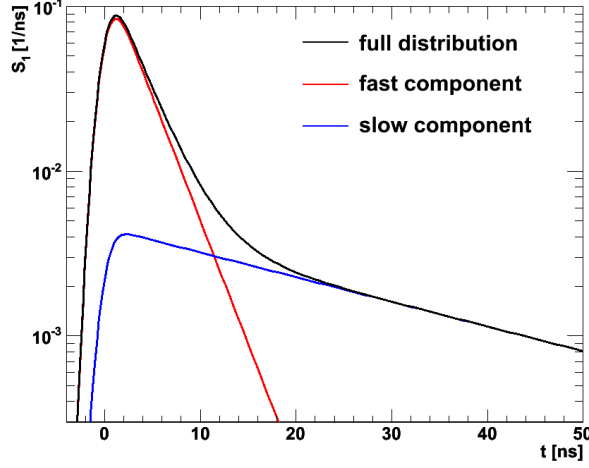
Fig. 4.22: Plot of the hit time distribution S_1 including only the decay time distribution of the scintillator and the time jitter of the PMT.
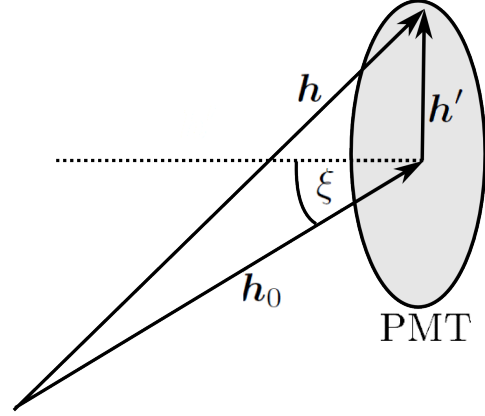
Fig. 4.23: Visualization of the different quantities needed to include the finite size of the PMTs in the overall PDF.

hit the PMT. To get the correct PDF it is therefore necessary to superimpose the PDFs for all surface elements. Therefore, equation (4.25) becomes

$$\tilde{P}_o(t|\boldsymbol{X}, \boldsymbol{r}_i, \hat{\boldsymbol{n}}_i) = \frac{1}{\mu_i A_{\text{PMT}}} \int\limits_{\boldsymbol{x}_s(\boldsymbol{X})}^{\boldsymbol{x}_e(\boldsymbol{X})} ds \int\limits_{\partial A_{\text{PMT}}} dA \left(\frac{d\mu_i}{ds}\right)(s, \boldsymbol{X}, \boldsymbol{r}', \hat{\boldsymbol{n}}_i) \cdot S_1(t - t_{sh}(\boldsymbol{X}, \boldsymbol{s}, \boldsymbol{r}')) \quad (4.28)$$

with $\boldsymbol{r}'$ being the variable associated with the dA integration, which covers the active surface of the PMT. Due to the computation time required to calculate this expression, it is completely impossible to do the integration over the PMT for each call of the minimization function. To improve the situation, a far field approximation is done. Hence, the vector $\boldsymbol{h}$ connecting $\boldsymbol{s}$ with $\boldsymbol{r}'$ is decomposed into two parts (cf. Figure 4.23)

$$\boldsymbol{h} = \boldsymbol{h}_0 + \boldsymbol{h}' \quad (4.29)$$
$$\boldsymbol{h}_0 = \boldsymbol{r}_i - \boldsymbol{s} \quad (4.30)$$
$$\boldsymbol{h}' = \boldsymbol{r}' - \boldsymbol{r}_i, \quad (4.31)$$

with $\boldsymbol{h}_0$ connecting the track element with the center of the PMT $\boldsymbol{r}_i$ and $\boldsymbol{h}'$ accounting for the difference between the center of the PMT and a point on the surface of the PMT. The smallest possible distance from a PMT at which light can be emitted is $1.5\,\text{m}$, given by the distance from the border of the active volume to the PMTs. As the radius of the PMT is $25\,\text{cm}$, the approximation $|\boldsymbol{h_0}| \gg |\boldsymbol{h}'|$ is obvious. Therefore, the norm of $\boldsymbol{h}$ can be decomposed into powers of $|\boldsymbol{h}'|$. Keeping only terms of $\mathcal{O}(|\boldsymbol{h}'|)$ yields

$$|\boldsymbol{h}| \approx |\boldsymbol{h}_0| + \frac{\boldsymbol{h}_0}{|\boldsymbol{h}_0|} \cdot \frac{\boldsymbol{h}'}{|\boldsymbol{h}'|} |\boldsymbol{h}'| + \dots \quad . \quad (4.32)$$

Inserting (4.29) into the explicit expression for $\left(\frac{d\mu_i}{ds}\right)(s, \boldsymbol{X}, \boldsymbol{r}', \hat{\boldsymbol{n}}_i)$ yields

$$\begin{aligned}
\left(\frac{d\mu_i}{ds}\right)(s, \boldsymbol{X}, \boldsymbol{r}', \hat{\boldsymbol{n}}_i) = & \left\langle \frac{dL}{dx} \right\rangle (s) \cdot \frac{1}{4\pi} \frac{A_{\text{PMT}}}{|\boldsymbol{h_0}+\boldsymbol{h}'|^2} \left(\frac{\boldsymbol{h}_0+\boldsymbol{h}'}{|\boldsymbol{h}_0+\boldsymbol{h}'|} \cdot \hat{\boldsymbol{n}}_i\right) \cdot \exp\left(-\frac{|\boldsymbol{h_0}+\boldsymbol{h}'|}{\lambda_{\text{att}}}\right) \frac{1}{R(\boldsymbol{s},\boldsymbol{r}')} \\
\approx & \left\langle \frac{dL}{dx} \right\rangle (s) \cdot \frac{1}{4\pi} \frac{A_{\text{PMT}}}{|\boldsymbol{h_0}|^2} \left(\frac{\boldsymbol{h}_0}{|\boldsymbol{h}_0|} \cdot \hat{\boldsymbol{n}}_i\right) \cdot \exp\left(-\frac{|\boldsymbol{h}'_0|}{\lambda_{\text{att}}}\right) \frac{1}{R(\boldsymbol{s},\boldsymbol{r}_i)} \\
= & \left(\frac{d\mu_i}{ds}\right)(s, \boldsymbol{X}, \boldsymbol{r}_i, \hat{\boldsymbol{n}}_i), \quad (4.33)
\end{aligned}$$
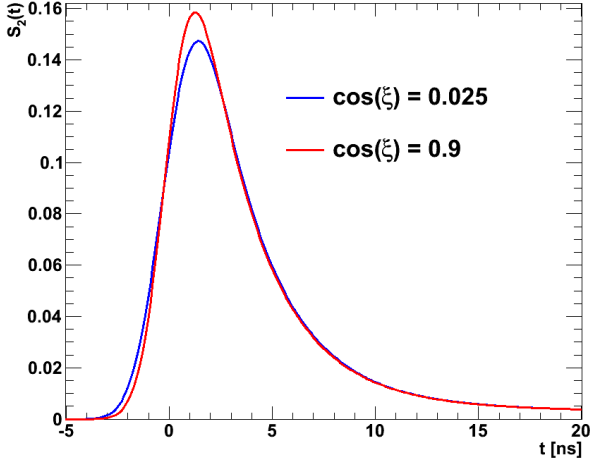
Fig. 4.24: Comparison of the expected hit time distribution for the case of shallow photon incidence and for steep photon incidence. The curve for shallow incidence is significantly wider than the curve for steep incidence.
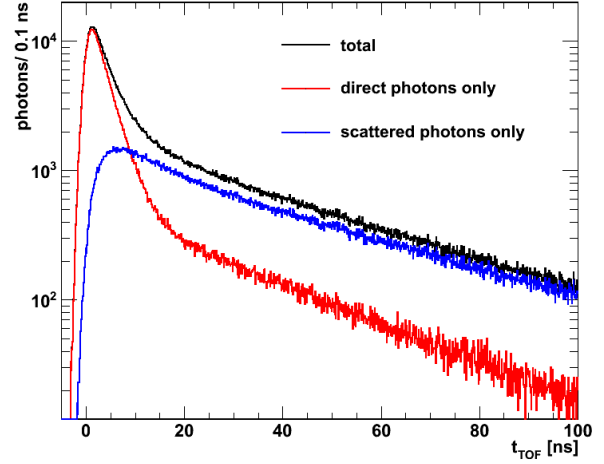
Fig. 4.25: Sum of the TOF-corrected hit time spectra of 50000 1 MeV pointlike electron events at the center of the detector. Additionally, the contributions of the direct and scattered photons are shown.

where (4.32) was used and $R(\boldsymbol{s}, \boldsymbol{r}') \approx R(\boldsymbol{s}, \boldsymbol{r}_i)$ was assumed. Note that $\boldsymbol{h}' \cdot \hat{\boldsymbol{n}}_i = 0$ for a flat PMT and that $|\boldsymbol{h}'|$ can be dropped from the exponential as $\lambda_{\mathrm{att}} \gg |\boldsymbol{h}'|$. Furthermore, using again (4.32), $t_{sh}(\boldsymbol{X}, \boldsymbol{s}, \boldsymbol{r}')$ can also be decomposed:

$$t_{sh}(\boldsymbol{X}, \boldsymbol{s}, \boldsymbol{r}') = t_s + \Delta t_\mu(\boldsymbol{x}_s, \boldsymbol{s}) + \frac{|\boldsymbol{h}_0 + \boldsymbol{h}'|}{c/n} \approx t_{sh}(\boldsymbol{X}, \boldsymbol{s}, \boldsymbol{r}_i) + \frac{|\boldsymbol{h}'|}{c/n}\left(\frac{\boldsymbol{h}_0}{|\boldsymbol{h}_0|} \cdot \frac{\boldsymbol{h}'}{|\boldsymbol{h}'|}\right). \quad (4.34)$$

Here the second part cannot be dropped as $\frac{|\boldsymbol{h}'|}{c/n} \sim 1\,\mathrm{ns}$ is of the same order as the time resolution of the PMT. Using (4.33) and (4.34) $\tilde{P}_o$ becomes

$$\tilde{P}_o(t|\boldsymbol{X}, \boldsymbol{r}_i, \hat{\boldsymbol{n}}_i) = \frac{1}{\mu_i A_{\mathrm{PMT}}} \int\limits_{\boldsymbol{x}_s(\boldsymbol{X})}^{\boldsymbol{x}_e(\boldsymbol{X})} ds \left(\tfrac{d\mu_i}{ds}\right)(s, \boldsymbol{X}, \boldsymbol{r}_i, \hat{\boldsymbol{n}}_i) \int\limits_{\partial A_{\mathrm{PMT}}} dA\; S_1\left(t - t_{sh}(\boldsymbol{X}, \boldsymbol{s}, \boldsymbol{r}_i) + \frac{|\boldsymbol{h}'|}{c/n}\left(\frac{\boldsymbol{h}_0}{|\boldsymbol{h}_0|} \cdot \frac{\boldsymbol{h}'}{|\boldsymbol{h}'|}\right)\right)$$

$$=: \frac{1}{\mu_i} \int\limits_{\boldsymbol{x}_s(\boldsymbol{X})}^{\boldsymbol{x}_e(\boldsymbol{X})} ds \;\left(\tfrac{d\mu_i}{ds}\right)(s, \boldsymbol{X}, \boldsymbol{r}_i, \hat{\boldsymbol{n}}_i) \cdot S_2(t - t_{sh}(\boldsymbol{X}, \boldsymbol{s}, \boldsymbol{r}_i), \xi(\boldsymbol{s}, \boldsymbol{r}_i)). \quad (4.35)$$

with ξ being the angle between the norm vector of the PMT and $\boldsymbol{h}_0$ as indicated in Figure 4.23. The integral over the surface of the PMT results in a simple dependence on ξ due to the rotational symmetry of the PMT around its normal vector.

The effect of the inclusion of the finite size of the PMTs is shown in Figure 4.24 where $S_2(t, \xi)$ is plotted versus t for two different values of ξ, one corresponding to steep incidence and one corresponding to shallow incidence. As the spread between the flight times over the PMT increases with increasing ξ the curve for shallow incidence shown in blue is smeared out with respect to the curve for steep incidence shown in red.

Finally, **scattering in the scintillator** has to be taken into account. At first glance, this seems to be a strange thing to do, as the signal used for the fits are only the first hit times of the PMT. As scattering always delays photons, most first hit photons should not be scattered, especially given the large number of photons produced in high energy

events. Simulations show however that neglecting the scattering leads to a significant systematic shift of the start point when trying to fit the track. This can be explained looking at Figure 4.25 which shows the sum of the TOF-corrected pulses of multiple point like events, as well as the contribution of scattered and direct light to the overall pulse. Obviously the contribution of scattered events is significant even at small TOF-corrected hit times indicating that scattering plays an important role even for first hits.

To include the scattering in the overall PDF, S_2 has to be modified

$$S_2(t - t_{sh}(\boldsymbol{X}, \boldsymbol{s}, \boldsymbol{r_i}), \xi(\boldsymbol{s}, \boldsymbol{r_i})) \longrightarrow S(t - t_{sh}(\boldsymbol{X}, \boldsymbol{s}, \boldsymbol{r_i}), \rho_s, |\Delta\varphi|, |\Delta z|), \tag{4.36}$$

where the correct arguments for S capable to account for the effects of scattering have been identified in Section 4.3.2 for the direct indirect ratio in equation (4.24). S is composed of two parts, one describing the hit time distribution of the unscattered photons given by S_2 with weight $R(\rho_s, |\Delta\varphi|, |\Delta z|)$ as defined in (4.23) and one describing the scattered photons with weight $(1 - R)$

$$S(t, \rho_s, |\Delta\varphi|, |\Delta z|) = R(\rho_s, |\Delta\varphi|, |\Delta z|)S_2(t, \xi) + (1 - R(\rho_s, |\Delta\varphi|, |\Delta z|))S_{sc}(t, \rho_s, |\Delta\varphi|, |\Delta z|) \tag{4.37}$$

with $S_{sc}(t, \rho_s, |\Delta\varphi|, |\Delta z|)$ being the hit time distribution of the scattered photons. It can be calculated by convolving S_2 with the PDF $P_{sc}(\Delta t \mid \rho_s, |\Delta\varphi|, |\Delta z|)$ for scattering to induce a certain delay Δt

$$S_{sc}(t, \rho_s, |\Delta\varphi|, |\Delta z|) = \left[S_2(t', \xi) \otimes P_{sc}(t' \mid \rho_s, |\Delta\varphi|, |\Delta z|) \right](t). \tag{4.38}$$

Common to all quantities connected to scattering a calculation of P_{sc} is nearly impossible and therefore the distribution is obtained from a Geant4 simulation of point like 1 MeV electron events at multiple points in the detector. In order to collect data with sufficient statistics, the approximation $P_{sc}(\Delta t \mid \rho_s, |\Delta\varphi|, |\Delta z|) \approx P_{sc}(\Delta t | |\boldsymbol{h}_0|)$ is used. The obtained distributions are displayed in Figure 4.26. They feature a shift to higher Δt with increasing $|\boldsymbol{h}_0|$ due to the higher possibility of multiple scattering.

The calculated S can be used to predict the timing distribution of a point source. Therefore, it is possible to compare the calculated results with Monte Carlo data. The result of the comparison using 1 MeV electrons in the center of the detector is shown in Figure 4.27 for an arbitrary PMT from the ring with the smallest absolute z-coordinate. An excellent match of the calculated distribution to the Monte Carlo is observed.

Putting everything together the overall PDF is given by

$$P_o(t|\boldsymbol{X}, \boldsymbol{r_i}, \hat{\boldsymbol{n}}_i) = \frac{1}{\mu_i} \int\limits_{\boldsymbol{x_s}(\boldsymbol{X})}^{\boldsymbol{x_e}(\boldsymbol{X})} ds \left(\frac{d\mu_i}{ds} \right)(s, \boldsymbol{X}, \boldsymbol{r_i}, \hat{\boldsymbol{n}}_i) \cdot S(t - t_{sh}(\boldsymbol{X}, \boldsymbol{s}, \boldsymbol{r_i}), \rho_s, |\Delta\varphi|, |\Delta z|). \tag{4.39}$$

At least for single PMTs it is possible to check the overall PDF by comparing it to the hit time distribution obtained by simulating multiple tracks with parameters $\boldsymbol{X}$. This is shown on the left of Figure 4.28 for the example of 500 MeV muons for a PMT close to the center of the detector. The obtained agreement between the predicted PDF and the distributions obtained from the Monte Carlo simulation is excellent.
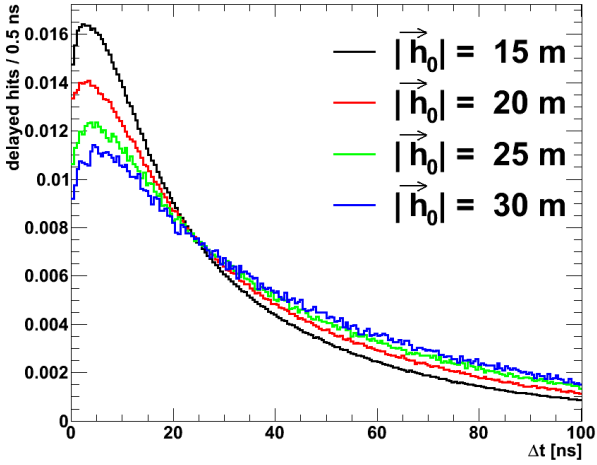
Fig. 4.26: Distributions of time delays due to scattering for various distances between point of photon emission and point of photon detection $|\boldsymbol{h_0}|$. The observed distribution gets shifted to higher time losses for rising $|\boldsymbol{h_0}|$.
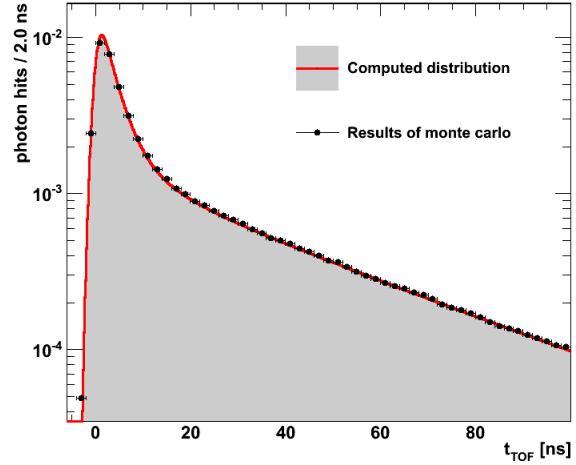
Fig. 4.27: Comparison of the predicted TOF-corrected hit time distribution of a point like event in the center of the detector, with the distribution obtained from Geant4. 1 MeV electrons were used to simulate point like events. The simulated distribution was obtained from the hits on the PMT ring with the smallest absolute z-coordinate.
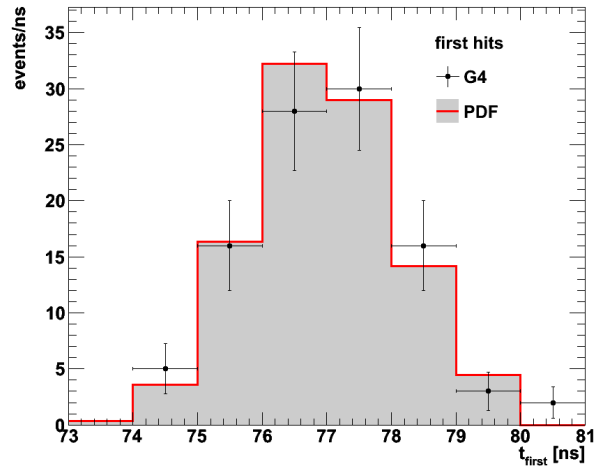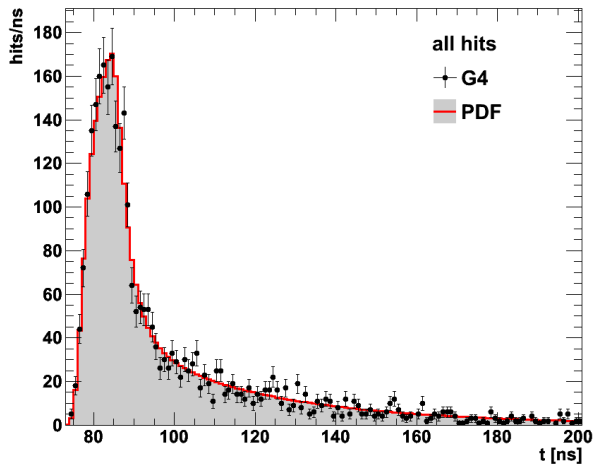
Fig. 4.28: Comparison of the overall PDF (left) and the PDF for the first hits (right) with the results obtained from Geant4. The expected distribution for a 500 MeV muon traveling from the center of the detector along the negative x-axis is shown gray shaded with red border while the black points represent the data obtained by simulating 100 events. The distributions are shown for a PMT with the coordinates $(0, 14.50, 0.41)$ m.
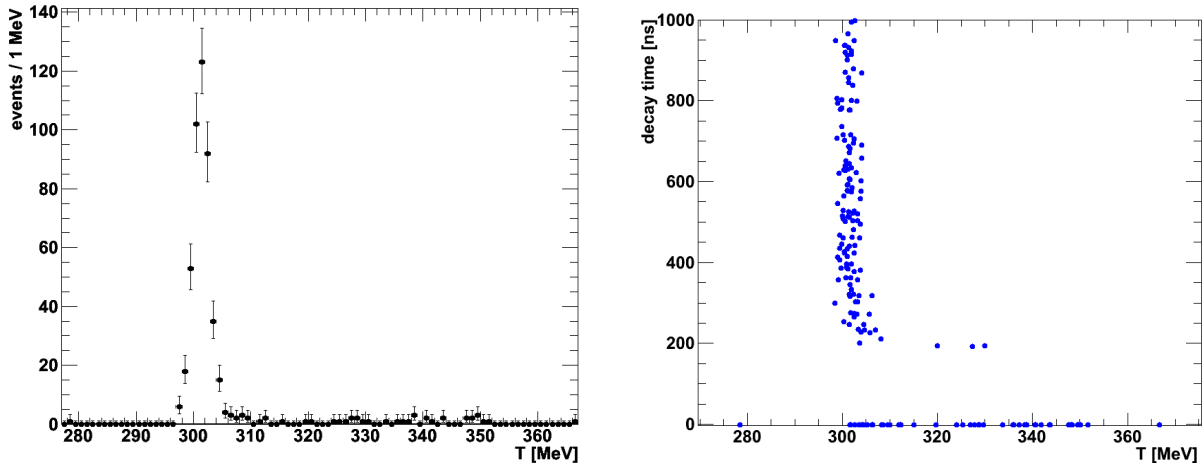
Fig. 4.29: Distribution of reconstructed kinetic energies for successfully reconstructed muons (left) and scatter plot of the reconstructed kinetic energy versus the reconstructed decay time. The distributions show the results obtained from 300 MeV muons traveling form the center of the detector along the negative x-axis. Events with a negative decay time have no identified muon decay. The kinetic energy distribution features a prominent peak around 300 MeV and a broad spectrum of outliers.

Having constructed the overall hit time PDF the **PDF for the first photon hit time** $P(t_i|\boldsymbol{X}, \boldsymbol{r}_i, \hat{\boldsymbol{n}}_i, q_i)$ can be calculated. It is given by the product of the overall PDF with the probability that non of the remaining $q_i - 1$ photon hits occurred at $t < t_i$

$$P(t_i|\boldsymbol{X}, \boldsymbol{r}_i, \hat{\boldsymbol{n}}_i, q_i) = \quad P_o(t_i|\boldsymbol{X}, \boldsymbol{r}_i, \hat{\boldsymbol{n}}_i) \left[1 - \int\limits_{-\infty}^{t_i} dt \quad P_o(t|\boldsymbol{X}, \boldsymbol{r}_i, \hat{\boldsymbol{n}}_i) \right]^{(q_i-1)} \cdot q_i \quad (4.40)$$

$$= \frac{1}{\mu_i} \int\limits_{\boldsymbol{x}_s(\boldsymbol{X})}^{\boldsymbol{x}_e(\boldsymbol{X})} ds \left(\frac{d\mu_i}{ds} \right) S(t_i - t_{sh}) \left[1 - \frac{1}{\mu_i} \int\limits_{\boldsymbol{x}_s(\boldsymbol{X})}^{\boldsymbol{x}_e(\boldsymbol{X})} ds \left(\frac{d\mu_i}{ds} \right) \int\limits_{-\infty}^{t_i} dt \ S(t - t_{sh}) \right]^{(q_i-1)} \cdot q_i, (4.41)$$

The combinatorial factor q_i is required as each of the photons can be the first one. As the last integral in (4.41) is a function of $t_i - t_{sh}$ it is possible to tabulate the results along with the values of S as a function of $t_i - t_{sh}, \rho_s, |\Delta\varphi|$ and $|\Delta z|$ to reduce computation times. For values in between the supporting points linear interpolation is used.
The results from the calculation for the first hit PDF can again be cross checked with the simulation as done above for the overall PDF. This is shown on the right of Figure 4.28 for the example of 500 MeV muons and a PMT with a small absolute z-coordinate. Again, the observed agreement is excellent, even though the real value of q_i has to be replaced by the mean value over all simulated events in order to do a comparison.

4.3.4 Results

The reconstruction has been tested on large number of muon tracks with varying parameters. First, the general structure of the resulting distributions as well as the characteristic quantities derived from this distributions are introduced using a sample of 500 equal tracks. Subsequently, the dependency of the performance on the kinetic energy of the muon is presented.

As a typical example, a set of 500 muons traveling from the center of the detector along the negative x-axis with a kinetic energy of 300 MeV is chosen. From the 500 simulated events the fit converged 481 times corresponding to about 96%. The results obtained from fits without convergence still provide useful information as the angle and the energy is typically reconstructed reliably but they are more likely to produce outliers in the start point distribution, especially in track direction.

The left of Figure 4.29 shows the distribution of reconstructed muon energies taking into account all simulated muons with a converging fit, including muons without an identified muon decay. The obtained distribution features a peak around the true value of the kinetic energy albeit with a very long tail to high energies and one outlier to lower energies. To better understand the outliers the decay time is plotted as a function of the energy on the right of Figure 4.29. Muons without identified decay are assigned a decay time of -1 ns. The outliers to higher energies can be subdivided into two groups. One group has a very low identified muon decay time close to the threshold, while the other features no identified muon decay at all. For muons without an identified decay, there is no possibility to neglect photons belonging to the muon decay. Therefore, not only the muon track, but also the muon decay are fitted. Thus, the reconstructed energy is too high. The case for the muons with very low decay times is similar. Here, the peak of the muon decay is before the threshold and the trigger occurred in the tail of the muon decay's photon distribution. Therefore, only a part of the muon decay is cut away, while the rest of the decay is included in the fit. The outlier to lower energies also does not feature an identified muon decay. It is most probably an in flight decay. The missing energy is lost in the neutrinos produced in the muon decay.
These effects can be be avoided by imposing a threshold of 250 ns for the decay time of the muon. The resulting distribution is visualized in Figure 4.30. The obtained distribution can be described by a Gaussian and does not feature any outliers. The obtained energy resolution is about 0.5%. Note that the distribution features a small shift compared to the expected value of 300 MeV.

The obtained values for the start time are shown in Figure 4.31 with the Monte Carlo truth being $t_s^{\mathrm{true}} = 0$. The distribution is very narrow and shows that the reconstruction of the start time is possible at sub nanosecond accuracy. Nevertheless, it features a significant systematic shift to positive times. The shift is basically constant over all energies and track types. Therefore, it can be compensated by subtracting the mean shift from the obtained values of t_s. The reconstructed start time of the muon is also a very sensitive control parameter for the goodness of the fit. If it could be determined beforehand by a different algorithm, a deviation from the expected value would be a safe signal that the fit result is not to be trusted.

The start point results are depicted in the first three plots of Figure 4.32. Except one outlier in the x_s distribution, all obtained values follow a Gaussian distribution and do not feature any significant systematic shifts. The obtained resolutions are in the order of a few centimeters. The resolution for z_s is worse than the resolutions obtained for x_s and y_s, as shifting the track in z-direction introduces only very small differences in the expected photon arrival times for the near PMTs as the movement is nearly perpendicular
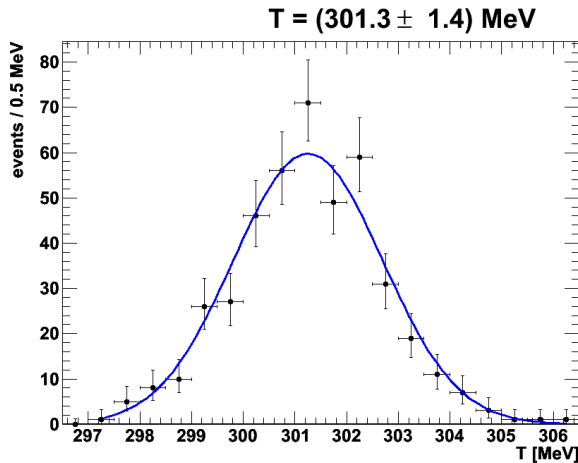
Fig. 4.30: Distribution of reconstructed energies for 300 MeV muons traveling from the center of the detector in negative x-direction with a decay time of at least 250 ns. The indicated value and error for T correspond to the mean and the standard deviaton of the fitted Gaussian.
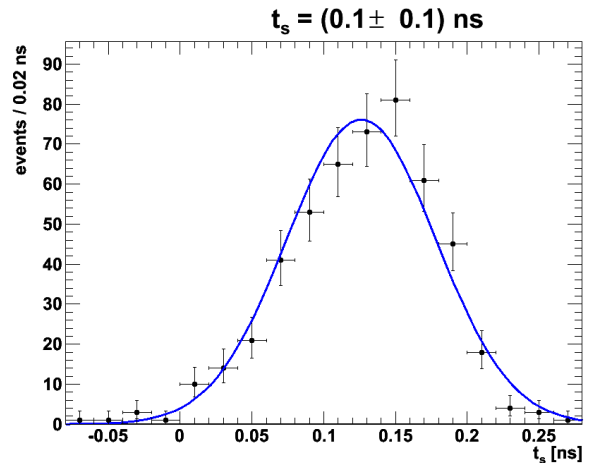
Fig. 4.31: Distribution of reconstructed muon start times for 300 MeV muons traveling from the center of the detector in negative x-direction. The indicated value and error for t_s correspond to the mean and the standard deviation of the fitted Gaussian.

to $\boldsymbol{h}_0$. This is not true for the PMTs with higher $|\Delta z|$, but these suffer from poor photon statistics and a high influence of scattering. Even though the resolutions for x_s and y_s are comparable in this example, the resolution typically is poorer for the coordinate along the track than the coordinate perpendicular to the track. The latter can be fixed by comparing the photon arrival times of opposing PMTs. Therefore, it is nearly independent of the remaining track parameters.

The lower right plot in Figure 4.32 shows the distribution of the obtained angular deviations of the reconstructed track from the true track. The fit is done according to Equation (4.9) and yields an angular resolution of about three degrees.

To assess the performance of the track reconstruction dependent on the energy, the fraction of converged muons versus the true kinetic energy is shown in Figure 4.33. The fit currently works reliably in the range between 200 MeV and at least 500 MeV. In this range the convergence is between 80% and 95%. It drops to higher as well as to lower energies. The drop to lower energies is due to the fact that fitting becomes more and more difficult with decreasing track length. At energies of 200 MeV, the overall track length is about 70 cm. Additionally, during the last part of the track, the speed of the muon no longer exceeds the speed of light. In this region the basic assumption of the Fermat cone breaks down which means that the slower regions of the track do not contribute to the useful signal. The reason for the break down of the convergence at higher energies is currently not totally understood. A possible explanation might be the larger event by event fluctuations of the track length at higher energies. As the kinetic energy and therefore the assumed length of the track is mostly determined by the charge PDF, the length assumed due to the CSDA and the real length might be in conflict to each other causing the fit to fail.
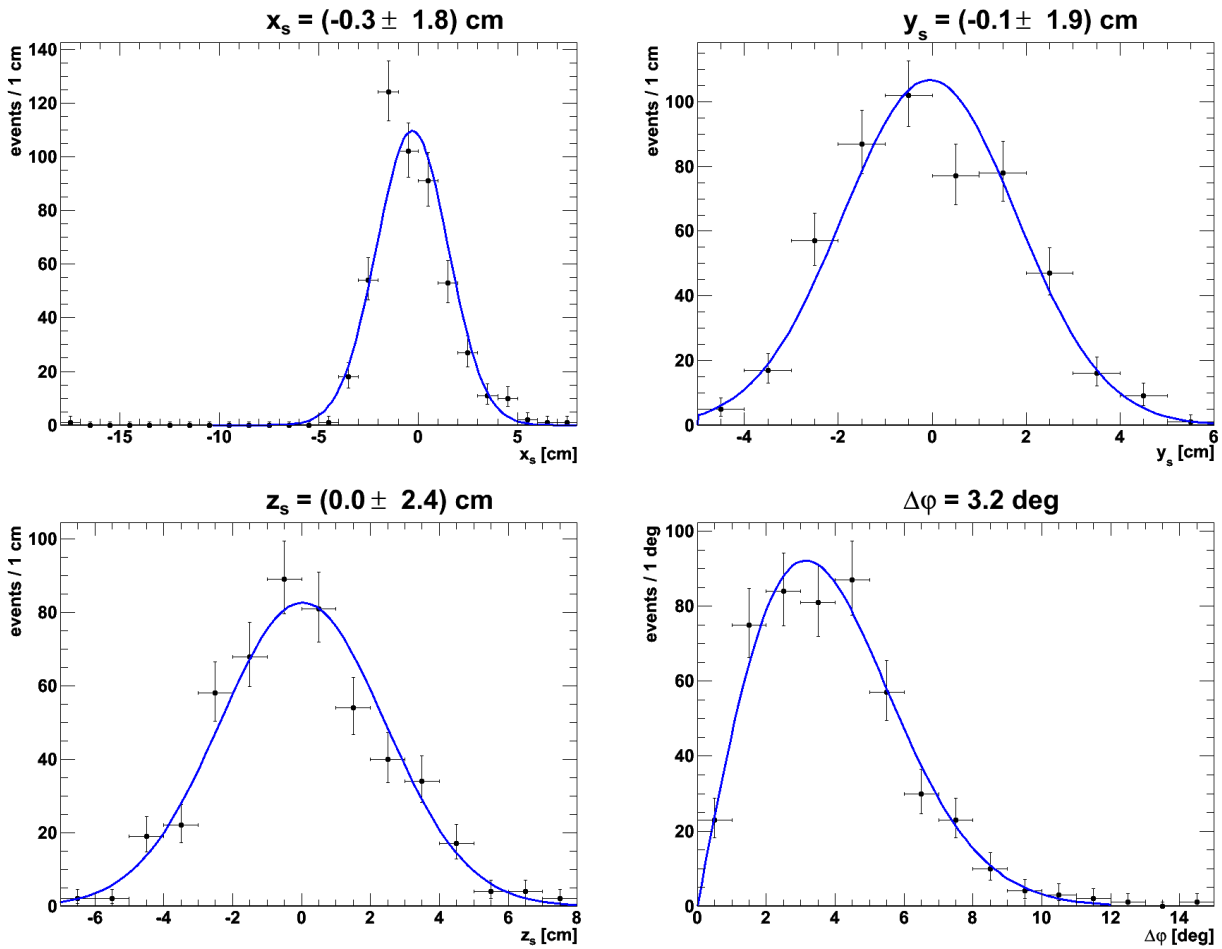
Fig. 4.32: Fit results for 300 MeV muons traveling from the center of the detector in negative x-direction. The first three plots show the obtained values for start point coordinates. Fitting the results with a Gaussian returns $x_s = (-0.3 \pm 1.8)$ cm, $y_s = (-0.1 \pm 1.9)$ cm and $z_s = (0.0 \pm 2.4)$ cm. The lower right panel displays the angular deviations of the reconstructed tracks from the true tracks. Fitting the distribution with Equation (4.9) yields an angular resolution of $\Delta\varphi = 3.2$ degrees.
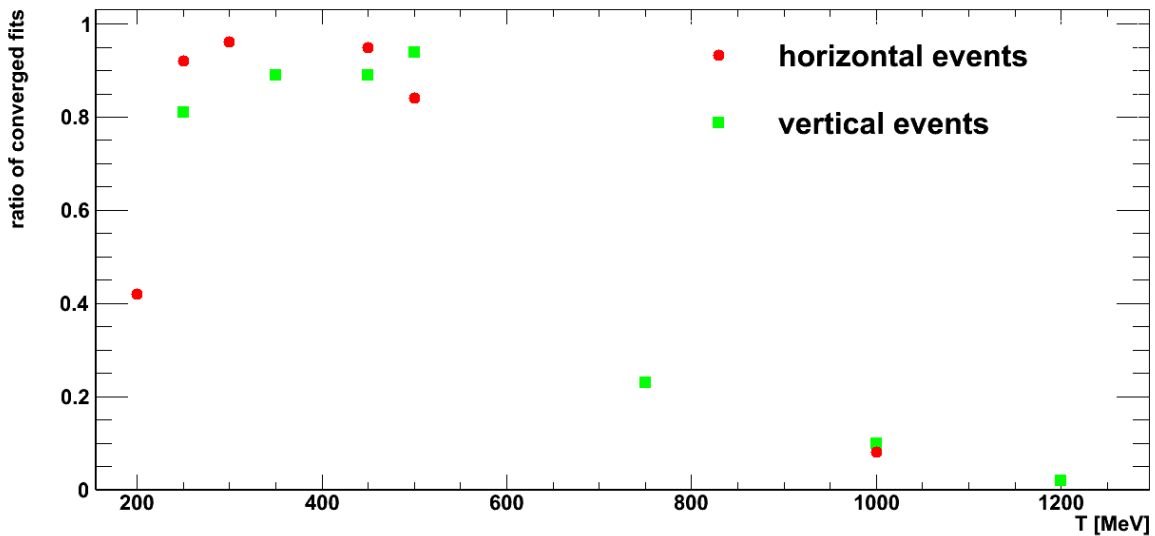
Fig. 4.33: Fraction of converged fits depending on the true kinetic energy of the muons.
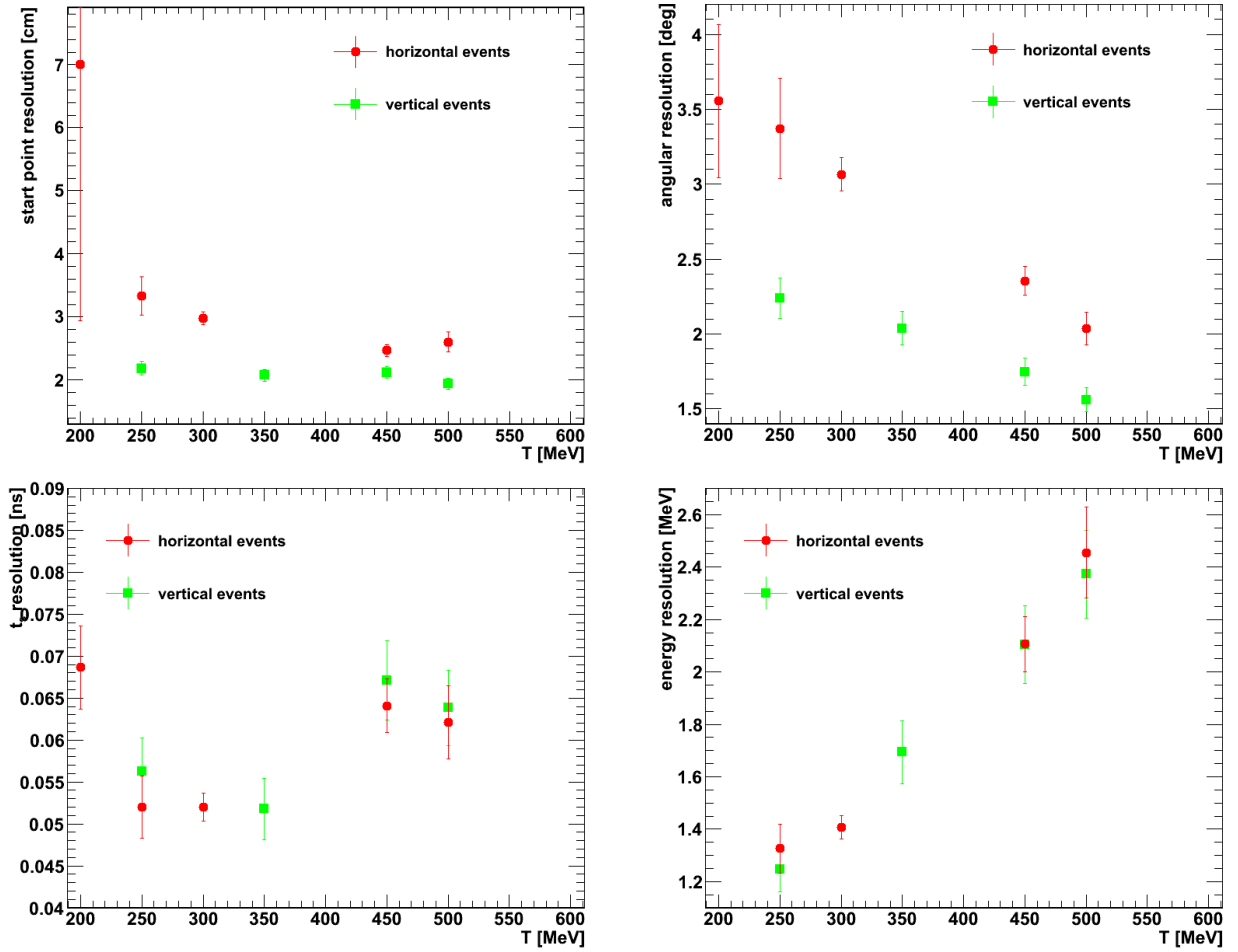
Fig. 4.34: Start point resolution, angular resolution, t_s-resolution and energy resolution (from top left to lower right) as a function of the true kinetic energy of the muons. The vertical tracks feature a better start point as well as angular resolution, while the horizontal tracks are slightly superior regarding the t_s-resolution. Both track types feature a comparable energy resolution, which does not evolve as $\sqrt{T}$, but linear with the kinetic energy.

Furthermore, the obtained resolutions for the start point, the direction, the start time and the energy are plotted dependent on the true kinetic energy of the simulated muons in Figure 4.34 in the energy range from 200 MeV to 500 MeV. The results obtained for horizontal and vertical tracks are shown separately.

For energies greater than 200 MeV, the start point resolution is basically constant in the order of a few centimeters, while it breaks down at 200 MeV. The performance of vertical muons surpasses the performance of horizontal muons over the whole energy range, as the start of the track can be effectively seen by more PMTs for the vertical case.

The angular resolution is in the order of a few degrees and improves with rising energy. Again, vertical events perform superior compared to horizontal events, as the straight Cerenkov-like light fronts which are especially suitable for direction reconstruction are better visible in the former case.

The resolution for the start time t_s of the event is excellent over the whole energy range. It is constantly below 0.1 ns and nearly independent of the energy. Here the values show a slight superiority of horizontal events which is probably due to the spherical light front of the start point being perfectly visible in this case.

The obtained energy resolution shows a nearly linear dependence on the energy i.e. $\Delta T/T \approx 0.5\%$ indicating that the energy resolution is dominated by systematical errors [17]. Here the influence of the software implementation of the PDF is the dominant factor. This shows that there is still room for further improvement of the energy resolution. The energy resolution shows no dependency on the direction of the track.

Additionally the track fitting has also been tested by simulating 300 MeV muons enclosing different angles ϑ with the z-axis. The corresponding plots can be found in appendix A Figures A.1 and A.2. The results show no significant changes with varying ϑ. This indicates that the dependency of the track reconstruction performance on ϑ is only weak.

Comparing the results obtained with the full fit to the results obtained by the estimates in Section 4.2, the results obtained by fitting show a superior performance. The only exception is the energy resolution which is comparable for the first estimates and maybe even better for higher energies. This is due to the fact that the expected number of detected photons features only a weak dependency on the point of photon emission. Additionally the barycenter by definition is the point on the track where the point like approximation works best. Hence, the error induced by the approximation of point like photon emission as done in Section 4.2.1 is very small. In contrast, the performance of the full fit is hampered by the high number of parameters.

Nevertheless, even though the energy estimation is better for pure muon tracks, it cannot be used to reconstruct CC neutrino interactions in the GeV range. At these energies, the neutrino typically transfers only a part of its energy to the lepton while the rest is transferred to other particles. Therefore, the total energy deposited in one event, which is reconstructed by the energy estimation, is no longer equivalent to the kinetic energy of the track. In contrast, the global fit, used with a modified PDF (see Section 6.3), is still able to recover the kinetic energy of the lepton by determining the track length.

Chapter 5

Electron-track reconstruction

The reconstruction of electron tracks follows the same basic principle as the muon-track reconstruction presented in Chapter 4. The PDF given by Equations (4.19) and (4.40) is still valid, albeit a different $\left\langle\frac{dL}{dx}\right\rangle$(s)-table has to be used, due to the different energy loss of electrons. As the discrepancy in energy loss of electrons and muons causes all the differences between electron and muon-track reconstruction, it is detailed in Section 5.1. As the the start point of the track and its barycenter are no longer well separated, the algorithm to discriminate between vertical and horizontal muon tracks, developed in Section 4.2.2, is not applicable to electron tracks. Hence, Section 5.2 presents a new algorithm to discriminate between horizontal and vertical tracks. Furthermore, a problem due to the different characteristic of the electron energy loss was encountered during the fit procedure which is called the "bremsstrahlung problem". It is described in Section 5.3 along with an algorithm to partially solve the problem. Finally, Section 5.4 presents the obtained performance of the electron-track reconstruction.

5.1 Energy loss of electrons

While muons and other heavy charged particles predominantly loose their energy via ionization and excitation of the passed material, electrons loose a significant amount of their energy by bremsstrahlung:

$$\left(-\frac{dE}{dx}\right) = \left(-\frac{dE}{dx}\right)_{\text{coll}} + \left(-\frac{dE}{dx}\right)_{\text{rad}}, \tag{5.1}$$

with the first term describing the energy loss due to collisions and the second term the energy loss due to radiation. As the cross section for bremsstrahlung is proportional to E/m_0^{-2}, the radiative energy loss can be neglected for muons at the energies of interest [23]. The overall dependency of the energy loss of electrons on the kinetic energy is shown in Figure 5.1 [82] along with its components from the collision energy loss and the radiative energy loss. While energy loss through collisions clearly dominates at lower energies radiative losses are dominant for high energies. The energy where $\left(\frac{dE}{dx}\right)_{\text{coll}} = \left(\frac{dE}{dx}\right)_{\text{rad}}$ is called critical energy E_c. From Figure 5.1 it can be determined to be 108 MeV in PXE. Note that in contrast to muons, the probability that an electron changes its direction due to interactions with matter is significantly increased due to its low mass. The only effect which keeps electrons in approximately the right direction is kinematic focusing.
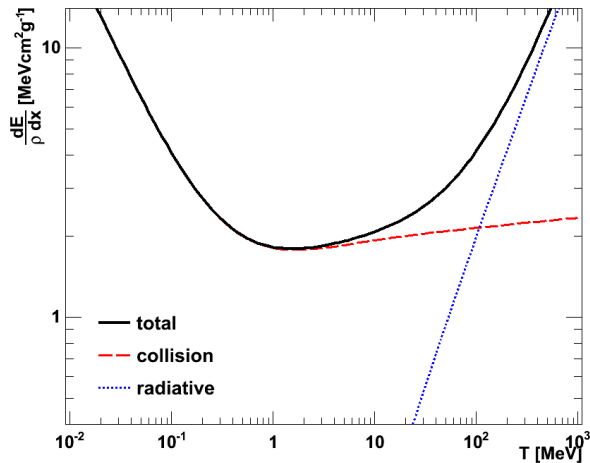
Fig. 5.1: Energy loss of electrons in PXE dependent on the kinetic energy of the electron. Data for the plot taken from [82]. The critical energy, where the radiative energy loss equals the collision loss, is 108 MeV.
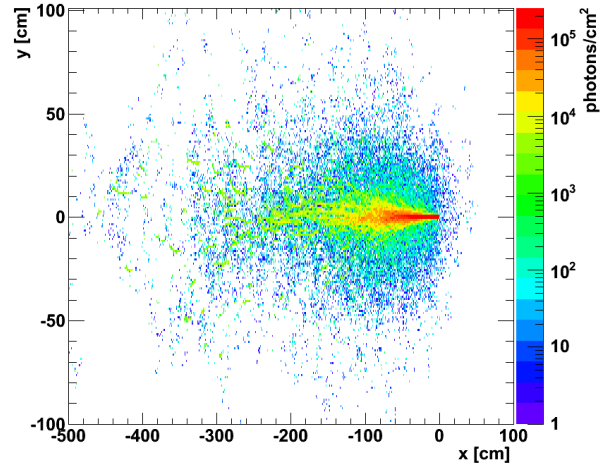
Fig. 5.2: Distribution of photons produced by 100 electrons with a kinetic energy of 300 MeV, traveling from the center of the detector along the negative x-axis. The obtained distribution is projected in the x-y plane.

The highly energetic γ-rays created due to bremsstrahlung of electrons typically produce further electrons and positrons, as their predominant interaction with matter is pair production. If the produced electrons and positrons are energetic enough, they can again produce gamma rays which subsequently produce more electron-positron-pairs and so on. Such a cascade is called electromagnetic shower. It typically breaks down when the energy of the produced particles drops below the critical energy. Assuming that each generation of an electromagnetic shower bisects the energy of the participating particles and considering that the energies of interest are below 1 GeV and $E_c = 108$ MeV, obviously no more than two or three generations in the development of the shower are possible in PXE. This number is unfortunately to low for a proper statistical treatment of the shower propagation which would allow using well tested approximation formulas for the shower shape (see e.g. [23]).

The onset of showering together with the increased deflection of electrons from the original direction has the effect of smearing the energy loss transverse to the track. Therefore, the term "electron track" is a bit misleading and means the "energy loss cloud created" due to an electron. This can also be seen in Figure 5.2 featuring the two dimensional distribution of scintillation photons produced by electrons with 300 MeV kinetic energy. The different energy loss of electrons has three major consequences for the track reconstruction:

- The one dimensional integral over the whole track, needed to calculate the first hit time PDF (4.41), is only an approximation. Basically, this integral would have to be replaced by a three dimensional integral over $\left\langle \frac{dL}{dV} \right\rangle$ covering a significant area around the track. However, this is impossible due to computation time constraints as the integration has to be performed for each call of the minimization function.

- The length of the track is no longer well defined, especially if showering occurs and if the particle multiplicity is higher than one. Therefore, the integral in Equation (4.41) has to be extended to cover the whole deposited energy and therefore all produced photons. This also implies that it is not possible to produce the $\left\langle \frac{dL}{dx} \right\rangle$-tables by
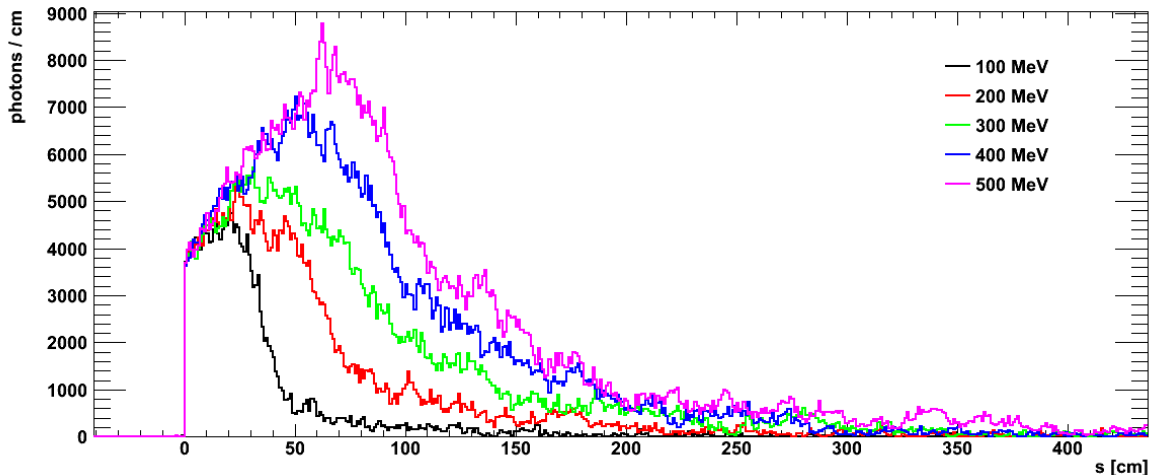
Fig. 5.3: Electron light yield per unit path length projected on the track, dependent on the singed distance to the start point s for multiple energies. The distributions are obtained by averaging over 100 events. They all feature a long tail due to produced bremsstrahlung gamma rays which can transverse significant distances in the scintillator.

scaling all track lengths to the medium track length as it was done in Section 4.3.2. Therefore, the $\left\langle \frac{dL}{dx} \right\rangle$-tables used for electron-track fitting are simply the averaged $\frac{dL}{dx}$-values from multiple events. As the electron energy loss does not feature the Bragg peak at the end of the track, this does not cause any problems.

- It is no longer possible to interpolate between two relatively distinct $\left\langle \frac{dL}{dx} \right\rangle$-tables by simply taking the table with the higher energy and starting at the point where the energy has dropped to the required energy as the electron might already have produced secondaries at this stage. Therefore, the $\left\langle \frac{dL}{dx} \right\rangle$-tables for intermediate energies are created by point wise linear interpolation between the two tables adjacent in energy. To obtain the required accuracy this requires a relatively small spacing in energy (50 MeV) between the different tables.

- The possibility of bremsstrahlung emission leads to much stronger event by event fluctuations as it is quite probable that an electron deposits a significant amount of its energy in one single bremsstrahlung photon. As the event by event fluctuations cannot be taken into account for each single electron track, but only their mean effect, they decrease the fit performance.

Examples for obtained electron $\left\langle \frac{dL}{dx} \right\rangle$-tables are shown in Figure 5.3 for multiple energies. For all the energies the obtained distribution features a long tail caused by bremsstrahlung photons which feature a significant interaction length in the scintillator. Compared to the $\left\langle \frac{dL}{dx} \right\rangle$-table for muons shown in Figure 4.20, the electron $\left\langle \frac{dL}{dx} \right\rangle$-tables feature a significantly higher noise. This is due to the high event by event fluctuations of electrons. For the construction of the PDF this does not cause a significant problem as $\left\langle \frac{dL}{dx} \right\rangle$ always appears in the product with the dime distribution S which is a rather broad distribution and therefore the obtained PDF has only a very small noise. Nevertheless, a smoother $\left\langle \frac{dL}{dx} \right\rangle$-table would definitely help, especially concerning the convergence of the fit. Hence, two attempts were made to smooth the distribution which both yielded unsatisfactory results. Therefore, currently the raw distribution is used.
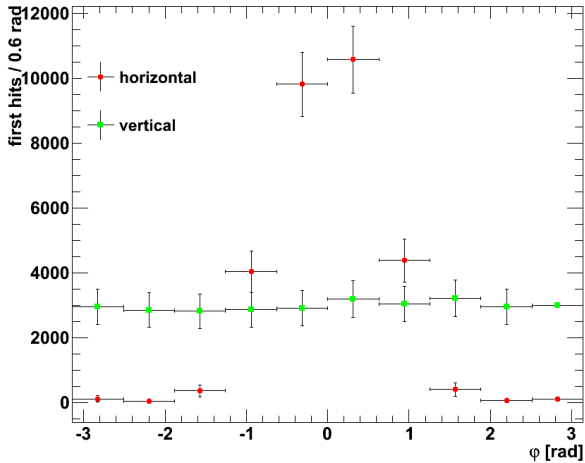
Fig. 5.4: φ-distribution of the 500 PMTs with the smallest TOF-corrected first hit time for horizontal and vertical events. The histogram is made by summing 100 events featuring 500 MeV electrons starting from the center of the detector.
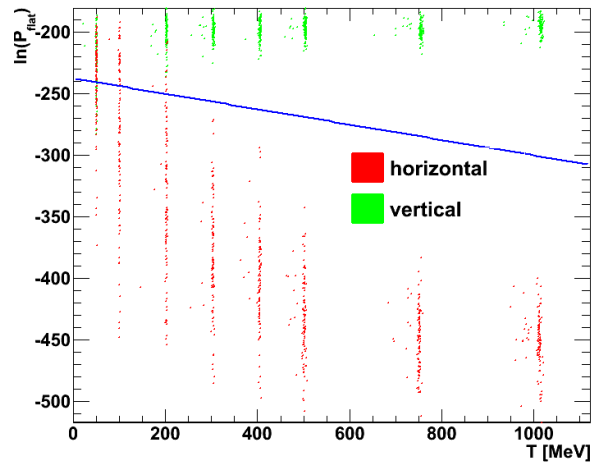
Fig. 5.5: Scatter plot of the logarithmic probability that the distribution of the first 500 TOF-corrected hits is flat in φ against the estimated energy of the electron. The blue line shows the boundary to discriminate between the two cases.

5.2   Vertical-horizontal discrimination

As discussed in Section 4.2.2 for the estimation of the track position and direction it is required to be able to discriminate between horizontal and vertical tracks. The method used for muons relied on the spatial distance of the start point of the track and the charge barycenter. Judging from the $\left\langle \frac{dL}{dx} \right\rangle$-tables in Figure 5.3, this is no longer the case for electrons. Therefore, a different method has to be used.

The method used for electrons relies on the observation of Figure 4.2. As already exploited to reconstruct the direction of horizontal events in Section 4.2.3 the PMTs with the smallest TOF-corrected first hit times are clustered around the point, where the extension of the track against the direction of the particle intersects with the wall for horizontal events. As already pointed out in Section 4.2.4, this is not observable for vertical events due to absorption and scattering. Therefore, the distribution of the polar angles φ of the PMTs with the smallest TOF-corrected first hits is flat for vertical events while it clusters for horizontal events. This behavior is shown in Figure 5.4 for the example of 500 MeV electrons starting from the center of the detector.

As an estimator to discriminate between the two cases, the logarithmic probability that the distribution of the first 500 TOF-corrected hits is flat is used. Assuming a flat histogram, the expected number of entries in each bin is fixed to

$$\mu_f = \frac{\text{total number of entries}}{\text{number of bins}} = \frac{\sum\limits_{i=1}^{N_{\text{Bins}}} n_i}{N_{\text{Bins}}}, \tag{5.2}$$

with n_i being the bin content of bin i and N_{Bins} the total number of bins in the histogram. The probability that the bin i has n_i entries is given by the Poisson distribution (3.4). Therefore, the logarithm of the probability $P_{\text{flat}}(\boldsymbol{n})$ for a given histogram to be flat is

given by

$$\ln\left[P_{\text{flat}}(\boldsymbol{n})\right] = \ln\left[\prod_{i=1}^{N_{\text{Bins}}} \frac{\mu_f^{n_i}}{n_i!}\exp(-\mu_f)\right] = -N_{\text{Bins}}\mu_f + \sum_{i=1}^{N_{\text{Bins}}}\left[n_i\ln(\mu_f) - \ln(n_i!)\right]. \quad (5.3)$$

Figure 5.5 shows the distribution of the obtained $\ln\left[P_{\text{flat}}(\boldsymbol{n})\right]$ values plotted versus the estimated energy of the electrons. The obtained results show a separations between horizontal and vertical electron tracks for energies above $T = 300\,\text{MeV}$. The boundary used to discriminate against the two cases is also shown in Figure 5.5 as a blue line. It is given by the equation

$$\ln\left[P_{\text{flat}}\right]^{\text{th}} = -\frac{5}{80}\cdot\frac{T}{\text{MeV}} - 237.5. \quad (5.4)$$

All results above this line are taken to be vertical while all events below this line are taken to be horizontal. The boundary was optimized to get maximal separation between purely vertical and purely horizontal tracks. Figure 5.6 shows the obtained efficiency dependent on the true kinetic energy of the electrons using only strictly horizontal and strictly vertical tracks. For energies above $300\,\text{MeV}$ no wrong decisions were made by the algorithm for all simulated events.

To test the discrimination algorithm for inclined electrons, additionally $300\,\text{MeV}$ electrons enclosing different angles to the z-axis were simulated. The obtained ratios of tracks tagged as horizontal and vertical are shown in Figure 5.7. The results show a smooth transition from events predominately identified as vertical to events predominately tagged as horizontal, with increasing angle between the track and the z-axis. As already observed for muons in Section 4.2.2, the point where ratios of events identified as horizontal and events identified as vertical are equal is not at 45 degrees, but at approximately 25 degrees. The algorithm therefore performs comparable to the one used for muon-track estimation. Thus, the rest of the track estimation presented in Section 4.2 is kept unchanged.

5.3   Bremsstrahlung problem

The first implementation of the electron-track reconstruction was a straight forward implementation of the muon-track fit, including the changes described in Section 5.1. While this works mostly fine, it produces a significant number of outliers. One group of these outliers shows two specific properties: The start point features a significant shift in track direction and the angle between the true and the reconstructed track is close to 180 degrees. Hence, these events were fitted with the wrong directionality i.e. from the end point to the start point. This is possible as the difference between the two directions is not as striking for the electrons as for the muons. The $\left\langle\frac{dL}{dx}\right\rangle$-distribution is much more symmetric for electrons than for muons, as it misses the Bragg peak. The asymmetry of the electron track is mainly caused by the bremsstrahlung tail which is prone to statistical fluctuations. Furthermore, the electron-track length is typically shorter, leading to a worse discrimination power due to timing.

To investigate the reason for this effect it is instructive to take a look at the distribution of charge barycenters for obtained electrons. Figure 5.8 shows this distribution for the example of $300\,\text{MeV}$ electrons traveling from the center of the detector along the negative x-axis. It has a significant tail to low x-values corresponding to a shift of the reconstructed barycenter in track direction, caused by bremsstrahlung photons. Comparing
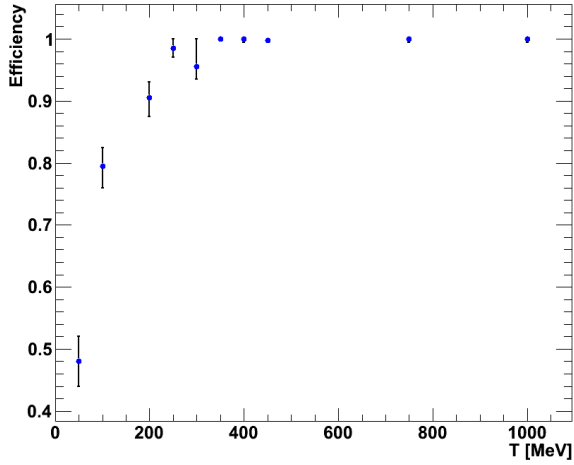
Fig. 5.6: Efficiency of electron vertical horizontal discrimination plotted versus the true kinetic energy T of the electron. The shown values are obtained using purely vertical and purely horizontal electrons starting at the center of the detector.
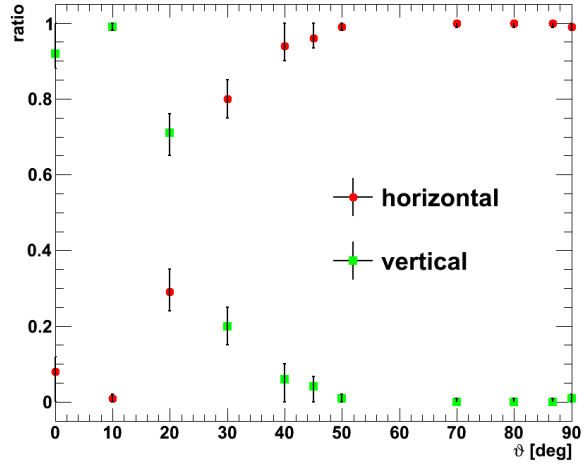
Fig. 5.7: Ratio of electrons tagged as horizontal and as vertical dependent on the angle ϑ the track encloses with the z-axis. The shown values are obtained from simulated 300 MeV electrons originating from the center of the detector.
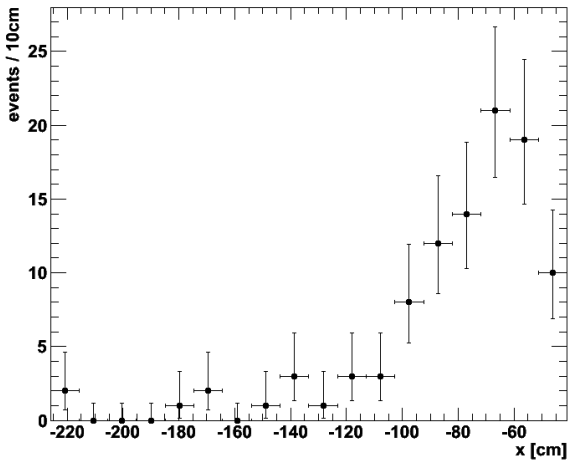
Fig. 5.8: Distribution of the x-coordinates of the reconstructed barycenters for 300 MeV electrons traveling from the center of the detector in negative x-direction. Note the significant tail in negative direction i.e. in track direction.
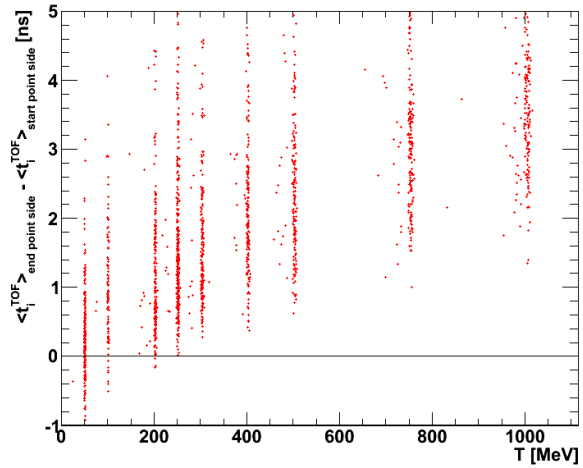
Fig. 5.9: Scatter plot of the difference between the mean TOF-corrected arrival times of the end and the start point side of the track (see text for details). The values were obtained using the true direction as input, therefore all values above zero show that the track direction is identified correctly. The boundary between the two cases is marked with a black line.

the obtained values with the $\left\langle \frac{dL}{dx} \right\rangle$-table for 300 MeV electrons shown in Figure 5.3, it is obvious that some barycenters are reconstructed significantly outside the peak in the $\left\langle \frac{dL}{dx} \right\rangle$-distribution. The events having a wrongly fitted direction feature a such significantly shifted barycenter. Furthermore, the wrong direction events were typically tagged as horizontal. The connection is made via the algorithms used to determine the first estimates used as input parameters for the fits for the case of horizontal muons (cf. Section 4.2.3). This algorithm directly calculates the start point position from the barycenter position and the estimated energy. Hence, a shifted barycenter leads to a shifted start point. If the shift is severe enough, the fit converges into a local minimum of the minimization function, which features a flipped track direction. Additionally, the reconstructed start point is totally of the true value.

To sum it up, the problem of electron tracks being fitted in the wrong direction is caused by bremsstrahlung photons which transport a significant amount of the particles energy in track direction. The resulting shift in the barycenter causes a wrong start value for the fits resulting in a flip in the fitted direction during the fit. As the whole problem is caused by bremsstrahlung emission of the electron it is called "bremsstrahlung problem".

This problem can be at least partially solved if there is a possibility to identify the mis-aligned tracks and correcting the start parameters afterwards. The track is subsequently refitted using the new start parameters. The performance of such an algorithm is given by the efficiency of the identification of wrong direction tracks.

Identifying the correct direction of fitted electron tracks:
The general idea to check whether the reconstructed direction of the track matches the correct direction or whether is has to be flipped, is based on an observation made for the TOF-corrected hit times already used to estimate the direction of horizontal muons: The TOF-corrected hit times of the first photon on each PMT are smaller for PMTs being closer to the start point of the track than to the end point of the track than for PMTs which are closer to the end point (cf. Figure 4.9).

The algorithm starts by constructing a plane G using the reconstructed direction vector as normal vector and the barycenter as origin point. This plane separates the detector in two parts, one containing the reconstructed start point of the track and one containing the reconstructed end point. Subsequently, the averages of the TOF-corrected first hit times for all PMTs on the start point side and for all PMTs on the end point side are calculated. The difference between those two mean times is used as estimator κ

$$\kappa = \left\langle t_i^{\mathrm{TOF}} \right\rangle_{\text{end point side}} - \left\langle t_i^{\mathrm{TOF}} \right\rangle_{\text{start point side}} . \tag{5.5}$$

κ is required to be positive for a correctly aligned track. To test the algorithm, it was applied to simulated electron events using the true direction as input parameter. Figure 5.9 shows the distribution of the obtained κ versus the estimated energy of the electron track. The plot shows a very good performance for energies greater than 300 MeV. For a better quantification of the performance, the efficiency to identify whether the track direction is correct or flipped is plotted in Figure 5.10 as a function of the true kinetic energy of the electrons. The plot shows that the algorithm works nearly perfectly for energies greater than 300 MeV, while still having a few deficits for lower energies.
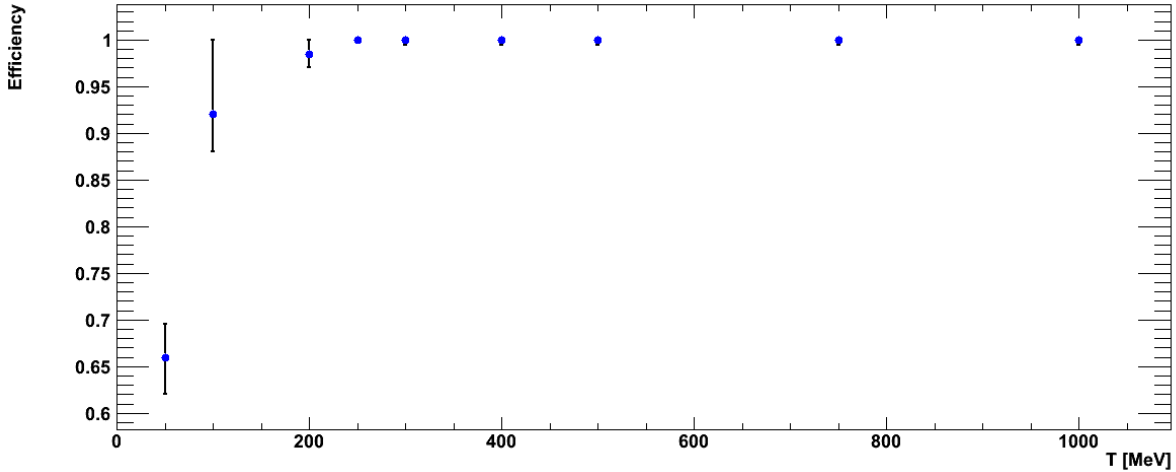
Fig. 5.10: Efficiency to correctly identify the electron-track direction as a function of the true kinetic energy of the electrons

Recovering a decent start point as input parameter for a new fit:
While the track fit which misidentified the track direction obviously does not feature a decent spatial or angular resolution the resolution for the start time t_s of the event is still excellent. It is typically below 0.5 ns. Therefore, the track start point can be recovered using the arrival times of the first TOF-corrected photon hits.

To suppress statistical fluctuations the algorithm uses $\bar{t}_{\text{TOF}}$, which is the average TOF-corrected hit time of the first 25 TOF-corrected first hits. Furthermore, two assumptions are made: First, the light is assumed to be detected at the point $\boldsymbol{x}_{\text{int}}$ where the extension of the track against the track direction $\hat{d}$ meets the wall. Second, all the light was assumed to be emitted at the start point $\boldsymbol{x}_s$. Using this assumptions, the start point of the track can be calculated

$$
\begin{aligned}
\boldsymbol{x}_s &= \boldsymbol{x}_p - \hat{\boldsymbol{d}} \cdot |\boldsymbol{x}_s - \boldsymbol{x}_p| \\
&= \boldsymbol{x}_p - \hat{\boldsymbol{d}} \cdot |\boldsymbol{x}_s - \boldsymbol{x}_{\text{int}} + \boldsymbol{x}_{\text{int}} - \boldsymbol{x}_p| \\
&= \boldsymbol{x}_p - \hat{\boldsymbol{d}} \cdot (|\boldsymbol{x}_s - \boldsymbol{x}_{\text{int}}| - |\boldsymbol{x}_{\text{int}} - \boldsymbol{x}_p|) \\
&\approx \boldsymbol{x}_p - \hat{\boldsymbol{d}} \cdot \bar{t}_{\text{TOF}} \cdot c/n.
\end{aligned}
\tag{5.6}
$$

The modulus can be split as the vectors are collinear. The track direction needed to evaluate equation (5.6) is taken from the estimated direction as determined according to Section 4.2.3 which typically points roughly in the correct direction.

Thus, having recovered a good estimate for the start point, the track is refitted using the new start point, the estimated direction and the start time of the event as recovered by the "flipped" fit as input values. The new fit typically converges to the correct minimum.

5.4   Performance

As the distribution of the electron-track fit results show some different features compared to the results obtained for muons presented in Section 4.3.4, it is instructive to look again
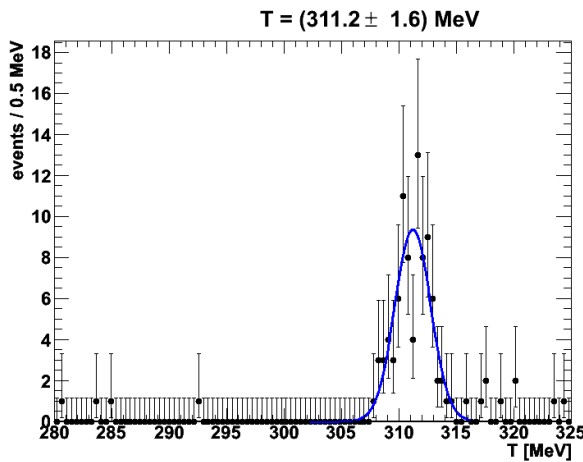
Fig. 5.11: Distribution of reconstructed energies for 300 MeV electrons traveling from the center of the detector in negative x-direction. The indicated value and error for T corresponds to the mean and the standard deviation of the fitted Gaussian. There are two outliers at 264 MeV and at 203 MeV which are not shown.
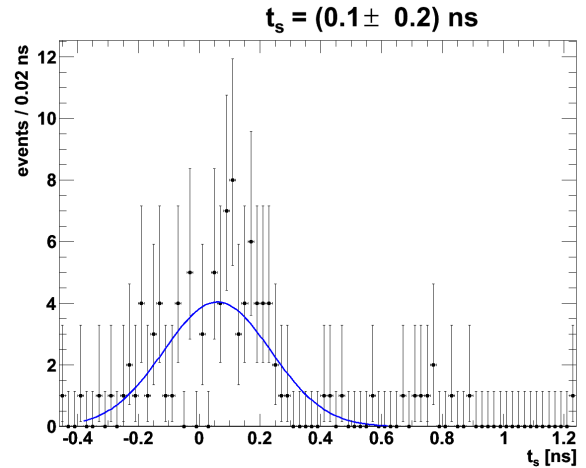
Fig. 5.12: Distribution of reconstructed electron start times for 300 MeV electrons traveling from the center of the detector in negative x-direction. The indicated value and error for t_s correspond to the mean and the standard deviation of the fitted Gaussian.

at an example first. To be able to compare the results for electrons and muons the parameters of the electron sample were chosen to match the parameters of the muon sample. It consists of 100 electrons with a kinetic energy of 300 MeV, traveling from the center of the detector along the negative x-axis. The binning used in the plots also corresponds to the binning used in Section 4.3.4.

92% of the fits converged which is in the same range as the convergence for muons tracks. The difference between the converged fits and the non converged fits, regarding the possibility to produce outliers in the distribution is not as striking as in the muon case, i.e. the not converged fits provide nearly the same information as the converged fits.

Figure 5.11 show the distribution of the reconstructed energies. It shows a prominent peak which is slightly shifted to higher energies, compared to the true value of the energy. While the peak is basically Gaussian leading to an energy resolution of (1.55 ± 0.12) MeV, the distribution features some outliers to lower energies. These outliers are due to inelastic interactions of bremsstrahlung radiation with carbon nucleii. The excited carbon nuclei can relax by emitting α-particles, protons or neutrons which are heavily quenched. Therefore, part of the energy of the bremsstrahlung photon is lost. These absorbed bremsstrahlung photons do also cause the systematic shift in the reconstructed energy, as they are also included in the $\left\langle \frac{dL}{dx} \right\rangle$-tables obtained from Geant4. Hence, the overall number of photons expected for a certain energy is shifted to lower values, which leads to a too high reconstructed energy for electron events without absorbed bremsstrahlung. This shift is significant for lower energies, while it basically does no play a role anymore for energies above 500 MeV.

The results for the start time t_s of the event are displayed in Figure 5.12. The true value for t_s is at the origin of the start time axis. Comparing the obtained distribution
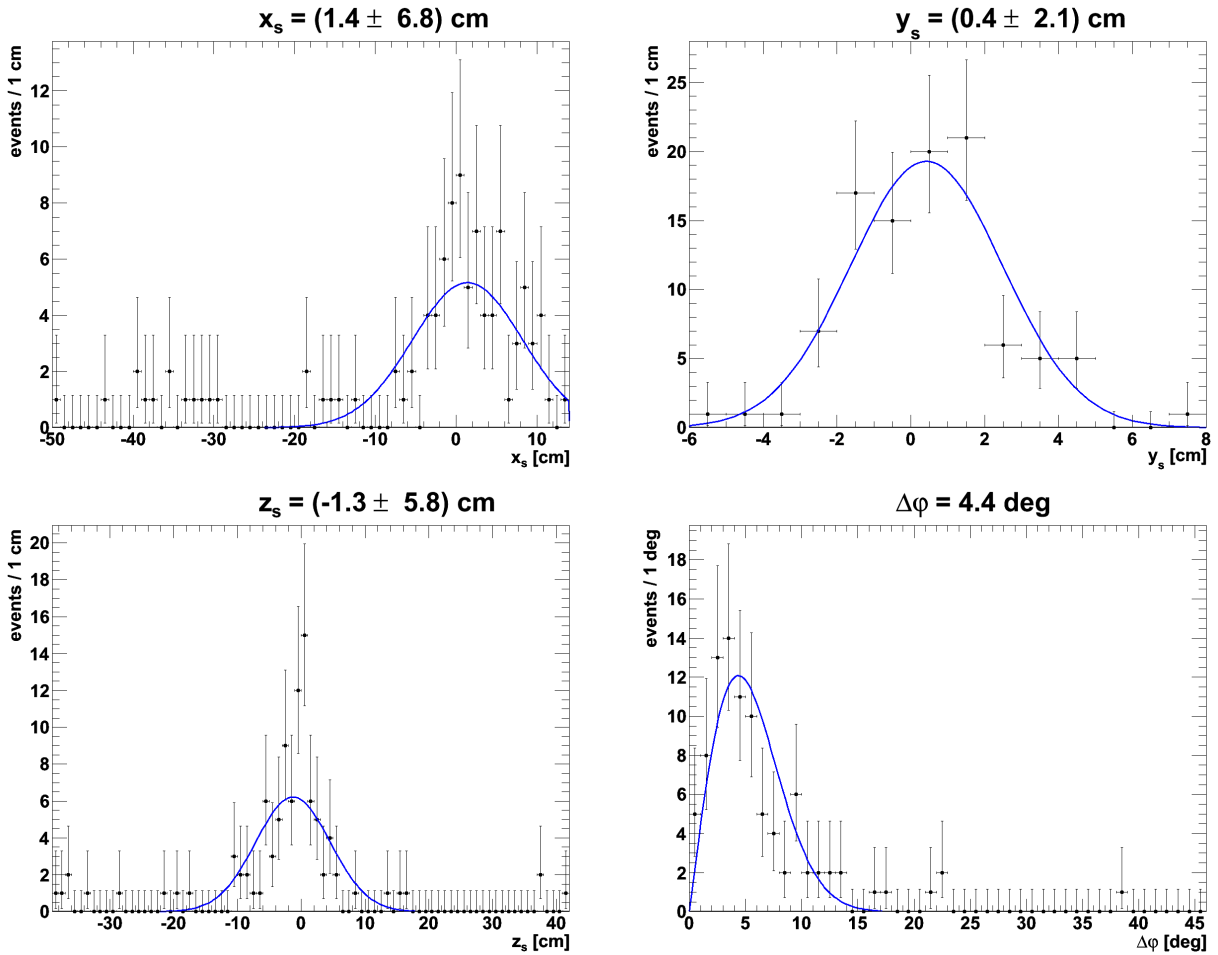
Fig. 5.13: Fit results for 300 MeV electrons traveling from the center of the detector in negative x-direction. The first three plots show the results for the start point coordinates. Guassian fits to the peaks lead to $x_s = (1.4 \pm 6.8)$ cm, $y_s = (0.4 \pm 2.1)$ cm and $z_s = (-1.3 \pm 5.8)$ cm. The lower right plot shows the angular deviations of the reconstructed form the true tracks. A fit using Equation (4.9) yields an angular resolution of 4.4 degrees.

with the corresponding distribution for muons featured in Figure 4.31, the spread of the electron results is significantly larger than the spread of the muon results. Thus, the electron start time resolution pared to the muon-track start time resolution. The obtained value of the Gaussian fit is about twice the value for muons and there additionally are a few outliers to higher start times. The higher uncertainty is due the the strong fluctuations in the energy loss of electrons. Nevertheless, the overall uncertainty is well below 1 ns and therefore should be sufficient for all possible applications in LENA.

The start point resolution is visualized in the first three histograms of Figure 5.13. As already observed for the start time of the event, the resolution for electrons is significantly worse than the corresponding resolution for muons, due to the high track by track fluctuations. This is reflected in the higher standard deviations, obtained by fitting a Gaussian to the distributions, as well as the much higher number of outliers obtained for electrons compared to muons. Furthermore, the resolution in track direction, i.e. the x_s-resolution in this case, and in z_s-direction is much poorer than the resolution in y_s-direction. The degradation in z_s-direction was also observed for muons and attributed to the small TOF changes, when the track is shifted in z-direction. In contrast, the relatively poor resolution in track direction was not observed for muons. It is caused by the high $\frac{dL}{dx}$-fluctuations of electron tracks, making a precise start point determination of the electrons challenging.

The lower right plot in Figure 5.13 finally shows the distribution of the angular difference between the obtained track and the reconstructed track. It is fitted with the PDF introduced in (4.9) and yields an angular resolution of 4.4 degrees. Note that the outliers are not included in the fit. Compared to the results obtained with muons, the angular resolution is worse, even though the difference between the electron angular resolution and the muon angular resolution is not as striking as in the case of the start point or start time resolution. The angular difference distribution also features some outliers, but not as much as e.g. the distribution of the track start point. Note that this sample of electrons does not contain one single track reconstructed with flipped direction even though eleven events were flipped after the initial fit. This shows that the algorithm presented in Section 5.3 works excellent at the energy given.

Turning to the dependency of the performance of the algorithm on the kinetic energy of the electron the ratio of converged fits versus the energy is plotted in Figure 5.14. In contrast to the muon-track fit, the convergence is fine over the whole energy range being constantly over 90%. The problem for higher energies observed for the muons therefore does not exist for the electrons. Even for lower energies the ratio of converged fits is still good. Nevertheless, fitting is not useful for energies smaller than 200 MeV as the reconstructed directions at these energies have only a small correlation with the true values of the track. The start point, the start time and the energy are still reconstructed at least partially reliably but this information can be gained with a much simpler and computationally more efficient point fit. The problem at these energies is that the longitudinal and the transverse extensions of the $\left\langle \frac{dL}{dx} \right\rangle$-distribution are comparable. Therefore, the assumption of an electron "track" breaks down, invalidating the used PDF.

Figure 5.15 shows the results of plotting the resolution as a function of true kinetic energy of the electron track. The same energy range as in the corresponding plots for muons is
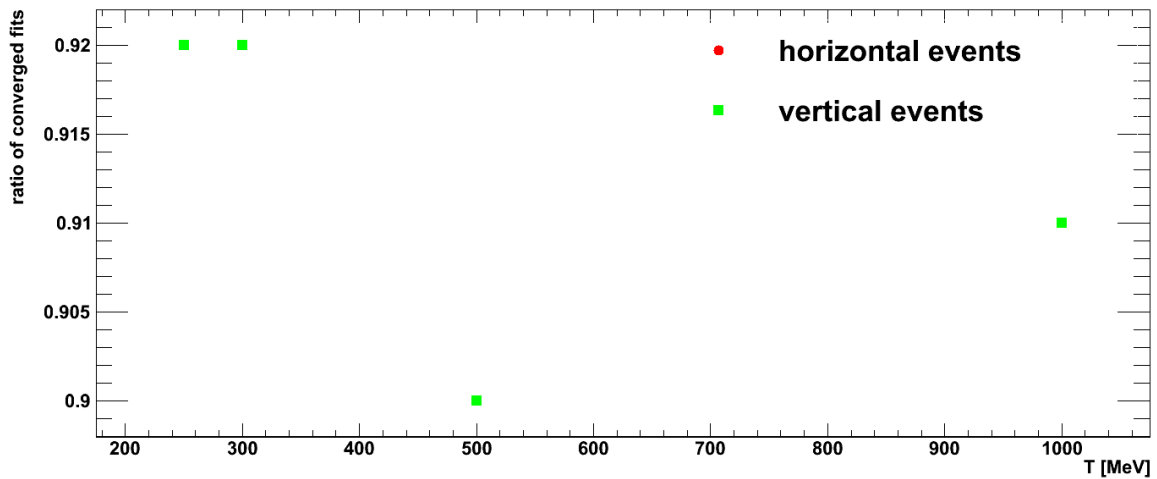
Fig. 5.14: Ratio of converged fits depending on the true kinetic energy of the electrons. In contrast to the muon-track fit, the convergence for electron fits is good over the whole energy range.
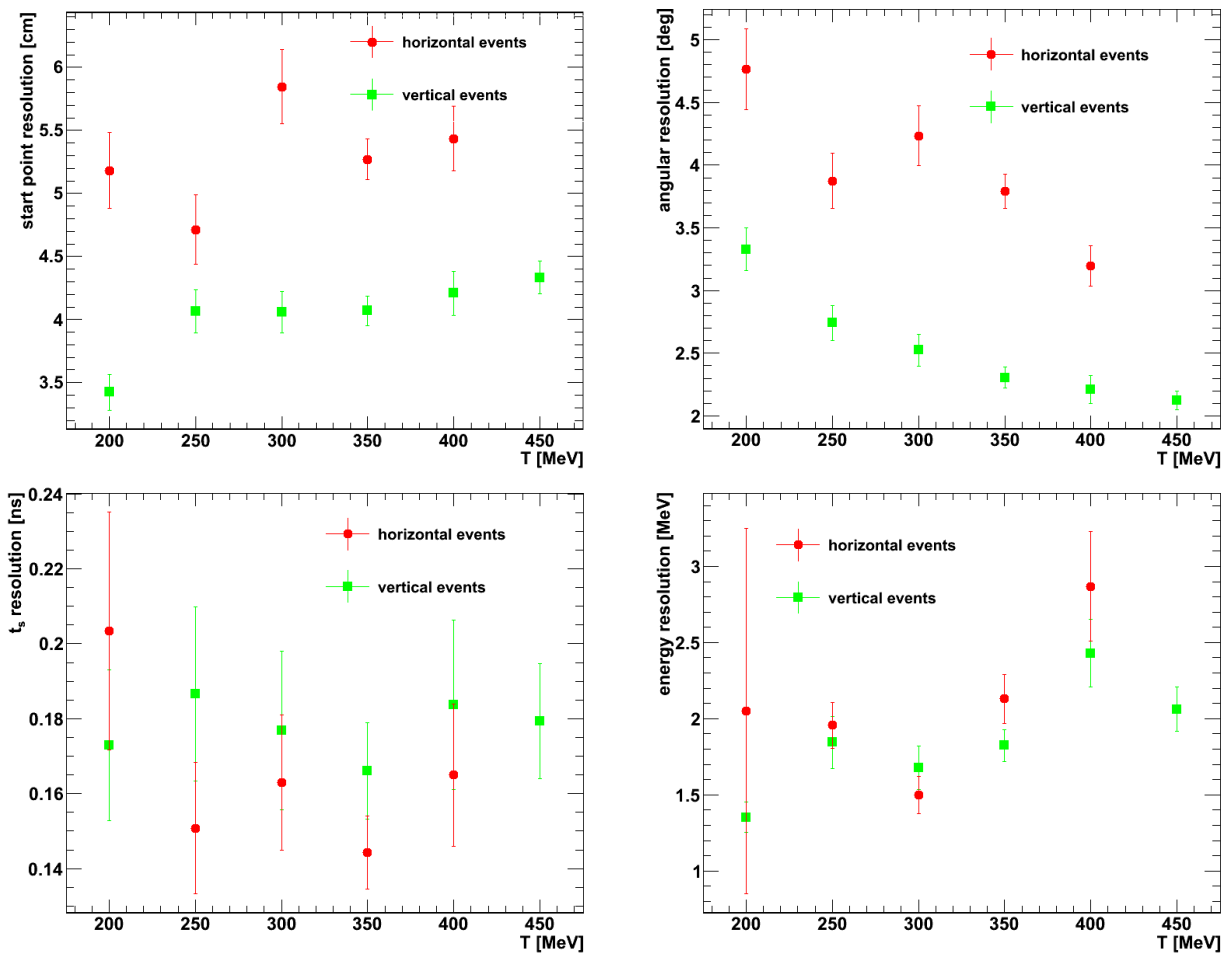
Fig. 5.15: Obtained start point resolution, angular resolution, t_s-resolution and energy resolution (from top left to lower right) depending on the true kinetic energy of the electrons. The vertical tracks feature a better start point as well as angular resolution while the horizontal tracks are slightly superior regarding the t_s-resolution.

used to allow a good comparison. The results obtained for strictly vertical and horizontal tracks are plotted separately.

The upper left plot in Figure 5.15 shows the start point resolution as a function of the kinetic energy of the electron. The start point resolution is basically constant over the whole energy range. As already observed for muon tracks, the start point resolution is better for vertical tracks compared to horizontal track. The effect is stronger for electrons though, as reconstructing the start point from the light emitted from back parts of the track is more challenging due to the high fluctuations.

The angular resolution plotted in the upper right plot of Figure 5.15 shows in principle the same behavior as observed for the muons: An improvement in resolution with increasing energy and a superior resolution for vertical events compared to horizontal events. The relative difference in resolution obtained for electron and muon tracks is smaller compared to the track start point. This indicates that the fluctuations in energy loss are stronger in longitudinal direction than in transverse direction.

The resolution obtained for the start time of the track plotted in the lower right corner of Figure 5.15 shows no significant changes with the energy of the electrons. Even though the obtained values are significantly poorer than the values obtained for muons the resolution should still be sufficient for all possible purposes.

Finally, the lower right plot shows the energy resolution obtained for electrons. Here the results for vertical and horizontal tracks are very similar. The obtained energy resolution is basically constant over the energy range with only small fluctuations. Note that the fluctuations of vertical and horizontal tracks are strongly correlated. This indicates that the energy resolutions could be influenced by the goodness of the respective $\left\langle \frac{dL}{dx} \right\rangle$-table and that an improvement might be possible case the $\left\langle \frac{dL}{dx} \right\rangle$-tables are redone with higher statistics.

Event though the requirements on computation time for track reconstruction will probably not be a limiting factor, it is interesting to note that the electron-track reconstruction, especially for lower energies, requires much more computation time than the muon-track reconstruction. This is due to the fact that the integration in (4.40) over the track has to be done numerically. Due to the bremsstrahlung tail of the electrons' $\left\langle \frac{dL}{dx} \right\rangle$-distribution, the integration range for electrons compared to muons is significantly increased which leads to longer computation times.

Summing up all the gathered observations the muon-track reconstruction outperforms the electron-track reconstruction in every aspect. The performance achieved for the electron-track fit is nevertheless astonishing regarding the additional challenges for electrons.

Chapter 6

LENA as a far detector for a β-beam

While Chapters 4 and 5 deal with the reconstruction of pure electron and muon tracks, this Chapter presents the final step towards a real neutrino event reconstruction by additionally taking the interaction vertex into account. This is accomplished in the framework of an assumed β-beam from CERN to Frejus providing a benchmark for the performance of LENA. The expected performance of a large water Cerenkov detector for the same β-beam has been published in [72].

Section 6.1 introduces the general concept of a β-beam and describes its primary properties. The different interaction types of beam neutrinos in LENA are presented in Section 6.2. To be able to fit these more complex events, the track fit has to be modified. This is detailed in Section 6.3, which also discusses the performance achieved by the fit algorithm, especially in the context of reconstructing the energy of the incident neutrino. Finally, Section 6.4 deals with a first estimation of the ϑ_{13} discovery potential using the $\overset{(-)}{\nu_e} \longrightarrow \overset{(-)}{\nu_\mu}$ appearance channels.

6.1   Fundamentals of β-beams

A β-beam was first proposed in 2002 by P. Zucchelli [74]. The basic idea is to create radioactive ions with a primary beam, accelerate them and store the accelerated ions in an elongated storage ring. The neutrinos produced in the decays on the straight sections form the neutrino beam. Due to high relativistic boost factors of the accelerated ions, the produced neutrinos are kinematically focused in forward direction. Compared to other beam types, the effectivity of the focusing is increased due to the low energies of the neutrinos ($\sim$MeV) in the rest frame of the ions. Apart from focusing, the boost also shifts the neutrino spectrum to higher energies.

This results in a beam with three unique features [74]:

- The beam contains only ν_e or $\bar{\nu}_e$ with virtually no contamination from other flavors.

- The spectrum as well as the intensity of the beam are well known.

- A good collimation is achieved for a low energy neutrino beam.

Whether the beam consists of electron neutrinos or electron anti-neutrinos is selected by using ions featuring either β^+ or a β^- decays. Typically, $^6_2\text{He}^{++}$ is proposed as parent ion for a $\bar{\nu}_e$-beam while $^{18}_{10}\text{Ne}^{10+}$ is favored for ν_e beams. The characteristic properties of the

parent nucleus	decay	decay time constant	endpoint of $e^{\pm}$ spectrum
$^{18}_{10}\text{Ne}$	$^{18}_{10}\text{Ne} \to {}^{18}_{9}\text{F} + e^{+} + \nu_e$	$\tau_{\text{Ne}} = 1.672\,\text{s}$	$E_{0,\text{Ne}} = 3.424\,\text{MeV}$
$^{6}_{2}\text{He}$	$^{6}_{2}\text{He} \to {}^{6}_{3}\text{Li} + e^{-} + \bar{\nu}_e$	$\tau_{\text{He}} = 0.807\,\text{s}$	$E_{0,\text{He}} = 3.507\,\text{MeV}$

Tab. 6.1: Characteristic quantities for the decay of $^{18}_{10}\text{Ne}$ and $^{6}_{2}\text{He}$. [87]
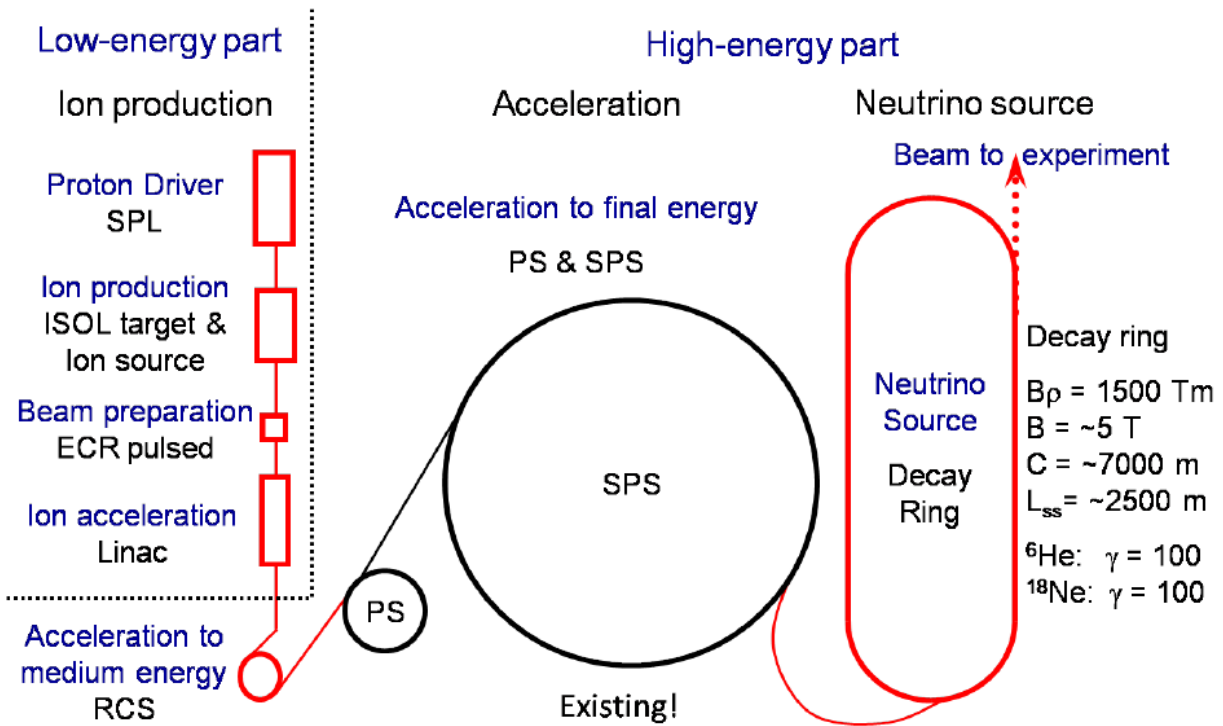
Fig. 6.1: Baseline concept for a β-beam at CERN [88]. The radioactive ions are produced by a primary proton beam and subsequently bunched and accelerated in various steps until they are fed into the decay ring. The parts shown in black are already existing facilities while the red parts would have to be built.

respective decays are shown in Table 6.1.

A possible baseline concept for a β-beam at CERN is shown in Figure 6.1. It features an ion production facility fed by an intense proton driver. Produced ions are bunched and accelerated in various steps. The final acceleration is planned to be accomplished by the existing CERN accelerators PS[1] and SPS[2]. To produce a neutrino beam, the accelerated ions are fed into a decay ring with two straight sections pointing towards the detector.

The possible neutrino energy in this baseline setup is determined by the capabilities of the SPS. Its power is sufficient to accelerate both proposed ions to a relativistic boost factor of about $\gamma = 100$ [88]. There is the idea [87] of running both ions at the same time but in different bunches. This would require to limit γ_{He} to about 60. Furthermore, there are ideas for a high-γ β-beam [87] with $\gamma \sim 10^3$ using the LHC[3] or some similar device to accelerate the ions. Such a high energy beam would allow to use the β-beam for extremely long baselines of the order of 10^3 km. As these approaches are hardly realizable, the baseline scenario of $\gamma_{He} = \gamma_{Ne} = \gamma = 100$ is used for the rest of this chapter.

With the principal parameters fixed, it is possible to calculate the expected differential $\overset{(-)}{\nu_e}$-flux at a far detector, which is given by the boosted neutrino spectrum of a $\beta^\pm$-decay. Neglecting the influence of the Fermi function of the daughter nucleus, the expected overall differential flux (neutrinos per unit area, time and energy interval) at a far detector with distance L to the beam source is given by [87]

$$\frac{d^3N}{dA\, dt\, dE_\nu} = \frac{1}{4\pi L^2} \frac{1}{m_e^5 f(m_e/E_0)} \frac{g}{\gamma(1-\beta\cos(\theta))} (E_0 - E_\nu^*) E_\nu^{*2} \sqrt{(E_0 - E_\nu^*)^2 - m_e^2} \qquad (6.1)$$

$$f(x) = \frac{1}{60x^5} \left\{ \sqrt{1-x^2}(2 - 9x^2 - 8x^4) + 15x^4 \log\left[\frac{x}{1-\sqrt{1-x^2}}\right] \right\}$$

$$E_\nu^* = \gamma E_\nu(1 - \beta\cos(\theta)),$$

with $\beta = \sqrt{1 - \gamma^{-2}}$, m_e being the rest mass of the electron, E_0 the end point energy of the electron spectrum, g the number of injected ions per unit time, θ the angle which the beam axis encloses with the connection between beem source and detector and E_ν the energy of the neutrinos. The resulting differential fluxes ($\gamma = 100, \theta = 0$) for ^{18}Ne and ^{6}He are plotted in Figure 6.2 as solid red line and blue dashed line, respectively. Note that both fluxes have been normalized to the same overall flux i.e. no value for the injection rate was assumed. The maxima of the spectra are in the range of 300 to 350 MeV.

To understand the physics potential of the β-beam, it is instructive to look at an approximative formula for the oscillation probabilities [12]

$$P(\overset{(-)}{\nu_e} \to \overset{(-)}{\nu_\mu}) = s_{23}^2 \sin^2(2\vartheta_{13}) \sin^2(\Delta_{13}) \qquad (6.2)$$

$$+ c_{23}^2 \sin^2(2\vartheta_{12}) \sin^2(\Delta_{12}) \qquad (6.3)$$

$$+ J \cos(\pm\delta - \Delta_{13}) \Delta_{12} \sin(\Delta_{13}) \qquad (6.4)$$

$$J = c_{13} \sin(2\vartheta_{12}) \sin(2\vartheta_{23}) \sin(2\vartheta_{13}),$$

where the upper sign is for neutrinos and the lower for antineutrinos. The remaining abbreviations are introduced in Section 1.2. The above equation is derived by expanding

---

[1]**P**roton **S**ynchrotron
[2]**S**uper **P**roton **S**ynchrotron
[3]**L**arge **H**ardron **C**ollider

the exact expression (1.8) in the small parameters ϑ_{13}, Δ_{12}/Δ_{13} and Δ_{12}. The last parameter is small as the energy and baseline of a β-beam are optimized to observe the first oscillation maximum in Δm_{13}^2. Additionally, the influence of matter effects is neglected, which is a good approximation for the short baselines and low energies of the discussed β-beam. For the corresponding equation including matter effects, see Equation (1.16).

Terms (6.2) and (6.4) are proportional to $\sin(2\vartheta_{13})$ to the second and first power, respectively. The remaining term (6.3) is proportional to Δ_{12} to the second power and is therefore negligible for higher energies, where $\Delta_{12} \rightarrow 0$. In this region, the observation of any signal above background therefore provides a clean indicator of $\vartheta_{13} \neq 0$.

The leading term (6.4) in ϑ_{13} has a prefactor of $\cos\left(\pm\delta - \frac{\pi}{2} \cdot \frac{\Delta m_{13}^2}{|\Delta m_{13}^2|}\right)$ at the first oscillation maximum of the Δm_{13}^2 driven oscillations. Hence, the discovery potential is strongly dependent on δ and on the sign of Δm_{13}^2, as long as only one chirality is observed. A change in sign of Δm_{13}^2 is equivalent to shifting δ by π. The discovery potential is minimal for $\cos\left(\pm\delta - \frac{\pi}{2} \cdot \frac{\Delta m_{13}^2}{|\Delta m_{13}^2|}\right) = 0$, i.e for $\delta = k\pi$, $k \in \mathbb{Z}$.

The full three-flavor oscillation probability[4] $\nu_e \rightarrow \nu_\mu$ is displayed in Figure 6.3 as a function of the neutrino energy for the CERN-Frejus baseline , including matter effects. The assumed values for the oscillation parameters are the best fit results from Table 1.1, with positive Δm_{13}^2 and $\delta = \pm\pi/2$ for the solid red and the dotted green curve, respectively. For comparison the blue dashed curve shows the transition probability for $\vartheta_{13} = 0$. It is basically zero for $E_\nu > 200\,\text{MeV}$ corresponding to the region where the middle term (6.3) disappears. Comparing the curves for positive and negative δ, the influence of δ on the discovery potential of ϑ_{13} is obvious.

Note that the sensitivity for a non-zero ϑ_{13} using the $\nu_e \rightarrow \nu_\mu$ appearance channel is mainly dependent on the capability of LENA to discriminate ν_μ induced events from ν_e induced events. The energy resolution is of minor importance as the oscillation maximum is rather broad.

6.2   Neutrino interactions in the β-beam energy range

To assess the capability of LENA as a far detector for a β-beam, the events resulting from neutrino interactions are generated in the Geant4-based Monte Carlo simulation already presented in Section 3.1. The final-state particles of the neutrino interactions are obtained[5] from the GENIE [93] neutrino event generator. This information is subsequently fed into the detector simulation.

The calculation of the overall cross section for neutrino interactions in LENA takes into account the neutrino cross sections on ^{12}C and on hydrogen. They are weighted according to their mass fractions. Hence, for PXE ($C_{16}H_{18}$ [40]), the cross section of carbon clearly dominates. The charged current (CC) cross sections for ν_e and ν_μ, divided by the neutrino energy, are shown in Figure 6.4 as a function of the neutrino energy. Additionally, the flavor-independent neutral current (NC) cross section is shown. All cross sections increase with energy, with the rise being faster than linear in the relevant energy region. As CC

---

[4]The oscillation probabilities are calculated using the GLoBES package [89, 90].

[5]The simulation of the neutrino interactions and the implementation of the results in the detector simulation was done by R. Möllenberg [94].
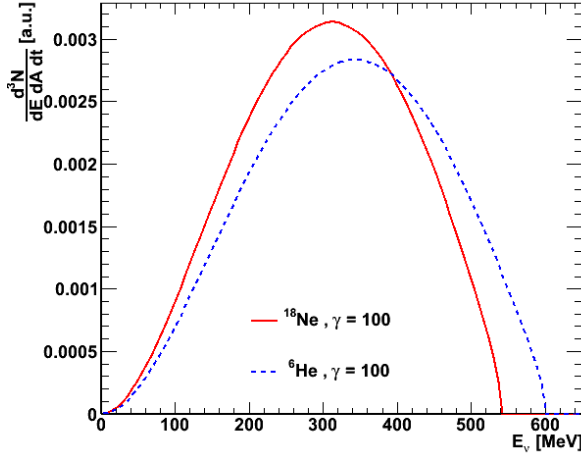
Fig. 6.2: Differential flux spectrum of the β-beam using ^{18}Ne and ^{6}He as parent ions and assuming an acceleration to $\gamma = 100$. Both differential fluxes are normalized to the same total flux.
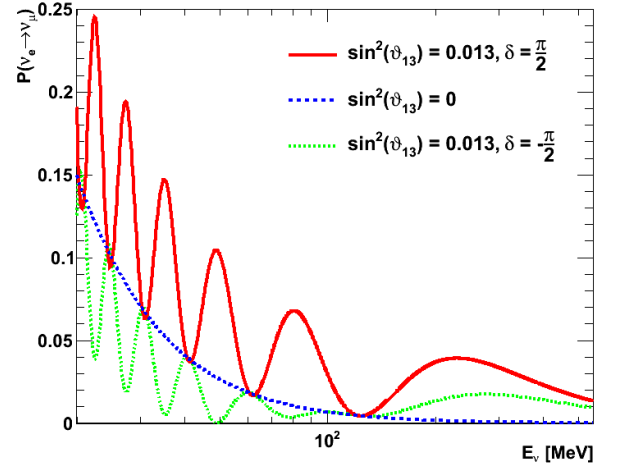
Fig. 6.3: Transition probability for ν_e to ν_μ oscillations for the CERN-Frejus baseline (130 km), including the influence of matter [89, 90, 91, 92]. The used values for ϑ_{12}, ϑ_{23} as well as the mass differences are taken from Table 1.1, the remaining parameters are indicated in the legend.
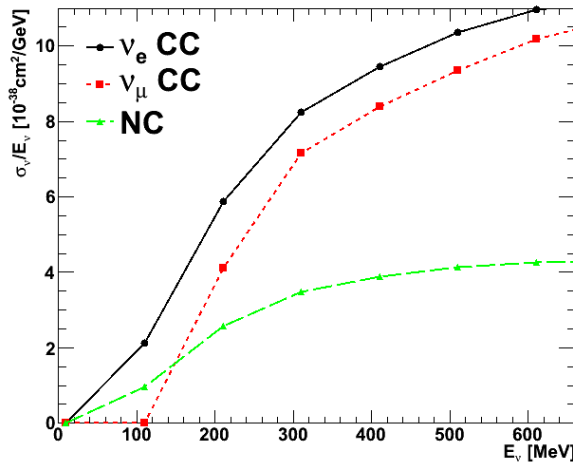
Fig. 6.4: Neutrino ^{12}C cross sections, divided by the neutrino energy, as a function of the neutrino energy, taken from GENIE [93]. The markers indicate calculated values.
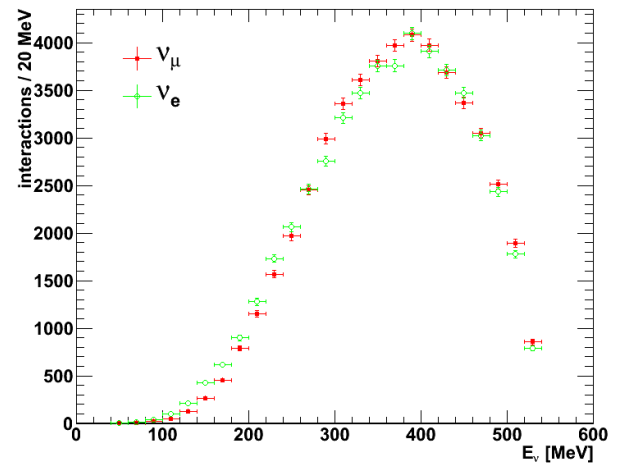
Fig. 6.5: Distribution of 50 000 ν_e and ν_μ interactions in LENA as a function of the neutrino energy. The underlying neutrino energy spectrum is the β-beam -spectrum (6.1), using the parameters of ^{18}Ne.
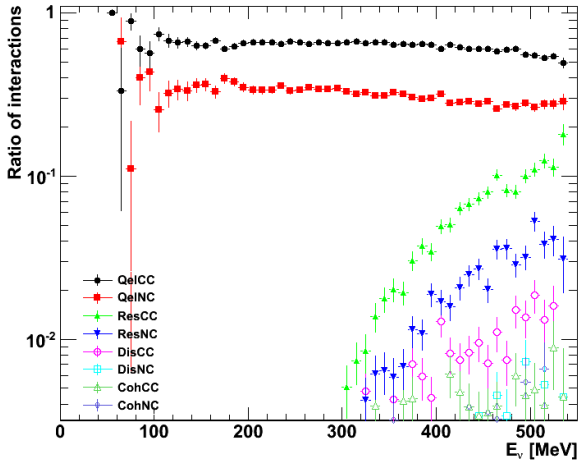
Fig. 6.6: Ratio of one specific interaction type with respect to the total number of interactions dependent on the energy of the incident neutrino. 50 000 simulated ν_e interactions using the ν_e flux shape of a ^{18}Ne based β-beam are included. The different interaction types are listed in the legend. Further explanations are given in the text.
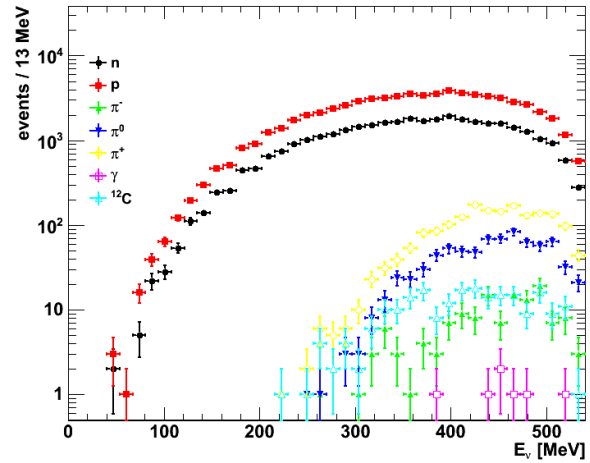
Fig. 6.7: Number of produced particles as a function of the energy. Shown are all non leptonic particles which were produced in 50 000 ν_e interactions from a ^{18}Ne based β-beam.

neutrino interactions always lead to the production of the associated charged lepton, the CC cross section for ν_e always surpasses the CC cross section for ν_μ due to the higher phase space available for electron final states. Furthermore, the kinematic production threshold for muons is about 200 times higher than the electron production threshold. The NC cross section is in the same order of magnitude as the CC cross section, leading to about one third of all β-beam events being NC interactions. NC interactions do not allow an identification of the neutrino flavor and constitute a background for the investigation of neutrino oscillations.

As the cross section increases with energy, the maximum interaction rate will be shifted to higher energies compared to the maximum of the neutrino spectrum. This can be confirmed by comparing the spectrum produced by a ^{18}Ne based β-beam (solid red line in Figure 6.2) with the distribution obtained for 50 000 ν_e (open green dots) and ν_μ (solid red dots) interactions shown in Figure 6.5. The spectral maximum is at about 300 MeV, while the maximum interaction rate is just below 400 MeV. The distributions for electron and muon neutrinos are quite similar. However, the electron neutrino spectrum features a slight shift to lower energies, as the relative difference between the ν_e and ν_μ cross sections is larger for smaller energies.

For the energy range of a β-beam there are four relevant types of neutrino interactions[95]:

- **Quasi-elastic scattering:**
  Quasi-elastic scattering (Qel) is the dominant process at β-beam neutrino energies. The neutrino energy is sufficient to resolve single nucleons in a nucleus but the substructure of the nucleons is not resolved. Therefore, the neutrino scatters elastically

on a quasi free nucleon. The CC Qel process reads

$$\nu_l + n \longrightarrow l^- + p^+ \tag{6.5}$$
$$\bar{\nu}_l + p^+ \longrightarrow l^+ + n. \tag{6.6}$$

The energy of the incident neutrino is therefore distributed among the lepton and the recoil nucleon. While the lepton can produce a track of significant length, the nucleon energy is too small to cause a significant deviation from a point-like energy distribution. The single lepton track can be fitted and its energy can be reconstructed. This event category is therefore perfectly suited to determine the oscillation parameters. Furthermore, Qel ν_μ events can be efficiently discriminated against NC interactions and ν_e induced interactions by the delayed muon decay electron.

Contrary, the corresponding NC interaction

$$\nu_l + x \longrightarrow \nu_l + x, \quad x \in \{p, n\}, \tag{6.7}$$

only features a recoil nucleon. The energy transfer is typically very small and the light output from the nucleon is strongly quenched. This allows to suppress NC events by an overall energy cut.

For carbon the interaction on the bound nucleons is influenced by nuclear properties: First, the target nucleon is not at rest due to the confinement to the nucleus. The mean momentum of a nucleon in ^{12}C is $227\,\mathrm{MeV}/c$ [96], of the same order of magnitude as the neutrino momentum. Thus, the effect on the momenta of the produced particles is quite severe. Furthermore, the products from the reaction are created inside the nucleus. Their interactions with other nucleons when leaving the nucleus have to be taken into account.

- **Resonant pion production:**
  Alternatively, a neutrino can scatter inelastically from a nucleon x, leaving the nucleon in an intermediate excited state x^*, typically $\Delta(1232)$. The decay to the ground state mostly occurs via the emission of a pion. The CC reaction

$$\overset{(-)}{\nu_l} + x \longrightarrow l + x^* \longrightarrow l + \pi + x', \quad x, x' \in \{p, n\}, \tag{6.8}$$

leads to the emission of three particles, a lepton, a pion and a recoil nucleon. At β-beam neutrino energies, both the lepton and the pion are able to produce extended tracks in the scintillator . Hence, reconstructing these events requires a specialized algorithm, fitting multiple tracks emerging from the interaction vertex at the same time. So far, this has been demonstrated in liquid scintillators only for multi GeV events [5]. The corresponding NC reaction

$$\overset{(-)}{\nu_l} + x \longrightarrow \overset{(-)}{\nu_l} + x^* \longrightarrow \overset{(-)}{\nu_l} + x' + \pi, \quad x, x' \in \{p, n\}, \tag{6.9}$$

results in only one particle which can probably be tracked.

The pions produced in these interactions cause a background for the flavor identification. A ν_μ can create a π^0 which decays into two γ-rays producing electromagnetic cascades. Therefore, it can be misidentified as an ν_e. Additionally, a ν_e producing a $\pi^\pm$ can be misidentified as a ν_μ because the $\pi^\pm$ predominantly decays to a $\mu^\pm$ with

$\tau = 26\,\mathrm{ns}$. For the given energies, $\pi^{\pm}$ typically decay at rest, which makes the decay difficult to tag: The signal of the low-energy π-decay muon (T=4.1 MeV) will vanish in the afterglow of the primary event.

- **Coherent pion production:**
  Instead of interacting with a single nucleon, the neutrino can interact with the whole nucleus A. This can also lead to pion production:

$$\overset{(-)}{\nu_l} + A \longrightarrow l + A + \pi^{\pm} \text{ (CC)}, \quad \text{and} \quad \overset{(-)}{\nu_l} + A \longrightarrow \overset{(-)}{\nu_l} + A + \pi^0 \text{ (NC)}, \qquad (6.10)$$

  albeit with different kinematics compared to the resonant pion production, as the energy transferred to the nucleus is typically very small.

- **Deep inelastic scattering:**
  Especially for neutrinos with higher energies, there is a non-negligible probability that the constituents of the nucleon are resolved and the neutrino interacts with a single quasi-free quark, destroying the nucleon. The subsequent hadronization leads to the emission of several mesons. Hence, this interaction type also results in pion production, hampering the electron-muon discrimination.

The ratios of the different ν_e interaction types with respect to the total number of interactions are shown in Figure 6.6 as a function of the neutrino energy. Each interaction type is split up into its CC and NC subparts. For neutrino energies below 300 MeV, all interactions are quasi-elastic scatterings. With increasing energy, the other interaction processes start to contribute, with the main contribution from CC resonant pion production.

The non-leptonic particles produced by 50 000 ν_e interactions are displayed in Figure 6.7 as a function of the incident neutrino energy. The underlying neutrino spectrum corresponds to a ^{18}Ne β-beam (confer Equation 6.1). While recoil nucleons dominate the distribution, there is also a non negligible contribution from π^+. It reaches percent level at neutrino energies exceeding 200 MeV. As CC resonant pion production, which is the dominant non-Qel interaction channel, always produces π^+ in ν_e interactions, the number of π^+ produced in a ν_e-β-beam exceeds the number of π^-. For an $\bar{\nu}_e$-β-beam , the rates of π^+ and π^- have to be exchanged. Table 6.2 summarizes the number of obtained pions in 50 000 simulated ν_e interactions for the ^{18}Ne and ^{6}He β-beam, respectively.

Note that the neutrino energies of a β-beam are on the lower end of the energy range covered by the GENIE event generator. While the cross section for CC Qel scattering is known quite precisely, the errors for the other event types are significantly larger [95]. Especially for NC events there is hardly any experimental data below 1 GeV. Therefore, the correct theoretical model is hard to determine. Furthermore, nuclear effects are non-negligible, and the nuclear models used for event generation are not yet consistent. Hence, the systematic error of the obtained distributions might be substantial. However, the simulated events form a sound basis to study the performance of the LENA detector.

6.3   Reconstruction of β-beam events

As already stated in Section 6.1, the sensitivity of the β-beam on ϑ_{13} depends mainly on the $\overset{(-)}{\nu_e} \longrightarrow \overset{(-)}{\nu_\mu}$ appearance channel. To exploit the information provided by this channel,

γ	mother nucleus	π^+	π^+ (NC)	π^-	π^- (NC)	overall percentage
100	^{18}Ne	1756	94	133	99	$(3.77 \pm 0.09)\%$
100	^{6}He	229	154	1647	226	$(3.75 \pm 0.09)\%$

Tab. 6.2: Overall number of resulting charged pions for the neutrino and the antineutrino beam configuration for 50 000 simulated interactions. The first two columns characterize the underlying beam, while the rest of the columns gives the numbers of obtained charged pions as well as the overall percentage that a pion is produced in an individual interaction. The given errors take into account statistics only.
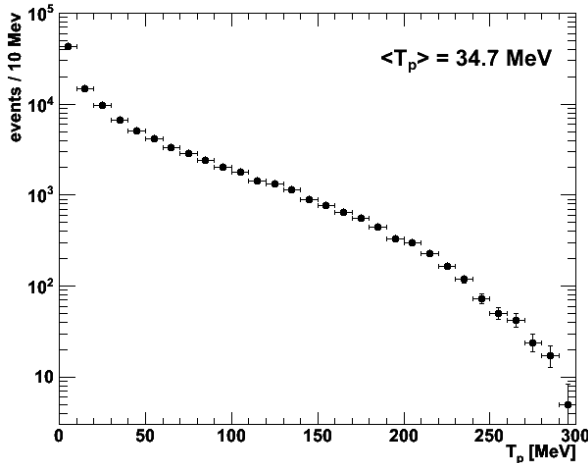
Fig. 6.8: Distribution of the kinetic energies of recoil nucleons for ν_μ CC Qel interactions. The plot shows the results from 50 000 ν_μ interactions. The mean kinetic recoil energy of the nucleon is $\langle T_p \rangle = 34.7$ MeV.
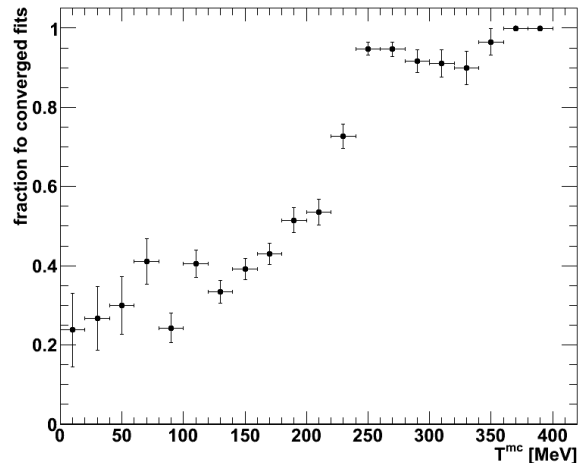
Fig. 6.9: Fraction of converged fits as a function of the true kinetic muon energy for 2716 simulated events featuring a muon decay.

the corresponding $\overset{(-)}{\nu_\mu}$-events have to be reconstructed. This is achieved with a specialized version of the muon-track fit, which is detailed in Section 6.3.1 for ν_μ interactions. The $\bar{\nu}_\mu$ performance has yet to be evaluated. To compare the expected with the measured neutrino spectrum, the neutrino energy has to be calculated from the reconstructed events (see Section 6.3.2).

6.3.1 Application of track fitting to β-beam events

The current version of the reconstruction is able to deal with CC Qel ν_μ events. More complex events with more than one visible track have yet to be implemented.

The CC Qel ν_μ interaction is

$$\nu_\mu + n \longrightarrow \mu^- + p. \tag{6.11}$$

Due to its high mass, the proton has a very high energy deposit per unit path length in the energy range of the β-beam. This has two consequences: First, according to Birk's formula (1.19), the number of photons created by the protons is heavily quenched. Second, the track length of the proton is very short. The spectrum of the kinetic energies of the recoil nucleons is displayed in Figure 6.8. The mean recoil kinetic energy of the produced

protons is 34.7 MeV, corresponding to a track length of the order of a millimeter [82].
Even for proton recoil energies of 300 MeV, the track length is of the order of 50 cm and
therefore still very hard to fit. Hence, the energy deposition of the proton is approximated
as point-like. Note that also neutrons can be produced at the vertex due to internuclear
scattering. While neutrons basically feature a longer range than protons, it is typically still
below the spatial resolution of LENA and can therefore also be approximated as point like.

Based on these observations, the Qel events are modeled as muon tracks with an ad-
ditional point-like energy deposition at the track start point $\boldsymbol{x}_s$. Hence, the number
of photons originating from the vertex n_γ^s is introduced as additional fit parameter, i.e.
$\boldsymbol{X} = (\boldsymbol{x}_s, t_s, \vartheta, \varphi, T, n_\gamma^s)$. Here, the number of photons is used instead of the nucleon
kinetic energy as a direct correlation between the two is difficult to obtain because of nu-
clear effects: If the recoil proton scatters off other nucleons (inside the nucleus) its energy
can be transferred partly to other nucleons or even the total nucleus. As the energy loss
of protons, neutrons and whole nuclei is different, the effective quenching factor depends
on the distribution of the recoil energy on the emitted particles. Hence, the correlation of
the total deposited energy with the number of emitted photons strongly depends on the
exact event configuration, which is not known ab initio.

The model of one single track with a point-like vertex can be described by the same prob-
ability density function (PDF) used to reconstruct single muons (cf. Equation (4.40)),
replacing the number of photons per unit path length $\left\langle \frac{dL}{dx} \right\rangle (s)$ by

$$\left\langle \frac{dL}{dx} \right\rangle' (s) = \left\langle \frac{dL}{dx} \right\rangle (s) + n_\gamma^s \cdot \delta(s), \qquad (6.12)$$

where $\delta(s)$ is the delta distribution. $\left\langle \frac{dL}{dx} \right\rangle$ and s are introduced in Sections 4.3.2 and 4.2.3.

To test the fit, 6100 ν_μ interactions at the center of LENA are simulated. To select
CC events, the fit is only applied to events with an identified muon decay. As the muon-
track fit requires a muon kinetic energy of at least 200 MeV for a proper result, events
with an estimated lepton energy of less than 150 MeV are discarded to save computation
time. After these initial cuts, 2716 events remain. From these events, 1448 are success-
fully fitted, corresponding to about 53%. As the above cuts do not discriminate against
pions, some fitted tracks might no be muon but pion tracks.

Figure 6.9 shows the fraction of converged fits as a function of the true kinetic en-
ergy. Comparing the obtained convergence for the β-beam and the single muons tracks
(cf. Figure 4.33) both reconstructions perform quite similarly.

The obtained deviations of the reconstructed from the true start points, d, are histogramed
in Figure 6.10. The mean deviation is $\langle d \rangle = (6.89 \pm 0.2)$ cm. Hence, the obtained start
point resolution is sufficient for all practical purposes.

More important from a physics point of view, is the resolution of the start time of the
event. It allows to associate the event to a specific bunch of the accelerator which is
crucial to discriminate β-beam-events from atmospheric neutrinos. Figure 6.11 features
the results obtained for the start time of the event, the true value[6] being $t_s^{mc} = 0$. As the
obtained distribution is non-Gaussian, the standard deviation $\Delta t_s = (0.279 \pm 0.005)$ ns

---

[6]For the rest of this chapter, all true values saved from the Monte Carlo are marked by the superscript
"mc".

is used to describe the start time resolution. As this is lower than the time spread of bunches running in a β-beam decay ring, which is in the range of 1 to 10 ns [97], it will not deteriorate the background discrimination capabilities.

The distribution of the angular deviations obtained for the reconstructed tracks as compared to the true tracks is shown on the left of Figure 6.12 as a function of the true kinetic energy of the muon. While there is hardly any correlation between reconstructed and true track direction for kinetic energies below 100 MeV, there is a good match for higher muon energies. This is quantified on the right of Figure 6.12 which shows the obtained angular resolution as a function of the true kinetic energy of the muon. The displayed values are created by binning the obtained values in lepton energy bins of 50 MeV. The resulting distributions are subsequently fitted with Equation (4.9) to obtain the angular resolutions for the individual bins. In contrast to the problem with the start point, the fit for the angular deviations works very well. For energies above 250 MeV, the performance of the single muon-track fit is nearly reached.

Finally, Figure 6.13 shows the performance of the energy reconstruction. The left figure shows the correlation between the true and the reconstructed kinetic energy of the track, while the kinetic energy resolution as a function of the true kinetic energy of the track is visualized in the right figure. The obtained values are one order of magnitude worse than the values obtained for single tracks (cf. Figure 4.34), as the introduction of n_γ^s as fit parameter decouples the overall number of detected photons from the kinetic energy of the track. Hence, the latter is mainly determined by the reconstructed track length, which is very difficult to determine at lower energies due to the superposition of the signal from the track and the vertex. At higher energies the energy resolution is limited by the range straggling of the muon, i.e. the event-by-event fluctuations of the track length. To determine the extent of this effect the β-beam track fit is applied on single track events with a kinetic energy of 350 MeV, leading to an energy resolution of about 14 MeV. In the latter case, the energy resolution can be improved by including the photon count at the vertex into the calculation of the muon-track energy, i.e. $T \rightarrow T + n_\gamma^s \cdot \epsilon_L$. Hence, the energy resolution obtained for the muon β-beam track fit is basically at the maximum possible value for kinetic energies above 300 MeV.

The results for n_γ^s are not shown, as currently the true number of photons emitted by the nucleons is not saved from the Monte Carlo. Therefore, no resolution for this parameter can be provided.

As a benchmark, the obtained resolutions are compared to the resolutions obtained in the Super Kamiokande experiment for sub GeV one ring events, i.e. events with only the muon being over threshold. The stated vertex resolution[7] is 22.1 cm with an angular resolution of 1.7 degrees and an energy resolution of approximately 2%. The vertex resolution in LENA is superior compared to Super Kamiokande due to the much better photon statistics in LENA. In contrast, the angular resolution in Super Kamiokande surpasses the angular resolution in LENA as in a water Cherenkov detector the spatial distribution of the detected photons allows an excellent direction reconstruction even for lower energies. Studies indicate however [5], that the angular resolutions are comparable for energies exceeding 1 GeV. Finally, the resolution for the track energy is again superior for the Super Kamiokande experiment, as in water Cherenkov detectors the overall

---

[7]In [98] a different definition for the vertex and angular resolution is used. The stated values have been transformed to the convention used in this thesis assuming the underlying distributions to be Gaussian.
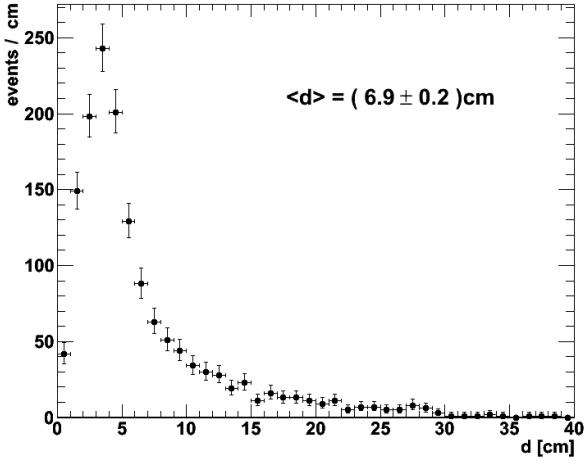
Fig. 6.10: Distance d between the reconstructed start point and its true value from 1448 successfully reconstructed β-beam-events with tagged muon. The mean deviation from the true value is $\langle d \rangle = (6.9 \pm 0.2)\,$cm.
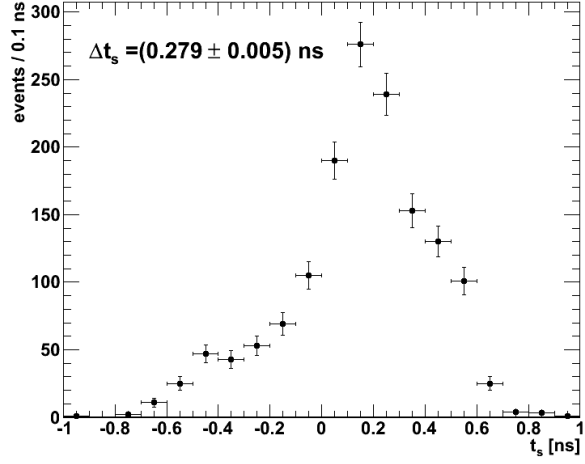
Fig. 6.11: Reconstructed start times t_s for 1448 successfully reconstructed β-beam-events with tagged muon. The obtained standard deviation is $\Delta t_s = (0.279 \pm 0.005)\,$ns.
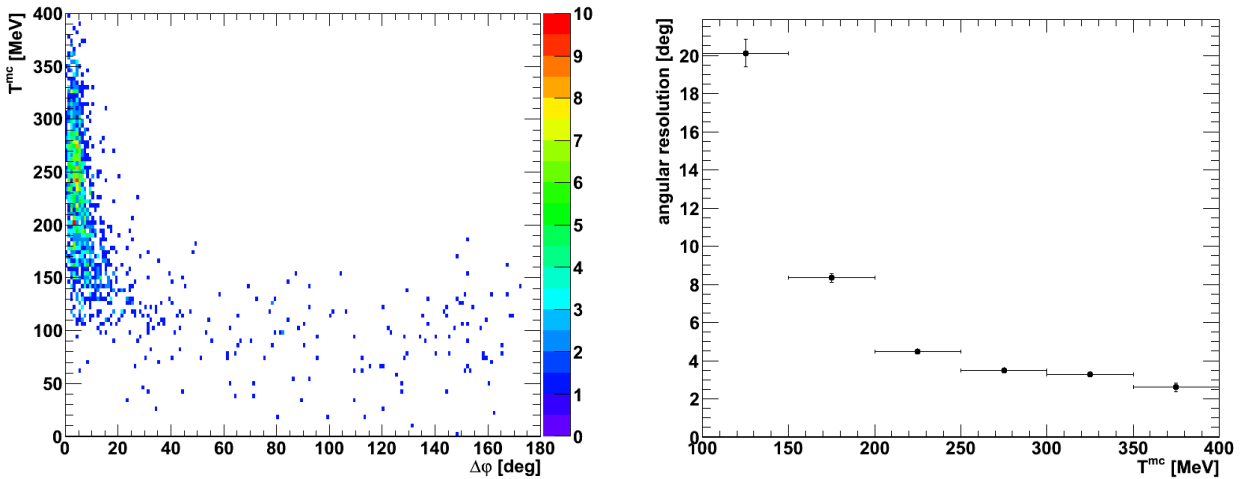
Fig. 6.12: Angular deviation $\Delta\varphi$ between fitted track and true track versus the true kinetic energy T^{mc} for 1448 successfully reconstructed β-beam events with tagged muon. The left plot shows the distribution of the obtained angular deviations $\Delta\varphi$ as a function of the true kinetic track energy T^{mc} while the right plot shows the obtained angular resolution as function of T^{mc}.

charge can be used to determine the track energy as other produced particles are below threshold, while in a liquid scintillator detector the kinetic energy of the particle has to be determined using the track length. While the absence of other visible tracks is a benefit for the reconstruction of the kinetic energy of the muon, it deteriorates the neutrino energy resolution (see Sections 6.3.2 and 6.4).

Taking all the results together, the developed track fit allows a solid reconstruction of β-beam events in case the final state lepton energy is at least 200 MeV.
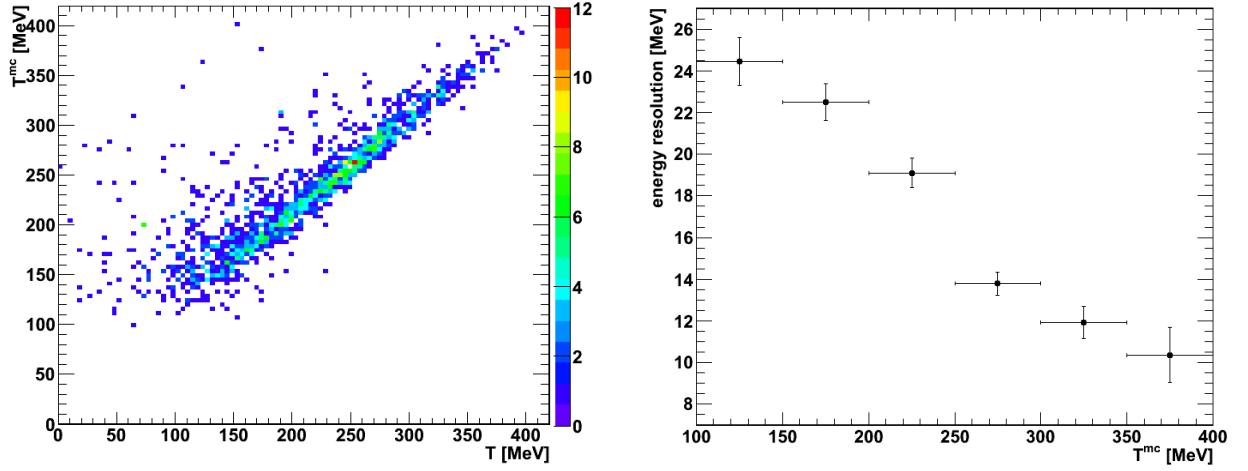
Fig. 6.13: Performance of the reconstruction of the kinetic energy for 1448 successfully reconstructed β-beam events with tagged muon. The left plot shows the correlation between the reconstructed (T) and the true (T^{mc}) kinetic energy. The obtained kinetic energy resolution as a function of the true kinetic energy is shown on the right.
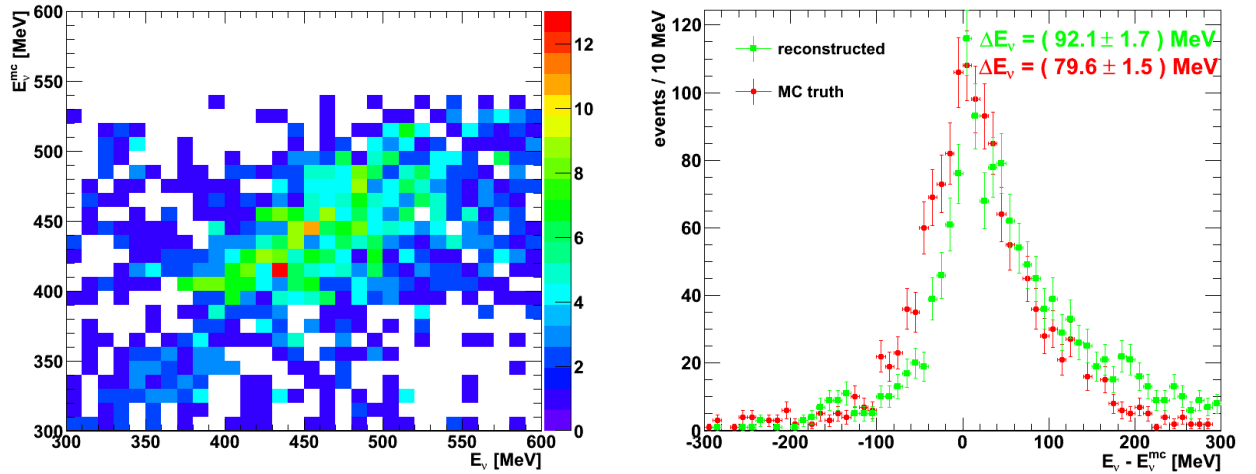
Fig. 6.14: Performance of the neutrino energy reconstruction for 1448 successfully reconstructed β-beam events with tagged muon. On the left the distribution of the reconstructed neutrino energy E_ν versus the true neutrino energy E_ν^{mc} is shown, while the difference between the reconstructed neutrino energy and the true neutrino energy is histogramed on the right. The distribution drawn with green boxes uses the results of the reconstruction algorithm as input, while the red dotted distribution uses the true values for E and $\vartheta_{\mathrm{scat}}$ as input. The obtained standard deviations are $(90.5 \pm 1.7)\,\mathrm{MeV}$ and $(75.3 \pm 1.4)\,\mathrm{MeV}$, respectively.

6.3.2   Reconstructing the neutrino energy

To obtain the oscillation parameters from the measured β-beam neutrino events, the energy spectrum of the neutrinos has to be reconstructed.

As the direction of the incoming neutrino is known in a beam experiment, two important kinematic scattering quantities can be gained from the reconstruction of the event: The energy E of the produced muon and the scattering angle ϑ_{scat}. To fix the scattering geometry, the target neutron is assumed to be at rest. Hence, the neutrino energy is given by [5]

$$E_\nu = \frac{2(m_n - E_B)E - E_B^2 + 2m_nE_b - m_\mu^2 + m_n^2 - m_p^2}{2[(m_n - E_b) - E + p_\mu \cos(\vartheta_{\text{scat}})]}, \tag{6.13}$$

where m_n, m_p and m_μ are the rest masses of the neutron, proton and muon, respectively, E_B is the binding energy of the target nucleon in the nucleus and p_μ is the momentum of the muon. As the binding energy is dependent on the energy level of the hit nucleon, a mean value of 25 MeV was chosen. The results obtained using 1448 reconstructed μ_ν interactions is displayed in Figure 6.14. On the left, the two dimensional distribution of the reconstructed neutrino energy E_ν versus the true neutrino energy E_ν^{mc} is shown. It already indicates that the correlation is only weak i.e, that the error for the neutrino energy is significantly higher than the error of the reconstructed muon energy. This is quantified on the right of Figure 6.14 where the difference between the true and the reconstructed neutrino energy is plotted. The green boxed curve uses the results obtained with the reconstruction as input parameters. Its spread is about 90 MeV, exceeding the lepton energy resolution by a factor of five to ten.

This rather high error has two components: First, the error induced due to deviations of the reconstructed scattering angle and muon energy from the true values. Second, to derive Equation 6.13 the target neutron was assumed to be at rest. This is only true for hypothetical free neutrons, but not for neutrons bound in a nucleus which have a rather high average momentum due to the Fermi motion (cf. Section 6.2). To disentangle the two effects, the neutrino energy of the successfully reconstructed events was reconstructed using the true values for the muon momentum and direction i.e. without the error induced by the reconstruction. The resulting distribution is displayed on the right of Figure 6.14 as red dots, leading to a standard deviation of about 80 MeV. Therefore, the larger part of the error of the reconstructed neutrino energy is due to nuclear effects and the reconstruction is close to the optimum.

Up to now, the analysis includes only information from the track. The overall quality of the reconstruction can be improved by taking also the energy deposited at the vertex into account. The most straight-forward possibility is to utilize the total number of detected photons, corresponding to a calorimetric measurement of the deposited energy. To transform the overall charge into a deposited energy T, the algorithm to estimate the kinetic energy of a track (cf. Section 4.2.1) is used. Hence, the estimated neutrino energy is[8] $T + m_\mu$.

Figure 6.15 shows the obtained results. The left panel shows the obtained correlation between the reconstructed and the true neutrino energy, which is significantly improved compared to the results from the track fit (see Figure 6.14). The plot also shows that the

---

[8]To be totally exact the mass difference between the neutron and the proton as well as the binding energy in the nucleus would also have to be added.
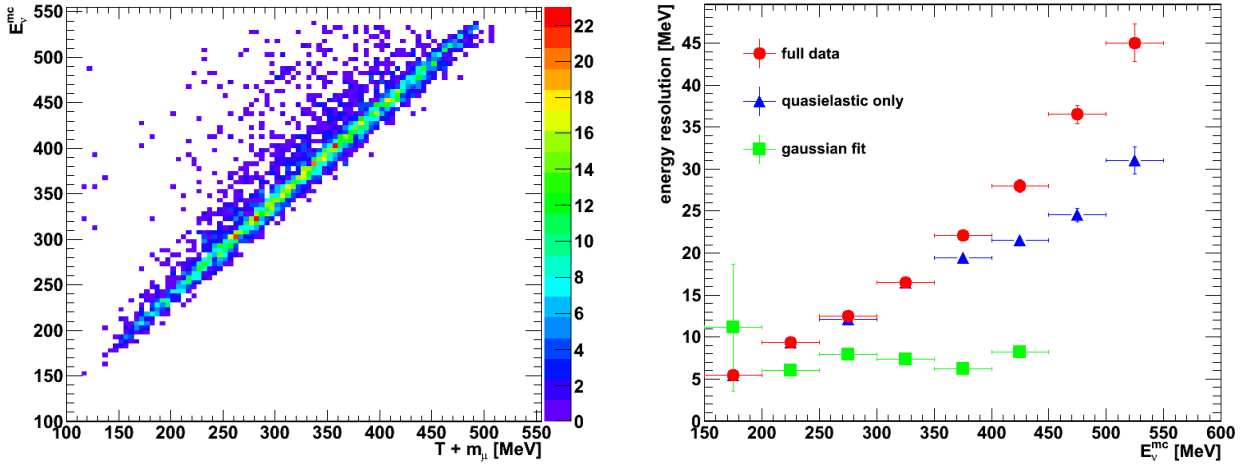
Fig. 6.15: Performance of the neutrino energy reconstruction for 3486 β-beam events with tagged muon. On the left the distribution of the estimated neutrino energy versus the true neutrino energy is shown, while the obtained energy resolution as a function of the true neutrino energy is shown on the right. The red points show the standard deviation the whole data in the respective energy bin while the green boxes indicate the standard deviations obtained by fitting a Gaussian to the peak i.e. neglecting the outliers. Additionally, the standard deviation taking only quasi-elastic events into account is shown (blue triangles).

mean estimated energy $t + m_\mu$ is below the true neutrino energy E_ν^{mc}, which is caused by light losses due to the quenched light output of the recoil nucleon. Furthermore, at higher neutrino energies, the distribution gets a tail of events featuring an estimated energy being significantly too small. The most significant outliers at higher neutrino energies are produced by events, with more than one produced particle, e.g. resonant pion production events, as the rest energy of the additional particles is not taken into account. These events can be basically discriminated by requiring exactly one muon decay, not at least one muon decay as done in Figure 6.14. Furthermore, outliers can be produced if a significant amount of the neutrino energy is transferred to the recoil nucleon. As recoil nucleons are strongly quenched, a part of the energy transferred to the nucleon is lost resulting in a reconstructed energy which is too low.

The obtained resolution in neutrino energy (neglecting the systematic shift) is shown on the right of Figure 6.15 as a function of the true neutrino energy. It is determined by calculating the standard deviation of the whole data in each energy bin (red dots) and by fitting a Gaussian to the peak of the distribution (green boxes), i.e. neglecting the outliers. To quantify the influence of events with more than one produced particle, the resolution obtained from quasi-elastic events only is additionally shown (blue triangles). The obtained resolutions are at least a factor of two better than the energy resolutions achieved using the event reconstruction relying on the scattering angle and nearly a factor two better than the theoretical optimum obtained using the Monte Carlo truth. The difference is even more striking looking at the errors obtained for the Gaussian fits. Moreover, there is still some room to improve the performance: A possible ansatz would be to combine the results from the track fitting with the energy estimation to tackle the outliers at low reconstructed energies.

For a comparison of the obtained neutrino energy resolutions for a water Cerenkov detector and the LENA detector, see the next section.

neutrino flavor	parent ion	usable decays per year	running time
ν_e	$^{18}_{10}$Ne	$2.2 \cdot 10^{18}$	4 a
$\bar{\nu}_e$	$^{6}_{2}$He	$5.8 \cdot 10^{18}$	4 a

Tab. 6.3: Quantities assumed for the β-beam.
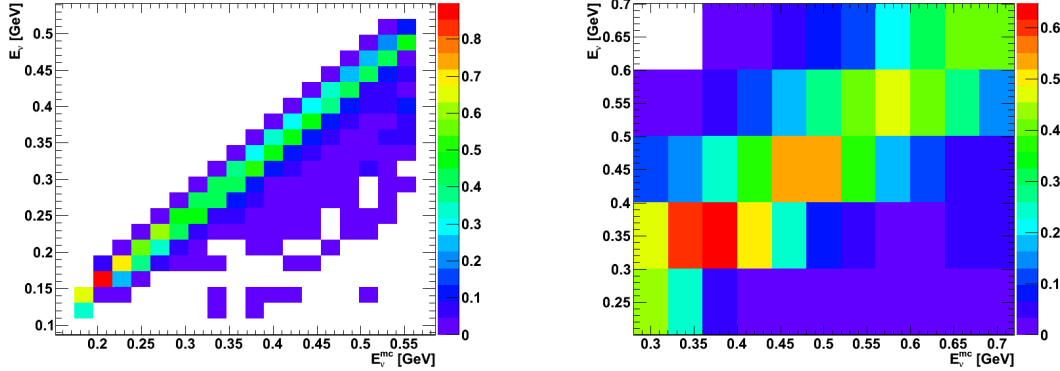
Fig. 6.16: Energy migration matrices for LENA (left) and MEMPHYS [72] (right). They show the probability $P(E_\nu | E_\nu^{\mathrm{mc}})$ that an event with true neutrino energy E_ν^{mc} is reconstructed with the energy E_ν.

6.4 Determination of the ϑ_{13} discovery potential

Based on the stated performance of the β-beam event reconstruction, it is possible to determine the physics reach of a neutrino beam from CERN to Frejus, using LENA as a far detector. This analysis was already done for MEMPHYS[9], a large water Cherenkov detector proposed for the Frejus site [72], providing a benchmark for the performance of LENA. As a test parameter, the ϑ_{13} discovery potential is chosen.

Calculations are based on the GLoBES[10] [89, 90] software package. GLoBES needs several input parameters to define an experiment.

The basic idea is to run the β-beam both in neutrino and in antineutrino mode. The used ions are ^{18}Ne and ^{6}He, respectively. Their properties are given in Table 6.1. Additionally, the number of usable decays per year $\dot{N}$ and the running time have to be fixed. The used values are taken from [72] to allow for a fair comparison. They are summarized in Table 6.3.

The baseline is fixed to 130 km by the distance between CERN and Frejus. As the neutrinos travel through the earth, matter effects principally have to be taken into account. The matter density of the earth in between CERN and FREJUS is approximated by the mean density taken from the onion shell model of the earth [91, 92], which is already implemented in GLoBES. However, due to the small neutrino energies and the short baseline, matter effects are basically negligible.

For the LENA detector a fiducial mass of 50 kt is assumed. This is, of course, over-

---

[9]Some of the parameters mentioned in this section are not identical to the parameters mentioned in [72]. They coincide with the provided GLoBES AEDL (abstract experiment definition language) file which was changed twice after the paper was issued but is still linked to [72]. It is provided at the GLoBES homepage.

[10]**G**eneral **Lo**ng **B**aseline **E**xperiment **S**imulator

channel	signal			background		
	efficiency	normalization error	tilt	efficiency	normalization error	tilt
$\nu_e \to \nu_\mu$	85%	2%	0.1%	85%	2%	0.1%
$\bar{\nu}_e \to \bar{\nu}_\mu$	85%	2%	0.1%	13%	2%	0.1%

Tab. 6.4: Efficiencies and systematics used for the implementation of the different channels in GLoBES.

estimating the volume as some events will not be fully contained. However, the difference is small as the maximum muon energy is of the order of 400 MeV, resulting in a track length of less than two meters.

Furthermore, the energy response of the detector to a neutrino interaction has to be defined. Given a true neutrino energy E_ν^{mc}, the probability density function $P(E_\nu | E_\nu^{\mathrm{mc}})$ to reconstruct the energy E_ν is called the detector response. GLoBES needs a discrete version of the detector response as input, the migration matrix. It can be calculated from the distribution of reconstructed versus true neutrino energies. Here, the migration matrix is based on the results of the last energy reconstruction that takes also the vertex into account (see Figure 6.15). The energy migration matrices of LENA and MEMPHYS are displayed in Figure 6.16 on the left and right, respectively. To create the migration matrix the systematic shift of the reconstructed compared to the true neutrino energy observed in Figure 6.15 was corrected by increasing the reconstructed neutrino energy by a constant value ($\approx 7\,\mathrm{MeV}$). It is given by the mean deviation of the peak positions in each row determined by Gaussian fits.
Compared to MEMPHYS, the energy resolution obtained with LENA is superior. A water Cerenkov detector is sensitive only to the light from the charged lepton, while the other particles produced at the vertex are below the Cerenkov threshold. Hence, the MEMPHYS reconstruction can only use the method relying on Equation 6.13 to reconstruct the neutrino energy, which is outperformed by the calorimetric measurement based on the total number of photons detected in LENA.

Finally, the signal and background channels as well as their respective efficiencies and cross sections have to be defined. Currently, the ν_μ and $\bar{\nu}_\mu$ appearance channels are implemented while ν_e disappearance is not taken into account, as there is yet no algorithm to discriminate between NC events and CC ν_e events. The corresponding cross sections calculated with GENIE (see Figure 6.4) were used for both signal and background channels.
The current event selection for signal events requires a tagged muon decay to discriminate against NC background, i.e. there is no pulse shape analysis of any kind implemented in the analysis yet. Consequently the LENA detector is sensitive to all CC events of $\overset{(-)}{\nu}_\mu$, the efficiency arising from the probability to tag the muon decay ($\sim 85\%$). This selection criterion also chooses ν_e events featuring charged pions with basically the same efficiency, leading to a significant background in the ν_μ appearance channel. This background is naturally suppressed in the $\bar{\nu}_\mu$ channel as $\bar{\nu}_e$ mainly produce π^- (cf. Section 6.2), which have a high probability to be absorbed in carbon before they decay. Therefore, only 13% of this background are included. Note that no background due to atmospheric neutrinos is considered, i.e. the duration of the beam bunches is assumed to be sufficiently short.
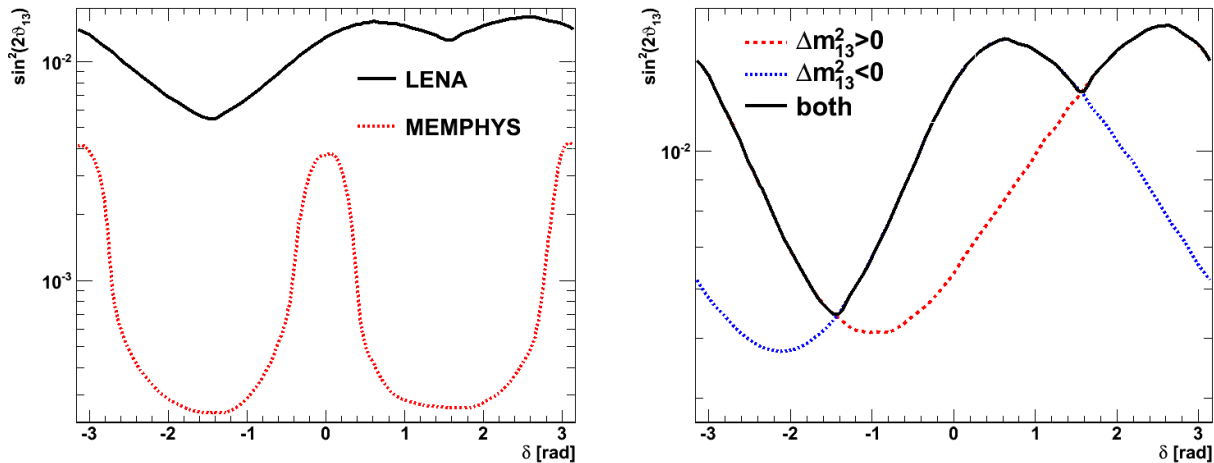
Fig. 6.17: 3-σ discovery potential as a function of δ using a β-beam from CERN to Frejus. On the left the discovery reach of LENA and MEMPHYS is displayed in comparison while on the right the superposition of the obtained discovery reach for LENA of the two possible signs of Δm_{13}^2 is shown. The areas above the lines indicate the parameter space where ϑ_{13} can be discriminated from $\vartheta_{13} = 0$.

The systematic errors implemented are the flux normalization of the β-beam which is assumed to be 2% and a systematic tilt of the energy spectrum, which is set to 0.1% as it should be covered by the migration matrices. Both values are very optimistic, especially the latter as it includes the uncertainty of nuclear effects on the energy resolution. However, they correspond to the assumptions made in [72] for MEMPHYS, therefore allowing a fair comparison. The assumed values for the efficiencies and the systematics are summarized in Table 6.4.

To determine the ϑ_{13} discovery potential, it is advantageous to use the prior knowledge on the other neutrino mixing parameters. The values used for the calculations are taken from Table 1.1. For the corresponding errors the larger of the given 1-σ errors is adopted as symmetric error. As the sign of Δm_{31}^2 is not known, the discovery reach is computed with both signs and the worse result is adopted. Note that the limits in the publication [72] are calculated only for $\Delta m_{13}^2 > 0$, while the limits for MEMPHYS shown in this thesis are computed with the same algorithm as the results for LENA, i.e. including both signs of Δm_{13}^2.

To test whether a β-beam experiment with LENA is able to discriminate a given $\vartheta_{13}^{\mathrm{probe}}$ at a certain δ^{probe} against the hypothesis $\vartheta_{13} = 0$, the same approach as in [72] was chosen: First the expected interaction rates per energy bin assuming $\vartheta_{13} = \vartheta_{13}^{\mathrm{probe}}$, $\delta = \delta^{\mathrm{probe}}$ and the best-fit oscillation parameters are computed. Subsequently, a fit to the obtained interaction spectrum with fixed $\vartheta_{13} = 0$ and free δ is performed. The other values are allowed to vary within their respective errors. If the resulting $\Delta\chi^2(\vartheta_{13} = 0|\vartheta_{13}^{\mathrm{probe}}) > n^2$, $n \in \{1, 2, 3\}$ [99], the experiment is able to discriminate $\vartheta_{13}^{\mathrm{probe}}$ against $\vartheta_{13} = 0$ at the n$-\sigma$ level. Hence, the 3-σ ϑ_{13} discovery potential is given by the value of $\vartheta_{13}^{\mathrm{probe}}$ for which $\Delta\chi^2(\vartheta_{13} = 0|\vartheta_{13}^{\mathrm{probe}}) = 9$.

The fit with fixed ϑ_{13} is currently seeded with δ^{probe}. However, the calculated discovery limit might actually not be reached in an experiment. It might be degraded by degeneracies: As the oscillation formula (6.2) depends on δ and ϑ_{13} there are typically two
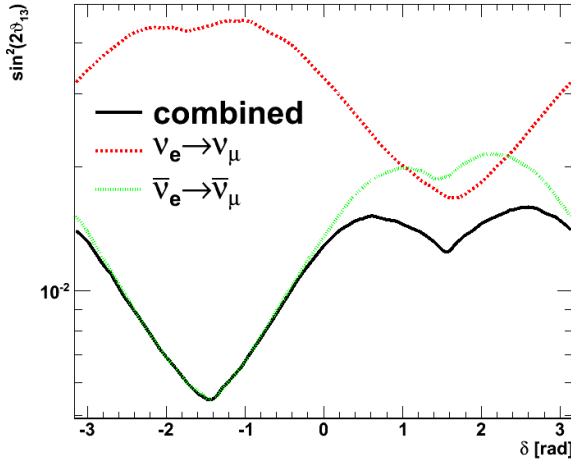
Fig. 6.18: The ϑ_{13} discovery potential as a function of δ for different oscillation channels. The dotted red and the green short dashed curve show the discovery potentials if only the $\nu_e \to \nu_\mu$ or the $\bar{\nu}_e \to \bar{\nu}_\mu$ appearance channel is used. The black line shows the combined discovery potential from both channels.
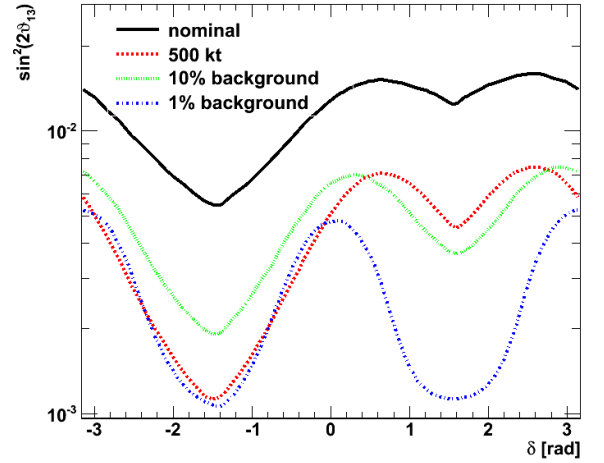
Fig. 6.19: The ϑ_{13} discovery potential as a function of δ for various hypothetical detector configurations. The considered configurations are: A 500 kt LENA and a 50 kt LENA with only 10% and 1% of the nominal background. The performance of the nominal LENA (50 kt, standard background) is shown for comparison.

disconnected solutions in the ϑ_{13}-δ-plane (intrinsic degeneracy). Furthermore, the transition probability also depends on the sign of Δm_{13}^2 which adds another two solutions (hierarchy-degeneracy), leading to a total of 4 possible solutions in the ϑ_{13}-δ-plane [14]. For a detailed study, the fit should be seeded with various δs and both signs of Δm_{13}^2 as input parameters to be sure that there are no further local minima spoiling the obtained discovery limit which is not implemented here due to the substantial computation time needed.

The results are presented in Figure 6.17. On the left, the discovery reach in $\sin^2(2\vartheta_{13})$ is shown as a function of δ for LENA (solid black line) and MEMPHYS (dotted red line). The obtained curve for LENA looks angled as always the worst discovery limit is adopted (depending on the sign of Δm_{13}^2). This is visualized on the right of figure 6.17 where the total discovery reach (solid black) is shown together with the underlying curves for positive (red dashed) and negative (blue dotted) Δm_{13}^2. As expected from Equation (6.2), the curves feature a phase shift with respect to each other. Contrary to the prediction, the shift is smaller than π, because the two channels feature different backgrounds and are inverse in δ. Another feature predicted from Equation (6.2) is visible in the MEMPHYS discovery reach: The sensitivity for a non-zero ϑ_{13} is worst for $\delta \in \{-\pi, 0, \pi\}$ (cf. Section 6.1).

Figure 6.18 displays the composition of the total discovery potential (solid black line) from the individual curves obtained for the $\nu_e \to \nu_\mu$ (red dotted line) and the $\bar{\nu}_e \to \bar{\nu}_\mu$ (vertically dashed green line) appearance channels. While the ν_μ appearance channel is more sensitive to a non-zero ϑ_{13} for $\delta > 0$, it is the other way round for the $\bar{\nu}_\mu$ appearance channel. This is due to the different relative sign of the terms (6.2) and (6.3) compared to the term (6.4). As the pion background is suppressed for the $\bar{\nu}_\mu$ channel, the overall sensitivity to ϑ_{13} is better for the $\bar{\nu}_\mu$ appearance channel compared to the ν_μ appearance

channel.

Compared to LENA, the ϑ_{13} discovery potential of MEMPHYS is about one order of magnitude better. This has two basic reasons:

- The fiducial mass of the MEMPHYS detector is set to 500 kt, i.e. the observed interaction rates for the same beam time are about a factor of ten higher than in LENA.

- The background discrimination is much more efficient than presently in LENA, where, at least for the $\nu_e \rightarrow \nu_\mu$ channel, basically all charged pions contribute to the background. In MEMPHYS, a cut on single ring events basically gets rid of the pions produced due to CC $\overset{(-)}{\nu_e}$ events as they feature two visible tracks (one from the pion and one from the electron) and therefore produce two ring events. This reduces the background by about a factor of ten (see Section 6.2). Subsequently, particle identification algorithms developed by SuperK are applied and additionally a tagged muon decay is required. Both measures reduce the background by nearly another order of magnitude, while keeping about 50% of the signal events [72].

The advantages of LENA, like the lower energy threshold and the better energy resolution, have no significant impact on the ϑ_{13} discovery reach, as most interactions are in the higher energetic part of the spectrum (cf. Figure 6.5) and the oscillation probability at the energies of interest is rather broad (see Figure 6.3).

To assess the impact of both shortcomings of LENA on its performance, the assumed properties of the LENA detector have been varied and the corresponding discovery reaches calculated. The results are displayed in Figure 6.19. The dotted red line shows the obtained ϑ_{13} discovery reach of a hypothetical 500 kt LENA. Is is significantly increased compared to the nominal value. Nevertheless, the performance is still significantly inferior to the performance of MEMPHYS, especially for $\delta > 0$, i.e. for which the ν_μ appearance search severely suffers from background.

In contrast, the green vertical dashed and the blue varying dashed curves show the obtained discovery limit for a (50 kt) LENA with a background which is hypothetically one and two orders of magnitude lower than the background in the nominal configuration. Naturally the reduction of the background level leads to a significantly improved ϑ_{13} discovery potential over the whole range of δ. The effect is most striking for the region with $\delta > 0$ which is most affected by π-background. In this region a reduction of the background by a factor 10 already outperforms the performance of a 500 kt LENA. Note that a higher background suppression also leads to the ϑ_{13} discovery limit being much more symmetric as both the ν_μ and the $\bar{\nu}_\mu$ appearance channels are no longer dominated by background but by limited statistics.

Consequently, the first step in improving the ϑ_{13} discovery reach of LENA is to improve the background discrimination.

It is interesting to compare the discovery reach of LENA with the predicted discovery reach of the Double Chooz experiment which is about $\sin^2(2\vartheta_{13})_{\text{limit}} = 2 \cdot 10^{-2}$. Hence, both experiments preform roughly equal. Nevertheless, the present performance of the LENA detector is still hampered by missing background identification. Given some improvements in this respect, LENA will significantly outperform Double Chooz.

Chapter 7

Measurement of the attenuation length in liquid scintillators

This Chapter presents a laboratory-scale experiment to determine the transparency of liquid scintillators which was designed and constructed in the scope of this thesis. Section 7.1 motivates the construction of the experiment and introduces the measured quantity. The used setup is presented in Section 7.2. The chapter concludes in Section 7.3 with an overview of the current status and planned future measurements.

7.1 Motivation

In a liquid-scintillator detector, photons are generated by charged particles created inside the active volume of the detector. Before they can be detected by the PMTs mounted on the wall of the detector, they have to transverse up to 50 m of liquid scintillator in LENA. The transparency of the scintillator directly influences the number of photoelectrons detected in the PMTs per MeV deposited energy in the scintillator. Hence, it has a strong impact on the energy threshold as well as on the low energy resolution at sub MeV energies. Furthermore, scattering in the scintillator changes the overall pulse shape. Therefore, it influences the low-energy position resolution as well as the tracking capabilities of LENA. For this reason, a precise knowledge of the optical properties of the considered scintillators is a prerequisite for the decision which scintillator to use. Furthermore, the quantities describing the optical properties of the scintillators are important input parameters for Monte Carlo simulations.

A photon propagating an infinitesimally short distance dx through a scintillator, has a probability dp of interacting with the scintillator, which is given by [23]

$$dp = \sum_k \sigma_k n_k \, dx = \rho \sigma \, dx, \quad \sigma := \sum_k \frac{f_k}{m_k} \sigma_k, \tag{7.1}$$

where the sum runs over all constituents of the scintillator, σ_k denotes the interaction cross section, n_k the number density, f_k the mass fraction and m_k the molecular mass of the respective constituent. Hence, the probability P that a photon does not interact while traveling a distance x through the scintillator is given by

$$\frac{dP}{dx} = -P\frac{dp}{dx} = -P\rho\sigma \Rightarrow P(x) = \exp(-\rho\sigma x) = \exp\left(-\frac{x}{\lambda_{\text{att}}}\right), \quad \lambda_{\text{att}} := \frac{1}{\rho\sigma}, \tag{7.2}$$

where λ_{att} is called the attenuation length. Equation (7.2) can be used to predict the intensity $I(x)$ of a parallel, monochromatic beam after transversing a distance x through the scintillator

$$I(x) = I_0 \exp\left(-\frac{x}{\lambda_{\mathrm{att}}}\right), \quad I_0 = I(x = 0). \tag{7.3}$$

Note that to derive equation (7.3) from (7.2) it is important that $I(x)$ contains only the photons with the exact emission wavelength and direction. Therefore, scattered or re-emitted photons are not included in $I(x)$. This cannot be fully achieved in an experiment due to the finite solid angle of the used detector.

Generally, there are multiple processes for a photon to interact with the scintillator, each with its own effective cross section $\sigma^{(i)}$ and associated interaction length λ_i. The overall quantities can be calculated by:

$$\sigma = \sum_i \sigma^{(i)} \quad \Rightarrow \quad \frac{1}{\lambda_{\mathrm{att}}} = \sum_i \frac{1}{\lambda_i}. \tag{7.4}$$

The most common processes in liquid scintillators are:

- **Absorption**
  In liquid-scintillators, absorption by the solvent is negligible in most cases, as the wavelength emitted by the fluor is far from any absorption bands of the solvent. Hence, absorption usually takes place either at the fluor or at small contaminations due to other organic molecules inherent to the scintillator featuring absorption bands in the relevant wavelength region [57]. These impurities are generated during the production process. The absorption of a photon by a scintillator molecule can either result in the energy being lost, i.e. the energy is transformed into internal heat or infrared photons which cannot be detected by PMTs, or the photon being re-emitted in the active wavelength region of the PMTs. In the latter case the re-emitted photons can still contribute to the measured signal. Nevertheless, much of their information is lost, as the re-emitted photon direction is uncorrelated to the previous direction of the photon. Furthermore it is delayed, as reemission is not instantaneous.
  As the various possible outcomes make a crucial difference in liquid scintillators each is associated to its own constant: λ_{abs} for the case of the energy being lost and λ_{iso} for the case the photon being isotropically re-emitted at a detectable wavelength.

- **Rayleigh-scattering**
  The scattering of light on bound electrons of atoms or molecules is called Rayleigh scattering. For wavelengths λ significantly larger than the resonance wavelength λ_0 of the electronic transition, the cross section is proportional to $(\frac{\lambda_0}{\lambda})^4$ [100]. Rayleigh-scattering has to be treated differently from absorption/reemission processes as it is instantaneous and the angular distribution of scattered photons is dependent on the polarization and the direction of the incident light. Hence, it has to be described with its own constant λ_{r}.

- **Mie-scattering**
  Mie scattering describes the interaction of photons with small solid particles, featuring a diameter smaller than the wavelength of the light [100]. The exact differential

cross section is dependent on the particle type (dielectric or metallic) and on the exact size of the scattering center. Up to now, no deviations from the expectations of Rayleigh scattering and isotropic absorption/re-emission have been found for the solvents PXE, LAB and PC (pseudocumene [3]) .[57]. Hence, this component is presently not included in the MC.

To correctly describe light propagation in liquid scintillators the values for λ_{abs}, λ_{iso} and λ_r have to be known. Note that all these quantities are wavelength dependent. Additionally, the index of refraction has to be known as it describes the group velocity of the photons as well as the probabilities for reflection and transmission at the optical boundaries (e.g. PMT glasses).

While all quantities relevant for scattering can be measured by looking at the scattered photons, there is no direct way to measure λ_{abs}. It can only be determined by measuring the attenuation length and the parameters connected to scattering. λ_{abs} is then determined by Equation (7.4) which reads

$$\frac{1}{\lambda_{att}} = \frac{1}{\lambda_{abs}} + \frac{1}{\lambda_{iso}} + \frac{1}{\lambda_r}, \tag{7.5}$$

with the quantities introduced above.

As the attenuation length is an important optical quantity, it was already measured in different setups for different scintillators. In [101], the attenuation length was measured using tubes of 25 cm, 50 cm and 1 m length at selected wavelengths (400, 430 and 450 nm) using different LEDs[1] as light sources. Another measurement, performed in the scope of the Double Chooz experiment, used an UV-Vis-spectrometer to measure the attenuation length for the wavelength region between 200 nm and 800 nm [102]. Here the sample was placed in a 10 cm cell made of quartz glass.

While the experiments provided good results, they both feature one significant shortcoming. The LENA detector is 100 m high and has a diameter of 30 m. To obtain a good signal with sufficient energy and time resolution the attenuation length at the peak emission of the scintillator ($\lambda_{peak} \approx 430$ nm) should be at least some ten meters. This can be achieved by extreme purification of the scintillator. In [41] an attenuation length of more than 10 m obtained for purified LAB at 430 nm is reported, also measured with an UV-Vis spectrometer. The problem is that for $\lambda_{att} \sim 10$ m the attenuation obtained for 1 m tubes or even only 10 cm long measuring cells is very low. As the measured effect is very small, the experiments presented above are very prone to errors and therefore the accuracy obtained for $\lambda_{att} \gtrsim 10$ m is poor.

Hence, an experiment which measures the attenuation length at longer distances is required. In this thesis, the targeted measuring length of 6 m was later reduced to 3 m, due to problems with the collimation optics.

7.2   Setup

Section 7.2.1 introduces the overall setup while the following sections describe in details the fluid handling (Section 7.2.2), the optics (Section 7.2.3) and the used data acquisition electronics (Section 7.2.4). Section 7.2.5 finally presents the data analysis.

---

[1]**L**ight **E**mitting **D**iode
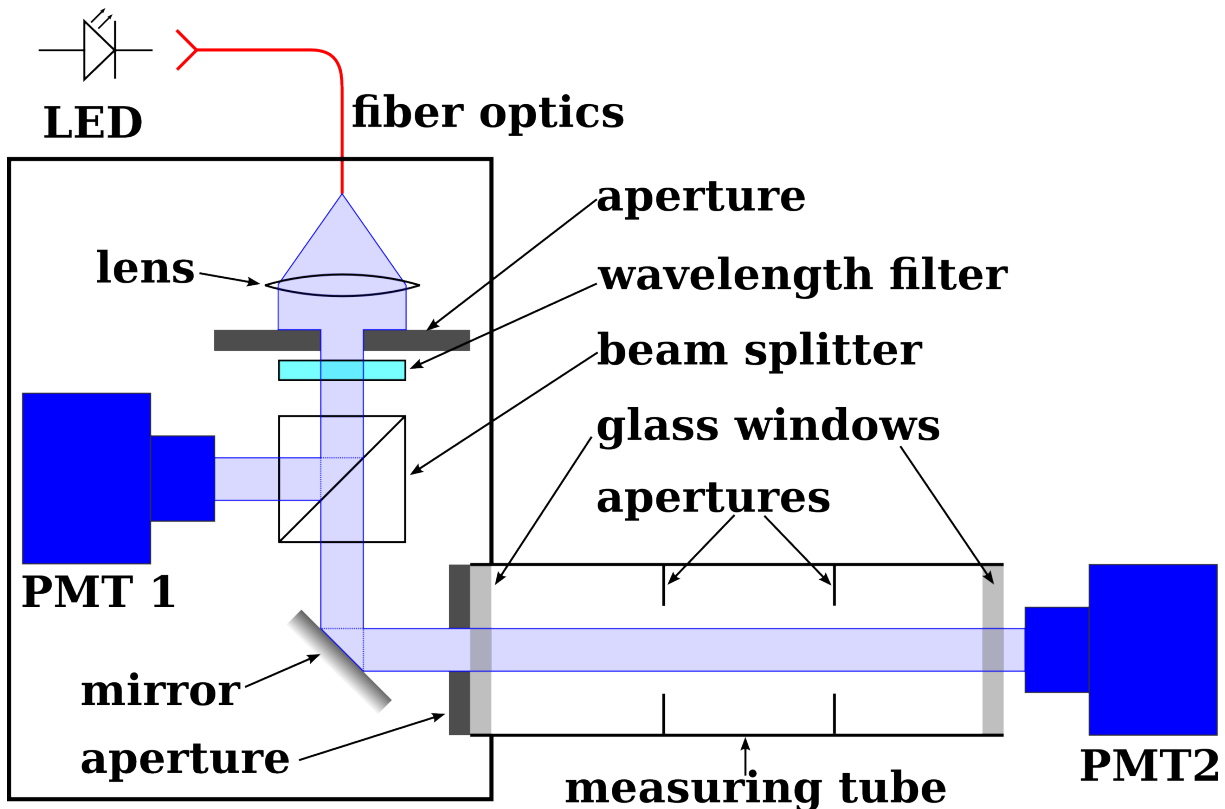
Fig. 7.1: Sketch of the attenuation length setup (not to scale). Light is produced by a LED and coupled into an optical fiber. The light exiting the optical fiber is collimated by a lens and an aperture. A wavelength filter is subsequently used to sharpen the emission spectrum of the LED. The beam is split into two parts by a non-polarizing beam splitter. One part is used to monitor the source intensity by a reference PMT (PMT 1). The other part is coupled into a tube, enclosed by two thin glass windows. The tube can be filled with scintillator. Light exiting the tube is detected by a second PMT. An additional aperture in front of the tube ensures that the beam enters the tube right at its center. Further apertures are installed inside the tube to suppress scattered light.

7.2.1 General Layout

The general idea for the setup is a bigger version of the setup used in [101]. A parallel light beam is propagated through a tube which can be filled with liquid scintillator. Measuring the intensity of the light exiting the tube for an empty (I_e) and a full tube (I_f) and comparing the results for tubes with different lengths allows to determine the attenuation length. The final goal is to measure the attenuation length for tubes from 1 m to 6 m in steps of 0.5 m. Up to now, the optics allows only measurements with a maximum tube length of 3 m.

The increased measurement length as well as the experience gained from previous experiments have motivated second thoughts on a number of subjects in the setup:

- To ensure that the differences between the intensities measured for the full and the empty tube are only due to the effects of the scintillator, it is important to be able to fill the setup without removing the tube. This is also necessary due to practical reasons, as the setup is too large to fit into one single black box. Therefore, the tube has to be fed through the wall of the black box, which makes removing the

tube difficult. Hence, a small-scale liquid handling system (see Section 7.2.2) is used which allows to fill and empty the tube without moving it.

- As the attenuation length is defined via the intensity of a parallel beam, scattered light must not be measured. This is not totally possible in reality, as a fraction of the scattered light will always be detected due to the acceptance angle of the light detector. While the error introduced due to the finite size of the detector is very small, care has to be taken that the tube does not act as a light guide transporting a significant amount of scattered light to the detector. Hence, the tube was blackened using the INOX-SPECTRAL [103] method, as already done in [101]. As a visual inspection of the tube showed that the blackened tube still had a high reflectivity for small scattering angles, additional apertures have been installed inside the tube to further suppress the detection of scattered light.

- For a comparison between different measurements, the intensity of the light source has to be kept constant. As this is difficult to ensure, the intensity of the beam is measured in addition before it enters the tube to correct the results with respect to the strength of the source. Additionally, given a pulsed light source of sufficient intensity, this allows measuring the time of flight through the scintillator and subsequently determining the group velocity.

- In previous measurements, for each measured length, a single tube with the respective length was used. Due to the increased measurement length, this is no longer possible due to economic reasons. Therefore, a modular design is used, which allows to construct tubes with the required lengths from tube segments with about $0.5\,\mathrm{m}$ and $1\,\mathrm{m}$ length.

This considerations resulted in the setup sketched in Figure 7.1. First, light from a LED is collimated to produce a parallel light beam. This beam is subsequently split into two parts, one to measure the source intensity which is detected by PMT 1 while the other is propagated through the tube and detected by a PMT 2. A photo of the setup is displayed in Figure 7.2. The displayed tube has a length of 3 meters. While the optical setup is hidden in the black box, various components of the fluid handling system are visible.

7.2.2   Fluid handling

The fluid handling system has to fulfill multiple purposes. Firstly, it has to allow filling and removal of the scintillator without moving the tube. Secondly, it has to be reliable enough to keep the scintillator in the experiment for typically three days without constant observation, due to the long measurement times. This is also important to allow long-term measurements to check the stability of the results versus time variations. Finally, the fluid system has to prevent any contamination of the scintillator which might result in a degradation of its optical properties. Hence, it has to provide a possibility to purge the tube and the scintillator with nitrogen to prevent oxidation of the scintillator.
The basic setup for the fluid handling system was suggested by [104]. The general idea is to use gravity to fill and empty the tube. Hence, the tube is connected to a scintillator tank with a flexible hose. Therefore, the tube can be filled by lifting the tank onto the so-called scintillator tower, while it can be emptied by setting the tank on the ground. In order to
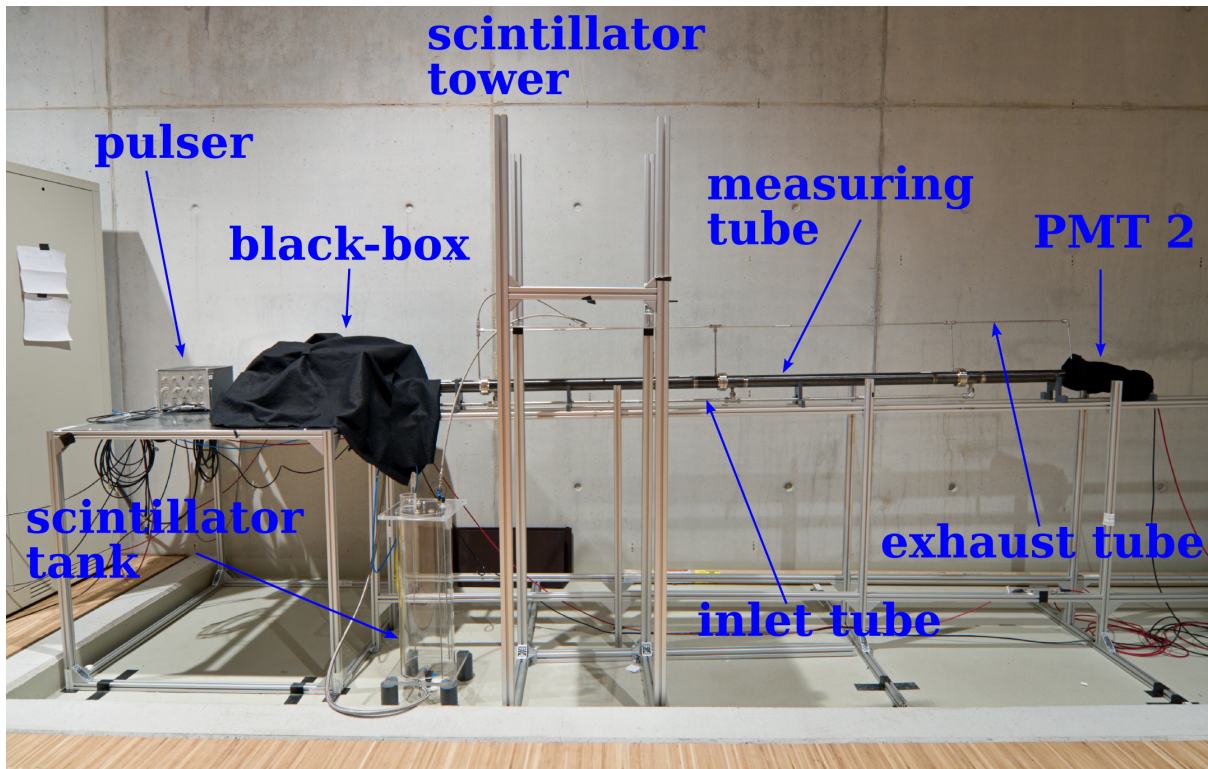
Fig. 7.2: Photo of the overall experimental setup.

keep a closed loop, two hoses are used, one to transport the scintillator between the tank and the measurement tube while the other guides the air from the measurement tube to the tank. As the apertures for suppression of scattered light were positioned between the segments of the tube, each single tube segment has to have its own scintillator inlet and air exhaust to allow for a complete filling and drainage of the tube. The different inlets and exhausts were grouped together to an inlet and an exhaust tube connected to the respective hoses. Furthermore, the tube has a slope of about $2\,\mathrm{cm/m}$ to prevent air bubbles when filling scintillator and to ensure a complete drainage of the scintillator afterwards. All components of the fluid system are clearly visible in Figure 7.2.

To purge the scintillator with nitrogen, the exhaust hose was disconnected from the tank and connected to a nitrogen bottle. Hence, the nitrogen was pressed through the tube and through the scintillator afterwards. This ensures not only a good purging of the scintillator but also removes much of the oxygen from the tube, preventing oxidation of the scintillator from remaining air bubbles.

7.2.3   Optics

The purpose of the optics system is to provide a parallel, monochromatic beam which is able to pass the measurement tube without hitting any of the apertures in the tube. Hence, the maximum beam diameter is given by the diameter of the PMT 2 which is $1\,\mathrm{inch} \approx 2.5\,\mathrm{cm}$.

A LED[2] is used as light source. It is available with a peak wavelength of 430 nm cor-

---

[2]Kingbright L-934MBDL
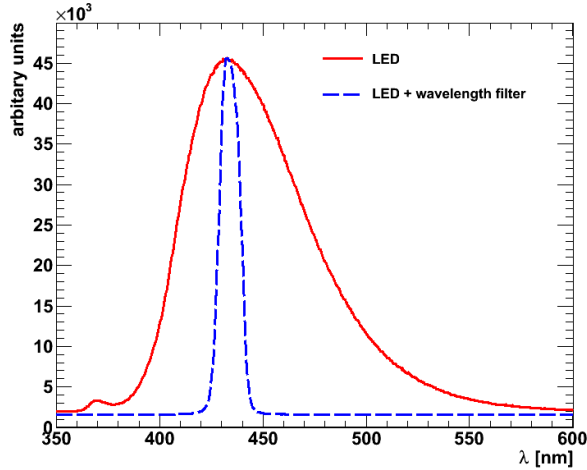
Fig. 7.3: Emission spectrum of the LED with and without wavelength filter. Both spectra are not to scale and have been adjusted to have the same maximum value.
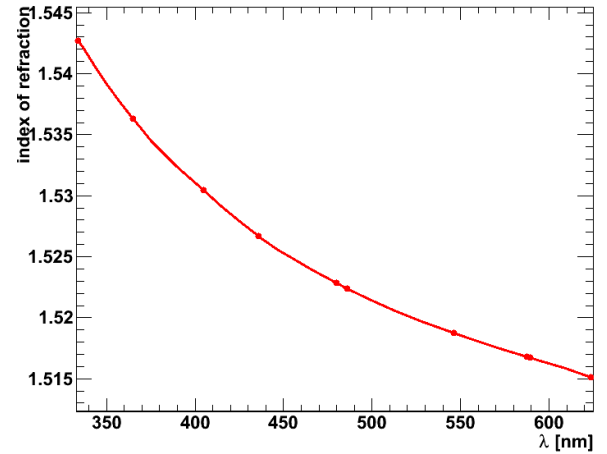
Fig. 7.4: Index of refraction of BK-7 glass as a function of the wavelength [105].

responding to the peak emission wavelength of the scintillator [21]. The LED's emission spectrum, measured using an Ocean Optics Maya 2000 spectrometer, is shown in Figure 7.3. As the spectrum is very broad, a wavelength filter was inserted behind the collimation optics, which restricts the spectrum to the range around 430 nm. The resulting spectrum after the filter is also shown in Figure 7.3. A great disadvantage of the wavelength filter is that it significantly reduces the beam intensity. With the filter in position, the PMTs no longer detect an overall light pulse, but only single photons. As the calibration of the optical system requires a beam which is visible with the naked eye, the calibration of the optical system is done without wavelength filter. Thus, the beam is at least vaguely visible.

For an ideal point-like light source and neglecting any lens errors, a parallel collimated beam of arbitrary diameter can be produced by putting the light source in the focal point of a lens. As any real source is extended, producing a real parallel beam is impossible. The beam diameter d_b in a distance d from the focusing lens with focal length f is [106]

$$d_b = (2 \cdot f \cdot \mathrm{NA} + d_f) + \frac{d_f}{f}d, \tag{7.6}$$

where d_f is the diameter of the source and NA is the numerical aperture of the source. The first term describes the width of the beam at the lens and the second term describes the additional divergence of the beam after the lens. Here a directed source without apertures was assumed. If apertures at the lens position are used, the first term in Equation (7.6) has to be replaced by the diameter of the aperture. An isotropic source corresponds to the case of an aperture with the diameter of the first lens. Note that diffraction was neglected in the derivation of Equation (7.6).

The spread of the beam obviously rises with the diameter of the light source. Therefore, a fiber optics with a core diameter of only $d_f = 100\,\mu$m and a numerical aperture NA $= 0.22$ is used to transport the light from the LED to the collimating system, the core of the fiber being smaller than the active area of the LED. On the one hand, a fiber optics leads to a significant loss in intensity. On the other hand this allows changing the light

source without having to readjust the optics and allows to use the multitude of industrial products developed for fiber optics.

Plugging the properties of the used fiber in Equation (7.6) and minimizing with respect to f yields an optimal focal length of $f = 3.7\,\mathrm{cm}$ for a distance of $d = 6\,\mathrm{m}$. This results in a spread of the beam of $2.7\,\mathrm{mm/m}$. Hence, the total widening of the beam for a 6 m tube is about 1.6 cm, i.e. well within limits. As $d_b(6\,\mathrm{m}) = 3.2\,\mathrm{cm}$ is still too large due to the first term in Equation (7.6), a circular aperture of 5 mm diameter is additionally positioned directly behind the lens.

The desired focal length of the collimating lens is matched very well by the properties of the Fiberguide Industries MACRO Collimator [106] with a nominal focal length of 38 mm. Therefore, it is used in the experiment. Even though the nominal properties of the collimator should be more than sufficient, the achieved result falls short of the expectations. The obtained beam divergence limits the usable tube length to 3 m. There are basically two possible reasons which can cause such a decrease in performance of a lens: Spherical aberration and chromatic aberration. As the lens used in the collimator is semi-planar and the aperture restricts the beam to the area close to the optical axis, the component due to spherical aberration should be negligible here.

The lens used in the collimator is made of BK-7 glass [106]. Its index of refraction as a function of the wavelength is shown in Figure 7.4. Assuming that the lens is perfectly adjusted for $\lambda = 430\,\mathrm{nm}$, a virtual image of the surface of the fiber will be produced at a distance of about 2.4 m in front of the lens at $\lambda = 546\,\mathrm{nm}$ where the LED still has a reasonable light output (see Figure 7.3). As the calibration of the optics has to be done without a wavelength filter to get a visible beam, this is a major problem. Hence, in the future the intensity of the light exiting the fiber optics has to be intensified to allow for a correct calibration of the collimation optics using the wavelength filter. Alternatively, a more monochromatic light source can be used.

After the collimation, the beam passes a non-polarizing beam splitter[3] where it is split into two beams: One for the reference measurements of the source intensity detected by PMT 1 and the other to be sent through the tube. As the tube has a small slope, the light is coupled into the tube using an adjustable mirror[4].

Two glass windows of two millimeters thickness enclose the tube. The glass was tested to be transparent for the light provided by the LED. The entrance window of the tube is covered by another circular aperture of 5 mm diameter to ensure that the beam enters the tube exactly on the tube's symmetry axis. This is important as a non-central beam in the tube is more susceptible to clipping. Furthermore, controlling additionally the centrality of the beam at the end of the tube, this ensures that the beam is not angled with respect to the tube. An angled beam would introduce a systematic error as the path of the beam is changed when the tube is filled with scintillator, due to the different index of refraction of scintillator compared to air.

The optical setup is mounted on an optical table, which is positioned inside a small black box to keep out ambient light. The measuring tube can be inserted through a light-tight opening in the side of the box. In addition, to protect PMT 1 in case the big opening needed for the tube is not totally light tight, it was additionally enclose by a smaller, semi-open box which blocks the direct light path to the entrance of the tube as well as to the collimation optics. The PMT 2 is positioned in an additional small black box,

---

[3]Thor Labs BS013 400-700 nm Beam Splitter Cube 25.4X25.4
[4]Thor Labs BB1-E02, 1 inch broadband mirror, 400-750 nm
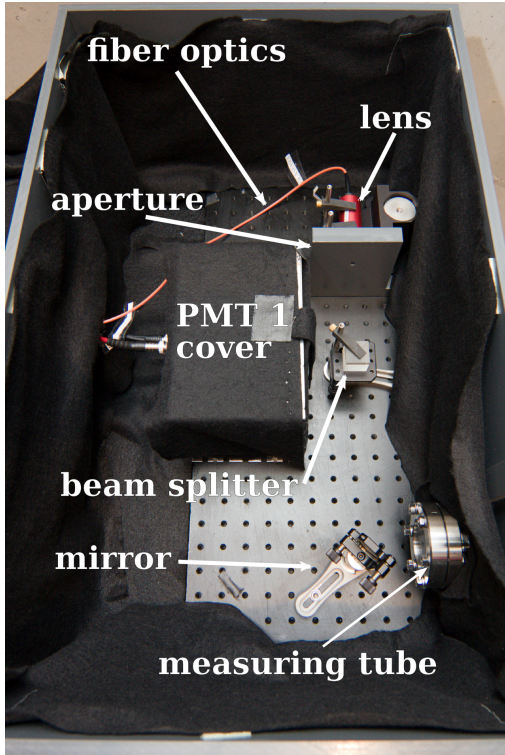
Fig. 7.5: Photo of the optical setup in the black box. Note that the wavelength filter is not shown in this picture. It is installed right after the aperture on its own mount.
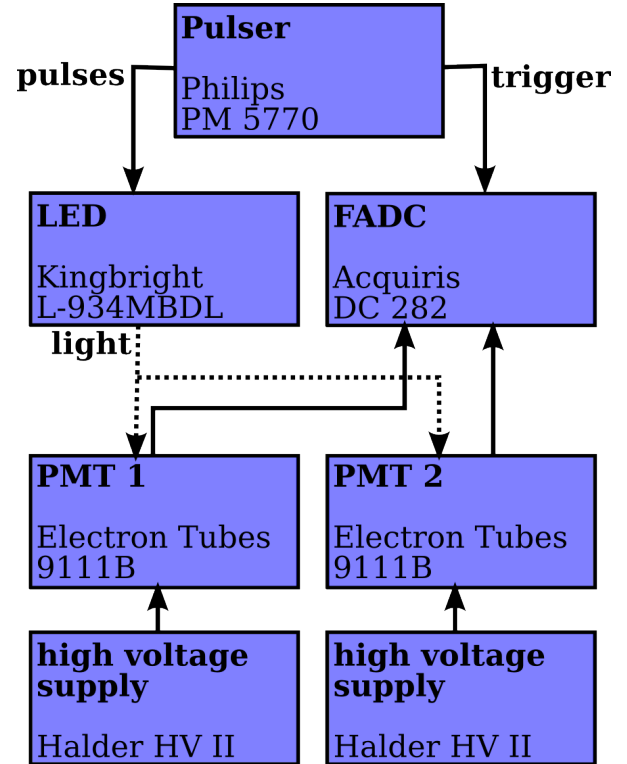
Fig. 7.6: Block diagram of the electronics setup.

mounted at the end of the tube.

Figure 7.5 shows a photo of the optics in the black box.

7.2.4   Electronics and data acquisition

Figure 7.6 shows a block diagram of the used electronic and DAQ components. The setup is fed by a pulse generator[5], which provides the pulses to drive the LED as well as a trigger signal for the DAQ. The pulses used to drive the LED are about 15 ns long. Their peak height was set to the minimum voltage sufficient to achieve saturation in the light output. Using an even higher peak voltage reduces the rise time of the light pulse, but also significantly shortens the lifetime of the LED due to the increased heat production. To additionally prevent the LED from overheating, the repetition rate was set to a relatively low value of 100 Hz.

The light of the reference beam and the beam transversing the tube is detected by two PMTs[6] operated in pulse-counting mode. Both PMTs feature a μ-metal shielding to suppress the influence of the earth's magnetic field, which is of special importance for PMT 2 which changes its position with varying tube length. Both PMTs show significant differences regarding the pulse height obtained for single photons. Hence, for PMT 2 a supply voltage of about -800 V allows single photon counting, while PMT 1 requires at

---

[5]Philips PM 5770

[6]Electron Tubes 9111B with an Electron Tubes RB 1107 Voltage divider

least -900 V to obtain a signal height which is significantly above baseline noise.
The produced signals are fed into a fast flash ADC which forms a compact system with
a readout PC[7]. It allows the sampling of two channels in parallel with a sampling rate of
2 GS/s each, at a resolution of 10 bits. A trigger is provided by the reference signal of the
pulser and is connected to trigger input of the flash ADC. The system is set up to record
the waveforms for $t \in [t_0 - 200, t_0 + 1800]$ ns, where t_0 is the trigger time. Using such a long
gate was necessary as the LED, even though driven with a relatively short pulse, produces
light pulses which decay only relatively slowly ($\tau \sim 400$ ns). For each measurement a total
of 3 000 pulses is recorded and completely saved to disk for subsequent offline analysis.

7.2.5   Data analysis

The data analysis is split up into two steps: First, a quantity $\varrho = a \cdot \frac{I_1}{I_2}$, which is propor-
tional to the ratio of the intensities of the beam measured at PMT 2 (I_2) and the refer-
ence beam (I_1), has to be extracted from the real data. Subsequently, the results from the
measurements of empty and full tubes at different lengths are combined to determine λ_{att}.

The obtained pulses are baseline corrected by averaging over the first 400 samples, i.e.
200 ns of each pulse. As this part of the pulse is before the trigger occurs, no signal
except dark noise of the PMTs is expected in this time window. Along with the baseline
correction, the standard deviation of the baseline noise σ_{bl} is computed.
Subsequently, the pulse heights and times are determined. Note that the obtained pulses
are negative in voltage. To be considered in the analysis, a peak has to deviate from the
baseline by at least $10\sigma_{\mathrm{bl}}$ which is a very conservative choice for the threshold. A peak
inhibits the detection of further peaks in a time window of width $t_{\mathrm{inhibit}} = 8$ ns starting at
the time the peak crosses the threshold. This time window is extended in case the signal
has not returned to the baseline at its end. Enforcing this veto window is necessary as the
PMTs suffered from ringing after the pulse, which is prone to trigger fake pulses without
the inhibit. The peak time and peak height are determined from the sample in the veto
window with the maximum deviation from the baseline.
In first approximation, the number of detected pulses is proportional to the intensity of
the light beam which impinges on the PMT. Due to the dead time of 8 ns after each pulse,
a detected pulse can shadow another pulse which is therefore undetected. Neglecting
the possibility of an extended dead time due to the pulse not being back at the baseline
level after 8 ns and assuming a constant count rate, the effect of the dead time can be
statistically corrected. The true number of pulses N in a time interval T is given by [23]

$$N = \frac{N_{\mathrm{m}}/T}{1 - (N_{\mathrm{m}}/T)t_{\mathrm{inhibit}}}T, \tag{7.7}$$

where N_{m} is the number of measured pulses. Due to the decay of the light pulse generated
by the LED, the obtained count rate is time dependent. Hence, the obtained pulses from
all acquired waveforms from a PMT are histogramed with 1 ns bins and Equation (7.7)
is applied binwise, taking into account that each bin is a superposition of the results
of multiple pulses. This results in an corrected overall number of detected pulses per
measurement and PMT which is be proportional to the intensity of the beam detected by

---

[7]Acqiris DC282 Fast Waveform Digitizer, Agilent Technologies, Santa Clara (US)

the respective PMT. Hence,

$$\varrho := \frac{N_2}{N_1} = a\frac{I_2}{I_1},$$ (7.8)

where $N_{1,2}$ is the corrected overall number of pulses detected on PMT 1 and 2, respectively.

The intensity expected at the PMT 1

$$I_1 = I_s \cdot f_{BS},$$ (7.9)

where I_s is the intensity after the wavelength filter and $f_{BS} \approx 0.5$ is the fraction of the intensity of deflected beam after the beam splitter. Consequently, the intensity at the PMT 2 is

$$I_2 = I_s \cdot (1 - f_{BS})\epsilon_m\epsilon_{ap}T_{AG}^2 T_G T_i^2 \exp\left(-\frac{x}{\hat{\lambda}_{att}}\right),$$ (7.10)

where ϵ_m and ϵ_{ap} are the efficiencies of the mirror and the aperture, T_{AG} denotes the transmission of the air/glass surface, T_i is the transmission of the surface between the glass and the content of the tube, T_G is the transmission of the bulk window and x is the length of the tube. Note that for the case of the empty tube $T_i = T_{AG}$ and $\hat{\lambda}_{att} \to \infty$. Hence, the ratio of the beam intensities I_2 and I_1 is

$$\frac{I_2}{I_1} = \frac{1 - f_{BS}}{f_{BS}}\epsilon_m\epsilon_{ap}T_{AG}^2 T_i^2 T_G^2 \exp\left(-\frac{x}{\hat{\lambda}_{att}}\right),$$ (7.11)

which is independent of the source intensity. Combining the measurements for an empty and a full tube at the same tube length, the ratio $\xi(x)$ of the obtained intensity ratios is given by

$$\xi(x) = \left(\frac{I_2}{I_1}\right)_{full} \Big/ \left(\frac{I_2}{I_1}\right)_{empty} = \left(\frac{T_i}{T_{AG}}\right)^2 \exp\left(-\frac{x}{\lambda_{att}}\right),$$ (7.12)

where λ_{att} is the attenuation length of the liquid scintillator. The value of $\xi(x)$ can also be computed from the experimental results as:

$$\xi(x) = \frac{\varrho_{full}}{\varrho_{empty}},$$ (7.13)

where $\rho_{empty,full}$ are calculated via equation (7.8) using the results of the measurement with empty and full tube, respectively. Hence, λ_{att} can be determined by fitting an exponential to the values $\xi(x)$ obtained by the experiment for different tube lengths. Note that Equation 7.12 only takes its simple form, if all the prefactors of the exponential in Equation (7.11) do not change between the measurement with full and with empty tube. This is the reason why the tube must not be moved during the filling process and why it is so important to achieve a beam which is very well centered with respect to the tube.

7.3   Status of the experiment and outlook

The experiment is fully set up and ready to take data. A few measurements were already conducted: First a series of measurements with ultra pure water was performed. Ultra
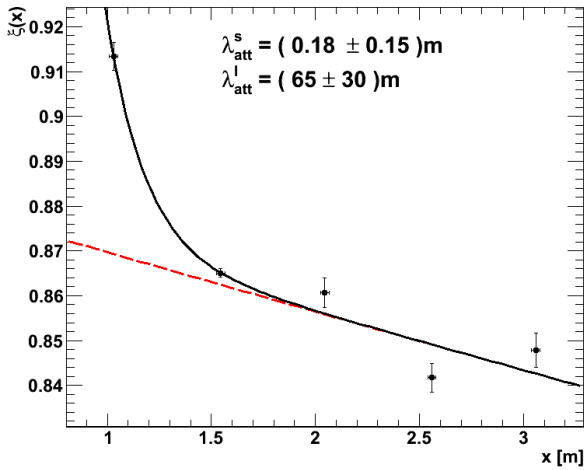
Fig. 7.7: Obtained values for $\xi(x)$ measured with ultra pure water as a function of the tube length. No wavelength filter was used. The fit is performed with a superposition of two exponentials, the exponential belonging to longer attenuation length (λ_{att}^l) is shown as a red dashed line. The obtained attenuation lengths are $(0.18 \pm 0.15)\,\mathrm{m}$ and $(65 \pm 30)\,\mathrm{m}$.
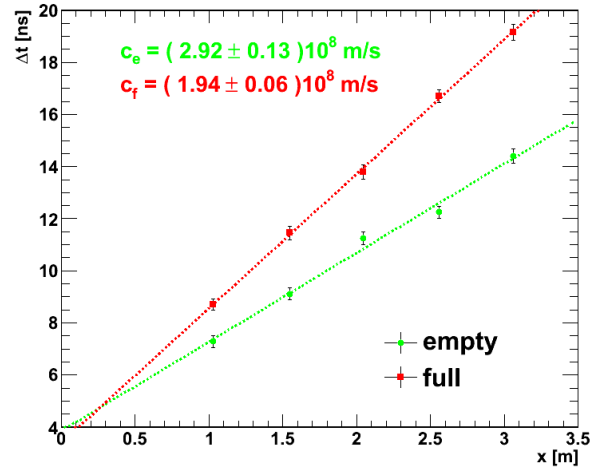
Fig. 7.8: Obtained pulse time differences between the pulses detected at PMT 1 and PMT 2 for a measurement with ultra-pure water. The obtained speeds of light in air and in water are $(2.92 \pm 0.13) \cdot 10^8\,\mathrm{m/s}$ and $(1.94 \pm 0.06) \cdot 10^8\,\mathrm{m/s}$, respectively.
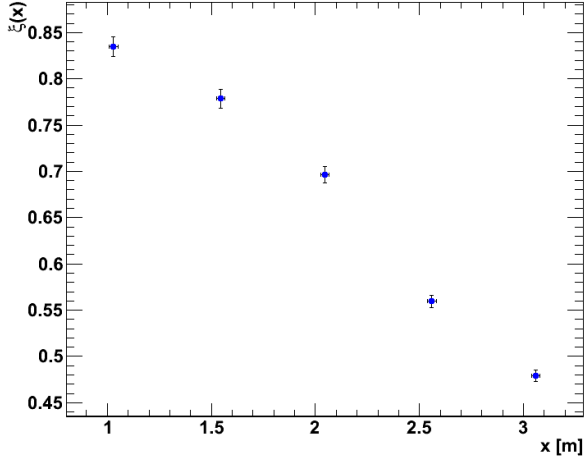
Fig. 7.9: Obtained values for $\xi(x)$ measured for the scintillator solvent LAB as a function of the tube length.
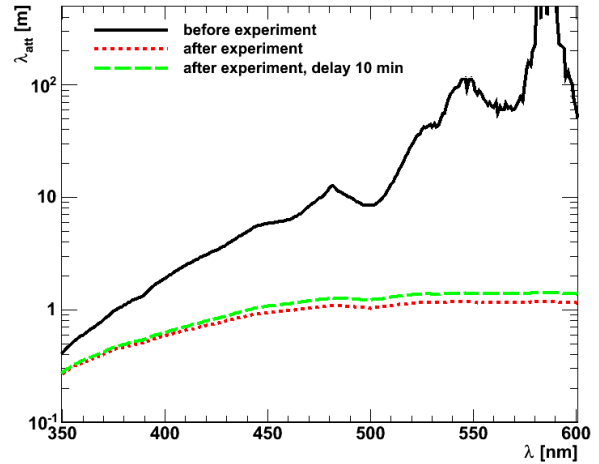
Fig. 7.10: Attenuation length of three LAB samples as a function of the wavelength, measured with an UV-Vis spectrometer. The solid black line shows the result obtained with a sample taken from the original LAB container. The green dashed and red dotted lines show the results of a sample taken directly from the inlet tube after the experiment. The latter curve is the same sample as the former, but the measurement was done 10 min later. The sample was not touched in between.

pure water can have attenuation lengths up to $100\,\mathrm{m}$ as proven by the Super Kamiokande experiment, albeit this takes very sophisticated cleaning and degassing systems. Normal experiments reach some tens of meters [107]. The basic idea is that ultra pure water is nearly totally transparent at the involved length scales. Therefore, $\xi(x)$ is expected to be nearly constant and greater than one, because $T_i > T_{\mathrm{AG}}$ as the differences between the refractive index of water and glass is smaller than the refractive-index difference between air and glass. This was only achieved using very fresh water and short distances.

The measurements with water were done without wavelength filter, as the attenuation length in water is expected to be nearly wavelength independent over the LED spectrum. This allows measuring with overall light pulses instead of single photons. Assuming linearity of the PMTs, ϱ is given by the ratio of the mean areas under the pulses. The obtained results for $\xi(x)$ is shown in Figure 7.7. It can reasonably well be fitted with the superposition of two exponential functions with one short (λ_{att}^s) and one long (λ_{att}^l) attenuation length. Note that the fit is significantly better when done only on $\varrho_{\mathrm{full}}(x)$, as the measurement of the empty tube at $2.5\,\mathrm{m}$ appears in Figure 7.7as an outlier.The fit returns a long attenuation length in the range of about $65\,\mathrm{m}$, which is a bit too short for pure water but the order of magnitude is correct. The short attenuation length is significantly below one meter. A subsequent measurement at an UV-Vis spectrometer showed, that the water was contaminated during the measurement. It showed a slightly increased overall absorption compared to water directly from the water purification system, as well as an additional absorption band at about $(375 \pm 25)\,\mathrm{nm}$. Hence, the absorption band overlaps with the spectrum of the LED. Therefore, one part of the light is attenuated very strongly resulting in the component with the short attenuation length.

Additionally, the measurement with overall pulses allows a determination of the time difference between the arrival times of the light pulses on the two PMTs. The arrival time of one single pulse is determined by a constant fraction discriminator implemented in the analysis software. The obtained mean arrival time differences between the two PMTs are plotted in Figure 7.8. For both, the empty and the full tube, the obtained results can be well fitted with a linear function. The speed of light in the respective medium is given by the inverse slope. For the empty tube, the result is in good agreement with the speed of light in a vacuum ($2.99792458 \cdot 10^8$ m/s [10]). The obtained speed of light in water corresponds to an effective index of refraction of $n_{\mathrm{H_2O}}^{\mathrm{eff}} = 1.51 \pm 0.08$. The deviation of the expected effective index of refraction $n_{\mathrm{H_2O}}^{\mathrm{eff}} = 1.37$ [108, 100] is below 2σ, i.e. it could be due to statistical fluctuations. Another possibility could be the influence of the impurities on the speed of light in water.

In all measurements with ultra pure water, ϱ_{empty} decreased as a function of distance. The total effect was in the order of a few percent. It is currently credited to problems with the collimation, which are most likely due to chromatic aberration as no wavelength filter was used.

In addition to the measurements with water, one complete measurement was done with liquid scintillator. The examined sample was pure LAB from Petresa. Previous measurements showed [102] that the scintillator is basically opaque for wavelengths below $400\,\mathrm{nm}$, Therefore, in this experiment, the wavelength filter was used. Hence, the measurements were done by pulse counting as described in Section 7.2.5. Figure 7.9 shows the results. The obtained values for $\xi(x)$ obviously do not follow an exponential law: Their slope tends to get steeper instead of flatter with rising tube length. Evaluating the first three

data points leads to an attenuation length of about 5.6 m while evaluating the last three points leads to an attenuation length of about 2.7 m, i.e. roughly half the value above.

To interpret this result it is important to note, that the measurement with the shortest tube length was done first. Therefore, the longer the measured tube, the later the measurement was done. Hence, a time dependent contamination of the scintillator was suspected. Consequently, the day after the experiment, one sample was taken directly from the inlet tube and another from the container where the LAB was stored before the experiment. Both samples were compared using an UV-Vis spectrometer. Figure 7.10 shows the results obtained using an analysis similar to that developed in [102]. The attenuation length calculated for the sample from the container (black solid line) is in the range of four to five meters in the wavelength region of the LED with filter. In contrast, the sample taken from the experiment (red dotted line) has an absorption length below 1 m in the same spectral region. This indicates that the measured values suffer from a massive contamination of the scintillator. To asses how much of the contamination is due to suspended particles which might settle to the ground given enough time, the sample from the experiment was remeasured 10 min later. The obtained results (green dashed line) show a slight improvement compared to the direct measurement, which is nevertheless not substantial.

Comparing the results from the UV-Vis spectrometer with the results obtained from the experiment developed in this thesis, the attenuation lengths obtained by combining neighboring $\xi(x)$ are in the range spanned by the red and the black curve in Figure 7.10. This indicates that the experiments seems to work correctly aside except for the contamination of the scintillator.

To get rid of the contamination, it is planned to repeatedly flush the tube with scintillator. As a totally filled tube requires nearly 10 l of scintillator, the scintillator exiting the tube will be filtered and reused for the next loop through the tube. The hope is to clean the tube of all impurities and afterwards be able to measure without contaminations of the fluid.

To improve the optical setup, the first step is to increase the obtained intensity after the collimation system to allow for a better visual inspection of the beam and especially its profile. Given that the chromatic aberration is the main problem concerning the optics, it can basically be solved by using the wavelength filter, provided the intensity is sufficient to calibrate the optics while the filter is in use. Nevertheless, this leads to the problem that a measurement at a different wavelength is very difficult, as the optics would have to be re-calibrated after each change of wavelength. As the wavelength dependency is physically important as λ_{att} strongly varies with wavelength in the region around 430 nm [102], it might become necessary to replace the used lens with a corresponding acromat. Furthermore the current DAQ will be replaced by an VME based system which allows much more freedom in programming the DAQ. Therefore, it might be possible to do some parts of the analysis online, which would be a great aid in rapidly detecting errors or scanning parameters.

To ascertain that the setup is working correctly, a well measured sample, like the scintillator of the Double Chooz experiment has to be studied. After successful verification of its functionality, the setup can be used to study the most promising candidates for the LENA scintillator. According to [43] the most promising candidates for solvents are LAB

or PXE. They will be used together with either the fluor PPO and Bis-MSB as wavelength shifter or with PMP as a single fluor. The assumed concentration for the primary fluor is about $2\,\mathrm{g/l}$ while the secondary fluor is assumed to have a concentration of about $20\,\mathrm{mg/l}$. Additionally there are some new candidates for solvents as, e.g., n-paraffin and DIN (2,5-di-isopropyl-naphtalene).

The first goal is to measure the attenuation length of the proposed scintillators at their proposed composition as well as of the solvent alone and of the solvent together with the primary fluor (in case a secondary fluor is used). Subsequently, the effects of varying the concentrations of primary and secondary fluor have to be tested. For the PPO concentration, [102] reports a decrease of the attenuation length with rising PPO concentration. Due to its small concentration, the effect of the secondary wavelength shifter on the attenuation length is generally thought to be negligible [43], although the experimental verification is still missing. Additionally the effects of different purification methods on the attenuation length have to be studied.

Chapter 8

Conclusions and Outlook

This thesis is centered on the reconstruction of sub-GeV neutrino interactions in the proposed 50 kt liquid-scintillator detector LENA [43]. Atmospheric neutrinos provide a natural source for neutrinos in the relevant energy region. Additionally, long baseline neutrino beams to LENA can deliver neutrinos at the GeV scale. A precise measurement of the flavor dependent energy spectrum of these neutrinos is sensitive to the unknown neutrino oscillation parameters: The mixing angle ϑ_{13}, the CP-violating phase δ and the sign of the atmospheric mass difference Δm_{13}^2.

To reach sufficient sensitivity to neutrino oscillations, the capability to determine the flavor of the incident neutrino is fundamental. While physically impossible for neutral current (NC) interactions, charged current (CC) interactions allow a determination of the neutrino flavor by tagging the produced lepton. As tau production is kinematically forbidden in the given energy range, the possibilities to discriminate electron and muon tracks in LENA were studied using a Geant4-based Monte Carlo simulation of the LENA detector.

First, an attempt was made to exploit the different overall pulse shapes of electrons and muons for particle identification [21]. To isolate the influence of the lepton flavor on the overall pulse shape, the impact of the interaction position on the particle identification was removed by a time of flight correction of the photon hit-times with respect to the barycenter of the event. Using its risetime and the width at 1/6 of its maximum to characterize the pulse, a pure electron track sample could be obtained for kinetic energies above 500 MeV with an efficiency of more than 70%. In contrast, to achieve a pure muon sample, as required for $\overset{(-)}{\nu_e} \to \overset{(-)}{\nu_\mu}$ appearance experiments, a kinetic energy of the final-state leptons of at least 1 GeV is required. Therefore, the muon-track identification currently relies on the detection of the decay electron. For pure lepton tracks, this method suppresses the contamination of the muon sample to below $4.2 \cdot 10^{-4}$ at 95% CL while achieving an efficiency of $(85.1 \pm 1.4)\%$.

In addition to the neutrino flavor, the neutrino energy has to be determined to obtain the neutrino spectrum. Hence, the physical properties of the final-state particles at the neutrino-interaction vertex have to be reconstructed. The dominant CC interaction process in the considered energy range is quasielastic scattering off a nucleon [93]. In this process, the energy of the neutrino is distributed to a recoil nucleon and to a charged lepton. While the range of the recoil nucleon typically is below the spatial resolution of

the detector, the track length of the lepton can reach several meters. An event reconstruction has to determine the vertex of the track as well as its direction and its kinetic energy. In water Cerenkov detectors, this is commonly accomplished by analyzing the spatial distribution of the detected photons. Due to the isotropic photon emission in liquid scintillators, this method is not applicable in LENA. Nevertheless, macroscopic tracks can be reconstructed by additionally taking the arrival times of the detected photons into account [5, 6].

To validate the principle, an algorithm to reconstruct pure muon tracks by a global fit to the integrated charge and the arrival time of the first photon on each PMT was devised. Its start parameters are provided by a set of fast methods (see Section 4.2) using only part of the available information. These estimates already achieved a spatial resolution of about 50 cm for the vertex, an angular resolution of better than 40 degrees, a start-time resolution better than 10 ns and an energy resolution of 0.5% at 300 MeV kinetic energy. Using the global fit improved the spatial resolution of the vertex to the range between 3 and 4 cm, the angular resolution to between 1.5 and 3.5 degrees and the start-time resolution to below 0.1 ns. An energy resolution of about 0.5% was achieved.

Taking the different energy loss of electrons compared to muons into account, the method for the muon-track fitting can be adapted to reconstruct electron tracks. It was supplemented with a specialized algorithm to recognize and correct tracks fitted with flipped directions due to the emission of high-energy bremsstrahlung γ-rays. The obtained spatial vertex resolution is between 3.5 and 6 cm, the angular resolution between 2.5 and 5 degrees and the start-time resolution is about 0.25 ns. The energy resolution was found to be between 0.5% and 1%. While the muon-track reconstruction clearly outperforms the electron track reconstruction, the results of the latter are still remarkably good considering the high event-by-event fluctuations of the electrons.

As the reconstruction of pure tracks works fine, it was extended to cover also full quasielastic muon-neutrino interactions. Hence, the fit additionally has to take the recoil nucleons into account. As the range of the recoil nucleons is typically below the spatial resolution of the detector, they are modeled as a point-like energy deposition at the vertex. The extended algorithm was tested on simulated muon-neutrino events with an energy spectrum corresponding to a $\gamma = 100$ β-beam from CERN to Frejus. Despite the more complex event geometry, the algorithm was found to work reliably for muons with a kinetic energy of $\gtrsim 200$ MeV. The fit achieves a spatial vertex resolution of about 7 cm, an angular resolution between 6 and 3 degrees depending on the energy of the muon track and an uncertainty in the determined kinetic energy of the muon of better than 10%.

Finally, the energy of the neutrino can be determined. As the recoil nucleons cannot be tracked individually, the hit nucleon was assumed to be at rest to fix the scattering geometry. Therefore, the neutrino energy was calculated kinematically from the muon properties. The obtained 1-σ neutrino energy resolution of about 90 MeV was found to be limited by nuclear effects. Their impact can be suppressed by taking not only the kinematics of the muon but also the energy deposited at the vertex into account. Associating the total number of photons in the event with the energy of the incident neutrino already leads to an energy resolution between 5% and 10%.

Subsequently, the performance of the neutrino-flavor discrimination and the reconstruction of the neutrino energy were used to determine the discovery potential for $\sin^2(2\vartheta_{13})$ for a β-beam from CERN to LENA in Frejus. Assuming a running time of four years for neutrinos and antineutrinos each, the discovery potential is in the range of $\sin^2(2\vartheta_{13}) \sim 10^{-2}$. Therefore, the performance is comparable to the Double Chooz Experiment and significantly inferior to a β-beam to the 500 kt water Cerenkov detector MEMPHYS at Frejus [72]. The discovery limit was found to be limited by the (current) inability of LENA to discriminate between ν_μ CC events and ν_e events with charged pions in the final state.

In summary, the possibility to reconstruct sub-GeV neutrino interactions in the LENA detector was successfully verified in simulations. The fitting algorithm is planned to be extended to cover more complex events with multiple tracks extending its applicability to higher energies. Additionally, the influence of detector properties and electronics on the performance of the reconstruction will be studied. Furthermore, the basic principle used to reconstruct lepton tracks in LENA can also be applied to fit contained or cosmic muons in currently existing neutrino detectors like Borexino. This would provide a proof of principle independent of Monte Carlo simulations. Supplementing the work on the track reconstructions, algorithms for a better background suppression for high energy neutrino events have to be developed.

Additionally, an experiment to determine the attenuation length of liquid scintillators was designed and setup in the scope of this thesis. The attenuation length is crucial for the performance of the LENA detector [57] as it strongly influences the number of photoelectrons per deposited energy as well as the measured overall pulse shape. Hence, it affects the energy resolution and threshold as well as the position reconstruction and tracking capabilities of LENA. Thus, it will have a strong impact on the decision which scintillator is used in the experiment. Furthermore, it is an important input parameter for Monte Carlo simulations.

In comparison to previous experiments [101, 102], the main improvement is that the setup allows to measure a light path of several meters in the scintillator. Hence, this experiment will extend the measurement range to scintillators with an attenuation length of more than 10 m as required for detectors of the size of LENA. The design goal was a measurement length of 6 m. Due to problems with the optics, currently only measurements up to 3 m are possible. First measurements were already performed. Due to massive problems with impurities of the samples, so far no conclusive results could be gained. The experiment will be improved and, once working correctly, will provide important input parameters for the decision which scintillator to use in LENA.

Appendix A

Results of muon track reconstruction versus azimuth angle
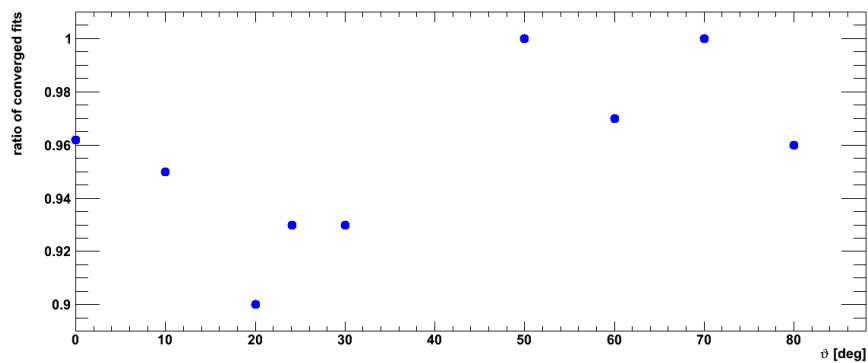
Fig. A.1: Ratio of converged fits versus azimuth angle of the track. The results were obtained using 300 MeV muons starting from the center of the detector. The ratio of converged fits stays above 90% for the whole range of the azimuth angle indicating that the fit works well for all the simulated muons.
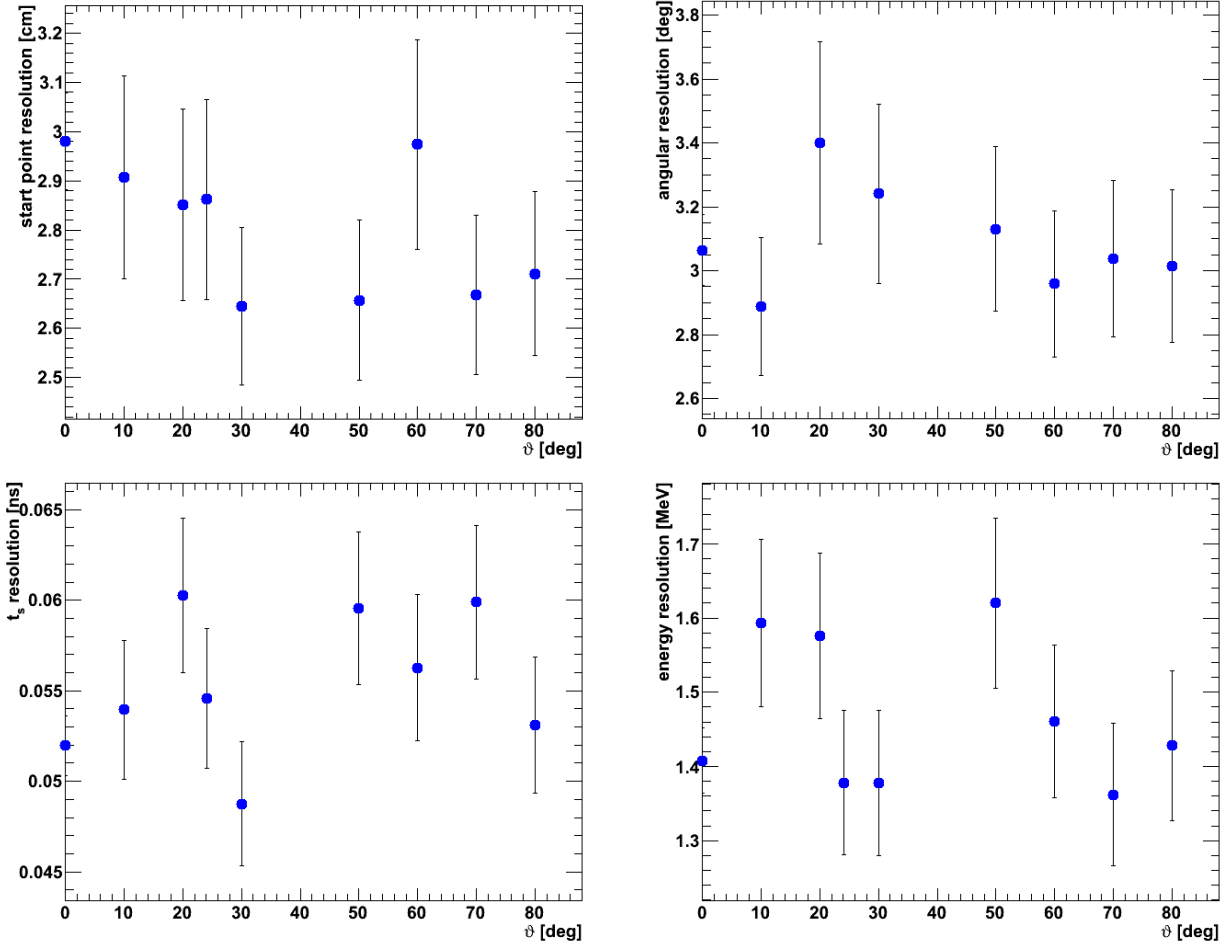
Fig. A.2: Obtained start point resolution, angular resolution, ts-resolution and energy resolution (from top left to lower right) depending on the true azimuth angle of the muons. The results are based on the reconstruction of simulated 300 MeV muons starting in the center of the detector. No significant changes are obtained over the angle.

Bibliography

[1] W. Pauli, *Collected Scientific Papers* (Interscience, New York, 1964).

[2] C. L. Cowan, Jr., F. Reines, F. B. Harrison, H. W. Kruse and A. D. McGuire, Science **124**, 103 (1956).

[3] G. Alimonti *et al.*, Nuclear Instruments and Methods in Physics Research A **600**, 568 (2009), [0806.2400].

[4] S. Abe *et al.*, Physical Review Letters **100**, 221803 (2008), [0801.4589].

[5] J. Peltoniemi, ArXiv e-prints (2009), [0909.4974].

[6] J. G. Learned, ArXiv e-prints (2009), [0902.4009].

[7] N. Schmitz, *Neutrinophysik* (Teubner Verlag, Stuttgart, 1997).

[8] T. Y. M. Fukugita, *Physics of Neutrinos*, 1 ed. (Springer-Verlag, Berlin, 2003).

[9] E. Recami, Electronic Journal of Theoretical Physics **10**, 1 (2006).

[10] C. Amsler et al. (Particle Data Group), Physics Letters **B667**, 1 (2008).

[11] L. Oberauer and F. von Feilitzsch, Reports on Progress in Physics **55**, 1093 (1992).

[12] A. Cervera *et al.*, Nuclear Physics B **579**, 17 (2000), [hep-ph/0002108].

[13] A. Y. Smirnov, Physica Scripta **2005**, 57 (2005).

[14] C. D. Orme, *Phenomenology of long baseline neutrino oscillation Beta Beam experiments and their related technologies*, PhD thesis, Durham University, 2009.

[15] R. Davis, Phys. Rev. Lett. **12**, 303 (1964).

[16] GNO, M. Altmann *et al.*, Phys. Lett. **B616**, 174 (2005), [hep-ex/0504037].

[17] C. Grupen and B. Schwartz, *Particle Detectors*, 2 ed. (Cambridge University Press, 2008).

[18] K. Abe *et al.*, ArXiv e-prints (2010), [1010.0118].

[19] Y. Fukuda *et al.*, Nucl. Instrum. Meth. **A501**, 418 (2003).

[20] A. de Bellefon *et al.*, ArXiv e-prints (2006), [arXiv:hep-ex/0607026].

[21] T. M. Undagoitia, *Measurement of light emission in organic liquid scintillators and studies towards the search for proton decay in the future large-scale detector LENA*, PhD thesis, Technische Universität München, 2008.

[22] G. F. Knoll, *Radiation detection and measurement*, 2 ed. (John Wiley and Sons, 1989).

[23] W. R. Leo, *Techniques for nuclear and particle physics experiments: a how-to approach*, 2 ed. (Springer-Verlag, 1994).

[24] T. Heindl *et al.*, EPL **91**, 5 (2010).

[25] T. Pollmann, Pulse shape discrimination studies in a liquid argon scintillation detector, diplom, Ruprecht-Karls-Universität, Heidelberg, 2007.

[26] A. Rubbia, J. Phys. Conf. Ser. **171**, 012020 (2009), [0908.1286].

[27] A. Rubbia, ArXiv e-prints (2004), [hep-ph/0402110].

[28] S. Amerio *et al.*, Nuclear Instruments and Methods in Physics Research Section A: Accelerators, Spectrometers, Detectors and Associated Equipment **527**, 329 (2004).

[29] B. Choudhary, LBNE : Physics Reach & Status, Talk at the Nufact 2010, Mumbai.

[30] T. Schwetz, M. Tórtola and J. W. F. Valle, New Journal of Physics **10**, 113011 (2008), [0808.2016].

[31] Y. Fukuda *et al.*, Physical Review Letters **81**, 1562 (1998), [hep-ex/9807003].

[32] Y. Ashie *et al.*, Physical Review Letters **93**, 101801 (2004), [hep-ex/0404034].

[33] S. Abe *et al.*, Physical Review Letters **100**, 221803 (2008), [0801.4589].

[34] CHOOZ, M. Apollonio *et al.*, Physics Letters **B466**, 415 (1999), [hep-ex/9907037].

[35] C. Weinheimer *et al.*, Phys. Lett. **B460**, 219 (1999).

[36] S. Hannestad, JCAP **5**, 4 (2003), [astro-ph/0303076].

[37] KATRIN collaboration, ArXiv e-prints (2001), [hep-ex/0109033].

[38] L. Oberauer, F. von Feilitzsch and W. Potzel, Nuclear Physics B - Proceedings Supplements **138**, 108 (2005), Proceedings of the Eighth International Workshop on Topics in Astroparticle and Underground Physics.

[39] M. Wurm *et al.*, ArXiv e-prints (2010), [1004.3474].

[40] BOREXINO Collaboration, ArXiv e-prints (2004), [physics/0408032].

[41] S. E. Quirk, *Purification of Liquid Scintillator and Monte Carlo Simulations of Relevant Internal Backgrounds in SNO+*, PhD thesis, Queen's University, Kingston, Canada, 2008.

[42] L. Oberauer, C. Grieb, F. V. Feilitzsch and I. Manno, Nuclear Instruments and Methods in Physics Research A **530**, 453 (2004), [physics/0310076].

[43] M. Wurm *et al.*, A next-generation liquid-scintillator neutrino observatory, To be published.

[44] R. Möllenberg, Monte Carlo Study of the Fast Neutron Background in LENA, Diploma Thesis.

[45] B. P. Heisinger, *Muonen-induzierte Produktion von Radionukliden*, PhD thesis, Technische Universität München, 1998.

[46] *Dèveloppement et caractérisation d'un ASIC de lecture de macro-cellule de photo-détecteurs de grande dimension*, PhD thesis, Université Paris 11, 2010.

[47] LAGUNA Collaboration *et al.*, ArXiv e-prints (2010), [1001.0077].

[48] A. Rubbia *et al.*, Laguna-lbno, FP 7 Infrastructure proposal, 2010.

[49] D. Autiero *et al.*, JCAP **11**, 11 (2007), [0705.0116].

[50] T. Enqvist *et al.*, CUPP – Centre for underground physics in Pyhäsalmi, in *Physics with a multi MW proton source (Cern Workshop 2004)*.

[51] D. Jolly, 2 Nuclear Power Plants Approved by Finland, newspaper, 2010, The new york times, July 1st, 2010.

[52] J. N. Bahcall, A. M. Serenelli and S. Basu, Astrophys. J. **621**, L85 (2005), [astro-ph/0412440].

[53] The Borexino Collaboration, C. Arpesella *et al.*, Physical Review Letters **101**, 091302 (2008), [0805.3843].

[54] M. Wurm *et al.*, Search for modulations of the solar 7Be flux in the next-generation neutrino observatory LENA, Submitted to Physical Review D.

[55] C. Galbiati *et al.*, Physical Review **C71**, 055805 (2005), [hep-ph/0411002].

[56] D. Franco, G. Consolati and D. Trezzi, Physical Review , 015504 (2011), [1011.5736].

[57] M. Wurm, *Cosmic Background Discrimination for Rare Neutrino Event Search in Borexino and LENA*, PhD thesis, Technische Universität München, 2009.

[58] M. Liebendörfer *et al.*, The Astrophysical Journal Supplement Series **150**, 263 (2004).

[59] M. Rampp, *Radiation Hydrodynamics with Neutrinos: Stellar Core Collapse and the Explosion Mechanism of Type II Supernovae*, PhD thesis, Technische Universität München, Max Plank Institute for Plasma Physics, 2000.

[60] K. Kotake, K. Sato and K. Takahashi, Reports on Progress in Physics **69**, 971 (2006), [astro-ph/0509456].

[61] H. A. Bethe, Reviews of Modern Physics **62**, 801 (1990).

[62] S. Choubey, B. Dasgupta, A. Dighe and A. Mirizzi, ArXiv e-prints (2010), [1008.0308].

[63] M. Wurm *et al.*, prd **75**, 023007 (2007), [astro-ph/0701305].

[64] M. Malek *et al.*, Physical Review Letters **90**, 061101 (2003), [hep-ex/0209028].

[65] A. Kibayashi and for the Super-Kamiokande Collaboration, ArXiv e-prints (2009), [0909.5528].

[66] T. Araki *et al.*, Nature **436**, 499 (2005).

[67] G. Bellini *et al.*, Physics Letters **B687**, 299 (2010), [1003.0284].

[68] K. A. Hochmuth *et al.*, Astroparticle Physics **27**, 21 (2007), [hep-ph/0509136].

[69] Super-Kamiokande, H. Nishino *et al.*, Physical Review Letters **102**, 141801 (2009), [0903.0676].

[70] Super-Kamiokande, K. Kobayashi *et al.*, Physical Review **D72**, 052007 (2005), [hep-ex/0502026].

[71] T. M. Undagoitia *et al.*, Physical Review **D72**, 075014 (2005).

[72] J.-E. Campagne, M. Maltoni, M. Mezzetto and T. Schwetz, JHEP **04**, 003 (2007), [hep-ph/0603172].

[73] J. Peltoniemi, ArXiv e-prints (2009), [0911.4876].

[74] P. Zucchelli, Physics Letters B **532**, 166 (2002).

[75] E. K. Akhmedov, M. Maltoni and A. Y. Smirnov, Journal of High Energy Physics **6**, 72 (2008), [0804.1466].

[76] F. J. P. Soler, C. D. Froggart and F. Muheim, editors, *Neutrinos in particle physics, astrophysics and cosmology* Scottish graduate series (CRC Press, Boca Raton, 2009).

[77] The Geant4 Collaboration, Nuclear Instruments and Methods in Physics Research Section **506**, A250 (2003).

[78] The Geant4 Collaboration, IEEE Transactions on Nuclear Science **53**, 270 (2006).

[79] FJames, *MINUIT-Funciton minimization and error analysis*, CERN, Computing and Networks division, CERN Program Library Long Writeup D506.

[80] I. Antcheva *et al.*, Computer Physics Communications **180**, 2499 (2009), 40 YEARS OF CPC: A celebratory issue focused on quality software for high performance, grid and novel computing architectures.

[81] The ATLAS Collaboration, G. Aad *et al.*, ArXiv e-prints (2009), [0901.0512].

[82] M.J. Berger, J.S. Coursey, M.A. Zucker and J. Chang, ESTAR, PSTAR, and AS-TAR: Computer Programs for Calculating Stopping-Power and Range Tables for Electrons, Protons, and Helium Ions (version 1.2.3), Online database, 2010.

[83] D. E. Groom, N. V. Mokohv and S. I. Striganov, Atomic Data and Nuclear Data Tables **76** (2001).

[84] Atomic and nuclear properties of materials for more than 300 materials, webpage, 2011.

[85] I. Bronstein and K. Semendjajew, *Taschenbuch der Mathematik* (BG Teubner Verlagsgesellschaft, Stuttgart Leipzig und Verlag Nauka, Moskau, 1991).

[86] R. B. Patterson *et al.*, Nucl. Instrum. Meth. **A608**, 206 (2009), [0902.2222].

[87] S. K. Agarwalla, A. Raychaudhuri and A. Samanta, Physics Letters , 33 (2005), [hep-ph/0505015].

[88] Conceptual design report for a beta-beam facility, EUROISOL Internal Task note, 2009.

[89] P. Huber, M. Lindner and W. Winter, Computer Physics Communications **167**, 195 (2005), [hep-ph/0407333].

[90] P. Huber, J. Kopp, M. Lindner, M. Rolinec and W. Winter, Computer Physics Communications **177**, 432 (2007), [hep-ph/0701187].

[91] A. M. Dziewonski and D. L. Anderson, Physics of The Earth and Planetary Interiors **25**, 297 (1981).

[92] F. D. Stacey, *Physics of the Earth*, 2 ed. (John Wiley & Sons Inc, Hoboken, 1977).

[93] C. Andreopoulos *et al.*, Nucl. Instrum. Meth. **A614**, 87 (2010), [0905.2517].

[94] Randolf Möllenberg, Technische Universität München, 2011, Private communication.

[95] S. Zeller, Comparisons of real and simulated data, Talk at NuInt02, Irvine.

[96] H. M. Gallagher, *Neutrino oscillation searches with the Soudan 2 detector*, PhD thesis, University of Minnesota, 1996.

[97] M. Lindroos and T. Nilsson, Nuclear Physics **A746**, 316 (2004), Proceedings of the Sixth International Conference on Radioactive Nuclear Beams (RNB6).

[98] F. M. Dufour, *Precise Study of the atmospheric neutrino oscillation pattern using Super-Kamiokande I and II*, PhD thesis, Boston University, 2009.

[99] K. Nakamura and P. D. Group, Journal of Physics G: Nuclear and Particle Physics **37**, 075021 (2010).

[100] W. Demtröder, *Experimentalphysik 2, Elektrizität und Optik*, 5 ed. (Springer-Verlag, Berlin, 2009).

[101] M. Wurm, Untersuchungen zu den optischen Eigenschaften eines auf PXE basieren-den Flüssigszintillators und zum Nachweis von "Supernovae Relic Neutrinos" mit dem zukünftigen Neutrinodetektor LENA, Diploma Thesis.

[102] J. Meyer, Realization and Characterization of the Muon Veto Scintillator and the Buffer Liquid of the Double Chooz Experiment, Diploma Thesis.

[103] INOX-COLOR GmbH & Co.K, 74725 Walldürn, Deutschland, Webpage, 2011.

[104] Patrick Pfahler, Technische Universität München, 2011, Private communication.

[105] SCHOTT, Data Sheet N-BK 7, 2007.

[106] Fiberguide Industries, Inc, *Collimators & Focus Guides, Technical Data REFER-ENCE SUMMARY*.

[107] J. Napolitano, Water conditioning for the daya bay experiment, Daya Bay Memo, 2007.

[108] M. Daimon and A. Masumura, Applied Optics **46**, 3811 (2007).

Danksagung